

STUDIES ON MICROSTRUCTURAL AND MAGNETOSTRICTIVE  
PROPERTIES OF SINTERED COBALT FERRITE DERIVED FROM  
NANOCRYSTALLINE MATERIALS

THESIS

*SUBMITTED TO THE*

UNIVERSITY OF PUNE

*FOR THE DEGREE OF*

DOCTOR OF PHILOSOPHY

*IN CHEMISTRY*

*BY*

K. KHAJA MOHAIDEEN

*UNDER THE GUIDANCE OF*

DR. P. A. JOY

PHYSICAL AND MATERIALS CHEMISTRY DIVISION

CSIR-NATIONAL CHEMICAL LABORATORY

PUNE 411 008

INDIA

*FEBRUARY 2013*



# सीएसआयआर-राष्ट्रीय रासायनिक प्रयोगशाला

(वैज्ञानिक तथा औद्योगिक अनुसंधान परिषद)

डॉ. होमी भाभा मार्ग, पुणे - 411 008. भारत

**CSIR-NATIONAL CHEMICAL LABORATORY**

(Council of Scientific & Industrial Research)

Dr. Homi Bhabha Road, Pune - 411 008. India.



## CERTIFICATE

Certified that the work incorporated in the thesis

**“Studies on Microstructural and Magnetostrictive Properties of Sintered Cobalt Ferrite Derived from Nanocrystalline Materials”**

submitted by Mr. K. Khaja Mohaideen for the Degree of Doctor of Philosophy in Chemistry was carried out by the candidate under my supervision at the Physical and Materials Chemistry Division of CSIR-National Chemical Laboratory, Pune. Such material as has been obtained from other sources has been duly acknowledged in the thesis.

Date:

**Dr. P. A. Joy**

Place: Pune

(Research Guide)

## DECLARATION

I hereby declare that the thesis entitled “**Studies on Microstructural and Magnetostrictive Properties of Sintered Cobalt Ferrite Derived from Nanocrystalline Materials**”, submitted for the Degree of Doctor of Philosophy in Chemistry to the University of Pune, has been carried out by me at the Physical and Materials Chemistry Division, CSIR-National Chemical Laboratory, Pune, India, under the supervision of Dr. P. A. Joy (Research Guide). The work is original and has not been submitted in part or full by me for any other degree or diploma to this or any other University.

Date:

K. KHAJA MOHAIDEEN

Place: Pune

*...Dedicated to my Parents...*

---

Haji Kamal

Hajiya Vahitha

## ***Acknowledgements***

*Firstly, I would like to express my deepest gratitude to my supervisor, Dr. P. A. Joy for his kind guidance, support and help in many respects throughout the past years. His efforts in imparting the theoretical knowledge and experimental skills in the field of magnetism and materials science are greatly appreciated. I am deeply impressed by his everlasting passion and conscientious attitude to the research, which are invaluable to me and I should treasure forever.*

*I am grateful to the present and past directors of NCL, Dr. Sourav Pal and Dr. S. Sivaram, for allowing me to use the laboratory facilities. I am very much grateful to Dr. Anil Kumar, Chairman, Physical Chemistry Division, for providing me access to the facilities in the division.*

*It gives me great pleasure to thank Dr. B. L. V. Prasad, Dr. P. P. Wadgaonkar, Dr. P. Manikandan, Mr. Menon, Dr. T. Raja and Dr. Gopinath for their valuable advice and help. I extend my gratitude to Mr. Deepak Jori, Mr. Punekar, Mr. Akbar and other office staffs for their timely help.*

*I thank all my seniors Dr. Joly, Dr. Deka, Dr. Shekhar, Dr. Raj and Dr. Seema for their help in my initial days in NCL. I would like to thank my colleagues Vijay and Sreeja for the nice time I shared with them. Also, I would like to thank late Harwade kaka for his care and help.*

*I had a nice time with all my labmates Mangesh, Pankaj, Lenin, Bindhu, Govind, Ramsundar, Jaya, Anjali, Manju, Ananth and Mohan. Constant interaction with them has gone a long way in helping me with my research work and also in maintaining a friendly working atmosphere in the group. Many thanks to them.*

*Also it gives me immense pleasure to express my sincere thanks to my friends Kannan, Dharma, Nagaraj, Deepak, Sridhar, Mohanraj, Ansary, Palani, Joyashish, Naren, Ketan, Edwin, Pandi, Anuj, Arul, Ashok, Raja, Vilas, Ravi, Bala, Dhanraj, Beena, Rajesh, Jijil, Soumya and Ashok for providing me with an excellent working ambience during the course of this work.*

*I would like to thank my seniors and friends Drs. Selva kannan, Pradeep, Bala, Mallikarjuna, Selva kumar, Ramesh and Shankar for their all kind of help extended to me. Their company provided me joyful moments during the stay in Pune. My special thanks to Balaji anna and his family for their support.*

*The words are not enough to express all my love and thankfulness towards my parents for allowing me to pursue my research. It is because of their blessings that I could reach here. It gives me a great pleasure to thank my brothers Rafik, Jaffar, Syed, Kumaran, sister Suraiya and Brother-in-law Jamal for their love, encouragement and never failing support shown during my research work. Special thanks to Rekha for her love, care and moral support.*

*I deeply acknowledge CSIR, New Delhi for financial assistance for my research work and granting Senior Research Fellowship.*

*I thank all those who have helped me directly and indirectly for the successful completion of my research work.*

K. KHAJA MOHAIDEEN

# Contents

<b>Abstract</b>	<b>1</b>	
<b>Chapter 1: Introduction</b>	<b>4</b>	
1.1	Materials Science	4
1.2	Functional Materials	5
1.3	Smart Materials	5
1.4	Nanomaterials	7
1.5	Magnetism	9
1.6	Spinel Type Ferrites	12
1.6.1	Crystal Structure of Spinel Ferrites	12
1.6.2	Magnetic Properties of Spinel Ferrites	14
1.7	Magnetic Anisotropy	15
1.8	Magnetic Domains	18
1.9	Magnetization Process	19
1.10	Magnetic Nanomaterials	20
1.11	Magnetostriction	23
1.11.1	Mechanism of Magnetostriction	25
1.11.2	Applications of Magnetostriction	25
1.11.3	Magnetostrictive Materials	27
1.11.4	Oxide Based Magnetostrictive Materials	29
1.11.5	Magnetostriction of Cobalt Ferrite	31
1.12	Scope of the Present Work	35
References		37

<b>Chapter 2: Experimental Methods</b>	<b>44</b>
2.1	Introduction 44
2.2	Methods of Synthesis 44
2.2.1	Ceramic Method 45
2.2.2	Autocombustion Method 46
2.2.3	Co-precipitation Method 48
2.2.4	Citrate Method 50
2.3	Compaction 50
2.4	Sintering 51
2.5	Characterization Techniques 52
2.5.1	Powder X-Ray Diffraction (XRD) 52
2.5.2	Transmission Electron Microscopy (TEM) 54
2.5.3	Scanning Electron Microscopy (SEM) 54
2.5.4	Vibrating Sample Magnetometer (VSM) 55
2.5.5	Thermo-Mechanical Analysis (TMA) 57
2.5.6	Density Measurements 59
2.5.7	Magnetostriction Measurements 61
References	64
<b>Chapter 3: Effect of Particle Size on the Magnetostriction of Sintered Cobalt Ferrite</b>	<b>68</b>
3.1	Introduction 68
3.2	Synthesis 70
3.3	Studies on As-synthesized Powder Samples 72
3.3.1	Phase Purity and Structural Characterization 72
3.3.2	Magnetic Measurements 77
3.3.3	TMA Analysis 82
3.4	Studies on Sintered Samples 83
3.4.1	XRD Studies 83
3.4.2	Density Measurements 85
3.4.3	Magnetic Measurements 86

3.4.4	Magnetostriction Studies	88
3.4.5	Microstructure	92
3.4.6	Effect of Particle Size	92
3.4.7	Effect of Magnetic Field Annealing	102
3.5	Conclusions	107
	References	109
<b>Chapter 4: Effect of Sintering Conditions on the Magnetostriction of Cobalt Ferrite</b>		<b>114</b>
4.1	Introduction	114
4.2	The Sintering Process	117
4.3	Studies on Sintered Samples	118
4.3.1	Microstructure and Density	118
4.3.2	Magnetic Properties	125
4.3.3	Magnetostriction Studies	128
4.3.4	Magnetic Field Annealing Studies	134
4.4	Conclusions	138
	References	139
<b>Chapter 5: Magnetostriction Studies on Self-Composites of Sintered Cobalt Ferrite</b>		<b>141</b>
5.1	Introduction	141
5.2	Preparation of Self-Composites	142
5.3	Magnetostriction Studies on Self-Composites	142
5.3.1	Two-Component Systems	142
5.3.2	Three-Component Systems	151
5.3.3	Effect of Magnetic Field Annealing	153
5.4	Microstructure	158
5.5	Discussion	158
5.6	Conclusions	164
	References	165

<b>Chapter 6: Magnetostriction Studies on Mn Substituted Cobalt Ferrite</b>	<b>166</b>
<b>Derived from Nanocrystalline Powders</b>	
6.1 Introduction	166
6.2 Synthesis	168
6.3 Results and Discussion	169
6.3.1 Powder XRD Analysis	169
6.3.2 Magnetic Measurements	172
6.3.3 Microstructure	177
6.3.4 Magnetostriction Studies	177
6.3.5 Effect of Sintering Temperature on $\text{CoFe}_{1.8}\text{Mn}_{0.2}\text{O}_4$	182
6.3.6 Effect of Magnetic Annealing on $\text{CoFe}_{1.8}\text{Mn}_{0.2}\text{O}_4$	184
6.4 Conclusions	186
References	187
<b>Chapter 7: Conclusions and Future Perspectives</b>	<b>189</b>

# List of Tables

1.1	Crystal types of ferrites.	12
1.2	Magnetostriction of some polycrystalline materials at room temperature [7].	29
1.3	Comparison of the physical properties of Terfenol-D and Cobalt Ferrite [7].	32
3.1	Details of the cobalt ferrite samples synthesized by the autocombustion method using metal nitrates and glycine.	73
3.2	Magnetic properties of the as-synthesized powder samples. M is the magnetization at 1200 kA/m, the highest field used for the measurement.	78
3.3	Magnetic and magnetostrictive properties of sintered pellets.	89
3.4	Details of the calcined G2 powders.	94
3.5	Magnetic and magnetostrictive characteristics of sintered pellets derived from as-synthesized and calcined G2 powders.	96
3.6	Different properties of as-synthesized powder samples synthesized by the co-precipitation and citrate precursor methods.	98
3.7	Magnetic and magnetostrictive properties of sintered pellets obtained by co-precipitation and citrate methods.	100
3.8	Comparison of the magnetostrictive properties of sintered pellets derived from powders of comparable sizes obtained by different synthesis methods.	101
3.9	Magnetostrictive properties of different samples, before and after magnetic field annealing.	103
5.1	Weight percentages of the powders G1 and G8 used for making the self-composites and the magnetostriction parameters.	144
5.2	Effect of sintering temperature on the magnetostriction characteristics of the self-composite with 80% G1 and 20% G8.	146
5.3	Characteristics of the self-composites with 80% G1 and 20% of different powder samples, sintered at 1450 °C.	146
5.4	Characteristics of the sintered self-composite with 80% G2 and 20% G8 as	147

well as G0.

- 5.5 Characteristics of the self-composites with varying ratios of G2 and G0, sintered at 1400 °C for 10 minutes. 151
- 5.6 Magnetostrictive properties of the three-component self-composites. 152
- 5.7 Magnetostriction characteristics before and after magnetic annealing for the two component self-composites, compared with the individual components. 156
- 6.1 Magnetic properties of the sintered samples of Mn substituted cobalt ferrite. 175
- 6.2 Magnetostrictive properties of  $\text{CoFe}_{2-x}\text{Mn}_x\text{O}_4$  and  $\text{Co}_{1-x}\text{Mn}_x\text{Fe}_2\text{O}_4$  series of compositions. 178
- 6.3 Properties of  $\text{CoFe}_{1.8}\text{Mn}_{0.2}\text{O}_4$  sample sintered at different temperatures. 183
- 6.4 Magnetostrictive properties of  $\text{CoFe}_{1.8}\text{Mn}_{0.2}\text{O}_4$  sample before and after magnetic field annealing. 186

# List of Figures

1.1	Different types of magnetism.	11
1.2	The crystal structure of spinel ferrites.	13
1.3	Spin-lattice-orbit interactions.	16
1.4	Schematic representation of the breakup of magnetization into domains. (a) Single domain, (b) Double domain, (c) Four domains, (d) Closed domain.	18
1.5	The magnetization process and a typical magnetic hysteresis loop.	20
1.6	The magnetostrictive effect, $\Delta L$ , is caused by the alignment of magnetic domains in a material due to a magnetic field, H.	24
1.7	Strain versus magnetic field, schematically.	26
1.8	The idealized behavior of length change corresponding to applied magnetic field.	26
2.1	Schematic diagram of the VSM components.	56
2.2	Schematic diagram of a Thermo-Mechanical Analyzer.	58
2.3	Schematic diagram of a strain gage.	62
3.1	Powder XRD patterns of as-synthesized cobalt ferrite powders using different glycine/nitrate ratios (G1 to G13) as well as by the ceramic method (G0). Impurity peaks are marked as *FeO and #Fe.	74
3.2	Variation of flame temperature and crystallite size with glycine/nitrate ratio.	75
3.3	TEM micrographs of some of the cobalt ferrite powders synthesized by the autocombustion method.	77
3.4	Room temperature M vs H curves of the as-synthesized powder samples.	79
3.5	Enlarged M-H curves of G1 and G2.	79
3.6	Zero field cooled (ZFC) and field cooled (FC) magnetization curves of G1 and G2, measured in a field of H=8 kA/m (100 Oe).	80
3.7	M-T curves of as-synthesized cobalt ferrite powders from different glycine/nitrate ratios compared with ceramic sample.	81

3.8	Sintering behavior of the cobalt ferrite samples synthesized from different glycine/nitrate ratios compared with ceramic sample.	82
3.9	Powder XRD patterns of the sintered samples.	84
3.10	Density of the sintered products as a function of G/N ratio.	85
3.11	Room temperature magnetization curves for the different sintered cobalt ferrite samples.	86
3.12	M-T curves of the sintered cobalt ferrite samples, measured in a magnetic field of 8 kA/m (100 Oe).	87
3.13	Magnetostriction curves of different sintered samples as a function of magnetic field measured along the parallel ( $\lambda_{\text{par}}$ ) and perpendicular ( $\lambda_{\text{per}}$ ) directions. The magnetostriction of the ceramic sample (SG0) is shown for comparison.	90
3.14	Strain derivative of different sintered samples as a function of magnetic field measured along the parallel direction.	91
3.15	Variation of (a) maximum value of magnetostriction along the parallel direction, (b) strain derivative, (c) anisotropic magnetostriction and (d) volume magnetostriction as a function of the particle size of the starting powders.	91
3.16	SEM images of the sintered samples. All micrographs shown are under the same magnification.	93
3.17	Powder XRD patterns of as-synthesized and calcined G2 powders.	94
3.18	Room temperature magnetization curves of the as-synthesized and calcined G2 powders.	95
3.19	Magnetostriction curves of different sintered samples derived from G2 as a function of magnetic field measured along the parallel ( $\lambda_{\text{par}}$ ) direction.	95
3.20	SEM images of the sintered samples derived from G2. All micrographs are under the same magnification.	96
3.21	Powder XRD patterns of $\text{CoFe}_2\text{O}_4$ samples synthesized by the citrate-gel and co-precipitation methods.	97
3.22	Room temperature magnetization curves of the as-synthesized powders synthesized by the co-precipitation and citrate methods.	98

3.23	Magnetostriction as a function of magnetic field recorded in the parallel direction to the applied magnetic field.	99
3.24	SEM images of the sintered samples synthesized by (a) co-precipitation and (b) citrate-gel methods.	100
3.25	Magnetostriction as a function of magnetic field recorded in the parallel direction to the applied magnetic field, for sintered pellets derived from powders of comparable sizes obtained by different synthesis methods. The sample codes are defined in Table 3.8.	101
3.26	Magnetostriction curves of SG0, SG1, SG2 and SG8, as a function of magnetic field, along the parallel (circles) and perpendicular (squares) directions. The open and closed symbols represent measurements before and after annealing in a field of 400 kA/m, respectively.	104
3.27	Field derivative of the magnetostriction for SG0, SG1, SG2, and SG8, parallel to the applied magnetic field. The open and closed symbols represent measurements before and after annealing in a field of 400 kA/m, respectively.	105
3.28	Anisotropic magnetostriction of SG0, SG1, SG2 and SG8 along the parallel direction. The open and closed symbols represent the measurements before and after annealing in a field of 400 kA/m, respectively.	106
4.1	Schematic representations of the sintering schedules of (a) single-stage sintering and (b) two-stage sintering or dual sintering.	116
4.2	SEM images of the single stage sintered samples, sintered at (a) 1500 °C, (b) 1450 °C, (c) 1400 °C, (d) 1300 °C, and (e) 1200 °C.	119
4.3	Variation of density as a function of sintering temperature for single stage sintered samples.	120
4.4	SEM images of two-stage sintered samples ( $T_1 = 1450$ °C and $T_2 = 1300$ °C) with different holding time at the lower temperature; (a) 10 min, (b) 1 h, (c) 5 h, (d) 10 h, (e) 20 h, (f) 40 h, and (g) 60 h.	121
4.5	Variation of density as a function of holding time for $T_1 = 1450$ °C and $T_2 = 1300$ °C.	122
4.6	SEM images of the two-stage sintered samples with $T_1 = 1450$ °C and	123

- different lower temperatures,  $T_2$  as (a) 1100 °C, (b) 1200 °C, (c) 1300 °C, (d) 1400 °C. The numbers on the right hand side corner indicate the density of the corresponding samples.
- 4.7 SEM images of the two-stage sintered samples with fixed holding time at different  $T_1$  and  $T_2$  as (a) 1500/1300 °C, (b) 1450/1300 °C, (c) 1350/1200 °C, (d) 1300/1150 °C, (e) 1250/1100 °C and (f) 1100/1000 °C. The numbers on the right hand side corner in the individual micrographs indicate the density of the corresponding samples. 124
- 4.8 Comparison of the room temperature initial magnetization curves of single stage sintered samples. Inset: Variation of coercivity as a function of sintering temperature. 125
- 4.9 Initial magnetization curves of two-stage sintered samples ( $T_1 = 1450$  °C,  $T_2 = 1300$  °C) for different holding times. Inset: coercivity as a function of holding time. 126
- 4.10 Room temperature initial magnetization curves of two-stage sintered samples, (a) for  $T_1 = 1450$  °C and at different  $T_2$ . Inset: variation of coercivity as a function of  $T_2$ ; (b) both  $T_1$  and  $T_2$  varied as indicated, inset: variation of coercivity as a function of  $T_1$ . 127
- 4.11 Magnetostriction curves measured along the parallel ( $\lambda_{\text{par}}$ ) and perpendicular ( $\lambda_{\text{per}}$ ) directions to the applied magnetic field for the samples sintered (single stage) at different temperatures. 129
- 4.12 (a) Variation of the maximum value of magnetostriction as a function of sintering temperature and (b) strain derivative of samples sintered at different temperatures as a function of magnetic field, measured along the parallel direction. 130
- 4.13 Magnetostriction curves measured along the parallel ( $\lambda_{\text{par}}$ ) and perpendicular ( $\lambda_{\text{per}}$ ) directions to the applied magnetic field for the two-stage sintered samples ( $T_1 = 1450$  °C,  $T_2 = 1300$  °C) with different holding time, as indicated. 131
- 4.14 Variation of the (a) maximum value of magnetostriction and (b) strain derivative along the parallel direction as a function of holding time for the 132

two-stage sintered samples for  $T_1 = 1450\text{ }^\circ\text{C}$  and  $T_2 = 1300\text{ }^\circ\text{C}$ .

- 4.15 Magnetostriction curves measured in the parallel direction for the two-stage sintered samples for  $T_1 = 1450\text{ }^\circ\text{C}$  and for different  $T_2$ , as indicated. 133
- 4.16 Magnetostriction curves measured in the parallel direction to the applied magnetic field for the two-stage sintered samples for different values of  $T_1$  and  $T_2$ , as indicated. 133
- 4.17 (a) Magnetostriction of single stage sintered sample (at  $1200\text{ }^\circ\text{C}$ ) as a function of magnetic field, along the parallel (circles) and perpendicular (squares) directions. (b) Field derivative of magnetostriction along the parallel direction. The open and closed symbols represent before and after magnetic field annealing, respectively. 135
- 4.18 (a) Magnetostriction of two-stage sintered sample as a function of magnetic field, along the parallel (circles) and perpendicular (squares) directions. (b) Field derivative of magnetostriction along the parallel direction. The open and closed symbols represent before and after magnetic field annealing, respectively. 136
- 5.1 Magnetostriction curves measured in the parallel direction for two-component self-composites derived from powders of G1 and G8. The numbers indicate weight percentages of the individual powders. 143
- 5.2 Magnetostriction curves measured in the parallel direction for self-composite of G1 and G8 (80:20) sintered at different temperatures. 145
- 5.3 Magnetostriction curves measured in the parallel direction for self-composites derived from 80% of G1 and 20% of different starting powders of G2, G8 and G0. 147
- 5.4 Magnetostriction curves measured in the parallel direction for the self-composites of G2 and G8 (80:20) sintered at different temperatures. 148
- 5.5 Magnetostriction curves measured in the parallel direction for the self-composites of G2 and G0 (80:20) sintered at different temperatures. 149
- 5.6 Magnetostriction curves measured in the parallel direction for the self-composites derived from powders G2 and G0 for varying compositions and sintered at  $1400\text{ }^\circ\text{C}$ . The numbers indicate weight percentages of the 150

- individual powders.
- 5.7 Magnetostriction curves measured in the parallel direction for the three- 153  
component self-composite samples. The sample codes are defined in Table  
5.6.
- 5.8 Magnetostriction curves of the two-component self-composites G1/G8, 155  
G1/G0 and G8/G0, as a function of magnetic field, measured parallel to the  
applied magnetic field before and after annealing in a field of 400 kA/m and  
field derivative of magnetostriction along the parallel direction for the  
different composites. The open and closed symbols represent before and  
after magnetic field annealing, respectively.
- 5.9 (a) Magnetostriction curves of the three-component self-composite 157  
G1/G8/G0 as a function of magnetic field, measured parallel to the applied  
magnetic field before and after annealing in a field of 400 kA/m and (b) field  
derivative of magnetostriction along the parallel direction. The open and  
closed symbols represent before and after magnetic field annealing,  
respectively.
- 5.10 SEM images of two-component self-composites of G1 and G8 sintered at 159  
1450 °C. (a) G1, (b) 90G1:10G8, (c) 85G1:15G8, (d) 80G1:20G8, (e)  
70G1:30G8, (f) 60G1:40G8, (g) 50G1:50G8, (h) G8.
- 5.11 SEM images of two-component self-composites of G2 and G0 sintered at 160  
1400 °C. (a) G2, (b) 90G2:10G0, (c) 85G2:15G0, (d) 80G2:20G0, (e)  
70G2:30G0, (f) 60G2:40G0, (g) 50G2:50G0, (h) G0.
- 5.12 Comparison of the SEM images of the three-component self-composites, 161  
with different weight percentages of G1/G8/G0. (a) 80/10/10, (b) 70/10/20,  
(c) 60/10/30, (d) 60/20/20, (e) 70/20/10, (f) 80/5/15, (g) 80/15/5.
- 5.13 Comparison of the SEM images of the sintered samples (a) G1, (b) G8, (c) 162  
G0, (d) G1/G8, (e) G1/G0, (f) G8/G0, (g) G1/G8/G0.
- 6.1 Powder XRD patterns of the as-synthesized samples of  $\text{CoFe}_{2-x}\text{Mn}_x\text{O}_4$  and 170  
 $\text{Co}_{1-x}\text{Mn}_x\text{Fe}_2\text{O}_4$  for different  $x$  values, as indicated.
- 6.2 Powder XRD patterns of the sintered samples of  $\text{CoFe}_{2-x}\text{Mn}_x\text{O}_4$  as well as 171  
 $\text{Co}_{1-x}\text{Mn}_x\text{Fe}_2\text{O}_4$  for different  $x$  values, as indicated.

- 6.3 Temperature dependence of the magnetization for different compositions of sintered  $\text{CoFe}_{2-x}\text{Mn}_x\text{O}_4$  and  $\text{Co}_{1-x}\text{Mn}_x\text{Fe}_2\text{O}_4$  samples. 173
- 6.4 Variation of the Curie temperature ( $T_c$ ), as a function of Mn concentration for the  $\text{CoFe}_{2-x}\text{Mn}_x\text{O}_4$  and  $\text{Co}_{1-x}\text{Mn}_x\text{Fe}_2\text{O}_4$  samples. 174
- 6.5 SEM images of sintered  $\text{CoFe}_2\text{O}_4$  (a) and for  $x = 0.1, 0.2$  and  $0.3$  in  $\text{CoFe}_{2-x}\text{Mn}_x\text{O}_4$  (b,d,f), and  $\text{Co}_{1-x}\text{Mn}_x\text{Fe}_2\text{O}_4$  (c,e,g). 176
- 6.6 Magnetostriction curves of different compositions of  $\text{CoFe}_{2-x}\text{Mn}_x\text{O}_4$  sintered samples as a function of applied magnetic field measured along the parallel ( $\lambda_{\text{par}}$ ) and perpendicular ( $\lambda_{\text{per}}$ ) directions. 179
- 6.7 Magnetostriction curves of different compositions of  $\text{Co}_{1-x}\text{Mn}_x\text{Fe}_2\text{O}_4$  sintered samples as a function of applied magnetic field measured along the parallel ( $\lambda_{\text{par}}$ ) and perpendicular ( $\lambda_{\text{per}}$ ) directions. 180
- 6.8 Variation of the (a) maximum value of magnetostriction and (b) strain derivative of sintered  $\text{CoFe}_{2-x}\text{Mn}_x\text{O}_4$  (circle) and  $\text{Co}_{1-x}\text{Mn}_x\text{Fe}_2\text{O}_4$  (square) as a function of Mn concentration. 181
- 6.9 SEM images of  $\text{CoFe}_{1.8}\text{Mn}_{0.2}\text{O}_4$  samples sintered at (a) 1200 °C (b) 1300 °C (c) 1400 °C and (d) 1450 °C. 182
- 6.10 Magnetostriction curves measured in the parallel direction to the applied magnetic field for the  $\text{CoFe}_{1.8}\text{Mn}_{0.2}\text{O}_4$  sample sintered at different temperatures. 183
- 6.11 (a) Magnetostriction curve of  $\text{CoFe}_{1.8}\text{Mn}_{0.2}\text{O}_4$  as a function of magnetic field measured in the direction parallel to the applied magnetic field before and after annealing, (b) Strain derivative of  $\text{CoFe}_{1.8}\text{Mn}_{0.2}\text{O}_4$ . The open and closed symbols represent measurements before and after magnetic field annealing, respectively. 185

# Abstract

Magnetostrictive materials are magnetic materials which can convert magnetic energy into mechanical energy and vice versa. These abilities make magnetostrictive materials useful in various applications as sensors and actuators. Terfenol-D, a magnetostrictive alloy of terbium, dysprosium and iron shows very large magnetostriction at room temperature and relatively small magnetic fields and is currently used for various applications. However, this material has many disadvantages such as the high brittleness, high cost of raw materials, high production cost, magnetostriction is highly anisotropic and therefore, requires single crystals. In order to overcome these limitations, recent research is focused on oxide based magnetostrictive materials.

Among the different magnetic oxides, cobalt ferrite is an ideal material for future magnetostrictive applications because of its relatively large magnetostriction, low cost, easy processability, etc. Studies showed that oxide based magnetostrictive materials, especially metal bonded cobalt ferrite composites, are excellent candidates for stress sensing applications due to a large magnetomechanical effect and high sensitivity. Magnetostriction value of 230 ppm and high strain derivative of  $1.3 \times 10^{-9} \text{ A}^{-1}\text{m}$ , without external load, are reported for metal bonded sintered polycrystalline cobalt ferrite. For sintered cobalt ferrite in the polycrystalline form, this is the highest value reported so far compared to the value of 600 ppm for single crystals. Cobalt ferrite is commonly synthesized by the ceramic process involving high-temperature solid state reactions and the magnetostrictive properties are studied on the sintered materials. The present thesis is on the studies on the magnetostrictive properties of sintered cobalt ferrite derived from nanocrystalline powders of cobalt ferrite with varying particle sizes and an attempt to enhance the magnetostriction coefficient of the sintered material to higher values by tuning some processing parameters. The thesis is divided in to seven chapters.

The first chapter is a general introduction to magnetism, magnetostriction and magnetostrictive materials. A review on the structural and magnetic properties of spinel ferrites is also included. General introduction to the field of smart materials, nanomaterials and nanomagnetic materials is also provided.

Chapter two describes the methods employed for the synthesis of nanocrystalline cobalt ferrite studied in the present work. All the experimental methods and characterization and measurement techniques used are briefly discussed in the specific sections.

Chapter three describes the synthesis and characterization of nanocrystalline cobalt ferrite and studies on the magnetostriction of sintered cobalt ferrite. Nanocrystalline cobalt ferrite powders of different sizes are synthesized by the autocombustion using the corresponding metal nitrates and amino acid, glycine, as fuel. The results are compared with the nanomaterials synthesized by other low-temperature methods viz., co-precipitation and citrate-gel as well as by the high-temperature ceramic method. It is found that the material derived by the autocombustion method give higher magnetostriction. The effect of particle size on the magnetostriction characteristics of sintered cobalt ferrite synthesized by the autocombustion method is studied in detail. It is found that the initial particle size has a strong influence on the sintering and magnetostrictive behavior of cobalt ferrite.

Chapter four describes the effect of sintering on the microstructure and magnetostriction of sintered cobalt ferrite. The influence of single and two-stage sintering processes on the densification, microstructure, and magnetostriction of sintered cobalt ferrite is investigated. From the present study, it is concluded that there is not much advantages on the two-stage sintering process over single stage sintering for getting higher magnetostriction and strain derivative for sintered cobalt ferrite.

Chapter five deals with the magnetostriction of a self-composite of sintered cobalt ferrite derived from a mixture of nanocrystalline powders of different sizes. The cobalt ferrite self-composites were prepared by mixing powders containing particles of different sizes synthesized by autocombustion and ceramic methods. Very high magnetostriction coefficient of 375 ppm and 400 ppm were obtained for the two-component and three-component systems, respectively. In the case of the self-composites, magnetostriction value is found to be not saturated even at the highest field of measurement (800 kA/m)

and therefore, it is possible to improve the magnetostriction values at higher fields. It is found that there is no direct correlation between the microstructure and magnetostriction in the case of the self-composites.

Studies on the magnetostriction characteristics of manganese substituted cobalt ferrite sintered from particles of 4 nm sizes with compositions  $0 \leq x \leq 0.3$  in  $\text{CoFe}_{2-x}\text{Mn}_x\text{O}_4$  as well as  $\text{Co}_{1-x}\text{Mn}_x\text{Fe}_2\text{O}_4$  are discussed in Chapter six. Nanoparticles of the substituted compositions are synthesized by an autocombustion method. Higher magnetostriction at low magnetic fields is obtained along with enhanced strain derivative for the sintered Mn substituted for Fe in cobalt ferrite derived from nanocrystalline materials compared to the corresponding bulk counterparts.

Chapter seven presents an overall conclusion and comparison of the work reported in the previous chapters on the magnetostriction characteristics of the sintered products. Scope for further work to enhance the magnetostriction coefficient and strain derivative of cobalt ferrite based materials, in comparison with the present work as well as the work reported in the literature are discussed.

# Chapter 1

## Introduction

### 1.1 Materials Science

Materials science and engineering plays a vital role in this modern age of science and technology. Materials science, as a discipline, has contributions from different science and engineering streams and is a convergence of physics, chemistry, biology, chemical engineering, mechanical, civil and electrical engineering, etc [1]. In fact, materials science is one of the oldest forms of applied science. Modern materials science is known to be directly evolved from metallurgy. Materials science is based on the development of revolutionary technologies such as plastics, semiconductors, and biomaterials. In the recent years, with significant attention to nanoscience and nanotechnology, research on materials science has been pushed to the forefront throughout the world.

Materials science is the studies on the correlation between processing, properties and relative changes in the performance of a material in a certain application to the structure of that material. Characterization of materials is an important component of materials science. The major factors that determine the structure of a material and thus its properties are its constituent chemical elements and the way in which they have been arranged in the crystal structure and processed into the final form. Thus, the properties and performance of a material are related through the material's microstructure. The ability to change the properties and performance of a material by suitable processing is what makes most materials useful for mankind. Materials are classified in to various groups based on either their properties such as electrical, magnetic, dielectric, optical, etc., or their type such as metals, ceramics, polymers, composites, electronic materials and biomaterials.

## 1.2 Functional Materials

Materials with their own peculiar properties and functionalities such as ferromagnetic, ferroelectric, semiconducting, etc, are called functional materials [2]. Their properties are sensitive to changes in the environmental parameters such as pressure, temperature, electric and magnetic fields, gas atmosphere, etc. Functional materials cover a wide range of organic and inorganic materials and include all types of materials, such as polymers, ceramics, metals, semiconductors and composites. The properties depend on how the materials are processed, and processing can often be used to tune, control and enhance the performance and functions. Therefore, processing of functional materials is of critical importance for various applications.

## 1.3 Smart Materials

Smart materials are a sub-class of functional materials. Smart materials respond to an external stimuli with particular changes in some variables [3]. For that reason they are often called as intelligent materials, responsive materials or adaptive materials. Their properties can be changed significantly depending on the changes in some external conditions such as temperature, moisture, magnetic or electric fields, pH and stress. They can change shape, size, colour, become stronger or produce a voltage as a result of the particular external stimuli. Smart materials can function reversibly such that they can act both as sensors as well as actuators. A sensor is a device that responds with a signal when strained and an actuator performs a responsive and adaptive function. Thus, the field of smart materials attempts to combine the functions of both sensors and actuators. Actuators can change shape, position, frequency or mechanical characteristics in response to changes in temperature, electric field and magnetic field. Similarly, sensors can produce a voltage, magnetization, colour, etc, when they are mechanically stressed. There are mainly four types of smart materials commonly used for sensors and actuators. They are, shape memory alloys, piezoelectric materials, magnetostrictive materials, and electrorheological/magnetorheological fluids.

## Shape Memory Alloys

Shape memory alloys exhibit the unique properties of pseudo-elasticity and shape memory effect [4]. They are generally alloys that can be deformed and reverse back to their original shapes when temperature is changed. Shape memory effect was first discovered in 1932 in silver-cadmium alloy. Generally, these materials can be elastically deformed at relatively low temperatures. When exposed at higher temperatures, they will return to their original shape. The shape memory effect is possible through a solid state phase change, a molecular rearrangement involving a change of phase such as a low temperature martensite phase to a high temperature austenite phase. This phenomenon provides a unique mechanism for remote actuation. Commercially available materials are Ni-Ti alloy and copper-based alloys such as Cu-Zn-Al and Cu-Al-Ni. Shape memory alloys are used in aeronautical applications, thermostats, surgical tools, hydraulic fittings, etc.

## Piezoelectric Materials

The piezoelectric effect was discovered in 1880 in single crystal of quartz by Jacques and Pierre Curie. They found that piezoelectric ceramics expand or contract when an external electric field is applied. These materials also generate an electric field when their dimensions are altered. Therefore, piezoelectric materials serve both as sensors as well as actuators by converting mechanical energy in to electrical energy and vice versa. Examples for piezoelectric materials are barium titanate ( $\text{BaTiO}_3$ ), lead zirconate titanate ( $\text{PbZr}_{1-x}\text{Ti}_x\text{O}_3$ ), etc. Zinc oxide is a relatively new found piezoelectric material that can be used in nanocrystalline form for piezoelectric applications. These materials are of very high demand because of their application as device actuators and transducers in sonar and ultrasonic systems [5]. However, piezoelectric materials have some limitations, such as they tend to be brittle and somewhat heavy. Also, the piezoelectric effect disappears above their Curie temperatures, which is material dependent. These are major problems for some advanced aerospace applications. Applications of piezoelectric materials include production and detection of sound, generation of high voltages, electronic frequency generation, in scanning probe microscopes, cigarette lighters, etc.

## Electro-/Magnetorheological Fluids

Electrorheological and magnetorheological fluids are liquids that experience dramatic changes in viscosity upon the application of electric and magnetic fields, respectively [6]. The effects are completely reversible in the sense that the fluids come back to the normal state immediately after the removal of the external field. However, these materials often exhibit abrasiveness and chemical instability. These smart fluids are suitable for applications in areas such as tunable dampers, vibration-isolation systems, in exercise equipments, clutches, brakes, and resistance controls. Modern automobiles use magnetic fluids for the vehicle's suspension damping.

## Magnetostrictive Materials

Magnetostrictive materials are magnetic materials exhibiting change in shape or dimension under the influence of an external magnetic field and they also exhibit change in their magnetization under the influence of a mechanical stress [7, 8]. Magnetic materials exhibit this property due to the changes in the magnetic domain structure upon the application of an external magnetic field. Because of the conversion of magnetic energy into mechanical energy and the reverse effect, these materials can be used as sensors and actuators. They are typically used in low-frequency, high-power sonar transducers, motors, and hydraulic actuators. Magnetostrictive materials are considered as promising candidates for achieving active damping of vibrations.

## 1.4 Nanomaterials

Nanoscience is the study of the fundamental principles of molecules and structures with dimensions roughly between 1 and 100 nanometers. These structures are known as nanostructures. Nanotechnology is the term used to cover the design, construction and utilization of functional structure with at least one characteristic dimension measured in nanometers [9-13]. Such materials and systems can be designed to exhibit novel and significantly improved physical, chemical and biological properties [14, 15]. The reason for such interesting and very useful behavior is that the characteristic structural features are intermediate in between isolated atoms and bulk

macroscopic materials. Research in nanotechnology is based on discoveries made in physics and chemistry. This is because it is essential to understand the physical and chemical properties of molecules or complexes of molecules in order to control them. Nanotechnology has the potential to create many new materials and devices with wide ranging applications, such as in medicine, electronics, and energy production. Nanomedicine, an offshoot of nanotechnology, refers to highly specific medical intervention at the molecular scale for curing diseases or repairing damaged tissues, such as bone, muscle, or nerve.

Nanomaterials are materials with particle size and morphological features below 100 nm. During the past decade, nanomaterials have attracted enormous interest of the research community worldwide. These materials, notable for their extremely small size, have the potential for wide-ranging applications. Therefore, nanoscience has become the focus of modern materials science, because of the potential technological importance, which stems from the unique physical properties of nanomaterials. Nanomaterials can be metals, ceramics, polymeric materials, or composite materials. Nanomaterials consist of a wide range of materials including nanocrystalline materials, nanocomposites, nanoparticles, nanotubes, and quantum dots. The common link between all these materials is that they all have microstructural features in the nanoscale. By virtue of its structure, nanomaterials exhibit different physical, chemical, optical, mechanical, electrical and magnetic properties than conventional materials. The interesting and unexpected properties of nanomaterials are mainly due to their very high surface area to volume ratio where the percentage of atoms at the surface of the particles becomes significant. Because of the small dimensions and extremely high surface area to volume ratio, many drastic changes take place on the surface of the nanosized materials. As a result, the nanomaterials possess exotic electronic, magnetic and optical properties, and high chemical reactivity. Many new interesting phenomena are observed in nanoparticles compared to their bulk counterparts.

## 1.5 Magnetism

Since the scope of the work reported in this thesis is on magnetostrictive materials related to spinel type cobalt ferrite, magnetism and magnetostriction in general and a review of the structural and magnetic properties of spinel type ferrites are discussed in the following sections.

Magnetism is an interesting phenomenon exhibited by materials and is associated with paired or unpaired electrons in the constituent atoms/ions in the materials [16-21]. It is the power of attraction of one material by another. The net magnetic moment of all the unpaired electrons in the constituent atom or ion in a material is responsible for the origin of interesting magnetic properties. Magnetism in solids arise from the magnetic ions or atoms distributed throughout a regular crystalline lattice on equivalent sites. There are different types of magnetism based on the magnetic behavior of materials in response to magnetic fields at different temperatures. The major types of magnetism are diamagnetism, paramagnetism, ferromagnetism, antiferromagnetism and ferrimagnetism [16-21].

### Diamagnetism

Diamagnetism is a very weak form of magnetism and is originating from the shielding currents induced by an applied magnetic field in the filled electron shells. In diamagnetic materials, all the electrons are paired so there is no permanent net magnetic moment per atom. Diamagnetic materials are slightly repelled by a magnetic field and the material does not retain the magnetic properties when the external field is removed. Diamagnetic properties arise from the realignment of the electron paths under the influence of an external magnetic field. Most elements in the periodic table, including copper, silver, and gold are diamagnetic.

### Paramagnetism

Paramagnetism is observed in materials that contain atoms/ions with unpaired electrons. It is a weak form of magnetism which displays a positive response to an applied magnetic field. These materials are slightly attracted by a magnetic field and

the material does not retain the magnetic properties when the external field is removed. The directions of the magnetic moments due to the unpaired electrons are realigned by the external magnetic field. Paramagnetic materials include titanium, molybdenum, lithium and tantalum.

## Ferromagnetism

Ferromagnetic materials are paramagnetic materials above a critical temperature called Curie temperature. Below the Curie temperature, because of the exchange interactions between in the individual magnetic moments, there is a spontaneous ordering of the moments along a particular direction. Ferromagnetic materials exhibit a strong attraction to magnetic fields and are able to retain their magnetic properties after the external field has been removed. They get their strong magnetic properties due to the presence of magnetic domains. In these domains, large numbers of atom's moments ( $10^{12}$  to  $10^{15}$ ) are aligned parallel so that the magnetic force within the domain is strong. When a ferromagnetic material is in the unmagnetized state, the domains are nearly randomly oriented and the net magnetic field for the part as a whole is zero. When a magnetizing force is applied, the domains become aligned to produce a strong magnetic field within the part. Iron, nickel, and cobalt are examples of ferromagnetic materials.

## Antiferromagnetism

Antiferromagnetism is another form of ordered magnetism in which the neighboring atomic magnetic moments are aligned in the opposite directions so that the net magnetic moment is zero. Antiferromagnetic materials are paramagnetic above a critical temperature called Neel temperature. Below the Neel temperature, the material exhibits no response to the external field, because of the antiparallel ordering of atomic magnets. At higher temperatures, some atoms break free of the orderly arrangement and align with the external field. This alignment and the weak magnetism it produces in the solid reach their peak at the Neel temperature. An antiferromagnet can be considered as consisting of two magnetic sub-lattices, each of which are ferromagnetically ordered but the moments in the two sub-lattices align in

the opposite direction leading to a zero net magnetic moment. Manganese is an example for antiferromagnetic material.

## Ferrimagnetism

Ferrimagnetism is like antiferromagnetism but there is incomplete cancellation of moments aligned in the opposite directions. In a ferrimagnet, the moments in the adjacent atoms are unequal in magnitude and the antiparallel order leads to a net magnetic moment. Ferrimagnetism is also like ferromagnetism in the sense that a spontaneous magnetic ordering takes place below a critical temperature called Curie temperature. The net magnetic moments line up spontaneously below the Curie temperature, to produce a net magnetization. Ferrites are classical examples of ferrimagnetic materials.

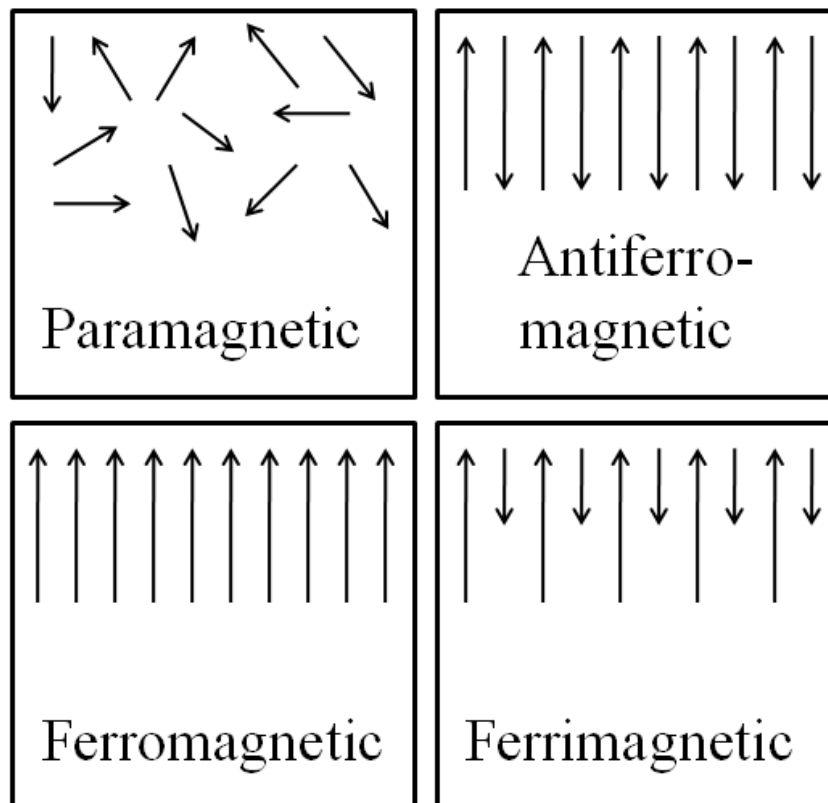


Figure 1.1: Different types of magnetism.

## 1.6 Spinel Type Ferrites

Ferrites are ceramic oxides containing iron oxide,  $\text{Fe}_2\text{O}_3$ , as a major component [22-24]. The history of ferrite materials can be traced back to centuries ago with the discovery of stones that attracted iron. The naturally formed ferrite is magnetite ( $\text{Fe}_3\text{O}_4$  or  $\text{FeO}\cdot\text{Fe}_2\text{O}_3$ ). The first synthetic ferrites were developed independently in Japan and Netherlands in the 1930s. Since then, intensive efforts have been devoted to this research area, which showed remarkable developments in both science and technologies of ferrite materials. The unique electric and magnetic properties of ferrite materials enable them to have a wide range of applications, such as microwave components, high-frequency devices, magnetic fluids and magnetic data storage. Ferrites are predominantly ionic and have very stable crystal structure. Ferrites can be classified into three groups, namely, spinel, garnet and magnetoplumbite. The details of these three types of ferrites are shown in Table 1.1.

The spinel type oxides have the general formula  $\text{AB}_2\text{O}_4$  where A is a divalent and B is a trivalent metal ion. The general chemical formula of spinel ferrites is  $\text{A}^{\text{II}}\text{Fe}^{\text{III}}_2\text{O}_4$  where  $\text{A}^{\text{II}}$  represents divalent ions, as mentioned in Table 1.1.

Table 1.1: Crystal types of ferrites.

Type	Structure	General Formula	Example
Spinel	Cubic	$\text{A}^{\text{II}}\text{Fe}_2\text{O}_4$	$\text{A}^{\text{II}}=\text{Fe}, \text{Cd}, \text{Co}, \text{Mg}, \text{Ni}, \text{Zn}$
Garnet	Cubic	$\text{A}^{\text{III}}_3\text{Fe}_5\text{O}_{12}$	$\text{A}^{\text{III}}=\text{Y}, \text{Sm}, \text{Eu}, \text{Gd}, \text{Tb}, \text{Lu}$
Magnetoplumbite	Hexagonal	$\text{A}^{\text{II}}\text{Fe}_{12}\text{O}_{19}$	$\text{A}^{\text{II}}=\text{Ba}, \text{Sr}$

### 1.6.1 Crystal Structure of Spinel Ferrites

The crystal structure of spinel ferrites is similar to that of the spinel mineral  $\text{MgAl}_2\text{O}_4$ , which is illustrated by Figure 1.2 [25-27]. For this type of structure, the unit cell contains eight formula units. The cubic closely packed arrays of oxygen ions result in the two kinds of interstitial sites denoted by tetrahedral sites (or A sites) and

octahedral sites (or B sites), as shown in Figure 1.2. The unit cell contains 64 tetrahedral sites and 32 octahedral sites, and only 8 A sites and 16 B sites are occupied by metallic ions [25]. The crystal structure is best described by subdividing the unit cell into 8 octants with edge  $\frac{1}{2}a$ , where  $a$  is the unit cell length of the cubic spinel lattice, which are arranged in identical manner in all the octants. Each octant contains four oxygen ions on the body diagonals and they lie at the corners of the tetrahedron. Each oxygen ion is located at a distance equal to one fourth of the length of the body diagonal from alternate corners of the octant. The positions of the metal ions are different in the two octants sharing a face. Each oxygen ion is surrounded by one tetrahedral ion (A site) and three octahedral ions (B site).

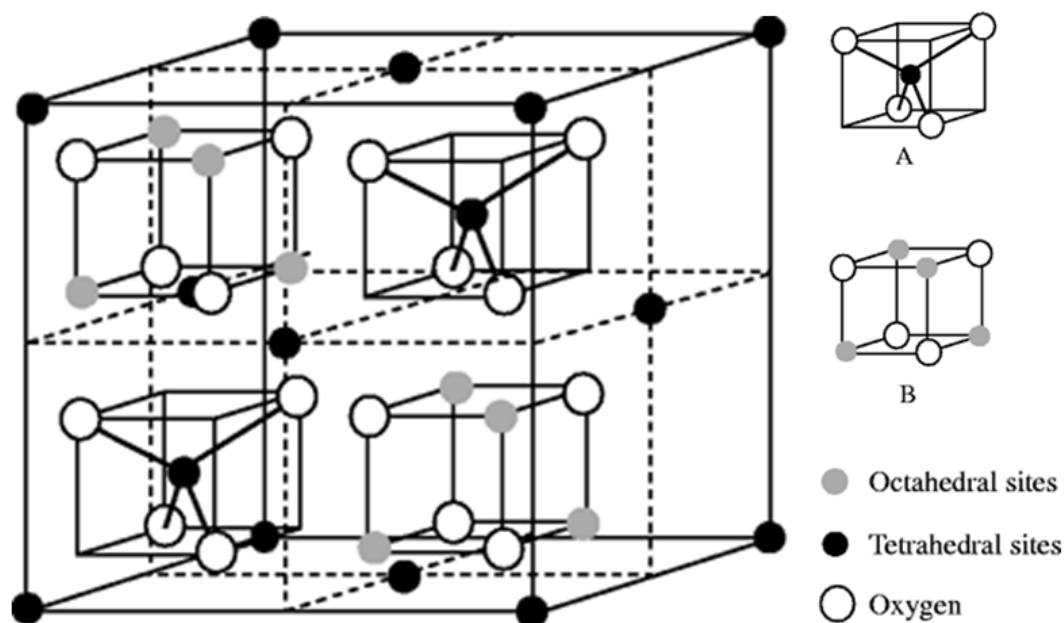


Figure 1.2: The crystal structure of spinel ferrites.

Spinel ferrites are classified into three types; normal spinel, inverse spinel and mixed spinel. In normal spinel all the divalent (A) cations occupy the tetrahedral sites and the trivalent (B) cations on the octahedral sites in the spinel lattice. This can be represented by the formula  $(A)^{tet}[B_2]^{oct}O_4$ . In the inverse spinel, the divalent cations

occupy the octahedral B sites while the trivalent cations are located on both A and B sites in equal proportions, represented by the formula  $(B)^{\text{tet}}[AB]^{\text{oct}}O_4$ . In the mixed spinel structure, both the divalent and trivalent cations are distributed in the tetrahedral and octahedral sites, represented by the formula  $(A_{1-x}B_x)^{\text{tet}}[B_{2-x}A_x]^{\text{oct}}O_4$ .

## 1.6.2 Magnetic Properties of Spinel Ferrites

According to the Neel's theory of ferrimagnetism, ferrimagnetic materials like cobalt ferrite,  $\text{CoFe}_2\text{O}_4$ , consist of two sub lattices (A and B). Within the individual sub lattices, the magnetic moments are arranged parallel to one another but the strong interactions between the two sub lattices results in the antiparallel arrangement of the ordered moments in the two sub lattices. A spinel ferrite then may be defined as the material which below a certain temperature (Curie temperature) shows a spontaneous magnetization, arising from the anti-parallel arrangement of the strongly coupled atomic dipoles [22-24]. If  $M_A$  and  $M_B$  are the moments of the sub lattices, then the ferrimagnetic moment is  $M_A - M_B$ , assuming  $M_A > M_B$ . The reasons for this inequality may be the presence of elements in different ionic states, e.g.  $\text{Fe}^{3+}$  and  $\text{Fe}^{2+}$ , different elements in the same or different ionic states e.g.  $\text{Fe}^{3+}$  and  $\text{Co}^{2+}$  and different crystalline fields acting at the two sites. The interactions between magnetic ions may be classified as A-A, B-B, A-B and B-A, where A-A represents the interaction of an ion on an A-site with the neighboring ion also on A-site, with same definitions for other terms. In the Neel's theory, it is assumed that the A-B and B-A interactions are identical and predominate over A-A and B-B interactions and thus favors the antiparallel arrangement of the magnetic moments of the two sub lattices.

It is well known that the magnetic properties of materials originate from mainly two factors i.e. exchange interaction and spin-orbit couplings. Exchange interactions provide information about the magnetic ordering of the materials, while the other factor determines the magnetization orientation within the material [28]. The magnetic properties of mixed ferrites depend on the preference for a given crystallographic site which an ion exerts in a single, the change in interaction between sub lattices (A-B interaction) with composition, weakening of A-B interaction due to

negative B-B and A-A interactions by the formation of angles and the character of the neighbors of a given ion on a given site which may change.

The spin moments of the trivalent cations in an inverse spinel are canceled (direction of moment on A sites is opposed to B sites) whereas the spin moments of the divalent ions are aligned, resulting in a net magnetic moment. Examples of inverse spinels are  $\text{CoFe}_2\text{O}_4$ ,  $\text{NiFe}_2\text{O}_4$  and  $\text{MgFe}_2\text{O}_4$  [29]. Out of different spinel type ferrites, there is a special interest in cobalt ferrite. Neutron diffraction studies revealed that cobalt ferrite ( $\text{CoO}\cdot\text{Fe}_2\text{O}_3$  or  $\text{CoFe}_2\text{O}_4$ ) is completely inverse [30]. Cobalt ferrite has the so called inverse spinel structure, with one half of  $\text{Fe}^{3+}$  ions on A sites and rest, together with  $\text{Co}^{2+}$  ions on B sites at room temperature. The cation distribution of cobalt ferrite changes with heat treatment [31]. The measured magnetic moment is 4  $\mu\text{B}$ , even though the theoretical value is 3  $\mu\text{B}$  [23]. Cobalt ferrite, with a partially inverse spinel structure, is one of the most important magnetic materials. The saturation magnetization of cobalt ferrite increases with increase in quenching temperature, due to the migration of Fe ions in A site to B site and Co ions in B site to A site [32].

## 1.7 Magnetic Anisotropy

The magnetization of a magnetic system is not free to rotate but is bound to a certain direction in which it is easy to be magnetized than in other directions is called magnetic anisotropy [21]. The existence of magnetic anisotropy indicates that the free energy of a magnetic system depends on the orientation of magnetization with respect to the directions characterizing the magnetic system. For magnetic materials, there are various magnetic anisotropies, such as crystal anisotropy or magnetocrystalline anisotropy, stress anisotropy, shape anisotropy, the anisotropies induced by magnetic annealing, elastic deformation and irradiation and exchange anisotropy. Out of these, the most important contribution is coming from magnetocrystalline anisotropy, followed by stress and shape anisotropies.

The magnetocrystalline anisotropy or crystal anisotropy is due to spin-orbit coupling, which is an intrinsic property of magnetic materials. It couples the magnetization to some crystallographic directions and plays an important role in a

variety of magnetic properties of materials, such as the domain structure, the shape of hysteresis loops, magnetization processes, the magnitude of coercive force and magnetic permeability. In a magnetic crystal, there exists a kind of interaction/coupling between two subsystems: the crystal lattice and the magnetic system consisting of interacting moments. The coupling can exist between the neighboring spins (spin-spin interaction), spin and orbit (spin-orbital interaction), spin and lattice (spin-lattice interaction), and orbital and lattice (orbital-lattice interaction).

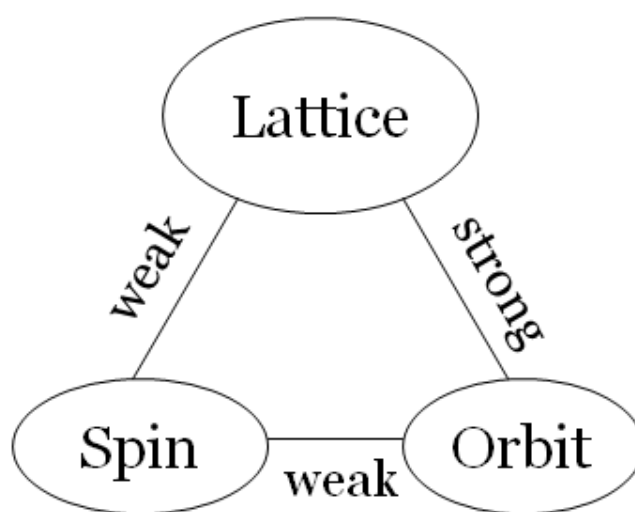


Figure 1.3. Spin-lattice-orbit interactions.

The spin-spin interaction is very strong and keeps neighboring spins parallel or antiparallel to one another. However, this associated exchange energy is isotropic, and depends on the angle between adjacent spins, not at all on the direction of the spin axis relative to the crystal lattice. Therefore, the spin-spin interaction cannot contribute to the crystal anisotropy. The orbit-lattice interaction is also strong, because the orientations of the orbits are fixed very strongly to the lattice because of the crystal field (electric field) created by the adjoining atoms. It is the strong orbit-lattice interaction that results in the partial or entire quenching of the orbital moment of electrons in crystalline materials. There is also interaction between the spin and orbital motion of each electron, but the interaction is weak when compared with the

orbital-lattice interactions. These relationships are summarized in Figure 1.3. When an external field tries to reorient the spin of an electron, the orbit of that electron also tried to be reoriented. Since, the orbit is strongly coupled with the lattice and therefore energy required to overcome this resistance can be called as the anisotropy energy which is required to overcome the spin-orbit coupling. Therefore, the magnetocrystalline anisotropy arises from the spin-orbit coupling which connects the magnetic moments to the atomic lattice through the electron orbits.

When an external stress or strain is applied, this can change the magnetocrystalline anisotropy and thereby alter the magnetization behavior of the materials. This effect is called inverse magnetostriction, the phenomenon that changes the sample dimensions if the direction of the magnetization is altered. The magnetostriction is the observed lattice deformation which accompanies the process of magnetization in a magnetic crystal. The origin of magnetostriction is mainly due to the spin-orbit interaction, which is also responsible for the magnetocrystalline anisotropy as mentioned above.

The third type of anisotropy is due to the shape. A magnetized body will produce magnetic charge at the surface. This surface pole or charge distribution, acting in isolation, is another source of a magnetic field. It is called as demagnetizing field. Consider a polycrystalline specimen that has no preferred orientation for its grains, and therefore no net magnetocrystalline anisotropy. If it is non-spherical in shape, it will be easy to magnetize it along a long axis than along a short axis. The reason is demagnetizing field will be less if the magnetization is along the long axis than if is along one of the short axes. This will produce an easy axis of magnetization along the long axis. For example, a sphere has no shape anisotropy. The magnitude of shape anisotropy depends on the saturation magnetization. In the case of magnetite, smaller than 20 microns, shape anisotropy is the dominant form of anisotropy. For larger sized particles, shape anisotropy is less important than magnetocrystalline anisotropy.

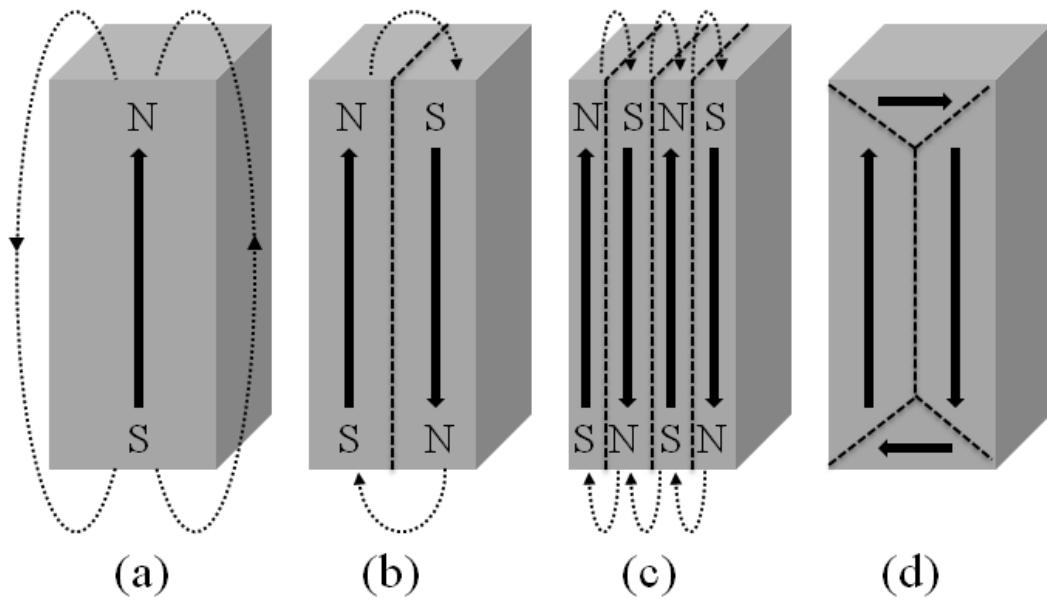


Figure 1.4: Schematic representation of the breakup of a magnet into domains. (a) single domain, (b) double domain, (c) four domains, (d) closed domain.

## 1.8 Magnetic Domains

Any ferromagnetic or ferrimagnetic material that is at a temperature below  $T_C$  (where  $T_C$  is the Curie Temperature, i.e. the temperature above which ferro- or ferrimagnetic materials become paramagnetic) is composed of small volume regions in which there is a mutual alignment of all the magnetic moments in the same direction. Such a region is called a domain and each domain is magnetized to its saturation magnetization [23]. Neighboring domains are separated by domain boundaries or walls across which the direction of magnetization is gradually changed. Normally, domains are microscopic in size, and for a polycrystalline sample, each grain may consist of more than a single domain. Thus, in a macroscopic specimen of material, there will be a large number of domains, and all may have a different magnetization orientation. The domains are formed in order to reduce the overall magnetostatic energy of the system and are separated from one another by domain or Bloch walls which are high energy areas defined as transition layer that separates adjacent regions

magnetized in different directions. The presence of this domain walls and their mobility both reversibly and irreversibly are directly responsible for magnetic hysteresis loop. The single domain configuration is a high energy configuration. By forming domains that are close on themselves, the net magnetic moment becomes zero and the system has a lower energy. This is schematically shown in Figure 1.4.

## 1.9 Magnetization Process

For ferro- and ferrimagnetic materials, when the magnetization ( $M$ ) is measured as a function of magnetic field ( $H$ ), it shows a non-linear behavior [16]. This  $M$ - $H$  behavior can be explained based on the concept of magnetic domains. When a ferromagnetic material is in the unmagnetized condition, the magnetic domains are randomly oriented so that the magnetic field strength in the piece of material is zero. When a small external magnetic field is applied, the net magnetization is initially due to the growth of the domains parallel to the applied magnetic field at the expense of other domains. Thus, at small values of  $H$ , the magnetic domains closer to the direction of the applied external field grow in size until all the domains are favorably oriented in the same direction. At large values of  $H$ , the net magnetic moment rotates in the direction of the applied field. When all the moments are oriented in the direction of the applied field, the magnetization  $M$  becomes constant or saturates, and this value of magnetization is known as saturation magnetization,  $M_s$ . But once saturated, a decrease in  $H$  to zero does not reduce  $M$  to zero. Hence, the material possesses some residual magnetization, and this is called remnant magnetization ( $M_R$ ). In order to demagnetize the substance after saturation (reduce the magnetic moment to zero), a negative field is required. The magnitude of this field at which magnetization becomes zero is called coercive field or simply coercivity ( $H_c$ ). The  $M$  versus  $H$  curve in the case of ferro- and ferrimagnets thus show magnetic hysteresis and is called the magnetic hysteresis loop. The magnetization process and a typical magnetic hysteresis loop are shown in Figure 1.5.

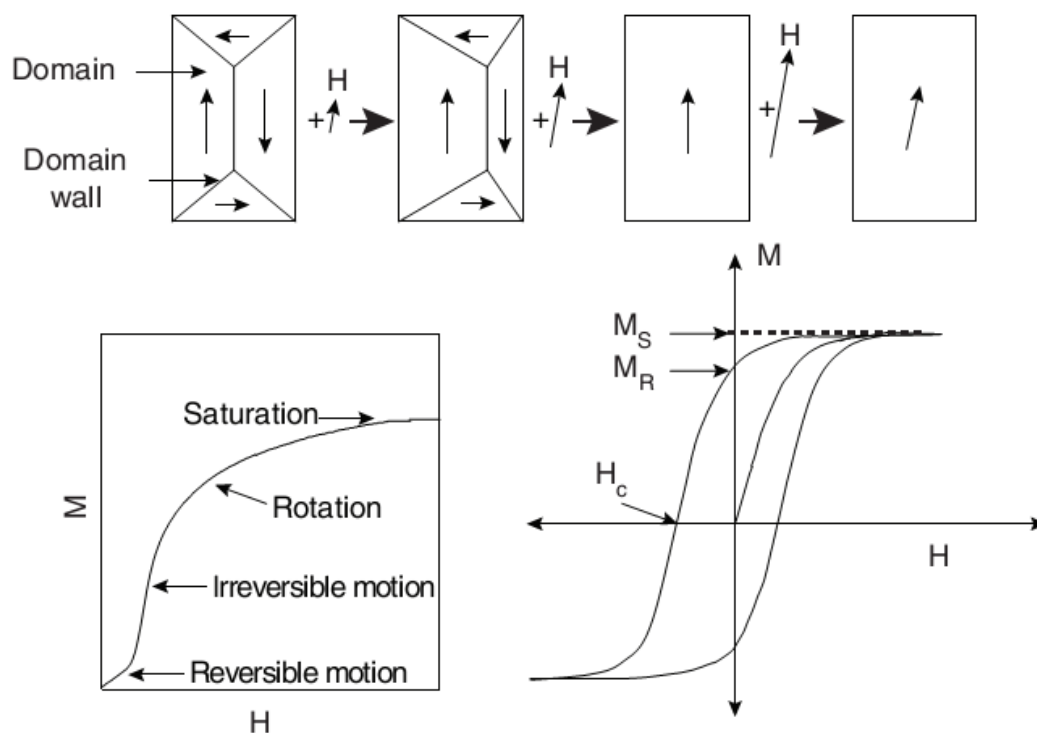


Figure 1.5: The magnetization process and a typical magnetic hysteresis loop.

## 1.10 Magnetic Nanomaterials

Nanosized magnetic materials are of special interest because the magnetic properties change drastically when the size of a magnetic particle is reduced below 100 nm and the modified properties are useful in many applications and devices [33-35]. Studies on nanomagnetism emerged as a major area of research in the recent years due to the potential applications of the nanosized magnetic materials. In large particles, energetic considerations favor the formation of magnetic domains. As the particle size decreases toward some critical size, formation of domain walls becomes energetically unfavorable and the particles are called single domain. A number of interesting magnetic phenomena arise when one or more of the dimensions of a magnetic particle are reduced to nanometer size, that are of the order of single domains. Ferro- and ferrimagnetic nanoparticles exhibit a behavior similar to paramagnetism and it is half-way between ferro/ferrimagnetism and paramagnetism. These particles are called superparamagnetic particles.

Superparamagnetism is a unique magnetic phenomenon for nanostructured materials. For ferro- or ferrimagnetic nanoparticles, below a critical particle size, they possess single domain magnetic structure. If the single domain nanoparticles are small enough, thermal agitation will directly lead to the fluctuation of direction of magnetization of the nanoparticles [36]. Therefore, the magnetization behavior of these small-sized particles is identical to paramagnetism, except for their large magnetic susceptibilities and magnetic moment. Because of these similarities and differences with respect to paramagnetism, such thermally agitated magnetic behavior of the single domain particles is termed superparamagnetism. For superparamagnetic materials, coercivity is zero. For typical superparamagnets,  $KV \approx 25kT_B$ , where  $k$  is the Boltzmann constant,  $K$  is the magnetic anisotropy constant, and  $V$  is volume of a particle. The temperature above which the thermal activation energy overcomes the magnetic anisotropy energy barrier and the nanoparticles become superparamagnetically relaxed, is known as the superparamagnetic blocking temperature,  $T_B$ . The magnetization direction starts flipping randomly and goes through rapid superparamagnetic relaxation above  $T_B$ .  $T_B$  depends on the volume of the particle and thus on the particle size. Generally, the blocking temperature decreases with decreasing particle size.

When the magnetization of a superparamagnetic material is measured while heating, after cooling in the absence of a magnetic field, it is called zero field cooled (ZFC) magnetic measurements. The sample is cooled to the lowest possible temperature and measurements are made while heating the sample in the presence of a small dc magnetic field. The temperature at which a maximum is observed in the ZFC magnetization curve is at the superparamagnetic blocking temperature  $T_B$ . On the other hand, when a sample is cooled to the lowest possible temperature in the presence of a small magnetic field and measurements are made while heating in the same field after cooling, it is called field cooled (FC) magnetization. FC and ZFC magnetizations deviate below  $T_B$  and overlap when the temperature rises above  $T_B$ . Such temperature dependence of the ZFC magnetization and the divergence of ZFC and FC magnetizations below  $T_B$  are the characteristic features of superparamagnetism.

Saturation magnetization of nanoparticles is strongly dependent on their size, anisotropy and interactions. Apart from superparamagnetic nature, magnetic materials possess magnetically disordered spin glass like layers near the surface due to the reduced spin–spin exchange coupling energy at the surface. The superparamagnetic blocking temperature depends on the effective anisotropy constant, the size of the particles, the applied magnetic field, etc. Owing to the large surface atoms/bulk atoms ratio, the surface spins make an important contribution to the magnetization and surface effects can lead to a decrease in the magnetization of small particles. This reduction has been associated with different mechanisms, such as the existence of a magnetically dead layer on the particles surface, the existence of canted spins, or the existence of a spin-glass-like behavior of the surface spins.

Apart from the magnetocrystalline and magnetostatic anisotropies present in the bulk materials which are also operative in nanoparticles, other kinds of anisotropy contributions also come into picture in magnetic nanoparticles. These are the surface anisotropy due to the changes in the coordination, broken bonds and magnetic exchanges at the surface of a particle. Since the surface area to volume ratio of a fine particle is larger than that of the bulk, the surface anisotropy contributions to the total anisotropy is considerable. Again, due to the smaller size of the particles, there will be considerable strain on the surface and this also contributes in the form of strain anisotropy. Finally, if the magnetic nanoparticles are closer together, there will be magnetic dipolar interactions between the particles and different types of magnetic exchange interactions at the interface between the particles. These two interactions also contribute to magnetic anisotropy. Hence, for magnetic nanoparticles, the additional magnetic anisotropy contributions determine the overall magnetic properties [36].

Magnetic nanoparticles find applications in high-density magnetic recording media for information storage [37, 38] and as magnetic sensors for different applications [39-41]. Since the size, shape, orientation, distribution, etc. of the magnetic nanoparticles can be manipulated by controlling the synthesis and processing conditions, it will be possible to tailor the nanoparticles for specific applications. Magnetic nanoparticles also offer many exciting opportunities in

biomedicine. Some of the major applications in biomedicine are targeted drug delivery, magnetic separation, magnetic hyperthermia and as agent for contrast enhancement in MRI [42-50].

## 1.11 Magnetostriction

Magnetostriction is a property of ferro- or ferrimagnetic materials that makes them change their shape or dimensions during magnetization, in the direction of the applied magnetic field (Figure 1.6). The magnetostrictive effect was first discovered by Joule in 1842 [8, 51]. This effect is also called as Joule effect. It is measured as the % strain,

$$\text{Magnetostriction coefficient, } \lambda = \Delta L/L$$

where, L is the length of the material in its un-magnetized state

$\Delta L$  is the resulting strain

$\lambda$  can be positive or negative depending on whether the effect is expansive or compressive.

$\lambda$  is called magnetostriction coefficient or magnetostrictive strain or simply magnetostriction. Using a bar of iron and a system of mechanical levers Joule was able to show that iron expands along the direction of magnetization in low fields, the expansion being reduced as the field strength is increased. This is distinct from volume magnetostriction which describes the uniform strain an object experiences by virtue of possessing a net magnetization. In addition to the effect already explained to show that the length of an iron bar changes when magnetized, the change in volume is very much smaller in comparison. Thus the longitudinal expansion must be accompanied by a transverse contraction. This he confirmed later by direct observation. Finally, he found the effects of external stresses on the magnetostriction of iron and showed that, under tension, it is a contraction for all field strengths.

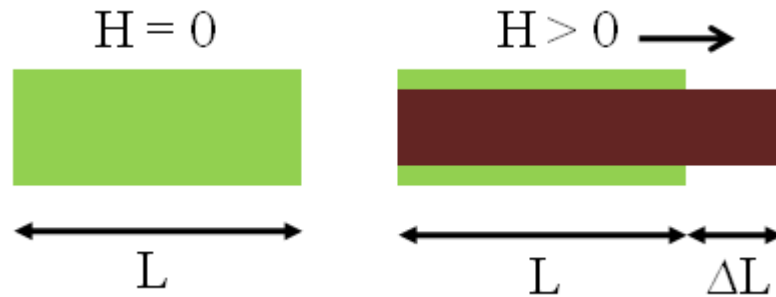


Figure 1.6: The magnetostrictive effect,  $\Delta L$ , is caused by the alignment of magnetic domains in a material due to a magnetic field,  $H$ .

Every magnetostriction effect has an inverse effect. The inverse Joule effect is called Villari effect [52]. When an external stress or strain is applied, the magnetization of the material changes, and this is called the Villari effect. Magnetostriction also influences all other inductive or transport magnetic effects. Another effect related to magnetostriction is the Wiedemann Effect [53]. The physical background to this effect is similar to that of the Joule effect, but instead of a tensile or compressive strain forming as a result of the magnetic field, there is a shear strain which results in a torsional displacement of the ferromagnetic sample. The inverse Wiedemann Effect is called Matteucci Effect [54]. This effect has received a lot of attention because of its relevance in magnetic torque sensors [55-59]. Alternating current fed to a coil creates a longitudinal magnetic field in a sample, and this in turn creates a magnetic flux density in the sample. The presence of the alternating magnetic flux can be detected by another coil, a pickup coil which measures the rate of change in the magnetic flux density. Twisting the ferromagnetic sample induces a change in the magnetization of the sample, which results in a change in the rate of change of the magnetic flux density. By detecting the magnetization change using the pickup coil, the change in shear stress can be measured and as a result the magnitude of the applied torque can be calculated. The Matteucci effect is modified by introducing a permanent magnetic bias in the ferromagnetic sample and this is used in sensor applications. An additional magnetostrictive effect is the Barret Effect [60]. In certain extreme operational conditions, the volume of the material may change in response to a magnetic field. For instance, the volume change of nickel is only  $10^{-7}$  at

80 kA/m. This volume change in response to a magnetic field and is so small that it can be neglected under normal operational conditions. The inverse Barret effect, the Nagaoka-Honda Effect [60], is the change of magnetic state by a change in the volume of a sample as a result of hydrostatic pressure. The two most widely used magnetostrictive effects are the Joule effect and the Villari effect.

### 1.11.1 Mechanism of Magnetostriction

The mechanism of magnetostriction at an atomic level is relatively a complex subject matter but on a macroscopic level may be segregated into many distinct processes [61]. The idealized behavior of length change corresponding to applied magnetic field is shown in Figures 1.7 and 1.8. In the region between 0 and 1, where the applied magnetic field is small, magnetic domains show almost no common orientation. In the region 1 to 2, ideally there should be a linear relation between strain and magnetic field; most devices are designed to operate in this region. Beyond point 2, non-linear behavior occurs due to the fact that most magnetic domains have aligned with magnetic field direction. At point 3, there is no further strain increase, due to saturation effect. In the strain vs. magnetic field graph, there is a linear region where the slope is high. This slope is called field derivative or strain derivative,  $d\lambda/dH$ . This is also sometimes known as the magneto-mechanical coupling factor. For effective and efficient operation, the strain derivative coefficient has to be as high as possible.

### 1.11.2 Applications of Magnetostriction

Magnetostrictive materials can convert magnetic energy into mechanical energy (actuator-type action) and vice versa (sensor-type action). Magnetostriction may also be useful as a complementary tool towards the studies of basic magnetism and the development of a complete atomic level theory of magnetism and magnetic materials. Static and dynamic magnetostrictive measurements, together with magneto-inductive and magneto-transport measurements are the basic tools for the determination of magnetic properties [7, 62].

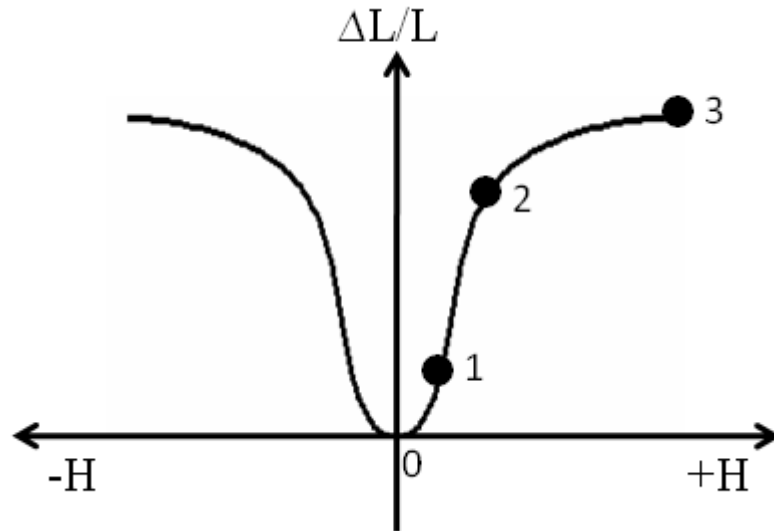


Figure 1.7: Strain versus magnetic field, schematically.

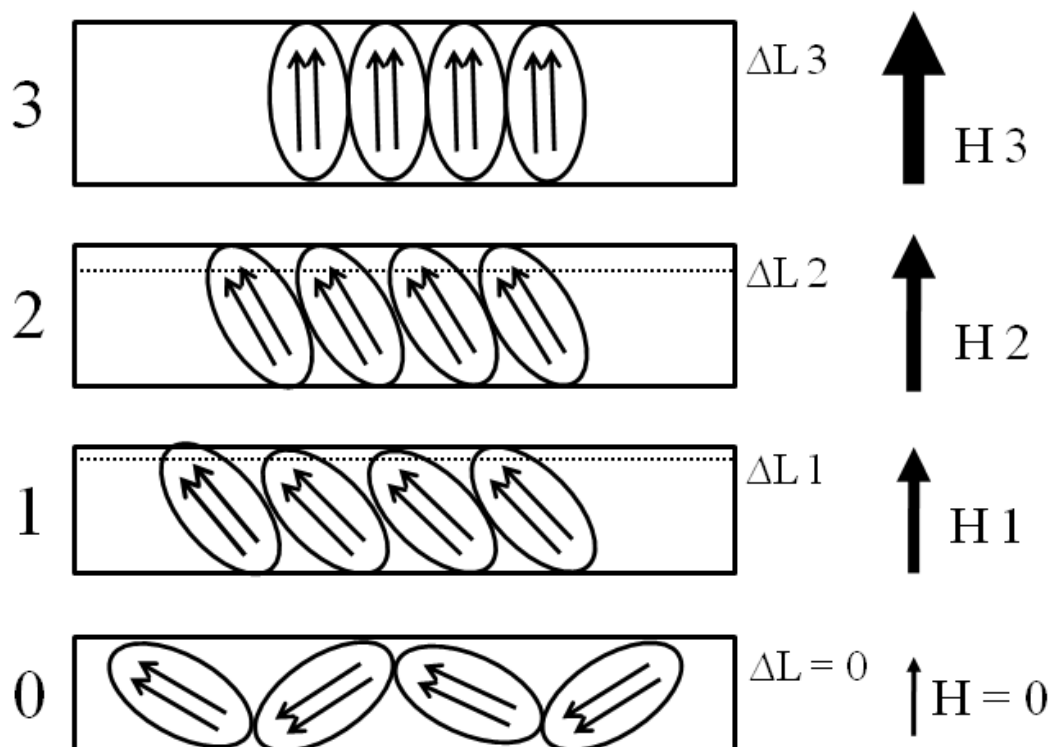


Figure 1.8: The idealized behavior of length change corresponding to applied magnetic field.

Magnetostrictive sensors and actuators are used in a wide range of applications such as sonar, aerospace applications, marine industries, automotive (suspension height, steering position, and transmission shifting, clutch position, and vibration control), medical (wheelchair tilt, hospital bed position, therapeutic machine control), appliances (washing machine drum position and fluid level measurements). Magnetostriction actuators are more useful than piezoelectric actuators in the sense that their driving voltages can be very low which is useful in medical applications, and in general simplifies the amplifier design. When a magnetostrictive material is subjected to an alternating magnetic field, the material vibrates at twice the frequency of that field, and this magnetostrictive vibration is the major source of the humming sound emitted by transformers. Conversely, if a magnetostrictive material is subjected to a mechanical stress, its magnetic permeability will change because of the inverse magnetostrictive effect. If, at the same time the material is subjected to an alternating magnetic field produced by a coil with an alternating current, the magnetic flux density pattern will also change as a result of the change in magnetic permeability. This effect can be detected in a separate “pick up” coil where the alternating magnetic flux will induce an alternating emf whose magnitude varies with the magnetic permeability of the material. This effect is exploited in magnetostrictive transducers, which are capable of converting electrical energy into mechanical energy.

### 1.11.3 Magnetostrictive Materials

Magnetostriction can play an important role in all magnetic materials because the magnetization of a ferromagnetic material is accompanied by changes in dimensions and vice versa. Sometimes, magnetostriction is detrimental and needs to be avoided or minimized because it tends to hinder the magnetization processes and to increase the coercivity and hysteresis loss. For instance, the magnetostriction in magnetic recording heads, and electric transformers should be eliminated if possible. On the other hand, highly magnetostrictive materials are good candidates for sensors and actuators due to their high sensitivity of magnetization to stress which can be used to develop non-contact sensors. Most common traditionally used ferromagnetic materials were iron, nickel, and cobalt. But the intrinsic problem with these materials

is their relatively small change in shape. Therefore, they have low magnetostriction values in the range of 10 to 50 ppm and this limits their use in engineering.

The engineering era of magnetostrictive materials began with the discovery of giant magnetostriction in rare earth alloys during 1960's [63]. Especially a rare earth metal alloy incorporating Terbium, Dysprosium and Iron named as Terfenol-D ( $Tb_{0.3}Dy_{0.7}Fe_2$ ), developed by Naval Ordnance Laboratory, USA in 1972 [64]. The name Terfenol-D is derived from *Terbium Fe Naval Ordnance Laboratory Dy*. It exhibits giant magnetostriction as high as 1000–2000 ppm in a considerably low magnetic field at room temperature and is particularly efficient in energy conversion [7]. Terfenol-D is often manufactured as rods with residual magnetic fields nearly perpendicular to the rod axis. This is because domains in the material with magnetic fields already aligned with the rod axis do not change in direction when an external magnetic field is applied along the rod axis. They do not therefore contribute to the magnetostriction. Consequently a rod which has domains aligned randomly will only produce about two fifths of the maximum possible magnetostriction. Therefore, it is desirable to arrange all the domains to be aligned in any direction, which is perpendicular to the rod axis. This can be approximated in the manufacturing process. Nevertheless a mechanical pre-load is required in order to achieve the initial condition of no alignment along the direction of the rod axis.

Till date Terfenol-D [65-68] continues to be the most sought after magnetostrictive material in wide range of applications. But the disadvantage of this material is the high cost of terbium and dysprosium and the raw materials increase the cost of production. The alloy is highly brittle and can be easily corroded. Also, its magnetostriction is highly anisotropic and therefore, single crystals are required for applications. Because of these limitations, especially the high cost, Terfenol based alloys are mostly used for strategic applications. Therefore, research work is still active to find out cost effective, new and better materials, for wide use in all kinds of applications.

Table 1.2: Magnetostriction of some polycrystalline materials at room temperature [7].

Material	Strain (ppm)	Material	Strain (ppm)
Fe	-14	HoFe <sub>23</sub>	87
Co	-93	ErFe <sub>23</sub>	-54
Ni	-50	Tm <sub>6</sub> Fe <sub>23</sub>	-38
Fe <sub>0.4</sub> Ni <sub>0.6</sub>	38	Sm <sub>2</sub> Fe <sub>17</sub>	-95
Fe <sub>0.4</sub> Co <sub>0.6</sub>	102	Tb <sub>2</sub> Fe <sub>17</sub>	-21
SmFe <sub>2</sub>	-2340	Dy <sub>2</sub> Fe <sub>17</sub>	-90
GdFe <sub>2</sub>	59	Ho <sub>2</sub> Fe <sub>17</sub>	-159
TbFe <sub>2</sub>	2630	Er <sub>2</sub> Fe <sub>17</sub>	-83
DyFe <sub>2</sub>	650	Tm <sub>2</sub> Fe <sub>17</sub>	-44
DyFe <sub>2</sub> (amorp)	57	TbCo <sub>3</sub>	98
HoFe <sub>2</sub>	120	Y <sub>2</sub> Co <sub>17</sub>	120
ErFe <sub>2</sub>	-449	Pr <sub>2</sub> Co <sub>17</sub>	504
TmFe <sub>2</sub>	-185	Dy <sub>2</sub> Co <sub>17</sub>	110
SmFe <sub>3</sub>	-317	Er <sub>2</sub> Co <sub>17</sub>	42
TbFe <sub>3</sub>	1040	Tb <sub>2</sub> Ni <sub>17</sub>	-6
DyFe <sub>3</sub>	528	Fe <sub>3</sub> O <sub>4</sub>	60
HoFe <sub>3</sub>	86	CoFe <sub>2</sub> O <sub>4</sub>	-230
ErFe <sub>3</sub>	104	NiFe <sub>2</sub> O <sub>4</sub>	-39
TmFe <sub>3</sub>	-64	Y <sub>3</sub> Fe <sub>5</sub> O <sub>12</sub>	-3

#### 1.11.4 Oxide Based Magnetostrictive Materials

Development of magnetostrictive materials based on ceramic oxide magnetic materials will have the added advantage over metals or alloys. Although the magnetostrictive strain is not as high as rare earth compounds, it is still an area of

interest because, oxide based magnets have high corrosion resistance, they are cost effective, very stable to different environments and can be processed into any shape and thin films forms to make devices. Another major advantage of oxide ferromagnets is that they can be produced by simple synthesis methods and also also they have high degree of compositional variability. Garnets, ferrites and the perovskite-type ferromagnetic oxides are known to exhibit relatively large magnetostrictive effects in single crystalline form either at low temperatures or at high magnetic fields [69-86]. A polycrystalline material with high magnetostriction at room temperature and working at relatively low magnetic fields can be developed by adjusting the composition, processing conditions, etc. of these oxides. Sayetat have studied the magnetostriction behavior of garnets like  $Tb_3Fe_5O_{12}$ ,  $DyFe_5O_{12}$ , and  $HO_3Fe_5O_{12}$  and found to exhibit very high magnetostriction up to 2400, 875, and 450 ppm, respectively, in the single crystalline form at a temperature close to  $-269\text{ }^\circ\text{C}$  [69]. However, the magnetostrictive strains are negligible at room temperature. Licci and Rinaldi have studied the systematic characterization of the magnetostriction properties of hexagonal ferrites and found that magnetostrictive strain measured in the same direction as that of the applied field is always positive except for the sample containing  $Fe^{2+}$  ions and larger strains were observed for the sample containing Ni and Co [70].

Similar to rare earth garnets, very high magneostriuctive strains are observed in perovskite oxides at low temperatures. Perovskite type oxides have advantages in the sense that they have very high magnetostrictive strains and doped perovskite type manganites show a wide variety of magnetic field induced phenomena. Ibarra *et al* have performed magnetostriction measurements on  $La_{0.60}Y_{0.07}Ca_{0.33}MnO_3$  and they found maximum magnetostrictive strain of 1200 ppm at 170 K under a high magnetic field of 14.2 T [71]. The authors found that two different mechanisms which is responsible for the magnetostriction above and below  $T_c$  and suggested a crossover at  $T_c$  from a ferromagnetic metallic low-volume state to a charge-localized and paramagnetic-insulator high-volume state. The magnetoelastic effect is thus produced by charge–lattice and spin–lattice coupling. Further studies explained the effect above  $T_c$  as due to the formation of small polarons [72]. Dabrowski *et al* have performed magnetostriction measurements on  $La_{1-x}Sr_xMnO_3$  ( $x = 0.11, 0.13, \text{ and } 0.165$ ) series of

compositions in magnetic fields up to 12 T and correlated the observed magnetostriction effects to the spin-lattice coupling [73]. Apart from these studies, there are several reports on the magnetostriction on perovskite manganites and cobaltites [74-82]. However, large magnetostrictive strains in the range of 800 to 1200 ppm were observed in the perovskites only at very low temperatures and also it requires very high magnetic fields. This requirement restricts the use of this kind of materials for practical applications for sensing and actuation.

On the other hand, spinel ferrites have relatively high magnetostrictive strains at room temperature as well as at low magnetic fields. The first studies on the magnetostriction behavior of various spinel ferrites,  $MFe_2O_4$  ( $M = Mn, Fe, Co, Ni$  and  $Zn$ ) were performed by Bozorth *et al* [83, 84]. The observed magnetostriction values for  $Mn_{0.98}Fe_{1.86}O_4$ ,  $Fe_3O_4$ ,  $Co_{0.8}Fe_{2.2}O_4$ ,  $Ni_{0.8}Fe_{2.2}O_4$  and  $Mn_{0.6}Zn_{0.1}Fe_{2.1}O_4$  are -35, -19, -590, -36, and -14 ppm, respectively. Bharathi *et al* have studied the substituted and pure nickel ferrite to understand the effect of substitution on structural distortion and to correlate with magnetostrictive characteristics [85]. They found that magnetostrictive strain of  $NiFe_2O_4$ ,  $NiFe_{1.925}Sm_{0.075}O_4$  and  $NiFe_{1.925}Ho_{0.075}O_4$  are -25, -34 and -24 ppm, respectively. The increase in magnetostriction in the case of  $NiFe_{1.925}Sm_{0.075}O_4$  could be attributed to the large negative magnetostriction value of Sm. Very recently, Atif *et al* studied the effect of substitution of Ni by Zn in  $Ni_{1-x}Zn_xFe_2O_4$  and showed that the substitution of Zn decreases the magnetostriction [86]. The maximum magnetostriction is decreased from -28 to -5 ppm by increasing the substitution level.

### 1.11.5 Magnetostriction of Cobalt Ferrite

As an important member in the family of spinel ferrites, cobalt ferrite ( $CoFe_2O_4$ ) based materials have been accepted as the promising candidates for a wide variety of applications including magnetic and magneto-optical data storage due to their good chemical stability and magnetic properties such as the high Curie temperature, relatively high saturation magnetization and high magnetic anisotropy [23]. Also, among different metal ferrites, cobalt ferrite is known for its relatively high magnetostriction, and there have been many attempts to make sintered polycrystalline

cobalt ferrite with high magnetostriction at very low magnetic fields [87]. Though the magnetostrictive strain and magneto-mechanical coupling factor are relatively low for cobalt ferrite, the material has the advantages over Terfenol-D because of its high electrical resistivity, low thermal conductivity, high Curie temperature, high sound velocity, high permeability, low cost and easy processability etc. These advantages of cobalt ferrite, along with its advantage as a ceramic, over Terfenol-D, will make it a better material for technological applications in future. The magneto-mechanical factor can be improved by making suitable compositions. Some of the physical properties of Terfenol-D and cobalt ferrite are compared in Table 1.3.

Table 1.3: Comparison of the physical properties of Terfenol-D and Cobalt Ferrite [7].

	<i>Terfenol-D</i>	<i>Cobalt Ferrite</i>
<b>Composition</b>	Tb <sub>0.3</sub> Dy <sub>0.7</sub> Fe <sub>1.92</sub>	CoFe <sub>2</sub> O <sub>4</sub>
<b>Mechanical Properties</b>		
Young's Modulus (GPa)	25-35	100-200
Sound Speed (m/s)	1640-1940	>5000
Tensile Strength (MPa)	28	~20
Compressive Strength (MPa)	700	100-200
<b>Thermal Properties</b>		
Coefficient of Thermal Expansion (ppm/°C)	12	6-10
Specific Heat (kJ/kg-K)	0.35	~0.7
Thermal Conductivity (W/m-K)	13.5	~0.005
<b>Electrical Properties</b>		
Resistivity (Ω-m)	58 x 10 <sup>-8</sup>	>10 <sup>5</sup>
Curie Temperature (°C)	380	510
<b>Magnetostrictive Properties</b>		
Strain (estimated linear) (ppm)	800-1200	~600
Energy Density (kJ/m <sup>2</sup> )	14-25	4-13
<b>Magnetomechanical Properties</b>		
Relative Permeability	3-10	>100
Coupling Factor	0.75	~0.2

Cobalt ferrite in its single crystalline form shows high magnetostrictive strain of ~600 ppm, depending on the composition and crystallographic direction [83, 84]. Recently many efforts have been made to attain large magnetostrictive strain in polycrystalline cobalt ferrite. McCallum *et al* studied the magnetostriction of metal bonded cobalt ferrite and it showed a strain of 230 ppm and high strain derivative of  $1.3 \times 10^{-9} \text{ A}^{-1}\text{m}$ , without external load [88]. These composites are excellent candidates for stress sensing applications due to the large magneto-mechanical effect and high sensitivity. The drawback of metal bonded cobalt ferrite composite is the large magneto-mechanical hysteresis at room temperature.

However, it has been reported that the degree of inversion in cobalt ferrite can be altered by heat treatment [31]. Since cation site occupancy is crucial in determining magnetostrictive properties, and this can be altered depending on heat treatment conditions, there is a need for a systematic study of the variation of heat treatment to produce desired magnetostrictive properties. A study by Bhamre and Joy has shown that the sintering conditions and microstructure can affect the magnetostrictive properties of polycrystalline cobalt ferrite [89]. The highest value of magnetostrictive strain is observed for the samples sintered at 1100 °C. Nlebedim *et al* studied the effect of quenching heat treatments and the influence of vacuum sintering on microstructure and magnetic properties of magnetostrictive cobalt ferrite [90, 91]. Both studies showed that the degradation of magnetostriction and strain derivative is due to cation redistribution and development of additional phase, respectively.

Most of the studies on the magnetostrictive properties of cobalt ferrite are concentrated on understanding the effect of cation substitution. The effect of substitution of various metal ions such as  $\text{Mn}^{3+}$ ,  $\text{Cr}^{3+}$ ,  $\text{Zn}^{2+}$ ,  $\text{Si}^{4+}$  and  $\text{Ga}^{3+}$  for cobalt and iron in  $\text{CoFe}_2\text{O}_4$  has been studied by various researchers [92-100]. Such a substitution affects the distribution of Fe ions in the octahedral and tetrahedral sites of the spinel lattice. A very small amount of substitution can affect the initial permeability and thereby affects the magneto-mechanical response [101]. Paulson *et al* studied the effect of substitution of Fe by Mn in  $\text{CoFe}_{2-x}\text{Mn}_x\text{O}_4$  and showed that the incorporation of Mn leads to a decrease in the magnetostriction and Curie temperature [92]. Caltun *et al* also studied the effect of Mn substitution for Fe and

found that by adjusting the Mn content, it could be possible to control the Curie temperature as well as magnetostriction parameters [97]. Bhome and Joy have also studied the effect of substitution of both Fe and Co by Mn on the magnetostrictive properties of  $\text{Co}_{1.2}\text{Fe}_{1.8}\text{O}_4$  [93, 94]. A strong dependence of magnetostriction on the Mn content is observed for both the cases. The substitution of Co by Mn increases the magnetostriction for small amount of substitution in  $\text{Co}_{1.2-x}\text{Mn}_x\text{Fe}_{1.8}\text{O}_4$ . A two-fold increase in the initial slope with large magnetostriction as compared to that of the parent compound is observed. These studies indicate that it is possible to tune the magnetic and magnetostrictive properties of cobalt ferrite by substituting Mn for Fe and Co. Lee *et al* studied the effect of substitution of Cr by Fe in  $\text{CoFe}_{2-x}\text{Cr}_x\text{O}_4$  and the results showed that the substitution of Cr for Fe in cobalt ferrite decrease the Curie temperature as well magnetostrictive strain and the rate of decrease was greater than that observed for similar levels of Mn substitution [95]. Nlebedim *et al* performed the temperature dependence of the magneostriptive properties of  $\text{CoFe}_{2-x}\text{Ga}_x\text{O}_4$  with  $x$  varies from 0 to 0.4 and they found that strain derivative was higher for  $\text{CoFe}_{1.98}\text{Ga}_{0.2}\text{O}_4$  in the temperature range of 250-300 K [99]. Somaiah *et al* have very recently studied the effect of the substitution of Zn by Fe in  $\text{CoFe}_{2-x}\text{Zn}_x\text{O}_4$  and they found that the magnetostriction decreases with increasing zinc content [100].

One of the most important processes of magnetic annealing is a treatment with magnetic field applied during the heating process. This technique has been found to produce a significant impact on the properties of many magnetic materials. Lo *et al* reported the improvements of both magnetostriction level and strain derivative of pure polycrystalline cobalt ferrite by magnetic annealing [102]. Results showed that cobalt ferrite annealed at 300 °C in air for 36 hours under a dc field of 318 kA/m induced a uniaxial anisotropy with the easy axis being along the annealing field direction. Under hard axis applied fields, the maximum magnetostriction measured along the hard axis at room temperature increased in magnitude from 200 ppm to 250 ppm after annealing and the strain derivative also increased from  $1.5 \times 10^{-9}$  to  $3.9 \times 10^{-9} \text{ A}^{-1}\text{m}$ . This result shows that magnetic annealing provides an alternative means other than chemical substitution for enhancing magneto-mechanical properties of cobalt ferrite for magnetoelastic stress or torque sensing applications. Zheng *et al* studied the

magnetic and magnetostrictive properties of magnetic-annealed polycrystalline cobalt ferrite [103]. The sintered cobalt ferrite samples were rapidly heated to 400 °C in about 80 s and kept at this temperature for 30 min. After magnetic annealing, the samples were slowly cooled to room temperature. The magnetic hysteresis loops showed obvious uniaxiality with an induced easy direction parallel to the annealing field. The uniaxial behavior was also observed in the magnetostrictive measurement, which showed a significantly enhanced magnetostriction of 273 ppm when the external field was applied perpendicular to the annealing field direction. Very recently, Atif *et al* reported that annealing the sintered compacts in a magnetic field after applying very high pressures at the time of compaction is efficient for obtaining higher magnetostriction and strain derivative [104]. Higher magnetostriction coefficient up to 400 ppm is reported when compacts are made at very high pressures before sintering and this has been attributed to the changes in the distribution of the cations at high pressures while compaction.

## 1.12 Scope of the Present Work

In most of the reported works on the studies on magnetostriction, cobalt ferrite is commonly synthesized by the ceramic process involving high-temperature solid state reactions. It is widely known that the sintered products derived from nanocrystalline materials exhibit enhanced magnetic permeability which depends on parameters such as microstructure, density, porosity and grain size etc., as compared to the sintered material derived from bulk [23, 105, 106]. So far, there have been no attempts to study the effect of nanocrystalline cobalt ferrite powders as starting materials and the initial particle size on the magnetostriction coefficient of the sintered products. Similarly, there are no studies so far reported on the effect of method of synthesis and sintering conditions on the compacts derived from nanocrystalline materials. In a preliminary study, some wet chemical synthesis methods such as co-precipitation, sol-gel and citrate-gel methods have been used to prepare cobalt ferrite nanoparticles in order to study the effect of the initial size of the particles on the magnetostrictive properties of the polycrystalline materials sintered under identical conditions [107]. It was found that nanoparticles of size ~40 nm, synthesized by an autocombustion

method, with a flaky and porous morphology, gave a sintered material with small grains and relatively larger magnetostriction of 200 ppm compared to the material synthesized by the ceramic method (160 ppm) reported in the same work. It was also found that nanoparticles of smaller size synthesized by other wet chemical methods gave lower magnetostriction coefficient. From this study, it was concluded that controlling the grain size of the sintered products is a must to get high magnetostriction values. Highest magnetostriction coefficient reported so far for sintered polycrystalline cobalt derived under simple processing conditions is 230 ppm with very low strain derivative. However, a magnetostriction coefficient of ~400 ppm is reported for powders synthesized by the ceramic method, compacted under very high pressures up to 200 MPa, sintered for a very long duration of 24 hours, and only after annealing the sintered compact in a magnetic field of 10 Tesla for 3 hours. Such a process is not cost effective for regular applications and sintered cobalt ferrite processed under simple processing conditions is desirable for practical applications. Therefore, the objectives of the present doctoral research were:

1. To synthesize nanocrystalline cobalt ferrite powders of varying particle size by the combustion method
2. To study the effect of initial particle size of the powders on the ultimate value of magnetostriction after sintering
3. To understand the role of synthesis method, particle size and sintering conditions on the magnetostriction of cobalt ferrite derived from nanocrystalline powders
4. To obtain high magnetostriction and strain derivative for cobalt ferrite sintered at low temperatures
5. To optimize the processing parameters for getting enhanced magnetostriction and strain derivative in sintered cobalt ferrite, and
6. To get highest possible magnetostrictive strain for sintered cobalt ferrite synthesized, compacted and processed under simple processing conditions suitable for various practical applications.

## References

- [1] J. F. Shackelford, *Introduction to Materials Science for Engineers* (Prentice Hall, New Jersey, 2009).
- [2] D. D. L. Chung, *Functional Materials: Electrical, Dielectric, Electromagnetic, Optical and Magnetic Applications* (World Scientific Publishing, Singapore, 2010).
- [3] M. V. Gandhi and B. D. Thompson, *Smart materials and Structures* (Chapman and Hall, London, 1992).
- [4] K. Otsuka and C. M. Wayman, *Shape Memory Materials* (Cambridge University Press, New York, 1999).
- [5] C. Galassi, M. Dinescu, K. Uchino and M. Sayer, *Piezoelectric materials: Advances in Science, Technology and Applications* (Kluwer Academic Publishers, New York, 2000).
- [6] A. D. Lantada and P. L. Morgado, *Handbook of Active Materials for Medical Devices: Advances and Applications* (Pan Stanford, Singapore, 2012).
- [7] G. Engdahl, *Handbook of Giant Magnetostrictive Materials* (Academic press, Sandiego, 2000).
- [8] E. W. Lee, *Rep. Prog. Phys.* 18 (1955) 184.
- [9] K. J. Klabunde and R. Richards, *Nanoscale Materials in Chemistry* (John Wiley & Sons Inc., New York, 2001).
- [10] J. A. Rodriguez and M. F. Garcia, *Synthesis, Properties, and Applications of Oxide Nanomaterials* (John Wiley & Sons, New Jersey, 2007).
- [11] A. S. Edelstein and R. C. Cammaratra, *Nanomaterials: Synthesis, Properties and Applications* (Taylor & Francis, New York, 1998).
- [12] C. A. Mirkin and C. M. Niemeyer, *Nanobiotechnology II: More Concepts and Applications* (Wiley-VCH, Weinheim, 2007).

- 
- [13] O. Shoseyov and I. Levy, *NanoBioTechnology: Bioinspired Devices and Materials of the Future* (Humana Press Totowa, New Jersey, 2008).
- [14] H. Gleiter, *Adv. Mater.* 4 (1992) 474.
- [15] G. A. Ozin, *Adv. Mater.* 4 (1992) 612.
- [16] C. Heck, *Magnetic Materials and their Applications* (Butterworth & Co. Pub. Ltd., London, 1974).
- [17] R. C. O'Handley, *Modern Magnetic Materials: Principles and Applications* (Wiley Interscience, New York, 2000).
- [18] K. H. J. Buschow and F. R. De Boer, *Physics of Magnetism and Magnetic Materials* (Kluwer Academic Publishers, New York, 2003).
- [19] du Tremolet de Lacheisserie, D. Gignoux and M. Schlenker, *Magnetism: Fundamentals* (Kluwer Academic Publishers, New York, 2003).
- [20] A. R. West, *Solid State Chemistry and its Applications* (John Wiley & Sons, Singapore, 2003).
- [21] B. D. Cullity and C. D. Graham, *Introduction to Magnetic Materials* (John Wiley & Sons, New Jersey, 2009).
- [22] J. Smit and H. P. J. Wijn, *Ferrites* (Philips Technical Library, Eindhoven, 1959).
- [23] A. Goldman, *Modern Ferrite Technology* (Van Nostrand Reinhold, New York, 1990).
- [24] B. Viswanathan and V. R. K. Murthy, *Ferrite Materials: Science and Technology* (Narosa Publishing House, New Delhi, 1990).
- [25] K. E. Sickafus, J. M. Wills and N. W. Grimes, *J. Am. Ceram. Soc.* 82 (1999) 3279.
- [26] F. S. Galasso, *Structure and Properties of Inorganic Solids* (Pergamon Press, Oxford, 1970).

- [27] O. Muller and R. Roy, *The Major Ternary Structural Families* (Springer Berlin, 1974).
- [28] J. B. Goodenough, *Magnetism and the Chemical Bond* (John Wiley & Sons, New York, 1963).
- [29] R. J. Teitel and M. Cohen, *Trans. AIME* 188 (1950) 1028.
- [30] E. Prince, *Phy. Rev.* 102 (1956) 674.
- [31] G. A. Sawatzky, F. Van Der Woude and A. H. Morrish, *J. Appl. Phys.* 39 (1968) 1204.
- [32] J. G. Na, T. D. Lee and S. J. Park, *J. Mater. Sci. Lett.* 12 (1993) 961.
- [33] V. M. Rotello, *Nanoparticles: Building Blocks for Nanotechnology* (Springer, New York, 2004).
- [34] R. W. Kelsall, I. W. Hamley, M. Geoghegan and J. Wiley, *Nanoscale Science and Technology* (John Wiley & Sons, West Sussex, 2005).
- [35] A. Thiaville and J. Miltat, *Science* 284 (1999) 1939.
- [36] J. L. Dormann, D. Fiorani and E. Tronc, *Adv. Chem. Phys.* 98 (1997) 283.
- [37] C. A. Ross, H. I. Smith, T. Savas, M. Schattensburg, M. Farhoud, M. Hwang, M. Walsh, M. C. Abraham and R. J. Ram, *J. Vac. Sci. Technol. B* 17 (1999) 3168.
- [38] B. D. Terris and T. Thomson, *J. Phys. D: Appl. Phys.* 38 (2005) R199.
- [39] D. L. Graham, H. A. Ferreira and P. P. Freitas, *Trends Biotechnol.* 22 (2004) 455.
- [40] J. Shi, Y. Zhu, X. Zhang, W. R. G. Baeyens and A. M. Garca-Campaa, *Trends in Anal. Chem.* 23 (2004) 351.
- [41] M. J. Toohey, *Sens. Actuators B* 105 (2005) 232.
- [42] R. Hergt, W. Andra, C. G. d'Ambly, I. Hilger, W. A. Kaiser, U. Richter and H. G. Schmidt, *IEEE Trans. Magn.* 34 (1998) 3745.
- [43] X. Batlle and A. Labarta, *J. Phys. D: Appl. Phys.* 35 (2002) R15.

- [44] A. Moser, K. Takano, D. T. Margulies, M. Albrecht, Y. Sonobe, Y. Ikeda, S. Sun and E. E. Fullerton, *J. Phys. D: Appl. Phys.* 35 (2002) R157.
- [45] I. Brigger, C. Dubernet and P. Couvreur, *Adv. Drug Delivery Rev.* 54 (2002) 631.
- [46] S. A. Agnihotri, N. N. Mallikarjuna and T. M. Aminabhavi, *J. Controlled Release* 100 (2004) 5.
- [47] T. C. Yih and M. Al-Fandi, *J. Cell. Biochem.* 97 (2006) 1184.
- [48] L. E. van Vlerken and M. M. Amiji, *Expert Opin. Drug Deliv.* 3 (2006) 205.
- [49] A. K. Gupta and A. S. G. Curtis, *J. Mater. Sci.: Mater. Med.* 15 (2004) 493.
- [50] A. Ito, M. Shinkai, H. Honda and T. Kobayashi, *J. Biosci. Bioeng.* 100 (2005) 1.
- [51] J. P. Joule, *Ann. Electr. Magn. Chem.* 8 (1842) 219.
- [52] E. Villari, *Ann. Phys. Chem.* 6 (1865) 87.
- [53] G. Widemann, *Ann. Phys. Chem.* 117 (1862) 193.
- [54] R. Skorski, *J. Appl. Phys.* 35 (1964) 1213.
- [55] A. Beth and W. W. Meeks, *Rev. Sci. Instr.* 25 (1954) 603.
- [56] H. Hase and R. Shoji, *US Patent* (1994) 5442966.
- [57] I. Sasada, A. Hiroike and K. Harada, *IEEE Trans. Magn.* 20 (1984) 951.
- [58] I. J. Garshelis and C. A. Jones, *J. Appl. Phys.* 85 (1999) 5468.
- [59] M. Liniers, V. Madurga, M. Vazquez and A. Hernando, *Phy. rev. B* 31 (1985) 4425.
- [60] A. G. Olabi and A. Grunwald, *Mater. Design* 29 (2008) 469.
- [61] S. Chikazumi and S. H. Charap, *Physics of Magnetism* (John Wiley & Sons, New York, 1964).
- [62] M. R. J. Gibbs, *Modern Trends in Magnetostriction Study and Application* (Kluwer Academic Publishers, Netherlands, 2000).

- [63] S. Legvold, J. Alstad and J. Rhyne, *Phys. Rev. Lett.* 10 (1963) 509.
- [64] A. E. Clark and H. S. Belson, *Phys. Rev. B* 5 (1972) 3642.
- [65] W. Wang, X. B. Luo, N. Zhang and Q. Y. Ma, *Sens. Actuators A* 171 (2011) 248.
- [66] C. Zhang, T. Ma and M. Yan, *J. Appl. Phys.* 110 (2010) 063901.
- [67] Y. V. Yang, Y. Y. Huang and Y. M. Jin, *Appl. Phys. Lett.* 98 (2011) 012503.
- [68] N. Galloway, M. P. Schulze, R. D. Greenough and D. C. Jiles, *Appl. Phys. Lett.* 63 (1993) 842.
- [69] F. Sayetat, *J. Magn. Magn. Mater.* 58 (1986) 334.
- [70] F. Licci and S. Rinaldi, *J. Appl. Phys.* 52 (1981) 2442.
- [71] M. R. Ibarra, P. A. Algarabel, C. Marquina, J. Blasco and J. Garcia, *Phys. Rev. Lett.* 75 (1995) 3541.
- [72] J. M. De Teresa, J. Blasco, M. R. Ibarra, J. Garcia, C. Marquina, P. Algarabel and A. Del Moral, *J. Appl. Phys.* 79 (1996) 5175.
- [73] B. Dabrowski, L. Gladczyk, A. Wisniewski, Z. Bukowski, R. Dybziński, A. Szewczyk, M. Gutowska, S. Kolesnik, C. W. Kimball and H. Szymczak, *J. Appl. Phys.* 87 (2000) 3011.
- [74] R. V. Demin, L. I. Koroleva and A. M. Balbashov, *Phys. Lett. A* 231 (1997) 279.
- [75] Y. F. Popov, A. M. Kadomtseva, G. P. Vorob'ev, V. Y. Ivanov, A. A. Mukhin, A. K. Zvezdin and A. M. Balbashov, *J. Appl. Phys.* 83 (1998) 7160.
- [76] B. Garcia-Landa, J. M. De Teresa, M. R. Ibarra, C. Ritter, R. Drost and M. R. Lees, *J. Appl. Phys.* 83 (1998) 7664.
- [77] D. A. Filippov, R. Z. Levitin, A. N. Vasil'ev, T. N. Voloshok, H. Kageyama and R. Suryanarayanan, *Phys. Rev. B* 65 (2002).
- [78] A. K. Pradhan, B. K. Roul, Y. Feng, Y. Wu, S. Mohanty, D. R. Sahu and P. Dutta, *Appl. Phys. Lett.* 78 (2001) 1598.

- [79] H. Ogasawara, M. Matsukawa, M. Yoshizawa, M. Apostu, R. Suryanarayanan, G. Dhalenne, A. Revcolevschi, K. Itoh and N. Kobayashi, *J. Magn. Magn. Mater.* 226 (2001) 990.
- [80] C. Marquina, M. R. Ibarra, A. I. Abramovich, A. V. Michurin and L. I. Koroleva, *J. Magn. Magn. Mater.* 226 (2001) 999.
- [81] A. Abramovich, L. Koroleva, A. Michurin, O. Gorbenko and A. Kaul, *J. Magn. Magn. Mater.* 242 (2002) 648.
- [82] A. I. Abramovich, L. I. Koroleva and A. V. Michurin, *J. Magn. Magn. Mater.* 258 (2003) 319.
- [83] R. M. Bozorth and J. G. Walker, *Phy. Rev.* 88 (1952) 1209.
- [84] R. M. Bozorth, E. F. Tilden and A. J. Williams, *Phy. Rev.* 99 (1955) 1788.
- [85] K. K. Bharathi, G. Markandeyulu and C. V. Ramana, *J. Phy. Chem. C* 115 (2011) 554.
- [86] A. Muhammad, M. Nadeem, R. Grossinger and R. S. Turtelli, *J. Alloys Compd.* 509 (2011) 5720.
- [87] Y. Chen, J. E. Snyder, C. R. Schwichtenberg, K. W. Dennis, R. W. McCallum and D. C. Jiles, *IEEE Trans. Magn.* 35 (1999) 3652.
- [88] R. W. McCallum, K. W. Dennis, D. C. Jiles, J. E. Snyder and Y. H. Chen, *Low Temp. Phys.* 27 (2001) 266.
- [89] S. D. Bhame and P. A. Joy, *J. Am. Ceram. Soc.* 91 (2008) 1976.
- [90] I. C. Nlebedim, N. Ranvah, P. I. Williams, Y. Melikhov, F. Anayi, J. E. Snyder, A. J. Moses and D. C. Jiles, *J. Magn. Magn. Mater.* 321 (2009) 2528.
- [91] I. C. Nlebedim, N. Ranvah, P. I. Williams, Y. Melikhov, J. E. Snyder, A. J. Moses and D. C. Jiles, *J. Magn. Magn. Mater.* 322 (2010) 1929.
- [92] J. A. Paulsen, A. P. Ring, C. C. H. Lo, J. E. Snyder and D. C. Jiles, *J. Appl. Phys.* 97 (2005) 044502.
- [93] S. D. Bhame and P. A. Joy, *J. Appl. Phys.* 99 (2006) 073901.

- [94] S. D. Bhame and P. A. Joy, *J. Appl. Phys.* 100 (2006) 113911.
- [95] S. J. Lee, C. C. H. Lo, P. N. Matlage, S. H. Song, Y. Melikhov, J. E. Snyder and D. C. Jiles, *J. Appl. Phys.* 102 (2007) 073910.
- [96] S. H. Song, C. C. H. Lo, S. J. Lee, S. T. Aldini, J. E. Snyder and D. C. Jiles, *J. Appl. Phys.* 101 (2007) 09C517.
- [97] O. F. Caltun, I. Dumitru, M. Feder, N. Lupu and H. Chiriac, *J. Magn. Magn. Mater.* 320 (2008) e869.
- [98] G. S. N. Rao, O. F. Caltun, K. H. Rao, B. Parvatheeswara Rao, H. L. Wamocha and H. H. Hamdeh, *Hyperfine Interact.* 184 (2008) 179.
- [99] I. C. Nlebedim, Y. Melikhov, J. E. Snyder, N. Ranvah, A. J. Moses and D. C. Jiles, *J. Appl. Phys.* 109 (2011) 07A908.
- [100] N. Somaiah, T. V. Jayaraman, P. A. Joy and D. Das, *J. Magn. Magn. Mater.* 324 (2012) 2286.
- [101] J. A. Paulsen, C. C. H. Lo, J. E. Snyder, A. P. Ring, L. L. Jones and D. C. Jiles, *IEEE Trans. Magn.* 39 (2003) 3316.
- [102] C. C. H. Lo, A. P. Ring, J. E. Snyder and D. C. Jiles, *IEEE Trans. Magn.* 41 (2005) 3676.
- [103] Y. X. Zheng, Q. Q. Cao, C. L. Zhang, H. C. Xuan, L. Y. Wang, D. H. Wang and Y. W. Du, *J. Appl. Phys.* 110 (2011) 043908.
- [104] A. Muhammad, R. Sato-Turtelli, M. Kriegisch, R. Grossinger, F. Kubel and T. Konegger, *J. Appl. Phys.* 111 (2012) 013918.
- [105] A. Verma and D. C. Dube, *J. Am. Ceram. Soc.* 88 (2005) 519.
- [106] J. Hu, M. Yan and W. Luo, *Physica B* 368 (2005) 251.
- [107] S. D. Bhame and P. A. Joy, *Sens. Actuators A* 137 (2007) 256.

# Chapter 2

## Experimental Methods

### 2.1 Introduction

The different methods employed for the synthesis of nanocrystalline cobalt ferrite and the techniques used for the characterization of the materials along with the details of the magnetostriction measurements which is the main content of this thesis are discussed in this chapter. Mainly the solution combustion method of synthesis, which is a wet chemical method, is used for the synthesis. Details of the different experimental techniques used in the present work such as powder X-ray diffraction (XRD), transmission electron microscopy (TEM), scanning electron microscopy (SEM), vibrating sample magnetometer (VSM), thermo-mechanical analysis (TMA), density measurements and magnetostriction measurements using strain gages are described in this chapter. The experimental details of different techniques employed for the characterization and measurements on the properties and performance parameters are discussed.

### 2.2 Methods of Synthesis

There are several methods commonly used for the synthesis of nanoparticles of oxide materials such as combustion, co-precipitation, sol-gel, etc., and the ceramic method is used for preparing bulk particles [1-7]. In the present work, combustion method is used to make cobalt ferrite nanoparticles of different sizes and some comparative studies are

made with the material synthesized by the co-precipitation, citrate-gel and ceramic methods. Hence these methods are described in the following sections.

### 2.2.1 Ceramic Method

Solid state method of synthesis is the most widely used technique for the preparation of polycrystalline solids [1]. This method is also called as ceramic method or high temperature method, because it involves heating the suitable constituents to high temperatures above 1000 °C. In this method, the constituent oxides or metal salts such as carbonates, salts of carboxylic acids, etc, which decomposes at low temperatures and produce the corresponding oxides, in the required stoichiometric amounts are taken and mixed thoroughly. After mixing, the ground dry powder is pre-calcined at a comparatively lower temperature. The purpose of pre-calcination is to decompose the carbonates, or other salts thereby reducing the evolution of gases in the final sintering, to assist in homogenizing the material, to reduce the effect of variations in the raw materials, and to control the shrinkage occurring during final calcination. After pre-calcination, the powder samples are ground well and heated repeatedly at different temperatures with intermediate grindings till the pure phase is formed. In many cases, after mixing, the powders are compacted into the form of pellets and heated for better reactivity.

The advantage of solid state synthesis or ceramic method is that the process is very simple and is the preferred method when larger quantities of the products are required. The main disadvantages are that it requires high temperatures because solid state reaction is diffusion limited, can be expensive, may give incomplete reaction, may give compositionally inhomogeneous products, there may be some loss of the reactants during repeated grinding and transferring to reaction crucibles, there is little chance of getting kinetic control, and may not get desired microstructure.

In the present work, cobalt ferrite was synthesized by the ceramic method, starting from cobalt carbonate and iron oxide taken in the stoichiometric ratio. For this, stoichiometric amounts of  $\text{CoCO}_3$  and  $\text{Fe}_2\text{O}_3$  in the 1:1 ratio (so that  $\text{Co:Fe}=1:2$ ) were

weighed and mixed together in an agate mortar. The mixture was first pre-calcined at 1000 °C for 12 h, cooled back to room temperature and again heated for 24 h at the same temperature after an intermediate grinding. The resulting powder was further heated at 1100 °C for 72 h with two intermediate grindings after every 24 hours of heating.

### 2.2.2 Autocombustion Method

Combustion synthesis, also known as the self-propagating high temperature synthesis (SHS) is a simple and efficient method for the synthesis of ceramic oxides [8, 9]. In a combustion reaction, the exothermicity of a redox chemical reaction is used for the preparation of a wide range of technologically important materials. The advantages of combustion synthesis over the ceramic method of synthesis are: expensive processing facilities and equipments can be avoided due to the simple and exothermic nature of the reaction, the short time duration of the exothermic reaction requires low operating and processing costs, many inorganic materials can be synthesized and consolidated into a final product in a single step by utilizing the chemical energy of the reactants, etc.

Solution combustion synthesis (SCS) is a branch of the combustion method for preparing metal oxides [10]. It involves rapid heating of water solution of an oxidizer and a fuel. The fuel used is usually a water soluble organic compound such as hydrazides, azines, urea, amino acids such as glycine, etc. The fuel serves different purposes such as, they are the source of C and H, which on combustion form CO<sub>2</sub> and H<sub>2</sub>O and liberate lot of heat as well as they form complexes with the metal ions facilitating homogeneous mixing of the cations in solution. The nature of the combustion reaction may differ depending on the fuel used. Usually metal nitrates are used as the oxidizer. The oxidizer and fuel are made into a solution, individually using water as the solvent, and finally solutions are mixed together. It ensures the mixing of metal ions at a molecular level thereby leading to homogeneous powders. The term autocombustion is also used for the combustion synthesis since the combustion reaction is initiated automatically without using any external aid.

The autocombustion method is very useful for synthesizing homogeneous materials at very low temperatures. This process has several advantages than the other methods of synthesis and some of the salient features of this method are; the oxides and their composites can be prepared at very low temperatures ( $< 673$  K), the products are homogenous and crystalline; they are soft, highly porous due to the liberation of large amount of gases during the reaction and fine with high surface area, narrow particle size distribution with nanosized particles, the materials prepared are of high purity, the particles show less agglomeration, large scale synthesis is possible and the method is relatively cheap.

This method is actually self-sustainable after the reaction is initiated and owing to the exothermic nature of the reaction, high internal temperature ensures the crystallization and formation of the oxides. Theoretically, the reaction products of a stoichiometric fuel-oxidizer mixture combustion reaction are  $N_2$  (when nitrogen containing fuels are used)  $H_2O$ ,  $CO_2$  and the fine agglomerated particles of the desired oxide composition. In practice, however, lab scale reactions do not proceed perfectly, resulting in noxious gasses, fuel residue and multi-phase product. Using proper fuels and oxidizers the reaction can be significantly altered without producing toxic gases. During combustion, the temperature of the flame can be very high for a short time which is sufficient to produce metal oxides. Therefore, at molecular level, sufficient heat energy is available for the formation of oxides from the oxidation of the fuel. The availability of the amount of energy and the homogeneity of the precursor solution make their formation easy.

The amino acid, glycine ( $H_2NCH_2COOH$ ) plays two important roles when used as the fuel in the synthesis. Firstly it forms a complex with metal ions involved, acting as a bidentate ligand [11]. The different end groups i.e., the carboxylic group and amino group can be utilized for complex formation. The zwitterionic character of glycine allows effective complexation with metal ions of varying ionic sizes. Also it enhances the solubility of metal ions thereby avoiding selective precipitation when water is evaporated. In the glycine-nitrate process (GNP) using metal nitrates as the oxidizer and glycine as fuel [11] the main controllable processing variable is the glycine-to-nitrate ratio, which

affects the flame temperature, product morphology and particle size of the resultant product. It is reported that maximum flame temperature of  $\sim 1773$  K is observed for glycine-to-nitrate ratio of  $\sim 0.55$  [11]. Usage of larger amounts of glycine per mole of metal ion is found to be more favorable to reduce the rate of reaction rate while the reaction remains spontaneous and self-sustaining. Another advantage of adding extra fuel is that the formation of intermediate nitrates of the metals can be avoided. Synthesis of technologically important oxides with interesting magnetic [12, 13], dielectric [14, 15], mechanical [16], optical [17] and catalytic [18] properties, using glycine nitrate process, has been reported in the literature.

In the present work, the synthesis method used is the glycine-nitrate process (GNP) where glycine used as a fuel, as already reported in the literature [13]. Stoichiometric amounts metal nitrates (cobalt and ferric nitrates) were dissolved separately, in minimum amount of distilled water. Glycine, corresponding to different glycine to nitrate ratios, was also dissolved separately in minimum amount of distilled water. All the three solutions were mixed thoroughly. The mixed solution was then transferred to a crystallizing dish and the dish with its contents was subjected to heating on a hot plate at a temperature of about  $200$  °C. After complete evaporation of water, the resulting viscous liquid ignited automatically giving rise to a fluffy mass.

### 2.2.3 Co-precipitation Method

The term co-precipitation stands for the precipitation of more than one species simultaneously [19]. Post treatments such as calcination, vacuum drying, etc are required to convert the precipitate formed to the desired products. It is a well-known method for the synthesis of nanosized particles of mixed metal oxides, as it possesses the advantage of greater homogeneity, greater reactivity along with the molecular level mixing. In this method, the synthesis of nanomaterials can be achieved by the co-precipitation of sparingly soluble products from aqueous solutions followed by thermal decomposition of these products. In certain cases, depending on the precipitation agent used, the desired metal oxides are obtained directly without any post treatment of the precipitate. A

controlled precipitation using a proper medium leads to a mixture of very fine particles. It is widely accepted that simultaneous nucleation, growth and agglomeration takes place during the co-precipitation reaction. However, co-precipitation method offers some advantages such as simple and rapid preparation, various possibilities to modify the particle surface state and overall homogeneity, control of particle size and distribution by controlling various process parameters such as concentration of the solutions, temperature, pH, rate of addition, etc and large scale production.

Co-precipitation methods are classified into two types. They are direct or normal co-precipitation method and the reverse co-precipitation method. In the normal co-precipitation reaction, the precipitating agent (such as alkali solution) is added to the metal salt solution whereas in the reverse co-precipitation method, metal solution is added to the alkali solution (NaOH or NH<sub>4</sub>OH). During a normal co-precipitation method, the pH value gradually increases, because alkali solution is dropped into the mixed metal solution. In the case of the reverse co-precipitation method, the mixed metal solution is directly dropped into an alkaline solution. In this case, there is not much variation in the pH of the alkaline solution and hence a constant pH can be maintained during the precipitation reaction. Consequently, it is expected that the nanoparticles, once formed, does not grow much in size in this reverse method as compared to the normal co-precipitation method.

Preparation of nanocrystalline cobalt ferrite by the co-precipitation method is already reported in the literature [20-23]. In the present work, cobalt ferrite is prepared by the reverse co-precipitation method. Cobalt and iron nitrates were taken in the stoichiometric ratio (1:2 molar ratio) and dissolved in distilled water. By using a burette, the mixed solution was added to 20% of KOH solution taken in a round bottom flask. A precipitate formed is filtered and washed several times with distilled water until the pH is around 7. The precipitate is dried overnight in an oven at 100°C which is eventually converted to a black powder of cobalt ferrite.

### 2.2.4 Citrate Method

The citrate method is a kind of sol–gel method for the synthesis of metal oxides using citric acid as a complexing agent [24]. It is a less time consuming method compared to the sol-gel method using metal alkoxides. In this method, a mixture of the corresponding metal salts and citric acid dissolved in a suitable solvent (water) and the resulting solution is heated for evaporation of the solvent. The solution becomes more and more viscous due to the continuous removal of the solvent during evaporation. Finally a gel is obtained and the dried gel up on calcination at a suitable temperature gives rise to the corresponding metal oxides. The citrate gel method is suitable for the synthesis of mixed metal oxides due to the molecular level mixing of the constituent metal ions. Also, the method is highly suitable for making nanocrystalline materials of different sizes and shapes by controlling the concentration of the metal ions, ratio of metal ions to citric acid, calcination temperature, etc. The citrate gel method has been widely used for the synthesis of nanoparticles of different mixed metal oxides, involving more than one metals, such as different types of ferrites, perovskites, etc., including cobalt ferrite [25-28].

In the present work, stoichiometric amounts of the corresponding metal nitrates were dissolved in distilled water. Water solution of citric acid was added to the metal ion solution keeping the metal to citric acid ratio as 1:2. The solution was evaporated on a water bath and finally a thick gel was formed. This precursor was dried in an oven at 100 °C and the dried precursor was calcined at 500 °C for 4 h to get the cobalt ferrite powder.

## 2.3 Compaction

Bulk or nanocrystalline powders obtained by various synthetic techniques have to be densified into different geometries, shapes and sizes to take full advantages of the properties of the materials and for various applications. Compaction is the initial process of forming of metal powders into compacts of desired shape and size with sufficient strength to withstand ejection from tool and subsequent handling up to the completion of

sintering operation without breakage or damage [29]. When a particulate solid is placed into space and pressure is applied, a reduction of volume will occur at low pressures and rearrangement of particles takes place, leading to close packing. At higher pressures, elastic deformation of the particles may occur, causing particles to flow into void spaces and increasing the area of interparticle contact. These stages continue until the compact density approaches the true density of the material. Density will vary with several parameters. Density variation increases with the applied pressure and with the height of the specimen for constant diameter. Density variation decreases with increasing diameter even at constant height-to-diameter ratio, and density variation is slightly reduced by the addition of a lubricant to the powder. Various methods of compaction are available such as pressure-less shaping technique, isostatic and uniaxial pressing such as cold pressure shaping technique and pressure shaping technique with heat, according to the strength and properties required.

In the present work, cold uniaxial pressing shaping technique was used to get green compacts. The powder sample was mixed with 2% solution of poly vinyl alcohol as a binder and pressed into cylindrical shaped specimen (dimensions with ~10 mm diameter x ~15 mm length) under a pressure of 8 MPa, using steel dies.

## 2.4 Sintering

Sintering is defined as the thermal treatment of a powder or compact at a temperature below the melting point of the main constituent for the purpose of increasing its strength by bonding together of the particles [30]. The sintering of a material usually causes many changes in its properties. In ceramics, strength, thermal conductivity, density and transparency are increased. In metals, conductivity, strength and ductility usually increase and density depends on the details of preparation. It is the most important and delicate processing technique producing the final product with desirable properties. In the compacted form the partially reacted particles press against each other over part of their surface, the remaining surface forming the boundaries of the interstitial voids or pores. At temperatures in the region of 1000 °C and above, the free surface containing the voids

decreases, the particles grow together to form crystallites and the density rises. The process of sintering is accomplished by bonding between the contacting particles at higher temperatures due to the accelerated diffusion. Sintering can be carried out at a range of temperatures, but the process will be accelerated towards the melting point. It takes place faster as the particle size decreases, since diffusion distances are shorter and curvature stresses are larger.

Sintering of the compacts made from cobalt ferrite nanoparticles has been carried out under different conditions and the details are described in the respective chapters.

## 2.5 Characterization Techniques

### 2.5.1 Powder X-Ray Diffraction (XRD)

Powder X-ray diffraction technique is the most important and widely used technique for the initial characterization, determination of phase formation and crystal structure determination of crystalline solids [31, 32]. The XRD pattern is the finger print of a crystalline material as this technique gives information on the structure, phase and purity of a material. This technique is based on Bragg's law, which states that,

$$n\lambda = 2d \sin\theta \quad (2.1)$$

where,  $\lambda$  = wavelength of the incident rays

$n$  = order of diffraction

$d$  = spacing between the diffracting planes

$\theta$  = angle of incidence of X-rays.

A monochromatic beam of X-rays is allowed to impinge on a sample. This beam is scattered by various planes in the crystal lattice in all directions. For only those planes which satisfy the Bragg's law (that is, for particular angle  $\theta$ ), the rays scattered by the crystal planes interfere constructively i.e. they reinforce each other to produce a very high intensity beam, while from all other planes, destructive interference occurs. The intensity

of the diffracted beam is much greater for the particular plane where the angle of incidence is equal to Bragg's angle. A recorder records this beam and a plot of  $I/I_0$  Vs  $2\theta$  is thus obtained. Thus by knowing ' $\theta$ ' and ' $\lambda$ ' values one can determine  $d$  values of the diffracting planes. From the  $d$  value one can directly determine the (hkl) values for that plane and thus crystal structure of the sample can be determined. In the case of known materials, phase characterization is possible by directly comparing the experimental XRD patterns with the standard patterns reported in the literature or with the JCPDS/ICDD data base.

It is widely known that the width of a diffraction peak increases when the crystallite size is reduced below a certain limit ( $< 100$  nm). Therefore, XRD patterns can be used to estimate the average size of very small crystallites, from the measured width of the peaks in the diffraction patterns. Generally, there will be a contribution to line broadening from the instrument due to various factors and this natural line width needs to be corrected before using for the calculation of crystallite size. The average crystallite size is calculated from X-ray line broadening using the Scherrer formula [31],

$$D = \frac{0.9 \lambda}{\beta \cos \theta} \quad (2.2)$$

where  $D$  is the crystallite size in Å,  $\beta$  is the half maximum line width, in radians, corrected for instrumental contribution to line broadening and  $\lambda$  is the wavelength of X-rays.

In the present work, powder XRD analysis was carried out on a Panalytical X'pert Pro model X-ray diffractometer, at the scan rate of  $2^\circ/\text{min}$  in the  $2\theta$  range of 10 to 80 degrees. The X-ray source used was Cu  $K\alpha$  radiation with a wavelength of 1.5416 Å. The diffractometer was calibrated with reference to a standard oriented Si wafer. The lattice parameters and  $d$ -spacings were calculated using a computer program 'Powder Cell for Windows', PCW version 2.4, developed by W. Krauz and G. Nolze [33]. The experimental XRD patterns were compared with the standard available data from the

Joint Committee on Powder Diffraction Standards (JCPDS), International Center for Diffraction Data, with the card number.

### 2.5.2 Transmission Electron Microscopy (TEM)

Transmission electron microscopy (TEM) is one of the methods that give images of individual nanostructures. It is an imaging technique whereby a beam of electrons is focused onto a specimen causing an enlarged version to appear on a fluorescent screen or can be detected by a CCD camera [34, 35]. TEM operates on the same basic principles as the light microscope but uses electrons instead of light. Virtually, TEM is useful for determining size, shape and arrangement of the particles which make up the specimen. The method is based on the use of electrons rather than light to examine the structure and behavior of the material. An image is formed from the interaction of the electrons transmitted through the specimen. The image is magnified and focused onto an imaging device. TEM gives high resolution than the light microscopes, owing to the small de Broglie wavelength of electrons. This enables us to study finer details of materials such as the size of the particles and their morphology.

The nanocrystalline materials synthesized in the present work were analyzed using a model SEI, PECNAI G2 TF30 transmission electron microscope. The powder sample was dispersed in a suitable organic solvent with a low boiling point like isopropanol and dropped on a carbon coated copper grids for analysis. The coated samples were allowed to dry for overnight to evaporate the solvents before the analysis.

### 2.5.3 Scanning Electron Microscopy (SEM)

The Scanning Electron Microscope (SEM) is a type of electron microscope capable of producing high resolution images of a sample surface. It is a very useful instrument to get information about topography, morphology, composition and microstructural information of materials [36]. Due to the manner in which the image is created, SEM images have a characteristic three dimensional appearance and are useful for judging the surface structure of a sample. It has compensating advantages, including the ability to image a

comparatively large area of specimen and the ability to image bulk materials. In a typical SEM, electrons are thermionically emitted from a tungsten or lanthanum hexaboride (LaB<sub>6</sub>) cathode and are accelerated towards an anode; alternatively, electrons can be emitted via field emission. Tungsten is used because it has the highest melting point and lowest vapor pressure of all metals, thereby allowing it to be heated for electron emission. The electron beam typically has an energy ranging from a few 100 eV to 50 KeV. The beam passes through pairs of scanning coils in the objective lens, which deflect the beam over a rectangular area of the sample surface. The electrons are detected by a scintillator photomultiplier device and the resulting signal is rendered into a two dimensional intensity distribution that can be viewed and saved as a digital image.

Particle topology of the powder samples and microstructure of the sintered samples in the present study were obtained to using a Quanta 200 3D (Dual beam ESEM) scanning electron microscope and tungsten filament as an electron source. For analysis of powder sample morphology, the powder sample was spread on an Al holder using isoamyl acetate. On the other hand, sintered pellets were fractured to expose the inner portion and mounded on a specimen mounting stub.

#### 2.5.4 Vibrating Sample Magnetometer (VSM)

The magnetic characteristics of materials as a function of applied field at different temperatures and as a function of temperature at different applied field strengths can be measured using a vibrating sample magnetometer (VSM). A material's complete magnetic behavior can be studied using a VSM. The instrument allows precise magnetization measurements to be made as a function of magnetic field strength, temperature and crystallographic orientation. VSM is based on Faraday's law which states that an emf will be generated in a coil when there is a change in a flux linked with the coil [37, 38]. It works on the principle that when a magnetic material is vibrated in a homogeneous magnetic field, magnetic flux changes are produced in the neighborhood of the sample with the vibration frequency. If the sample is vibrated periodically, it can induce an electrical signal in a pickup coil. The signal intensity is proportional to the

magnetic moment produced in the sample, the vibration amplitude and the frequency. The last two terms can be nullified by comparing with the signal generated from a set of reference coils vibrating with the same frequency and amplitude, after passing through a differential amplifier. Schematic diagram of a VSM is shown in Figure 2.1.

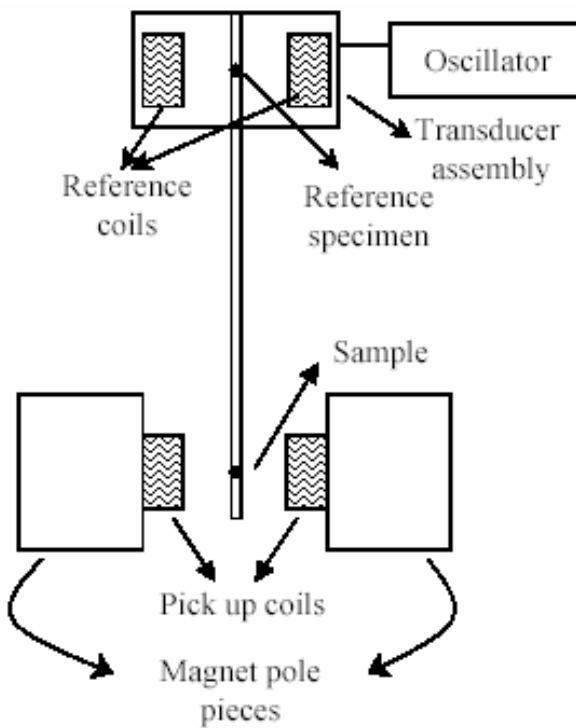


Figure 2.1: Schematic diagram of the VSM components.

In the VSM, the sample is filled in a vertical tube and is fitted to a rod. This rod is then vibrated between the poles of a powerful electromagnet. The upper part of the rod is connected to a transducer. It converts a sinusoidal ac drive signal, provided by an oscillator into a sinusoidal vertical vibration of the sample rod. The position of the tube is adjusted to have maximum flux concentration at the sample. The rod is vibrated at  $\sim 80$

Hz. The change in flux is recorded by the coil and is used for further calculation of the magnetic moment of the sample.

Magnetic measurements in the present work are performed on an EG&G PAR 4500 vibrating sample magnetometer. The VSM was calibrated using a standard Ni sample. The sample holder used is made of a non-magnetic polymer material, Kel-F (poly(chlorotrifluoro)ethylene). Field dependence of magnetization was measured up to a maximum field of  $\pm 1200$  kA/m at room temperature. For high temperature measurements, an electrically heated oven was attached to the VSM to heat the sample (300–973 K). Here, a constant field is applied and the magnetization was measured by varying the temperature from 300 K to 973 K at a constant heating rate of 2 K/min. For zero field cooled (ZFC) measurements, the sample was cooled to the lowest possible temperature in zero magnetic field and then magnetization was recorded while warming it back to room temperature under a constant field. In the case of field cooled (FC) measurement, a constant field was applied during cooling down to the lowest possible temperature and the magnetization was measured under the same magnetic field while heating back to room temperature.

### 2.5.5 Thermo-Mechanical Analysis (TMA)

Thermo mechanical analyzer (TMA) provides measurement of penetration, expansion, contraction and extension of a material as a function of temperature [39]. Moreover, this technique is highly useful to measure the stress and strain of polymers. It consists of a probe connected mechanically to the core of a linear variable differential transformer. The core is coupled to the sample by means of a quartz probe and a thermocouple is used for the measurement of sample temperature. Any movement of the sample is translated into moment of the transformer core and result in an output proportional to the displacement of the probe. Its sign is an indication for the direction of movement and this can be measured as a function of temperature. In the penetration and expansion modes, the sample rest on a quartz stage surrounded by the furnace. Under no load, expansion with temperature is observed. We can calculate the coefficient of linear expansion from

the slope of the resulting curve. A weight tray attached to upper end of the probe allows to predetermine the force applied to samples to study variation under a load. The instrument is suitable to study the sintering behavior of pressed green compacts, by measuring the shrinkage of the compact as a function of temperature. The schematics of a thermomechanical analyzer is shown in Figure 2.2.

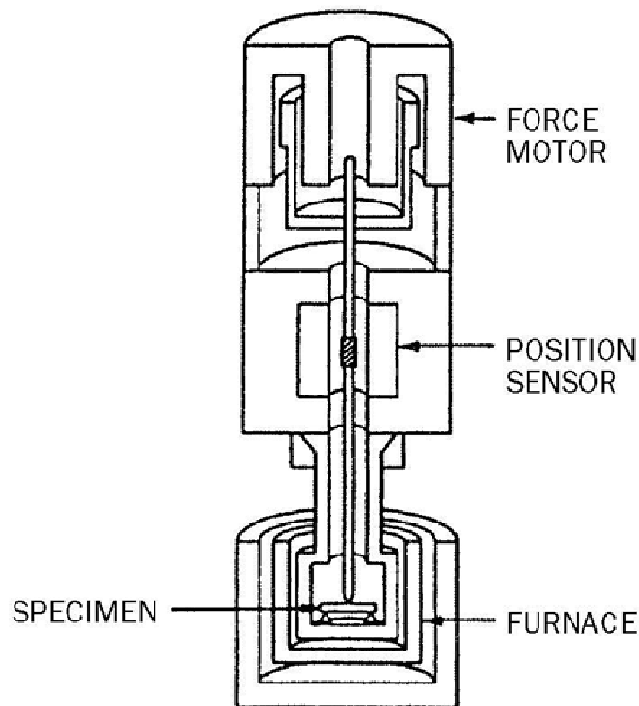


Figure 2.2: Schematic diagram of a Thermo-Mechanical Analyzer.

A Perkin Elmer Instrument, Pyris Diamond TMA, was used to study the sintering behavior of the ferrite samples in terms of linear shrinkage as a function of temperature. The temperature range employed is 30 °C to 1500 °C at a heating rate of 5 °C/min. An alumina probe was used as the TMA probe. The sample pellet (5 mm thickness) was kept inside the sample tube on an alumina plate and a constant force of 100 mN was applied to

it. An independently connected linear voltage differential transformer (LVDT) and core detected the changes in sample thickness as a function of temperature. The data is collected by a computer and the output can be plotted as  $\Delta L/L$  versus temperature, where  $L$  is the length or thickness of the sample.

### 2.5.6 Density Measurements

Densities of the sintered discs were calculated from the volume and the weight of the discs as well as by the Archimedes method. Both methods gave comparable values of the densities. The relative density was calculated from the ratio of the measured density to the theoretical density calculated from the crystal structure parameters. The theoretical density was calculated from the following equation [32],

$$\rho = \frac{\text{Formula weight}}{\text{Molar volume}} = \frac{FW \times Z}{(V \times N_A)} \quad (2.3)$$

where,  $FW$  is the formula weight

$Z$  is the number of formula units in each unit cell

$V$  is the volume of the unit cell and

$N_A$  is Avogadro's number

The theoretical density of  $\text{CoFe}_2\text{O}_4$  is calculated as shown below. The formula weight of  $\text{CoFe}_2\text{O}_4$  is 234.63 g. Spinel ferrites have eight formula units per unit cell. Therefore, the weight of one unit cell is  $8 \times 234.63 = 1877.04$  g. The volume of a cube of side length  $a$  is  $a^3$ . The unit cell length,  $a$ , of  $\text{CoFe}_2\text{O}_4$  is 8.391 Å [40]. Therefore, the volume of a unit cell is  $a^3 = 590.80 \text{ \AA}^3$  ( $1 \text{ \AA}^3 = 10^{-24} \text{ cm}^3$ ) and  $N_A \times V = 355.84 \text{ cm}^3$ .

$$\text{Theoretical density of } \text{CoFe}_2\text{O}_4 (\rho) = \frac{1877.04}{355.84} = 5.275 \text{ g/cm}^3$$

## Archimedes method of measurement

Archimedes' principle states that when a body is immersed in a fluid there is a buoyant force acting upward on the body equal to the weight of the displaced fluid [41]. Density of a solid of known mass can be thus measured from the mass of the liquid displaced when the solid is immersed in the liquid kept in a container. A solid is weighed first in air, then while immersed in water; the difference in the two weights, according to Archimedes' principle, is the weight of the water displaced by the volume of the solid. The specific gravity of the solid is the ratio of its weight in air to the difference between its weight in air and its weight immersed in water. Specific-gravity bottle (pycnometer) is used to determine the density of homogeneous solid object that does not dissolve in a working liquid (water). First, we need to measure the weight of pycnometer together with inserted object  $m_0+m_S$ . Add water and determine the weight  $m'_{H_2O}$  (measured weight minus  $m_0+m_S$ ). The volume of added water  $V'_{H_2O}$  can be obtained as,

$$V'_{H_2O} = \frac{m'_{H_2O}}{\rho_{H_2O}} \quad (2.4)$$

The volume of measured solid object  $V_S$  is the difference between the volume of water that fills the empty pycnometer  $V$  and volume  $V'_{H_2O}$ .

$$V_S = V - V'_{H_2O} \quad (2.5)$$

Density of the solid  $\rho_S$  can be then calculated as,

$$\rho_S = \frac{m_S}{V_S} \quad (2.6)$$

### 2.5.7 Magnetostriction Measurements

Magnetostriction is the change in the size (length, volume) of a magnetic material when an external magnetic field is applied. Magnetostriction is an important parameter determining the domain structure, the magnetization process and the coercive field of a magnetic material. The magnitude and sign of the magnetoelastic energy determines the stress dependence of the hysteresis loop, which can be used for sensor applications. In practice, the magnitude of measured strain is very small and therefore, the strain is expressed as microstrain ( $\mu\epsilon$ ), which is  $\epsilon \times 10^{-6}$ . Therefore, the accurate determination of the magnetostrictive strain is very important. Various methods are available to measure the magnetostriction by direct and indirect methods. Direct methods are by using strain gages, capacitance transducers and interferometer methods. The indirect methods are Beckner-Kersten method which is more simple and determined from stress dependence of the hysteresis loop [42] and small angle magnetization rotation (SAMR) methods [43]. SAMR method can be used to measure the magnetostriction from 4.2 K to high temperatures. Other techniques such as capacitance dilatometry [44-46] and laser deflection methods [47] are also available for the measurement of magnetostriction.

Among all the methods, strain gage method is widely recognized as the most practical technology for the measurement of magnetostrictive strain [48]. Strain gage is a semiconductor device whose resistance varies nonlinearly with strain. The most widely used gage is the bonded metallic strain gage. Strain gage method was developed by Goldman [48]. Birss *et al* found that strain gages can be successfully used for magnetostriction measurements in the temperature range of -196 to 400 °C [49]. The metallic strain gage consists of a very fine resistive wire wound back and forth on a polyamide film as shown in Figure 2.3. The cross sectional area of the grid is minimized to reduce the effect of shear strain and Poisson strain [50].

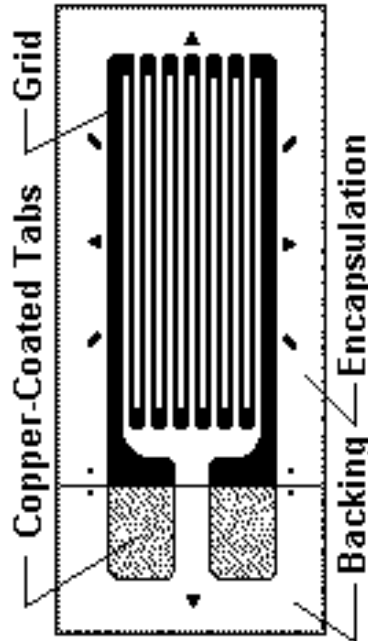


Figure 2.3: Schematic diagram of a strain gage.

The grid is bonded to a thin backing, called the carrier, which is attached directly to the test specimen. Therefore, the strain experienced by the test specimen is transferred directly to the strain gage, which responds with a linear change in electrical resistance. Strain gages are available commercially with nominal resistance values from 30 to 3000  $\Omega$ , with 120, 350, and 1000  $\Omega$  being the most common values. It is very important that the strain gage be properly mounted onto the test specimen so that the strain is accurately transferred from the test specimen, through the adhesive and strain gage backing, to the foil itself.

The change in resistance of the gage as a function of applied magnetic field is recorded and converted into the magnetostrictive strain by using the relation,

$$\frac{\Delta L}{L} = \frac{\Delta R/R}{G.F} \quad (2.7)$$

where,  $L$  is the length of the material in its unmagnetized state,  $\Delta L$  is the change in length in a magnetic field,  $R$  is the gage resistance at zero applied magnetic fields,  $\Delta R$  is the change in the gage resistance at a known applied magnetic field strength and G.F. is the gage factor. Usually gage factor is provided by the manufacturer.

In the present study, the samples used for magnetostriction measurements were made on cylindrical shaped specimens. The magnetostriction measurement was carried out on circular rod shaped specimen with dimensions with  $\sim 7$  mm diameter x  $\sim 10$  mm length. After grinding the sides of the pellets and making a flat surface along the length of the rod, the strain gage was mounded with special binding solutions (adhesive M-Bond 610) on the flat surface. The strain gages used in the present study were obtained from Vishay Micro-Measurements, USA (strain gage type EK-09-062-AP, matrix size of 6.6 mm x 4.1 mm, gage size 2.90 mm x 1.57 mm). The calibration of the strain gage was carried out by measuring magnetostriction of Ni metal. The gage resistance was measured by the four probe method of resistance measurements using a Keithley 2010 multimeter. The four probe method is one of the standard and most widely used methods for the measurement of resistivity.

Magnetostriction,  $\lambda = \Delta L/L$ , the relative change in the length of the sample in an applied magnetic field, was measured on the sintered pellets at room temperature using 350  $\Omega$  resistive strain gauges.  $\lambda_{\text{par}}$  is the magnetostriction measured when the applied external magnetic field is parallel to the cylindrical axis of the sintered pellet and  $\lambda_{\text{per}}$  is for the magnetic field applied perpendicular to this direction.

## References

- [1] J. M. Honig and C. N. R. Rao, *Preparation and Characterization of Materials* (Academic Press, San Diego, 1981).
- [2] C. N. R. Rao, *Chemical Approaches to the Synthesis of Inorganic Materials* (Wiley Eastern Ltd., New Delhi, 1994).
- [3] D. Segal, *Chemical Synthesis of Advanced Ceramic Materials* (Cambridge University Press, New York, 1991).
- [4] A. S. Edelstein and R. C. Cammaratra, *Nanomaterials: Synthesis, Properties and Applications* (Taylor & Francis, New York, 1998).
- [5] J. P. Jolivet, M. Henry and J. Livage, *Metal Oxide Chemistry and Synthesis: From Solution to Solid State* (Wiley, New York, 2000).
- [6] G. Cao, *Nanostructures & Nanomaterials: Synthesis, Properties & Applications* (World Scientific Publishing Company, Singapore, 2011).
- [7] G. A. Ozin and A. C. Arsenault, *Nanochemistry: A Chemical Approach to Nanomaterials* (Royal Society of Chemistry, Cambridge, 2005).
- [8] J. J. Moore and H. J. Feng, *Prog. Mater. Sci.* 39 (1995) 243.
- [9] J. J. Moore and H. J. Feng, *Prog. Mater. Sci.* 39 (1995) 275.
- [10] K. C. Patil, S. T. Aruna and T. Mimani, *Current Opinion Solid State Mater. Sci.* 6 (2002) 507.
- [11] L. A. Chick, L. R. Pederson, G. D. Maupin, J. L. Bates, L. E. Thomas and G. J. Exarhos, *Mater. Lett.* 10 (1990) 6.
- [12] C. C. Hwang, T. Y. Wu, J. Wan and J. S. Tsai, *Mater. Sci. Eng. B* 111 (2004) 49.
- [13] N. Kikukawa, M. Takemori, Y. Nagano, M. Sugasawa and S. Kobayashi, *J. Magn. Mater.* 284 (2004) 206.

- [14] R. Peng, C. Xia, Q. Fu, G. Meng and D. Peng, *Mater. Lett.* 56 (2002) 1043.
- [15] G. Zhu, X. Fang, C. Xia and X. Liu, *Ceram. Int.* 31 (2005) 115.
- [16] M. Mazaheri, M. Valefi, Z. R. Hesabi and S. K. Sadrnezhad, *Ceram. Int.* 35 (2009) 13.
- [17] Y. Xijuan, X. Pingbo and S. Qingde, *Phys. Chem. Chem. Phys.* 3 (2001) 5266.
- [18] X. Guo, D. Mao, G. Lu, S. Wang and G. Wu, *J. Catal.* 271 (2010) 178.
- [19] S. Laurent, D. Forge, M. Port, A. Roch, C. Robic, L. Vander Elst and R. N. Muller, *Chem. Rev.* 108 (2008) 2064.
- [20] X. Yang, X. Wang and Z. Zhang, *J. Cryst. Growth* 277 (2005) 467.
- [21] Y. Qu, H. Yang, N. Yang, Y. Fan, H. Zhu and G. Zou, *Mater. Lett.* 60 (2006) 3548.
- [22] Z. Zi, Y. Sun, X. Zhu, Z. Yang, J. Dai and W. Song, *J. Magn. Magn. Mater.* 321 (2009) 1251.
- [23] I. H. Gul, A. Maqsood, M. Naeem and M. N. Ashiq, *J. Alloys Compd.* 507 (2010) 201.
- [24] S. Kumar, K. S. Gandhi and R. Kumar, *Ind. Eng. Chem. Res.* 46 (2007) 3128.
- [25] C. Cannas, A. Falqui, A. Musinu, D. Peddis and G. Piccaluga, *J. Nanopart. Res.* 8 (2006) 255.
- [26] B. S. Chauhan, R. Kumar, K. M. Jadhav and M. Singh, *J. Magn. Magn. Mater.* 283 (2004) 71.
- [27] F. Deganello, G. Marci and G. Deganello, *J. Eur. Ceram. Soc.* 29 (2009) 439.
- [28] S. Prasad, A. Vijayalakshmi and N. S. Gajbhiye, *J. Therm. Anal. Calorim.* 52 (1998) 595.
- [29] G. Y. Onoda and L. L. Hench, *Ceramic Processing before Firing* (Plenum, New York 1978).

- [30] S. J. L. Kang, *Sintering: densification, grain growth and microstructure* (Butterworth-Heinemann, Oxford, 2005).
- [31] B. D. Cullity and S. R. Stock, *Elements of X-ray Diffraction* (Prentice Hall, NJ, 2001).
- [32] A. R. West, *Solid State Chemistry and its Applications* (John Wiley & Sons, Singapore, 2003).
- [33] W. Kraus and G. Nolze, PowderCell for Windows (PCW), version 2.4 (The software is freely available from <http://ccp14.ac.uk>).
- [34] G. Thomas, *Transmission Electron Microscopy of Metals* (John Wiley & Sons, New York, 1962).
- [35] D. B. Williams and C. B. Carter, *Transmission Electron Microscopy: A Textbook for Materials Science Vol. I-IV* (Plenum Press, New York, 1996).
- [36] J. Goldstein, D. E. Newbury, D. C. Joy, C. E. Lyman, P. Echlin, E. Lifshin, L. Sawyer and J. R. Michael, *Scanning Electron Microscopy and X-ray Microanalysis, 3rd ed.*, (Kluwer Academic/Plenum Publishers, New York, 2003).
- [37] S. Foner, *Rev. Sci. Instrum.* 30 (1959) 548.
- [38] B. D. Cullity and C. D. Graham, *Introduction to Magnetic Materials* (John Wiley & Sons, New Jersey, 2009).
- [39] J. D. Menczel and R. B. Prime, *Thermal Analysis of Polymers* (John Wiley & Sons, New York, 2009).
- [40] JCPDS - *International Centre for Diffraction Data* (ICDD), PDF Number 22-1086 (Powder Diffraction File-4<sup>+</sup> 2009).
- [41] D. A. Huerta, V. Sosa, M. C. Vargas and J. C. Ruiz-Suarez, *Phy. Rev. E* 72 (2005) 031307.
- [42] R. Becker and M. Kersten, *Z. Phys.* 64 (1930) 660.

- 
- [43] K. Narita, J. Yamasaki and H. Fukunaga, *IEEE Trans. Magn.* 16 (1980) 435.
- [44] V. T. Cherepin, N. I. Glavatska, I. N. Glavatsky and V. G. Gavriljuk, *Meas. Sci. Technol.* 13 (2002) 174.
- [45] P. T. Squire and M. R. J. Gibbs, *J. Phys. E: Sci. Instrum.* 20 (2000) 499.
- [46] M. Rotter, H. Muller, E. Gratz, M. Doerr and M. Loewenhaupt, *Rev. Sci. Instrum.* 69 (1998) 2742.
- [47] Q. Y. Yan, R. J. Gambino, S. Sampath and Q. Huang, *J. Appl. Phys.* 97 (2005) 033902.
- [48] A. Goldman, *Modern Ferrite Technology* (Van Nostrand Reinhold, New York, 1990).
- [49] R. R. Birss and E. W. Lee, *J. Sci. Instrum.* 37 (1960) 225.
- [50] M. Sullivan, *Rev. Sci. Instrum.* 51 (1980) 382.

# Chapter 3

## Effect of Particle Size on the Magnetostriction of Sintered Cobalt Ferrite

### 3.1 Introduction

Ferrites are the most widely used magnetic materials for many technological applications [1-4]. For many of the technological applications, ferrite powders need to be compacted into specific shapes and sintered under suitable conditions to tune the performance parameters. The properties of the sintered products are generally affected by the composition, stoichiometry, processing conditions, microstructure, density, grain size, etc, and these are very important factors determining the final performance of the ferrites [3]. In the recent years, research work is focused on nanocrystalline ferrites due to their importance in understanding the fundamentals in nanomagnetism as well as for their potential applications, including biomedical applications [5-10]. There are several reports in the literature on the magnetic properties of spinel ferrites derived from nanoparticles with different crystallite sizes [11, 12]. Sintered ferrite products derived from nanocrystalline powders have been shown to exhibit improved performance parameters, such as magnetic permeability and dielectric constant, compared to their bulk counterparts [13-18].

Among the different spinel type ferrites, cobalt ferrite,  $\text{CoFe}_2\text{O}_4$ , is known for its high magnetocrystalline anisotropy and high coercivity due to the presence of highly

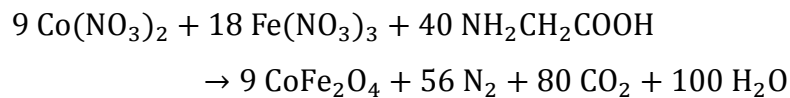
anisotropic  $\text{Co}^{2+}$  ions [19, 20]. In addition, the material has good mechanical hardness, chemical stability, and high saturation magnetization. Cobalt ferrite,  $\text{CoFe}_2\text{O}_4$ , has the mixed spinel structure, represented as  $(\text{Co}_{1-x}\text{Fe}_x)^{\text{T}}[\text{Co}_x\text{Fe}_{2-x}]^{\text{O}}\text{O}_4$ , where  $x$  is the degree of inversion, which depends on the heat treatment conditions, and the superscripts T and O represent the tetrahedral and octahedral sites in the spinel structure, respectively [21]. There are several studies reported in the recent literature on the magnetostrictive properties of sintered, un-substituted [22-31] and substituted [32-41] polycrystalline cobalt ferrite, as discussed in detail in Chapter 1. In brief, the magnetostriction coefficient and strain derivative of sintered cobalt ferrite depend on the processing parameters such as the method of synthesis, pressure applied while making the compacts for sintering, sintering atmosphere, temperature, and duration of sintering [26, 27, 31, 42]. Since cobalt ferrite is an ideal ceramic material for future magnetostrictive applications, it is necessary to achieve relatively large magnetostrictive strain at room temperature by changing the synthesis and processing conditions. The highest value of magnetostriction coefficient so far reported for sintered polycrystalline cobalt ferrite is 230 ppm, synthesized by the ceramic method and processed under simple conditions [23].

Preliminary studies have shown that relatively larger magnetostriction coefficient (~200 ppm) can be obtained for sintered cobalt ferrite derived from nanocrystalline powders compared to the material derived from bulk powders [25]. Out of three different low temperature methods used for the synthesis of nanoparticles, particles of size of 30 nm synthesized by an autocombustion method gave higher values of magnetostriction when compared to the nanoparticles synthesized by other low-temperature methods such as co-precipitation and citrate-gel methods and having smaller particle sizes (10-15 nm). However, so far there have been no detailed and systematic studies reported in the literature to explore the effect of initial particle size of the starting powders used for compaction and the sintering conditions on the magnetostriction characteristics of the sintered compacts derived from nanocrystalline materials.

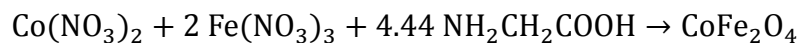
Nanocrystalline cobalt ferrite can be synthesized by various wet chemical methods such as co-precipitation [43, 44], sol-gel [45-47], hydrothermal [48, 49], autocombustion [25, 50, 51], microemulsion [52, 53], etc. Out of this, autocombustion method is a very simple process to obtain nanocrystalline cobalt ferrite. Kikukawa *et al* have reported that the particle size of cobalt ferrite can be varied in the glycine-nitrate process by changing the fuel (glycine) to oxidizer (nitrate) ratio in the combustion synthesis [51]. Nanosized particles could be obtained by using smaller glycine to nitrate (G/N) ratios. The objective of the present work is to study the effect of the initial particle size of the powders on the ultimate value of magnetostriction of cobalt ferrite after sintering. The nanocrystalline cobalt ferrite powders of varying particle sizes below 100 nm are synthesized by the autocombustion method by changing the glycine to nitrate ratio, as reported in the literature [51].

### 3.2 Synthesis

Cobalt ferrite nanoparticles were synthesized by the autocombustion method, using glycine (G) as fuel and the corresponding metal (M) nitrates (N) as the oxidizer, following the previous reports [25, 50, 51]. The main controllable processing variable is the G/N or M/G ratio. G/N ratio corresponds to the complete combustion is called the stoichiometric ratio. For the synthesis of cobalt ferrite from the corresponding metal nitrates, the stoichiometric G/N ratio is 0.55:1 or M/G ratio is 1:1.47 according to the reaction,



(or)



where,  $G/N = 4.44/(2 \times 3 + 1 \times 2) = 4.44/8 = 0.555$ .

For the synthesis of cobalt ferrite, stoichiometric amounts of cobalt nitrate,  $\text{Co}(\text{NO}_3)_2 \cdot 6\text{H}_2\text{O}$  (Aldrich), and ferric nitrate,  $\text{Fe}(\text{NO}_3)_3 \cdot 9\text{H}_2\text{O}$  (Aldrich), taken in the 1:2 molar ratio, were dissolved separately, in minimum amount of distilled water. Glycine (Merck), corresponding to different glycine to nitrate ratios, ranging from 0.05 to 0.75, was also dissolved separately in minimum amount of distilled water. All the three solutions (cobalt nitrate, ferric nitrate, glycine) were mixed thoroughly by ultrasonication for 2 minutes. The mixed solution was then transferred to a crystallizing dish and the dish with its contents was subjected to heating on a laboratory hot plate at a temperature of about 200 °C. After complete evaporation of water, the resulting viscous liquid ignited automatically giving rise to a fluffy mass. This procedure was repeated for different G/N ratios. The sample codes and the corresponding G/N ratios are indicated in Table 3.1.

To compare the properties of the nanocrystalline cobalt ferrite as well as the sintered products derived from the nanocrystalline powders, bulk cobalt ferrite was also synthesized by the ceramic method, starting from the oxides of cobalt and iron taken in the stoichiometric ratio. For this, stoichiometric amounts of  $\text{CoCO}_3$  (Aldrich) and  $\text{Fe}_2\text{O}_3$  (Aldrich) were weighed and mixed together in an agate mortar. The mixture was first heated at 1000 °C for 12 h and again for 24 h at the same temperature after an intermediate grinding. The resulting powder was further heated at 1100 °C for 72 h with two intermediate grindings.

To study the effect of particle size on magnetostriction of sintered cobalt ferrite, nanocrystalline cobalt ferrite powders were also synthesized by co-precipitation and citrate methods. For the co-precipitation method, cobalt and iron nitrates were taken in the 1:2 molar ratio and dissolved in 100 ml distilled water. By using a burette, the mixed solution was added to 20% of KOH (SD Fine Chemicals) solution taken in a round bottom flask. The precipitate formed was filtered and washed several times with distilled water until the pH is around 7. The precipitate was dried overnight in an oven at 100 °C which was eventually converted to a black powder of cobalt ferrite. For the citrate gel method, stoichiometric amounts of the corresponding metal nitrates were dissolved in

distilled water. Water solution of citric acid (SD Fine Chemicals), corresponding to two moles of citric acid per mole of metal, was added to the metal ion solution. The resulting solution was evaporated on a water bath and finally a thick gel was formed. This precursor gel was dried in an oven at 100 °C and the dried precursor was calcined at 500 °C for 4 h to get the cobalt ferrite powder.

### 3.3 Studies on As-synthesized Powder Samples

#### 3.3.1 Phase Purity and Structural Characterization

Figure 3.1 shows the powder XRD patterns of the different cobalt ferrite samples synthesized by varying the G/N ratio from 0.05 to 0.75 (sample codes G1 to G13). All the reflections in the experimental patterns are very broad, and the width of the reflections decreases with increasing G/N ratio, indicating increasing crystallite size. Only the most intense reflection of cobalt ferrite is observed for G1 as a very broad peak. The next most intense reflection started appearing with increased intensity for G2 and G3 and all the reflections of cobalt ferrite are observed for sample G4 and others. For the combustion synthesis of cobalt ferrite using glycine, the complete combustion reaction corresponds to the G/N ratio of 0.55, according to the balanced reaction as explained in section 3.2. It is found that single phase ferrite is formed up to the G/N ratio of 0.47 (sample G10). FeO is found to be formed as an impurity phase at the stoichiometric G/N ratio of 0.55 (sample G11). At higher G/N ratios, due to the presence of excess glycine, Fe metal impurity is formed, as indicated in Figure 3.1. Kikukawa *et al* previously reported that single phase spinel type ferrites can be obtained from precursors with a G/N ratio less than about 0.5 [51].

Table 3.1: Details of the cobalt ferrite samples synthesized by the autocombustion method using metal nitrates and glycine.

<b>Sample Code</b>	<b>G/N ratio</b>	<b>M/G ratio</b>	<b>Flame temperature (<math>\pm 1^\circ\text{C}</math>)</b>	<b><math>D_{\text{XRD}}</math> (<math>\pm 1\text{nm}</math>)</b>	<b>Lattice parameter (<math>\text{\AA}</math>)</b>
G0	Ceramic method				8.382
G1	0.05	0.125	190	3	8.340
G2	0.09	0.25	215	4	8.340
G3	0.14	0.375	230	5	8.381
G4	0.19	0.5	385	7	8.385
G5	0.23	0.675	442	14	8.384
G6	0.28	0.75	640	22	8.390
G7	0.33	0.875	720	34	8.385
G8	0.38	1.0	770	40	8.393
G9	0.42	1.125	811	61	8.387
G10	0.47	1.25	934	78	8.389
G11	0.55	1.47	867	55	8.389
G12	0.66	1.67	856	57	8.380
G13	0.75	2.0	573	60	8.350

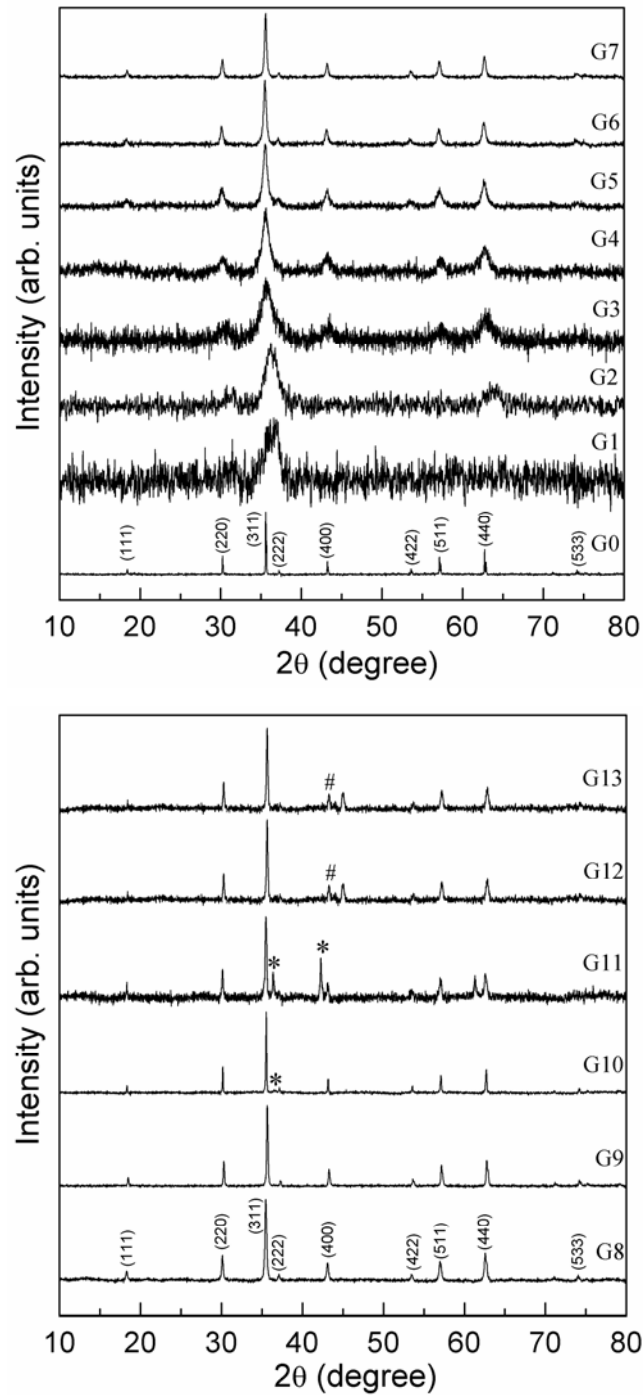


Figure 3.1: Powder XRD patterns of as-synthesized cobalt ferrite powders using different glycine/nitrate ratios (G1 to G13) as well as by the ceramic method (G0). Impurity peaks are marked as \*FeO and #Fe.

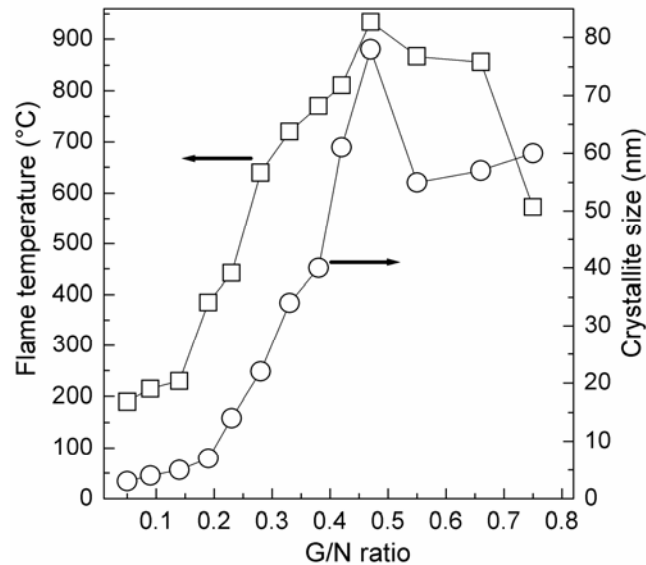


Figure 3.2: Variation of flame temperature and crystallite size with glycine/nitrate ratio.

It is known that the temperature of the combustion reaction has an important effect on the crystallite size of the resulting powder [51]. By adjusting the G/N ratio, one can control the reaction temperature and thereby control the crystallite size of the products. The temperature of the combustion reaction was measured by a Laser thermometer (METRAVI MT-14). As shown in Figure 3.2, flame temperature initially increased with increasing the G/N ratio, highest flame temperature is obtained for G/N = 0.47 and the flame temperature is decreased further with increasing glycine content. It was found that from G1 to G10, flame temperature increases and correspondingly, the crystallite size also increases. This is due to the increasing exothermicity of the combustion reaction with increasing amount of the fuel [54]. A low flame temperature of 190 °C was observed in the case of G1. The highest flame temperature of 934 °C was obtained for G10 for which the G/N ratio is close to stoichiometric ratio (0.47). At this G/N ratio, complete combustion reaction takes place. When the G/N ratio is further increased beyond 0.47, the flame temperature was found to be decreased due to the lesser amount of the oxidizer available for the combustion reaction.

The average crystallite size is calculated using the Scherrer formula,  $D_{\text{XRD}} = 0.9\lambda/\beta\cos\theta$ , where  $D_{\text{XRD}}$  is the crystallite size. The calculated average crystallite sizes are shown in Table 3.1. The crystallite size increases with increasing G/N ratio and reaches a maximum for G/N = 0.47 at which the flame temperature also is maximum. There is a direct correlation between the flame temperature and the crystallite size, similar to that reported by Chick *et al* [54], in the case of synthesis of perovskite oxides using the glycine-nitrate process. Relatively smaller crystallite sizes are obtained when impurity phases are also formed along with the ferrite phase for  $G/N \geq 0.5$ . The cubic lattice parameter is calculated for all the samples by least squares method of refinement of the XRD patterns and the values are given in Table 3.1. For G3 to G12, the calculated lattice parameter is comparable to the value reported for cobalt ferrite (8.391 Å, JCPDS # 22-1086) [55]. For G1 and G2, the values are slightly smaller, probably because only few peaks are observed and the peaks are very broad, so that there could be errors in the calculation of the lattice parameter. The lattice parameter is slightly smaller for G12 and G13, possibly due to the formation of a different composition because Fe impurity in large amounts is observed in these samples.

The transmission electron micrographs of some of the as-synthesized powder samples (G2, G4, G6 and G8) are shown in Figure 3.3. The average particle sizes are obtained as 6, 8, 25 and 45 nm, respectively for G2, G4, G6 and G8 and these values are found to be comparable to the average crystallite sizes calculated from XRD line broadening. This clearly shows that nanocrystalline cobalt ferrite has been formed by the present method of synthesis. Since the average crystallite sizes calculated for G2, G4, G6 and G8 are comparable to the particle sizes obtained from TEM measurements, the average crystallite size is considered as the particle size for all samples. Therefore, the crystallite sizes are used as particle sizes in the rest part of this thesis.

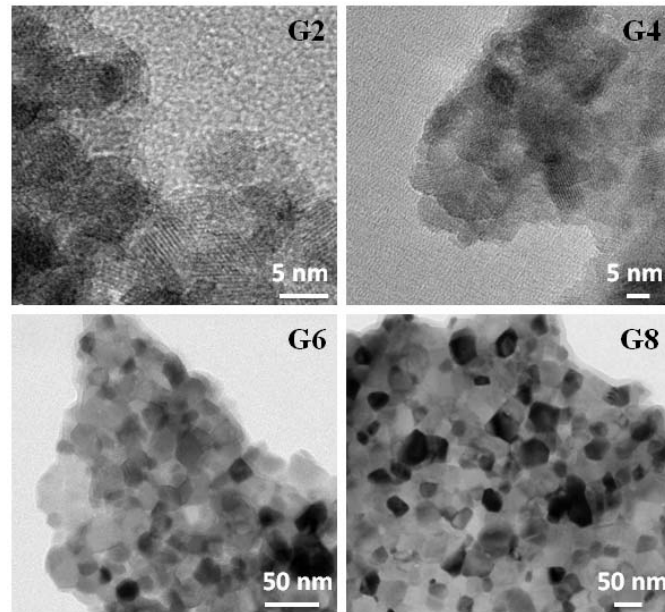


Figure 3.3: TEM micrographs of some of the cobalt ferrite powders synthesized by the autocombustion method.

### 3.3.2 Magnetic Measurements

Room temperature magnetic measurements on the as-synthesized powder samples are shown in Figure 3.4. Since formation of impurity phases is observed in samples G11, G12 and G13, magnetic studies have been performed on samples G1 to G10 only. Magnetic hysteresis loop is not observed for G1 and G2 (Figure 3.5) having very small particle sizes of 3 nm and 4 nm, respectively, indicating superparamagnetic nature of the particles. This is further confirmed from field cooled (FC) and zero field cooled (ZFC) magnetization measurements for the samples G1 and G2 as shown in Figure 3.6. Both FC and ZFC magnetization are measured in a field of 8 kA/m (100 Oe). Superparamagnetic particles are characterized by a maximum at the superparamagnetic blocking temperature in the zero field cooled magnetization measurements. The blocking temperatures for G1 and G2 are obtained as 90 K and 150 K, respectively. These values are comparable to that reported in the literature for cobalt ferrite nanoparticles of similar sizes [56].

As shown in Figure 3.4 and Table 3.2, magnetization of the as-synthesized samples is not saturated at the highest field of measurement and the magnetization decreases with decreasing particle size. This is due to the increasing surface contribution for smaller particles where the surface layer is considered to be magnetically dead [57, 58]. Similarly, the coercivity initially increases with particle size, reaches a maximum value for G7 of particle size 34 nm, and then decreases. This behavior corresponds to the change over from single domain to multi-domain particles above a critical size. The critical size of 34 nm obtained for the present cobalt ferrite is comparable to the critical size reported for other spinel ferrites [59-62].

Table 3.2: Magnetic properties of the as-synthesized powder samples. M is the magnetization at 1200 kA/m, the highest field used for the measurement.

<b>Sample Code</b>	<b>M (Am<sup>2</sup>/kg)</b>	<b>H<sub>c</sub> (kA/m)</b>
G1	0.7	0
G2	1.9	0
G3	13.2	15.0
G4	26.3	32.5
G5	43.2	60.1
G6	62.0	72.6
G7	67.5	74.0
G8	69.8	67.3
G9	75.6	62.0
G10	67.5	81.5
G11	41.2	89.2
G12	85.8	68.3
G13	91.2	65.9

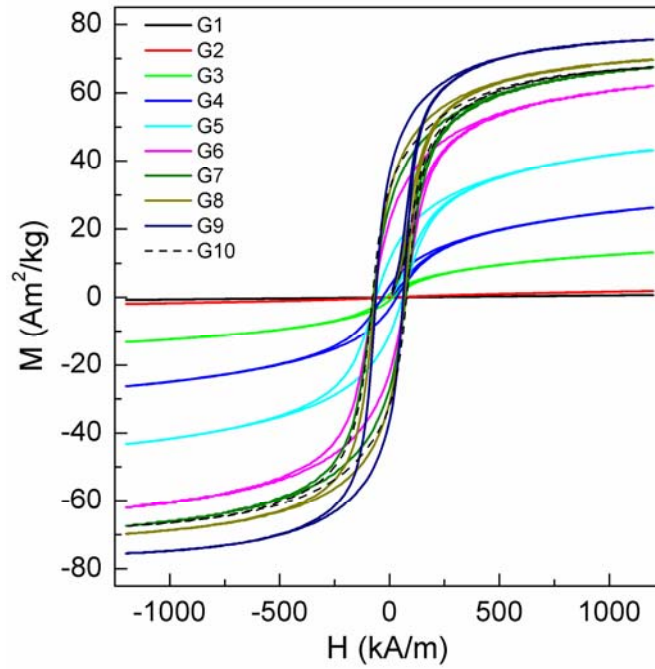


Figure 3.4: Room temperature M vs H curves of the as-synthesized powder samples.

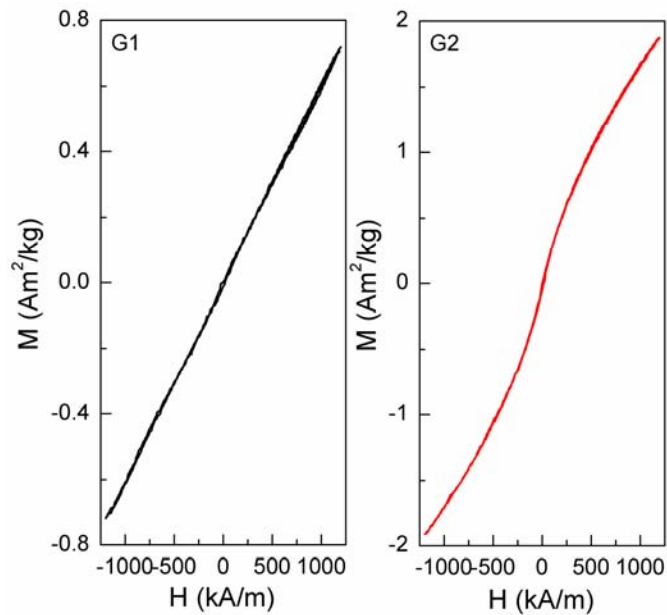


Figure 3.5: Enlarged M-H curves of G1 and G2.

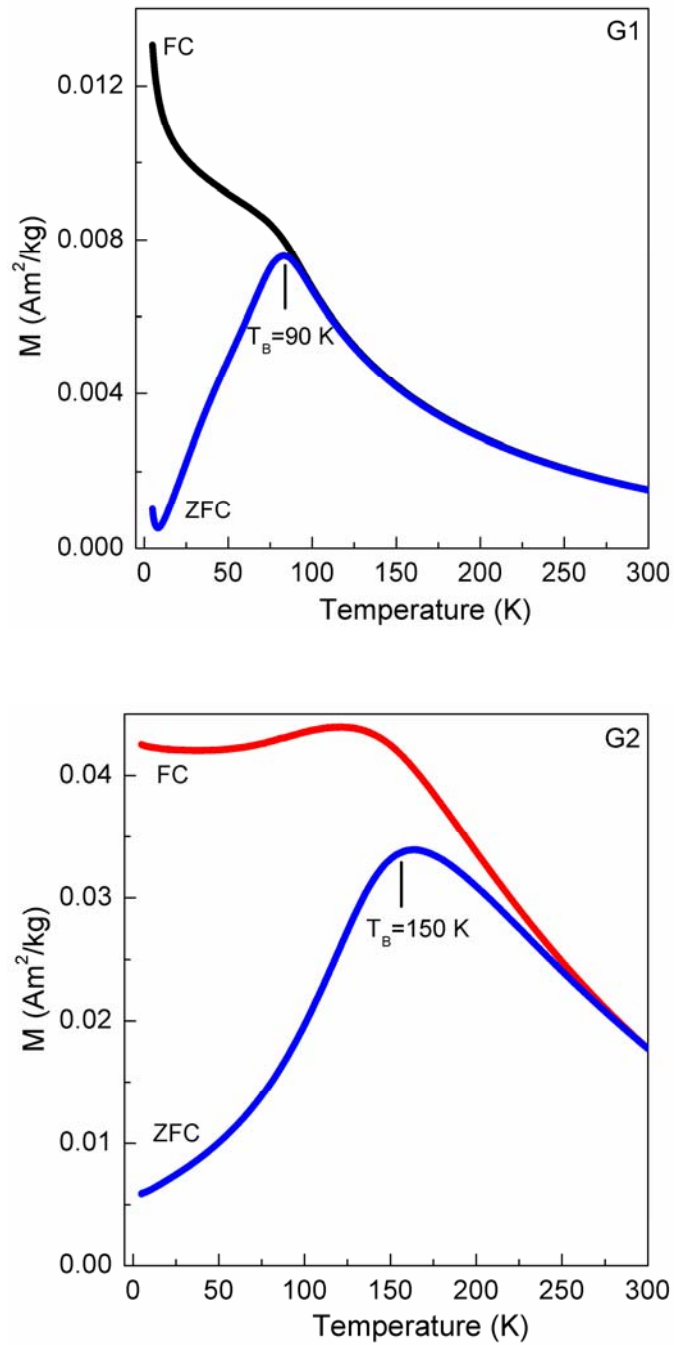


Figure 3.6: Zero field cooled (ZFC) and field cooled (FC) magnetization curves of G1 and G2, measured in a field of  $H=8 \text{ kA/m}$  (100 Oe).

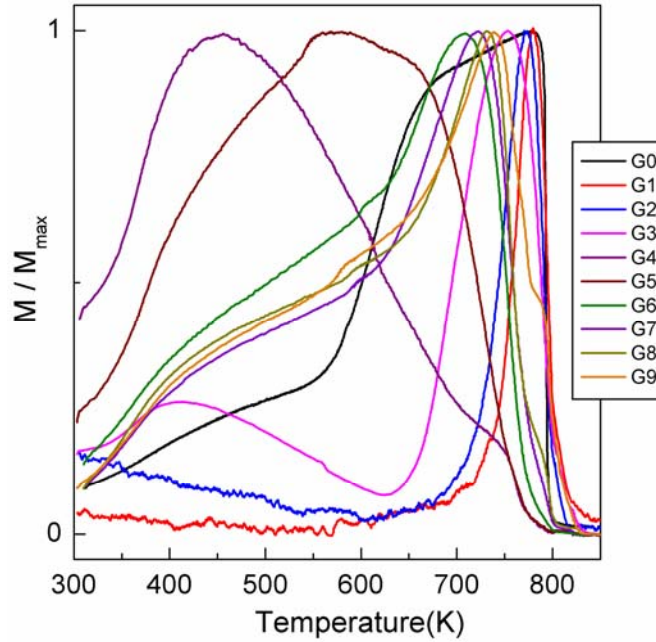


Figure 3.7: M-T curves of as-synthesized cobalt ferrite powders from different glycine/nitrate ratios compared with ceramic sample.

Temperature variation of magnetization for all the as-synthesized samples has been measured above room temperature, in a field of 8 kA/m, as shown in Figure 3.7. Strikingly, only the samples G1, G2 and G3 showed a sharp magnetic transition at the expected Curie temperature of cobalt ferrite. The measured Curie temperature is close to 793 K and is comparable with that of the bulk powder as well as the value reported in the literature [35, 63]. The large increase in the magnetization above 600 K for G1, G2 and G3 is likely to be due to the growth of the particles at higher temperatures, as reported previously for other ferrites [58]. Whereas all the rest of the samples showed either more than one magnetic transition or a lower transition temperature in the temperature range 700-800 K. This is likely to be due to the compositional inhomogeneity such that different particles in a sample can have different compositions in the series  $\text{Co}_{1+x}\text{Fe}_{2-x}\text{O}_4$  close to  $x = 0$  and/or the formation of  $\text{CoFe}_2\text{O}_4$  with different degree of distribution in

different particles represented as  $(\text{Co}_{1-x}\text{Fe}_x)^{\text{T}}[\text{Co}_x\text{Fe}_{2-x}]^{\text{O}}\text{O}_4$  during the formation of the product in the combustion reaction.

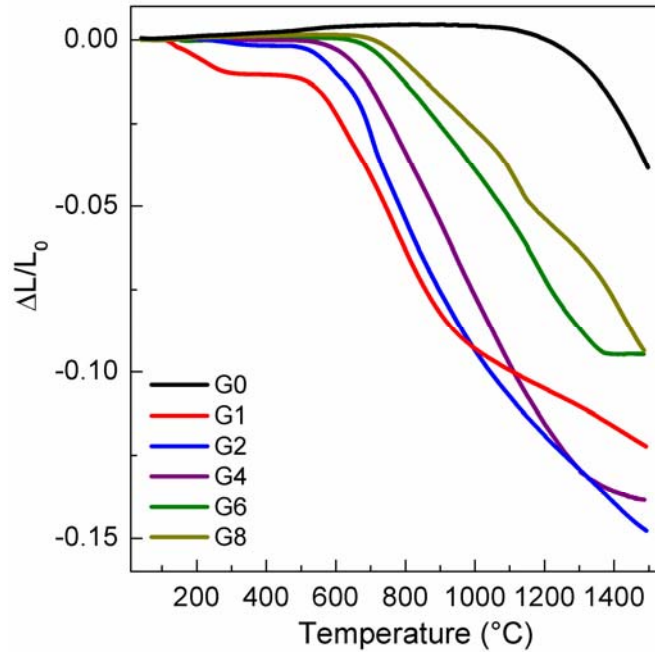


Figure 3.8: Sintering behavior of the cobalt ferrite samples synthesized from different glycine/nitrate ratios compared with ceramic sample.

### 3.3.3 TMA Analysis

For magnetostriction studies, the samples need to be sintered into specific shapes. The sintering characteristics of the samples are, therefore, studied by thermo-mechanical analysis (TMA). Sintering curves of different samples synthesized by the autocombustion method are compared with that obtained by the ceramic method in Figure 3.8. The sintering behavior of the powder samples synthesized by autocombustion method differs from that of the powder samples synthesized by the ceramic method. In the case of the ceramic sample (G0), effective sintering starts only above 1200 °C. However, for the

nanocrystalline samples G1 and G2, the onset of the sintering process is about 500 °C and this temperature slowly increases up to 800 °C for G8 with increasing crystallite size. These results show that the nanocrystalline cobalt ferrite can be sintered at relatively lower temperatures compared to the ceramic sample, as reported previously [25]. However, TMA analysis shows that the shrinkage is continued with increasing temperature and that the samples are not completely sintered up to a maximum temperature of 1500 °C.

### 3.4 Studies on Sintered Samples

Most of the studies reported in the literature on sintered cobalt ferrite are made on compacts sintered at 1450 °C [22, 23, 25]. Also, TMA studies indicate that the sintering is not completed up to the temperature of 1500 °C. Hence, all the samples were sintered under identical conditions for comparison of the results. Pressed compacts were heated in a programmable furnace to a temperature of 1450 °C at the heating rate of 5 °C/min and held at this temperature for 10 minutes. The samples were then cooled back to room temperature at the rate of 20 °C/min.

#### 3.4.1 XRD Studies

Figure 3.9 shows the X-ray diffraction patterns of the sintered samples. The sample codes SG0 and SG1 to SG10 correspond to the sintered samples derived from the corresponding powders G0 and G1 to G10. In the XRD patterns, all the observed peaks correspond to spinel ferrite and no other impurity phases are formed after sintering. XRD patterns of all the sintered samples are identical and matching well with that of the pattern shown and indexed for the bulk sample (SG0). The lattice parameter for the sintered samples SG1 to SG9 is found to be comparable to that obtained for the bulk sample and the literature value for cobalt ferrite (8.391 Å). Unusually low value for the lattice parameter is obtained for SG10. This could be due to a slight difference in the composition for this sample. A very low intensity impurity peak due to FeO was observed in the XRD pattern of the corresponding powder sample G10 (see Figure 3.1).

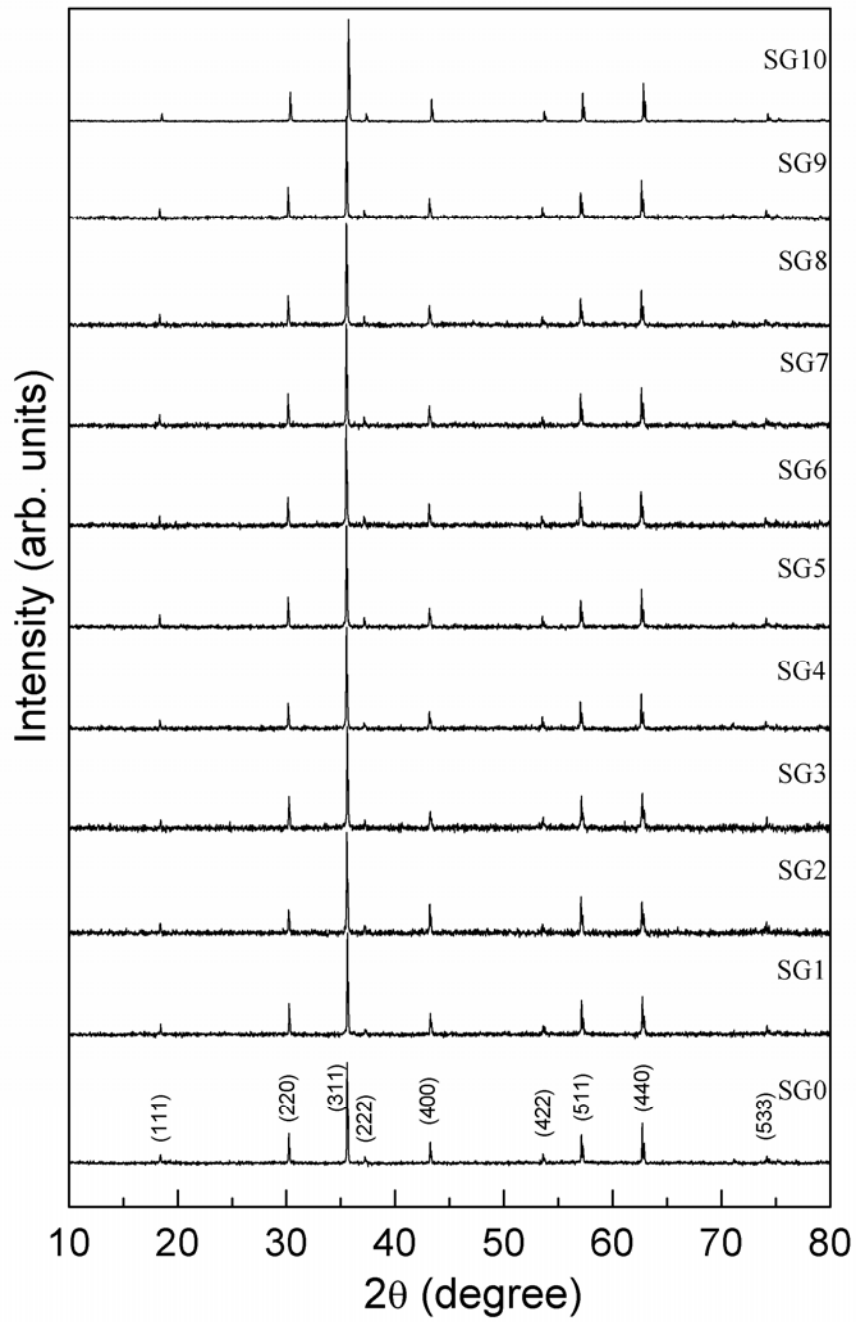


Figure 3.9: Powder XRD patterns of the sintered samples.

### 3.4.2 Density Measurements

Figure 3.10 shows the variation of the density of the sintered pellets as a function of G/N ratio. The densities of the sintered pellets were calculated from the volume and the weight of the pellets, as well as by the Archimedes method. The relative density was calculated from the ratio of the measured density to the theoretical density of cobalt ferrite ( $5.276 \text{ g/cm}^3$ ) calculated from the crystal structure parameters. Density is almost comparable for SG1 and SG2 and then increased to the highest density of 86% for SG4. Density is further decreased down to  $\sim 79\%$  with increasing G/N ratio. The variation in the sintered density for particles with larger sizes could be due to the characteristics of the powders obtained under different G/N ratios. The relatively larger density of SG10 compared to SG9 could be due to the presence of minor amounts of impurity, as discussed in the previous section. Large increase in the flame temperature in the combustion reaction was observed for larger G/N ratios (Figure 3.2) which could affect the surface characteristics of the powders and control the sintering behavior and hence the density of the sintered compacts.

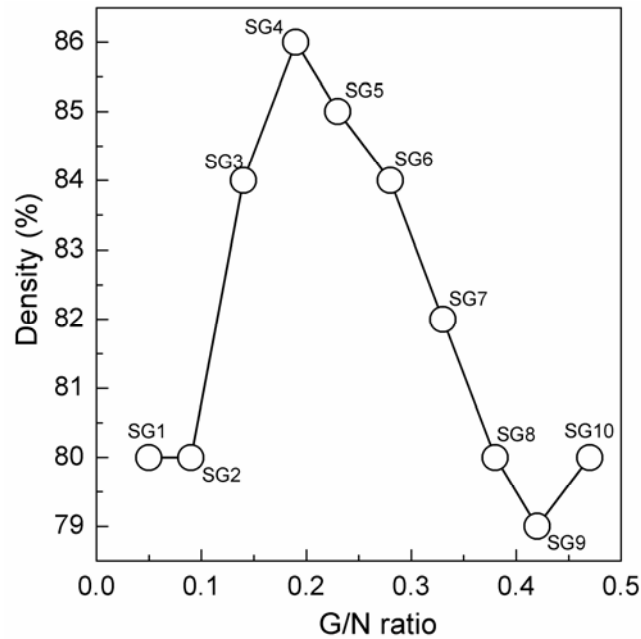


Figure 3.10: Density of the sintered products as a function of G/N ratio.

### 3.4.3 Magnetic Measurements

Magnetic measurements were carried out on crushed small pieces of sintered pellets. It has been shown previously that magnetic characteristics of the crushed pieces of sintered cobalt ferrite with arbitrary sizes and shapes affect the magnetic characteristics due to the random orientation of the grains with respect to the direction of the applied magnetic fields as well as due to the shape anisotropy [64]. Since the sintered sample SG10 showed a difference in the lattice parameter, probably due to a different composition, further studies are made on sintered samples from SG1 to SG9 only. In the case of the sintered samples, the magnetization is found to be saturated and the saturation magnetization varies between 77.9 to 83.4 Am<sup>2</sup>/kg, for the samples SG1 to SG9, as shown in Figure 3.11 and Table 3.3. There is a corresponding variation of the coercivity also. The small variation in the saturation magnetization and coercivity could be due to the cation distribution as well as the microstructure and orientation of the grains in the sintered products.

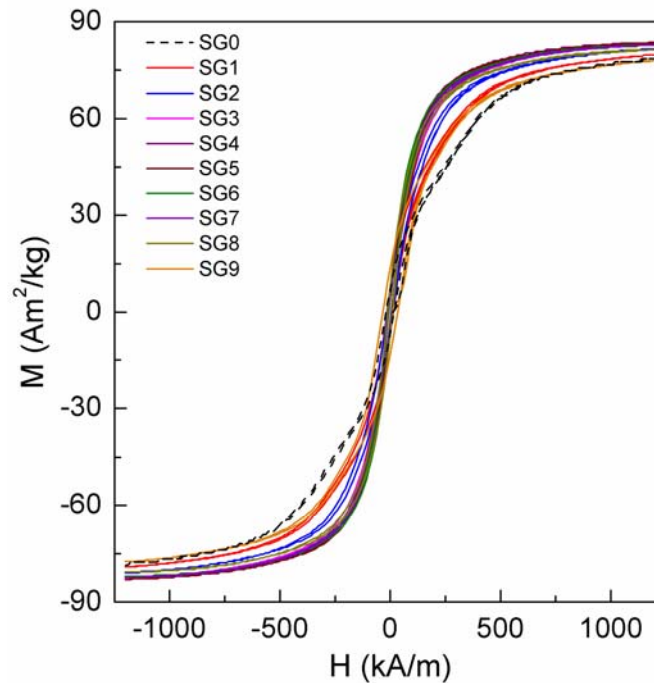


Figure 3.11: Room temperature magnetization curves for the different sintered cobalt ferrite samples.

Temperature variation of magnetization for all sintered samples (SG1 to SG9) measured above room temperature is shown in Figure 3.12. It is found that all sintered samples show comparable  $T_c$ s, close to the reported value for the bulk material ( $\sim 793$  K). The large increase in the magnetization above 600 K and the flat region between 700 K and  $T_c$  are due to the changes in the magnetocrystalline anisotropy of cobalt ferrite [64]. Curie temperature is a measure of the degree of distribution of the cations in the tetrahedral and octahedral sites of the spinel lattice. The comparable  $T_c$ s of the sintered products indicate almost similar distribution of the cations in all the samples. The cation distribution in the tetrahedral and octahedral sites of the spinel lattice is expected to affect the magnetization, magnetic anisotropy and Curie temperature of the material. The magnetic properties of different sintered samples are compared in Table 3.3.

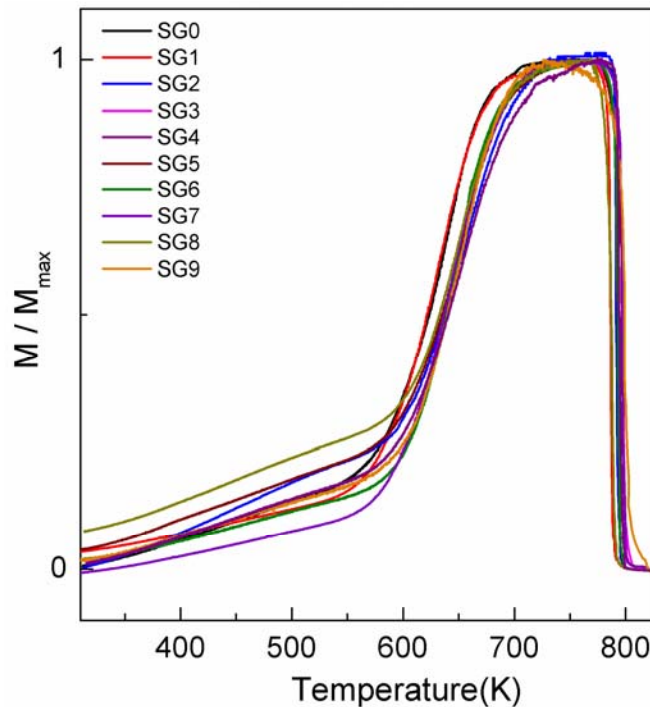


Figure 3.12: M-T curves of the sintered cobalt ferrite samples, measured in a magnetic field of 8 kA/m (100 Oe).

### 3.4.4 Magnetostriction Studies

Some of the previous studies reported on the magnetostriction measurements on sintered cobalt ferrite are made on samples sintered at 1450 °C [23, 25]. Hence, to compare the magnetostriction characteristics of sintered samples derived from the nanocrystalline powders with that reported in the literature, all the studies are made on pressed pellets sintered at 1450 °C for 10 minutes. Figure 3.13 shows the magnetostriction curves recorded up to a maximum magnetic field strength of 800 kA/m, in the parallel ( $\lambda_{\text{par}}$ ) and perpendicular ( $\lambda_{\text{per}}$ ) directions, respectively, with respect to the direction of the applied magnetic field. The magnetostriction is negative along the parallel direction, as reported [26, 29, 32, 34]. Higher magnetostriction is obtained along the parallel direction for all the samples sintered from nanocrystalline materials ( $\geq 200$  ppm) compared to the value of 150 ppm for the sample prepared by the ceramic method with a starting particle size  $> 1 \mu\text{m}$  and processed under identical conditions. Maximum value of magnetostriction above 300 ppm is achieved for the samples sintered from the smallest particles (G1 and G2), with the highest value of 315 ppm for SG2. SG1 and SG2 show some peculiarities in the magnetostriction along the perpendicular direction also. These two samples show negative magnetostriction along the perpendicular direction and all other samples show positive values along this direction. This is an indication for the favorable alignment of the domains and easy axis of magnetization in the sintered pellets derived from very small particles. Moreover, compared to SG1, SG2 shows higher magnetostriction at lower magnetic fields and maximum value of magnetostriction for SG2 is obtained at a lower field. However, higher magnetostriction at low fields (below 200 kA/m) is obtained for sample SG8. These differences are much clear in Figure 3.14 which shows the strain derivative ( $d\lambda/dH$ ) as a function of magnetic field measured along the parallel direction.

The anisotropic magnetostriction,  $\lambda_a = \lambda_{\text{par}} - \lambda_{\text{per}}$  as well as the volume magnetostriction  $\omega = \lambda_{\text{par}} + 2\lambda_{\text{per}}$  are also of interest for these two samples. Figure 3.15 shows the variation of maximum value of magnetostriction ( $\lambda_{\text{max}}$ ) along the parallel direction, maximum value of the strain derivative, anisotropic and volume

magnetostrictions as a function of the particle size of the starting powders. The magnitude of  $\lambda_a$  is comparable for all samples, whereas the signs are different for SG1 and SG2. Similarly, these two samples show very high volume magnetostriction of around 400 ppm and for all other samples, the value is less than 200 ppm. Thus, the samples sintered from very small particles, G1 and G2, show extremely large values for the magnetostriction coefficient. Apart from the changes in the value of magnetostriction, the slope of the magnetostriction ( $d\lambda/dH$ ) is also an important factor for stress sensing applications. Higher values of the strain derivative are desirable for better magnetomechanical coupling [32]. The highest value of strain derivative of  $1.97 \times 10^{-9} \text{ A}^{-1}\text{m}$  is obtained in the case of SG2 which is larger than the previously reported strain derivative value of  $1.3 \times 10^{-9} \text{ A}^{-1}\text{m}$  for bulk material [23].

Table 3.3: Magnetic and magnetostrictive properties of sintered pellets.

Sample Code	Density (%)	$M_s$ ( $\text{Am}^2/\text{kg}$ )	$H_c$ (kA/m)	$T_c$ ( $^\circ\text{C}$ )	$\lambda_{\text{max}}$ (ppm)	$d\lambda/dH$ ( $10^{-9}\text{A}^{-1}\text{m}$ )
SG0	89	78.5	19.1	521	-151	-0.56
SG1	80	79.6	14.1	515	-307	-1.14
SG2	80	81.6	12.4	520	-315	-1.97
SG3	84	82.8	7.4	525	-205	-1.03
SG4	86	83.3	5.5	523	-200	-1.12
SG5	85	83.4	6.7	524	-218	-1.00
SG6	84	82.8	6.0	521	-232	-1.06
SG7	82	82.8	8.1	524	-252	-1.49
SG8	80	81.3	11.1	516	-254	-1.35
SG9	79	77.9	33.6	526	-235	-1.01

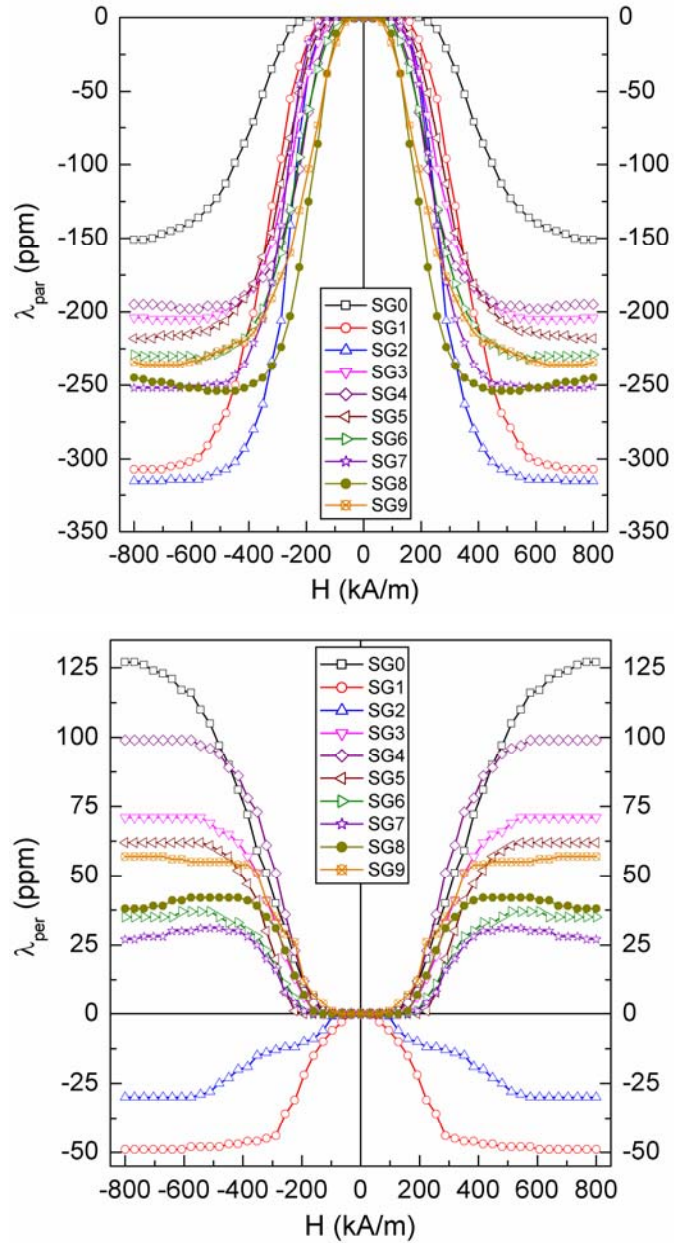


Figure 3.13: Magnetostriction curves of different sintered samples as a function of magnetic field measured along the parallel ( $\lambda_{\text{par}}$ ) and perpendicular ( $\lambda_{\text{per}}$ ) directions. The magnetostriction of the ceramic sample (SG0) is shown for comparison.

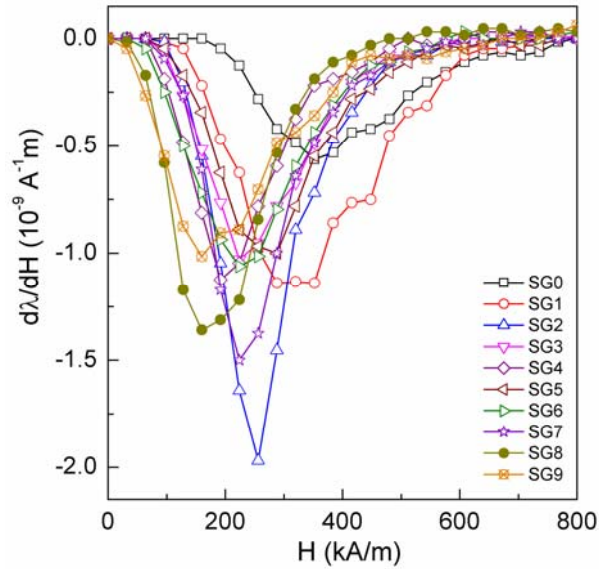


Figure 3.14: Strain derivative of different sintered samples as a function of magnetic field measured along the parallel direction.

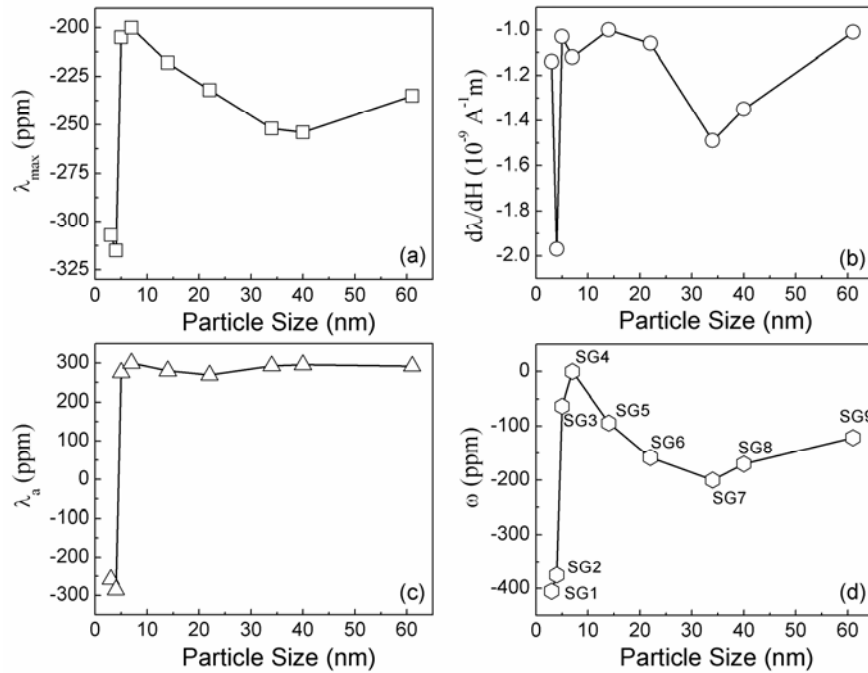


Figure 3.15: Variation of (a) maximum value of magnetostriction along the parallel direction, (b) strain derivative, (c) anisotropic magnetostriction and (d) volume magnetostriction as a function of the particle size of the starting powders.

### 3.4.5 Microstructure

A comparison of the coercivity and density of the sintered products and magnetostriction parameters, as shown in Table 3.3, indicate that in general, there are no correlations between the magnetic characteristics or the density with the maximum value of magnetostriction. However, there are some minor correlations observed with the microstructure of the sintered compacts as shown in Figure 3.16. SG1 and SG2 with the highest magnetostriction ( $\lambda > 300$  ppm) show microstructures with clear and small grains. For SG3 to SG6, larger grains with intra-grain pores and defects are observed, even though these samples show lower porosity and higher sintered densities in the range 84–86% compared to 80% density for SG1 and SG2. For SG7 to SG9, continuous and fused grains without any shape are observed. Thus, it appears that the microstructure, which depends on the initial particle size, could be one of the decisive factors for the higher and lower values of magnetostriction and strain derivative of the sintered samples.

### 3.4.6 Effect of Particle Size

The results from the magnetostriction studies on different sintered samples derived from starting powders of different particle sizes show that the maximum value of the magnetostriction coefficient is not exactly correlated with the initial particle size, even though compacts derived from the smallest particles show higher magnetostriction coefficient. However, the different particle sizes are obtained by changing the glycine to nitrate ratio during the synthesis. It is possible that the powder characteristics are different because of the different amounts of fuel used and this affects the sintering characteristics and microstructure and thereby the ultimate value of magnetostriction. To study the effect of particle size on the maximum value of magnetostriction, the particle size of G2, which shows the highest value of magnetostriction after sintering (SG2) is changed by pre-calcination at different temperatures. It is known that particle growth takes place if nanocrystalline materials synthesized at low temperatures are further calcined at higher temperatures [65, 66]. Therefore, the as-synthesized G2 powder was calcined at two different temperatures to vary the particle size.

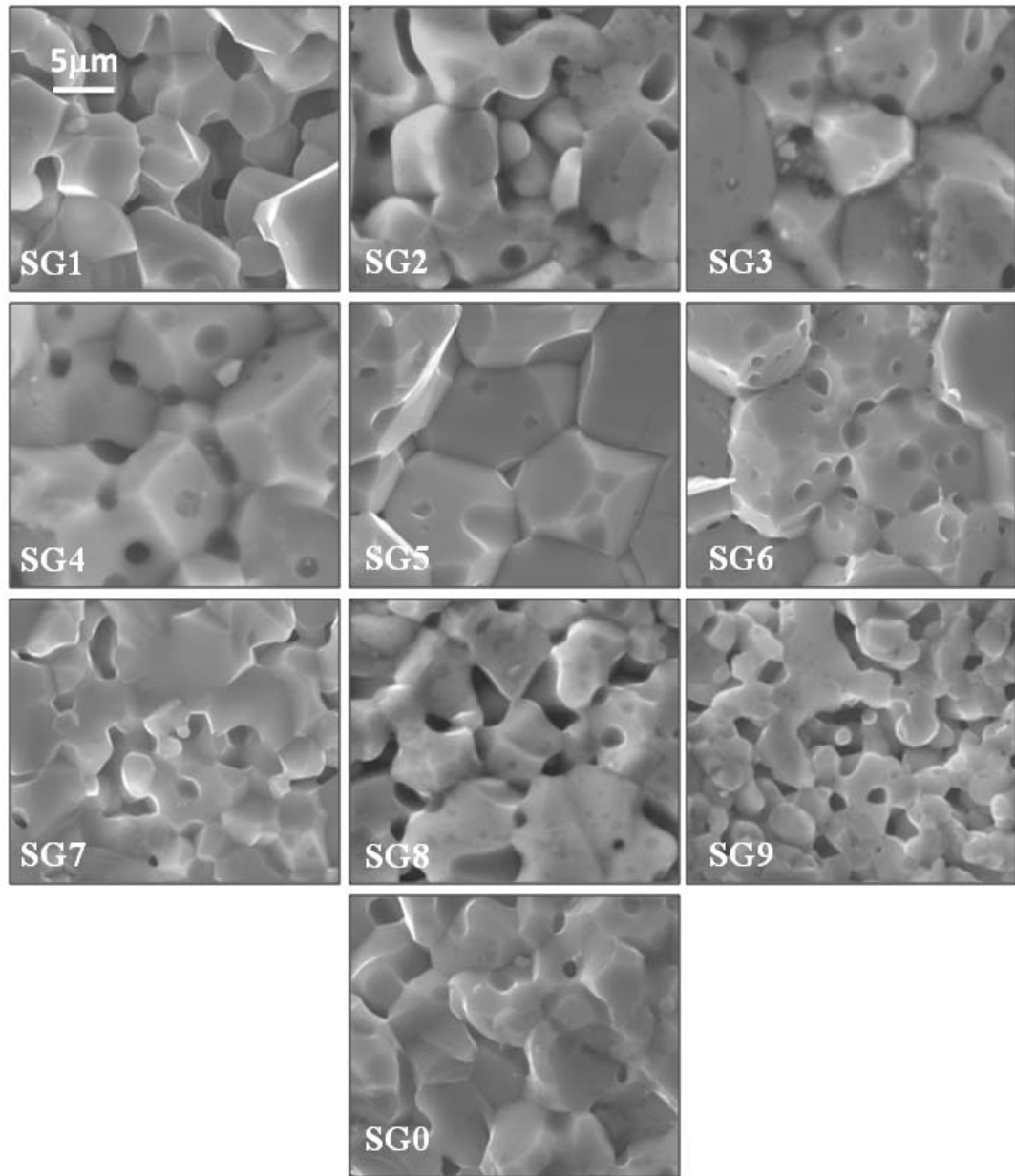


Figure 3.16: SEM images of the sintered samples. All micrographs shown are under the same magnification.

XRD patterns of the calcined powders are shown in Figure 3.17. The average crystallite sizes of the calcined powders are calculated using the Scherrer equation and the values are shown in Table 3.4. The calculated average crystallite size is assumed as the average particle size. There is substantial increase in the particle size after calcining at the two different temperatures for different durations. Similarly, there is an increase in the magnetization as well as coercivity of the powders with increasing particle size, as expected. The magnetization curves of the calcined powders are compared in Figure 3.18 and the magnetic parameters are compared in Table 3.5.

Table 3.4: Details of the calcined G2 powders.

Sample Code	Calcination conditions	$D_{\text{XRD}}$ ( $\pm 1\text{nm}$ )
G2	As-synthesized	4
G2a	180 °C/30min	7
G2b	400 °C/5hr	21

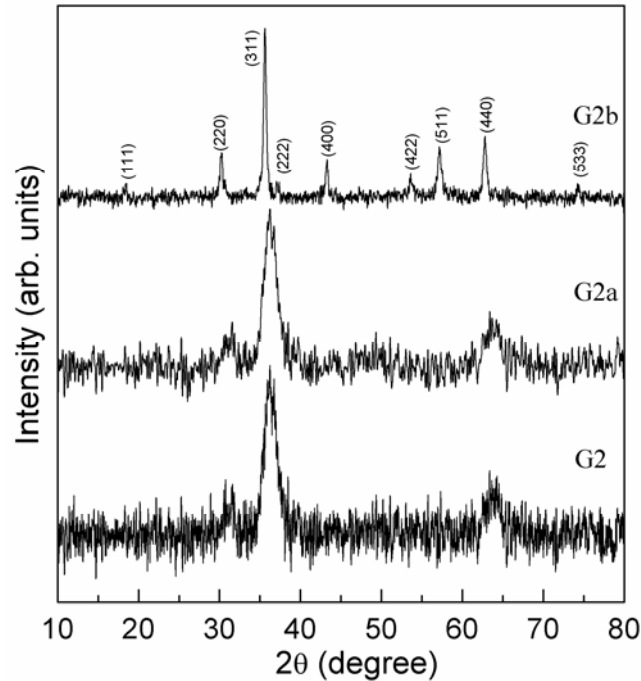


Figure 3.17: Powder XRD patterns of as-synthesized and calcined G2 powders.

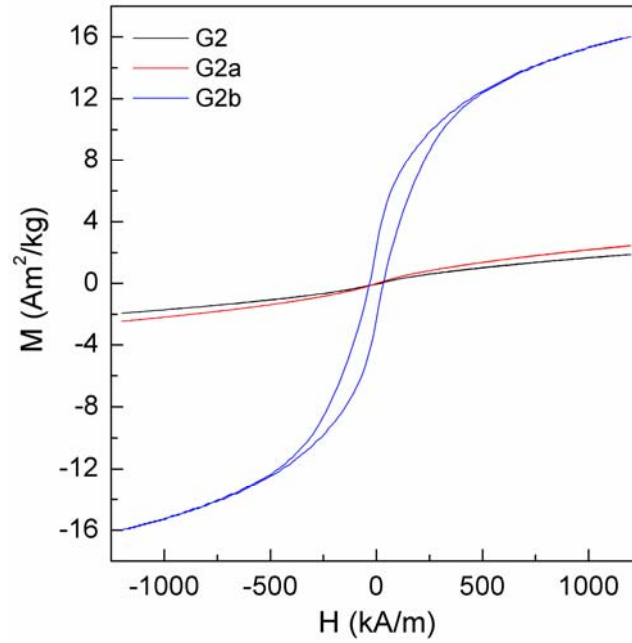


Figure 3.18: Room temperature magnetization curves of the as-synthesized and calcined G2 powders.

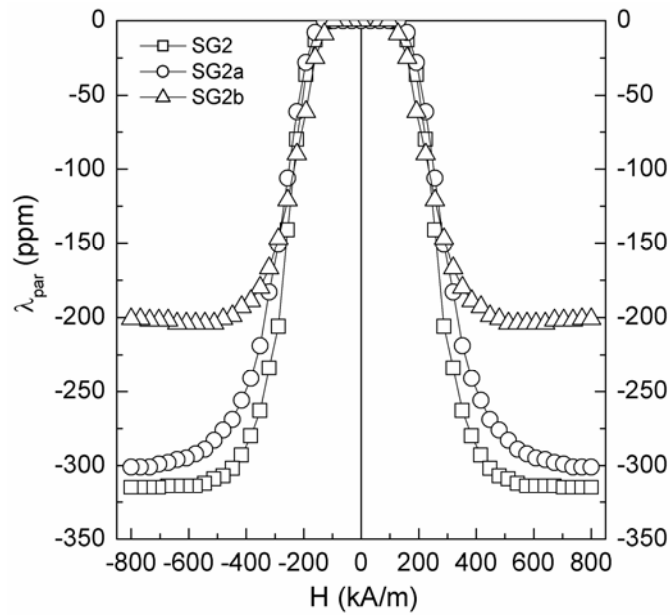


Figure 3.19: Magnetostriction curves of different sintered samples derived from G2 as a function of magnetic field measured along the parallel ( $\lambda_{\text{par}}$ ) direction.

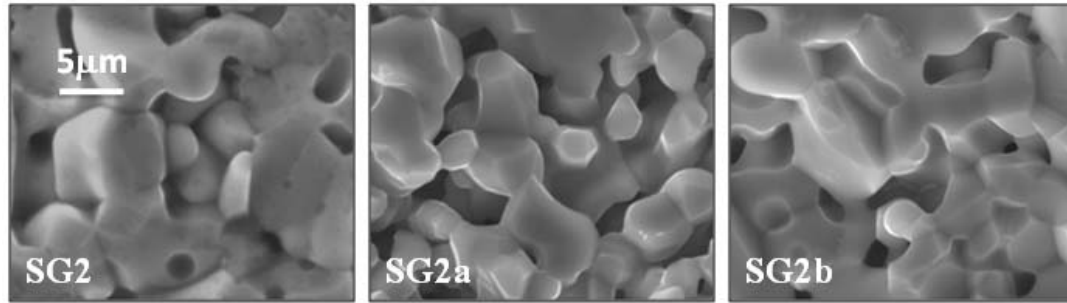


Figure 3.20: SEM images of the sintered samples derived from G2. All micrographs are under the same magnification.

Table 3.5: Magnetic and magnetostrictive characteristics of sintered pellets derived from as-synthesized and calcined G2 powders.

Sample code	D (%)	$M_s$ ( $\text{Am}^2/\text{kg}$ )	$H_c$ (kA/m)	$\lambda_{\max}$ (ppm)
SG2	80	81.6	12.4	-315
SG2a	80	82.0	15.8	-301
SG2b	78	84.1	15.1	-204

Magnetostriction of the pellets sintered from the calcined powders derived from G2 is measured as a function of magnetic field. The results are shown in Figure 3.19. The maximum value of magnetostriction is decreased after increasing the particle size of the starting powder, as expected. The SEM figures shown in Figure 3.20 indicate that there is not much difference in the microstructures of the sintered compacts derived from the as-synthesized and pre-calcined G2 powders, suggesting that there is not much role for the microstructure also in deciding the value of magnetostriction. An important observation is that the decrease in the maximum value of magnetostriction of the sintered samples

derived from the pre-calcined powders with different particle sizes (G2a and G2b) is much more than that observed for sintered compacts derived from the as-synthesized starting powders of comparable particle sizes (G4 and G6). This shows that apart from the particle sizes of the starting powders, there are other factors such as the characteristics of the starting powders contributing to the maximum value of magnetostriction of the sintered compacts. The characteristics of the starting powders can be varied by the synthesis conditions.

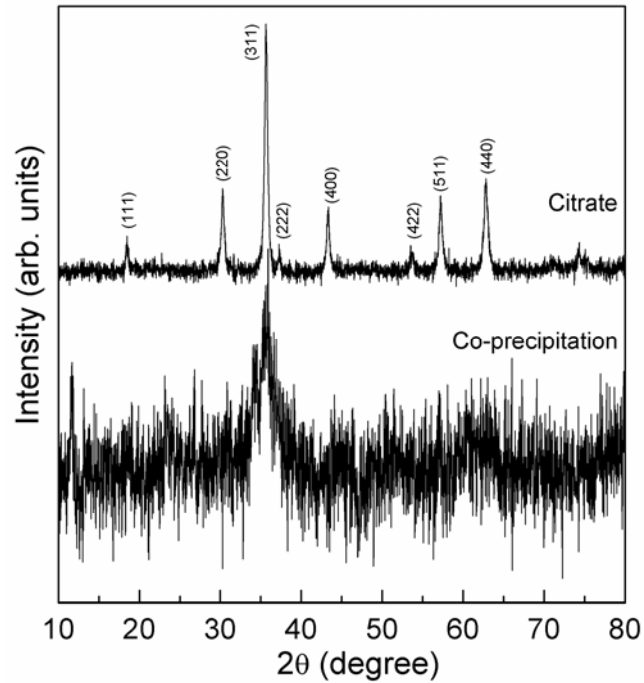


Figure 3.21: Powder XRD patterns of CoFe<sub>2</sub>O<sub>4</sub> samples synthesized by the citrate-gel and co-precipitation methods.

To verify the above assumptions, nanocrystalline powders of cobalt ferrite were synthesized by co-precipitation and citrate-gel methods. Figure 3.21 shows the XRD patterns of single phase cobalt ferrite obtained by co-precipitation and citrate precursor methods. Only the most intense peak of cobalt ferrite is observed in the XRD pattern of the sample prepared by the co-precipitation method and the peak is very broad than that

of the peaks observed in the XRD pattern of the powder synthesized by the citrate precursor method, indicating smaller crystallite size in the former case. The average crystallite size is calculated using the Scherrer formula and the calculated values are shown in Table 3.6.

Table 3.6: Different properties of as-synthesized powder samples synthesized by the co-precipitation and citrate precursor methods.

Synthesis method	$D_{\text{XRD}}$ ( $\pm 1\text{nm}$ )	$M_s$ ( $\text{Am}^2/\text{kg}$ )	$H_c$ ( $\text{kA/m}$ )
Co-precipitation	5	6.4	0
Citrate	22	65.0	82.6

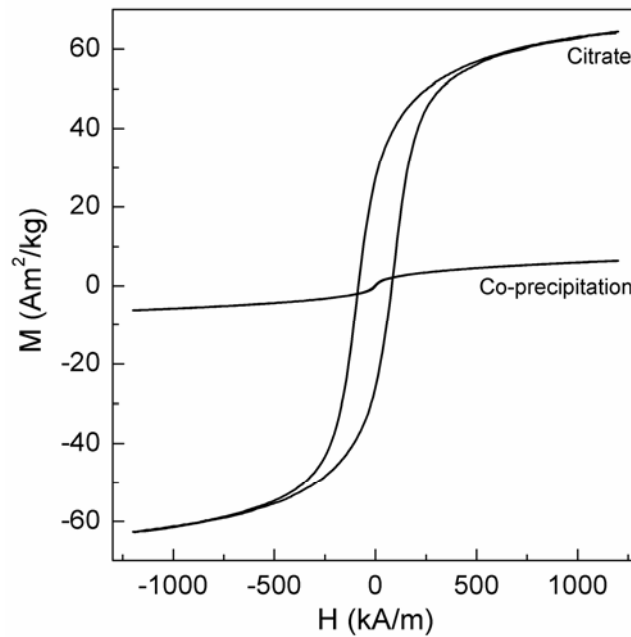


Figure 3.22: Room temperature magnetization curves of the as-synthesized powders synthesized by the co-precipitation and citrate methods.

Room temperature magnetic measurements on the as-synthesized powder samples obtained by co-precipitation and citrate-gel methods are shown in Figure 3.22. The as-synthesized powder obtained by the co-precipitation method of particle size 5 nm show superparamagnetic behavior as expected for such small particles. High magnetization with large coercivity is obtained for the sample synthesized by the citrate-gel method of particle size of 22 nm.

Figure 3.23 shows the magnetostriction curves of sintered samples obtained by the co-precipitation and citrate methods. Maximum value of magnetostriction as 160 ppm is obtained for sintered sample obtained by the co-precipitation method and 216 ppm in the case of sintered sample obtained by the citrate method. The microstructures of both sintered samples are almost comparable, as shown in Figure 3.24. Even though the particle size of the powders obtained from co-precipitation method is comparable with that of the sample G2 synthesized by the combustion method, the maximum value of magnetostriction of the former is nearly one half of the value of the latter.

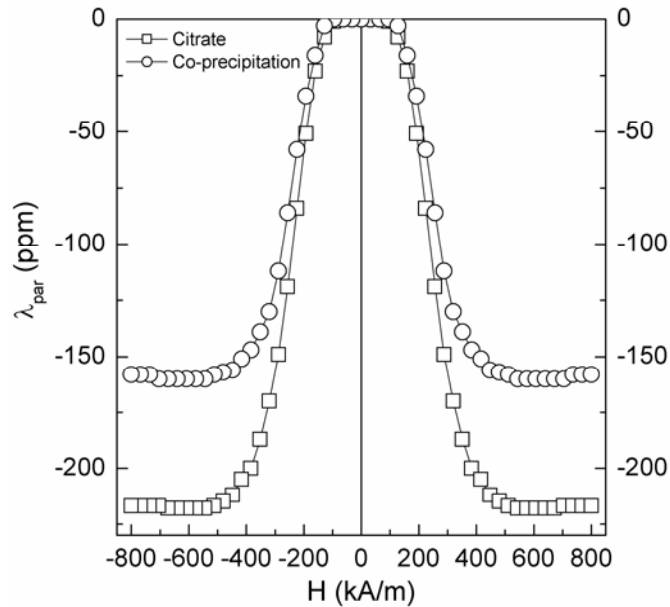


Figure 3.23: Magnetostriction as a function of magnetic field recorded in the parallel direction to the applied magnetic field.

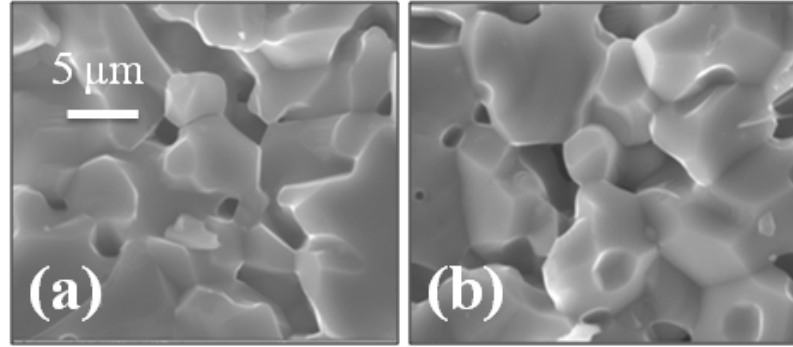


Figure 3.24: SEM images of the sintered samples synthesized by (a) co-precipitation and (b) citrate-gel methods.

Table 3.7: Magnetic and magnetostrictive properties of sintered pellets obtained by co-precipitation and citrate methods.

Synthesis method	D (%)	$M_s$ ( $\text{Am}^2/\text{kg}$ )	$H_c$ (kA/m)	$\lambda_{\max}$ (ppm)	$d\lambda/dH$ ( $10^{-9}\text{A}^{-1}\text{m}$ )
Co-precipitation	78	78.5	12.4	-160	-0.84
Citrate	87	82.3	10.9	-215	-1.05

The magnetostriction characteristics of the sintered samples derived from starting powders of comparable particle sizes obtained by the three different methods are compared in Figure 3.25 and Table 3.8. The results show that for particles of comparable sizes, sintered compacts derived from the powders obtained by the autocombustion method give higher values of magnetostriction and strain derivative. Also, there is not much correlation between the sintered density and magnetostriction characteristics. From these results it can be concluded that the magnetostriction of sintered ferrite depends on and can be controlled by the synthesis and processing conditions and by adjusting the particle size of the initial starting powders used for sintering the pellets.

Table 3.8: Comparison of the magnetostrictive properties of sintered pellets derived from powders of comparable sizes obtained by different synthesis methods.

Synthesis Method	Sample Code	$D_{\text{XRD}}$ ( $\pm 1\text{nm}$ )	$D$ (%)	$\lambda_{\text{max}}$ (ppm)	$d\lambda/dH$ ( $10^{-9}\text{A}^{-1}\text{m}$ )
Autocombustion	G2	4	80	-315	-1.97
Co-precipitation	Cop	5	78	-160	-0.84
Autocombustion	G3	5	84	-205	-1.03
„	G2a	7	80	-301	-1.40
„	G4	7	86	-200	-1.12
„	G2b	21	78	-204	-1.01
„	G6	22	84	-232	-1.06
Citrate-gel	Cit	22	87	-215	-1.05

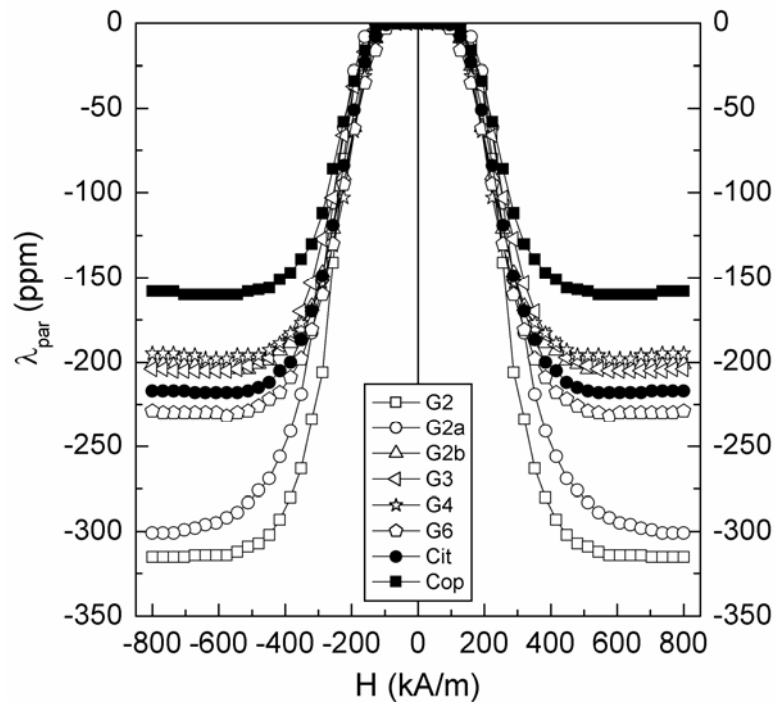


Figure 3.25: Magnetostriction as a function of magnetic field recorded in the parallel direction to the applied magnetic field, for sintered pellets derived from powders of comparable sizes obtained by different synthesis methods. The sample codes are defined in Table 3.8.

### 3.4.7 Effect of Magnetic Field Annealing

Magnetic field annealing has been reported to be very effective in enhancing the magnetostriction coefficient and strain derivative of cobalt ferrite due to the induced easy axis direction parallel to the annealing field, which affects magnetization processes and domain configuration [24, 30]. Higher magnetostriction coefficient perpendicular to the direction of the annealing field has been achieved by magnetic field annealing because of the reorientation of the domains along the measurement direction. In a very recent study, Muhammed *et al* investigated the effect of different powder compaction pressures in the range of 87 to 278 MPa and magnetic field annealing in an external magnetic field of 8000 kA/m (10 T), at 300 °C for 3 hours [31]. The field annealing process causes an induced uniaxial anisotropy, which results in a reduction of coercivity as well as increase in the magnetostrictive strain up to 400 ppm along the hard axis for the compacts made under a very high pressure of 150 MPa.

In the present work, we have compared the effect of magnetic field annealing on the samples SG1, SG2 where the starting particle sizes are very small and comparable for G1 and G2. These two samples gave comparable values for maximum magnetostriction but SG2 showed relatively larger magnetostriction at lower magnetic fields as well as high strain derivative of  $1.97 \times 10^{-9} \text{ A}^{-1}\text{m}$  along the parallel direction among all the other samples. Moreover, the compacts were made under a very low pressure of 8 MPa compared to the high pressures used in the reported work where high magnetostriction is observed [31]. For comparison of the results, sintered cobalt ferrite sample SG8 which gave higher magnetostriction at lower magnetic fields when compared to SG1 and SG2, derived from G8 with intermediate particle size of 40 nm, as well as the sample obtained by ceramic method (SG0) also are studied after magnetic field annealing. Magnetic field annealing of the sintered pellets was carried out at 300 °C in a magnetic field of 400 kA/m for 30 min. The sample was cooled back to room temperature in the presence of the same field after annealing. The annealing field was applied perpendicular to the

cylindrical axis of the sintered pellet which is perpendicular to the measurement direction as well as the direction of the measuring field in the case of  $\lambda_{\text{par}}$ .

Figures 3.26 shows the magnetostriction curves of the sintered samples SG1, SG2, SG8 and SG0, measured at room temperature, as a function of magnetic field applied along the parallel ( $\lambda_{\text{par}}$ ) and perpendicular ( $\lambda_{\text{per}}$ ) directions, before and after magnetic field annealing. The maximum values of magnetostriction and strain derivative of the different sintered samples, before and after field annealing, are compared in Table 3.9. The relative change in the maximum value of magnetostriction after and before field annealing,  $\Delta\lambda_{\text{par}} = (\lambda_{\text{H}} - \lambda_0) / \lambda_0$ , measured along the parallel direction, where  $\lambda_0$  and  $\lambda_{\text{H}}$  are the maximum value of magnetostriction before and after field annealing, respectively, is compared in Table 3.9. It is observed that there is not much change in the maximum value of magnetostriction after field annealing for sample SG1, whereas 10%, 39% and 83% increases are observed for the samples SG2, SG8 and SG0, respectively. Even though SG8 showed relatively lower maximum value of magnetostriction and strain derivative before field annealing compared to SG2, comparable values for maximum value of magnetostriction and strain derivative are obtained after magnetic field annealing for both samples.

Table 3.9: Magnetostrictive properties of different samples, before and after magnetic field annealing.

Sample Code	Before magnetic annealing		After magnetic annealing		$\Delta\lambda_{\text{par}}$ (%)
	$\lambda_{\text{par}}$ (ppm)	$d\lambda_{\text{par}}/dH$ ( $10^{-9}\text{A}^{-1}\text{m}$ )	$\lambda_{\text{par}}$ (ppm)	$d\lambda_{\text{par}}/dH$ ( $10^{-9}\text{A}^{-1}\text{m}$ )	
SG1	-307	-1.14	-304	-1.70	-1
SG2	-315	-1.97	-345	-2.12	+10
SG8	-254	-1.35	-353	-2.03	+39
SG0	-151	-0.56	-276	-1.38	+83

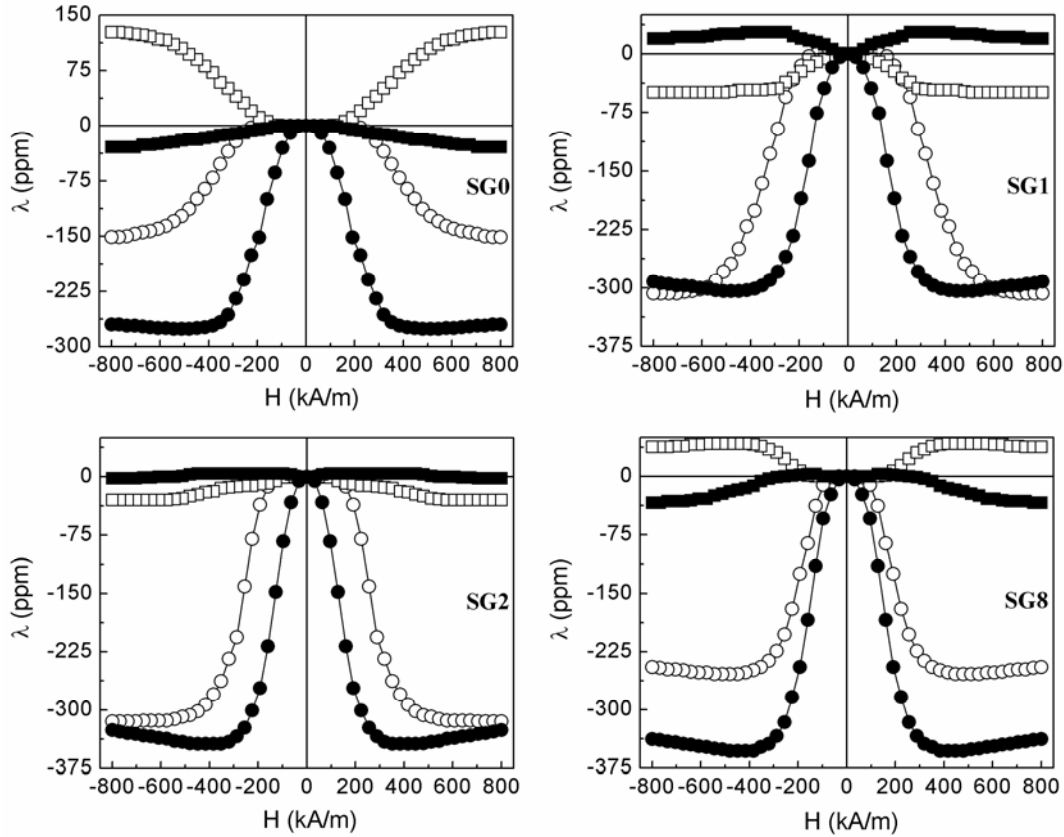


Figure 3.26: Magnetostriction curves of SG0, SG1, SG2 and SG8, as a function of magnetic field, along the parallel (circles) and perpendicular (squares) directions. The open and closed symbols represent measurements before and after annealing in a field of 400 kA/m, respectively.

Another important observation is that, after annealing the sample in a magnetic field, higher magnetostriction is observed at lower magnetic fields for all samples and the field at which maximum magnetostriction is observed is reduced to 300 kA/m. This is clearly evident from the strain derivative curves of all samples compared in Figure 3.27, before and after magnetic field annealing. There is not much change in the strain derivative of SG2 after magnetic annealing, except that the maximum value is shifted to

lower fields. On the other hand, about 50% increase in the strain derivative at low fields is observed after magnetic field annealing for samples SG1 and SG8 whereas 150% increase is observed for the bulk sample (SG0), as shown in the Figure 3.27. These observations show that higher magnetostriction can be achieved without magnetic field annealing if the sintered compacts are made from smaller particles obtained by the autocombustion method of synthesis and magnetic field annealing is very effective in enhancing the magnetostriction and strain derivative for samples sintered from larger particles.

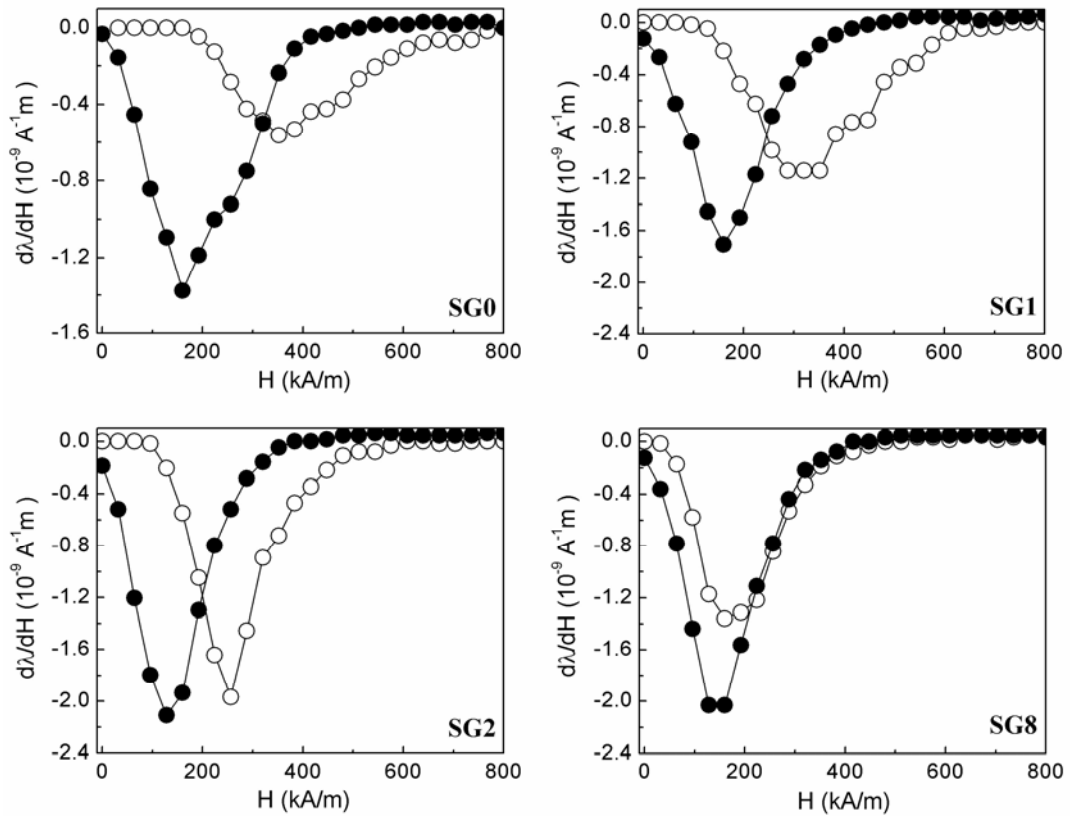


Figure 3.27: Field derivative of the magnetostriction for SG0, SG1, SG2, and SG8, parallel to the applied magnetic field. The open and closed symbols represent measurements before and after annealing in a field of 400 kA/m, respectively.

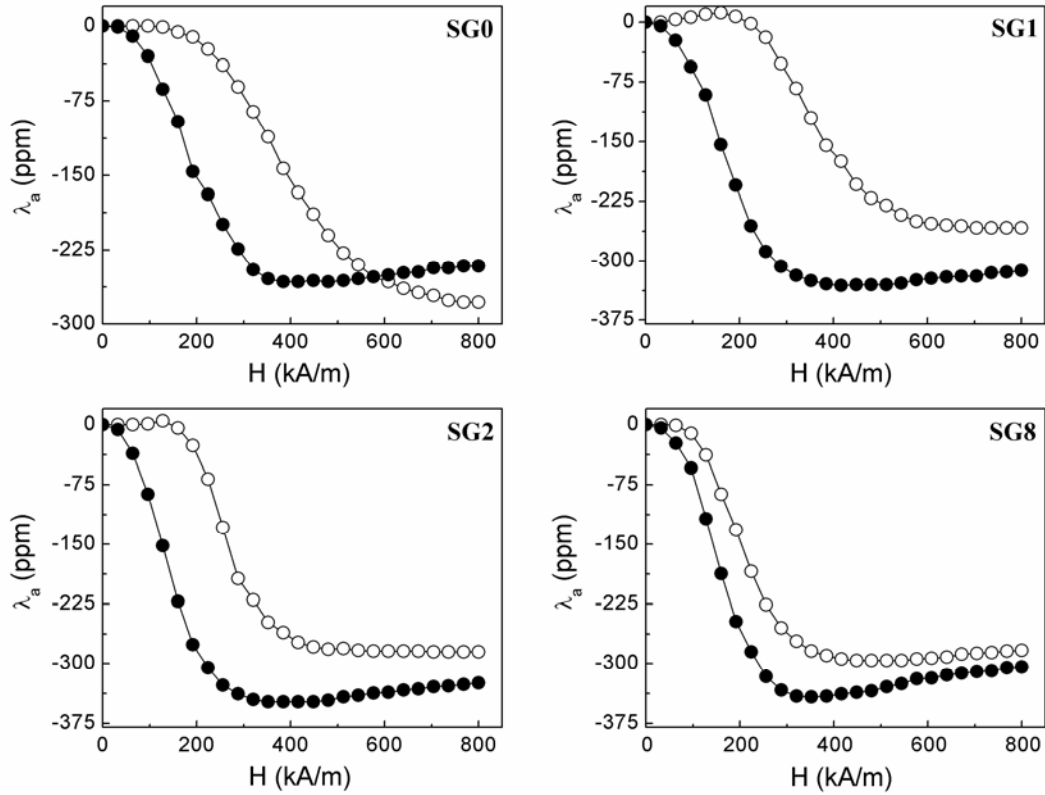


Figure 3.28: Anisotropic magnetostriction of SG0, SG1, SG2 and SG8 along the parallel direction. The open and closed symbols represent the measurements before and after annealing in a field of 400 kA/m, respectively.

The maximum value of magnetostriction for the bulk sample SG0 is obtained as 151 ppm, less than the reported values, probably due to the difference in the processing parameters compared to the reports in the literature [23]. As shown in Figure 3.26 and Table 3.9, after annealing the sample in a magnetic field, the maximum value of magnetostriction of SG0 is increased to 275 ppm. Similarly, the strain derivative is increased from  $0.56 \times 10^{-9} \text{A}^{-1} \text{m}$  to  $1.38 \times 10^{-9} \text{A}^{-1} \text{m}$ , after magnetic annealing.

It is interesting to note that the magnetostriction coefficients  $\lambda_{\text{par}}$  and  $\lambda_{\text{per}}$  have opposite signs for the sintered samples derived from the larger particles (SG8 and SG0)

before magnetic annealing, whereas both values have the same sign after magnetic annealing. In the case of SG2, both  $\lambda_{\text{par}}$  and  $\lambda_{\text{per}}$  are negative before and after magnetic field annealing. However,  $\lambda_{\text{par}}$  increases and the transverse value decreases (less negative) after the field annealing. Similarly, the sign of  $\lambda_{\text{per}}$  is reversed for the sample derived from the smaller particles (SG1 and SG2) and after magnetic annealing,  $\lambda_{\text{par}}$  and  $\lambda_{\text{per}}$  have opposite signs. Similar features have been reported previously [31], indicating changes in the different single crystal contributions to the polycrystalline behavior after magnetic field annealing and that isotropic case is not valid.

It is found that the magnitude of anisotropic magnetostriction,  $\lambda_a = \lambda_{\text{par}} - \lambda_{\text{per}}$ , is comparable before and after magnetic field annealing, for SG0, SG1, SG2 and SG8, as shown in Figure 3.28. Comparable values for the anisotropic magnetostriction are obtained for the samples derived from the nanocrystalline particles derived from the autocombustion method. This shows that higher magnetostriction characteristics can be obtained for sintered compacts derived from nanocrystalline powders synthesized by the autocombustion method using glycine as the fuel.

### 3.5 Conclusions

The magnetic and magnetostrictive properties of sintered cobalt ferrite derived from nanocrystalline powders synthesized by the autocombustion method using glycine have been investigated. The results show that the particle size of the as-synthesized powders is one of the factors deciding the magnetostriction parameters of the compacts made from powders synthesized by this method. High values of the magnetostriction coefficient and strain derivative are obtained for compacts sintered from particles of very small sizes obtained from the autocombustion method. However, comparison of the effect of the initial particle size derived from different methods of synthesis indicated that particle size alone is not the deciding factor for the high values of magnetostriction. For the powders derived from the autocombustion method, there are no correlations between the magnetic and magnetostrictive parameters of the sintered products. However, some correlation between the magnetostriction and microstructure of the sintered products is observed.

The present results indicate that sintering nanocrystalline powders of very small particle sizes obtained by the autocombustion method is effective for obtaining high values of magnetostriction for sintered cobalt ferrite. Pre-sintering of the particles during synthesis, and pores in the grain and orientation of the grains in the sintered products are the likely parameters controlling magnetostriction.

Magnetostriction values of 315 ppm without magnetic annealing and 345 ppm after magnetic annealing, at room temperature, are the highest values reported so far for sintered polycrystalline cobalt ferrite obtained under simple processing conditions. The present results show that it is possible to get very high magnetostriction and coupling coefficient for sintered cobalt ferrite derived from nanocrystalline powders of very small particle size synthesized by the autocombustion method using glycine.

## References

- [1] J. Smit and H. P. J. Wijn, *Ferrites* (Philips Technical Library, Eindhoven, 1959).
- [2] E. P. Wohlfarth, *Ferromagnetic Materials: A Handbook on the Properties of Magnetically Ordered Substances* (North-Holland, Amsterdam, 1980).
- [3] A. Goldman, *Modern Ferrite Technology* (Van Nostrand Reinhold, New York, 1990).
- [4] B. Viswanathan and V. R. K. Murthy, *Ferrite Materials: Science and Technology* (Narosa Publishing House, New Delhi, 1990).
- [5] S. B. Darling and S. D. Bader, *J. Mater. Chem.* 15 (2005) 4189.
- [6] D. S. Mathew and R. S. Juang, *Chem. Eng. J.* 129 (2007) 51.
- [7] N. A. Frey, S. Peng, K. Cheng and S. Sun, *Chem. Soc. Rev.* 38 (2009) 2532.
- [8] L. Zhou, J. Yuan and Y. Wei, *J. Mater. Chem.* 21 (2010) 2823.
- [9] Z. Zhang, A. J. Rondinone, J. X. Ma, J. Shen and S. Dai, *Adv. Mater.* 17 (2005) 1415.
- [10] R. N. Panda, J. C. Shih and T. S. Chin, *J. Magn. Magn. Mater.* 257 (2003) 79.
- [11] E. V. Gopalan, P. A. Joy, I. A. Al-Omari, D. S. Kumar, Y. Yoshida and M. R. Anantharaman, *J. Alloys Compd.* 485 (2009) 711.
- [12] J. Wang, *Mater. Sci. Eng. B* 127 (2006) 81.
- [13] S. Deka and P. A. Joy, *J. Am. Ceram. Soc.* 90 (2007) 1494.
- [14] S. Komarneni, E. Fregeau, E. Breval and R. Roy, *J. Am. Ceram. Soc.* 71 (1988) C26.
- [15] T. Nakamura, *J. Magn. Magn. Mater.* 168 (1997) 285.

- [16] A. Costa, E. Tortella, M. R. Morelli and R. Kiminami, *J. Magn. Magn. Mater.* 256 (2003) 174.
- [17] W. C. Hsu, S. C. Chen, P. C. Kuo, C. T. Lie and W. S. Tsai, *Mater. Sci. Eng. B* 111 (2004) 142.
- [18] S. H. Hong, J. H. Park, Y. H. Choa and J. Kim, *J. Magn. Magn. Mater.* 290 (2005) 1559.
- [19] R. M. Bozorth, E. F. Tilden and A. J. Williams, *Phy. Rev.* 99 (1955) 1788.
- [20] H. Shenker, *Phy. Rev.* 107 (1957) 1246.
- [21] M. R. Deguire, R. C. Ohandley and G. Kalonji, *J. Appl. Phys.* 65 (1989) 3167.
- [22] Y. Chen, J. E. Snyder, C. R. Schwichtenberg, K. W. Dennis, R. W. McCallum and D. C. Jiles, *IEEE Trans. Magn.* 35 (1999) 3652.
- [23] R. W. McCallum, K. W. Dennis, D. C. Jiles, J. E. Snyder and Y. H. Chen, *Low Temp. Phys.* 27 (2001) 266.
- [24] C. C. H. Lo, A. P. Ring, J. E. Snyder and D. C. Jiles, *IEEE Trans. Magn.* 41 (2005) 3676.
- [25] S. D. Bhame and P. A. Joy, *Sens. Actuators A* 137 (2007) 256.
- [26] S. D. Bhame and P. A. Joy, *J. Am. Ceram. Soc.* 91 (2008) 1976.
- [27] I. C. Nlebedim, N. Ranvah, P. I. Williams, Y. Melikhov, F. Anayi, J. E. Snyder, A. J. Moses and D. C. Jiles, *J. Magn. Magn. Mater.* 321 (2009) 2528.
- [28] I. C. Nlebedim, N. Ranvah, P. I. Williams, Y. Melikhov, J. E. Snyder, A. J. Moses and D. C. Jiles, *J. Magn. Magn. Mater.* 322 (2010) 1929.
- [29] I. C. Nlebedim, J. E. Snyder, A. J. Moses and D. C. Jiles, *J. Magn. Magn. Mater.* 322 (2010) 3938.
- [30] Y. X. Zheng, Q. Q. Cao, C. L. Zhang, H. C. Xuan, L. Y. Wang, D. H. Wang and Y. W. Du, *J. Appl. Phys.* 110 (2011) 043908.

- [31] A. Muhammad, R. Sato-Turtelli, M. Kriegisch, R. Grossinger, F. Kubel and T. Konegger, *J. Appl. Phys.* 111 (2012) 013918.
- [32] J. A. Paulsen, A. P. Ring, C. C. H. Lo, J. E. Snyder and D. C. Jiles, *J. Appl. Phys.* 97 (2005) 044502.
- [33] S. D. Bhame and P. A. Joy, *J. Appl. Phys.* 99 (2006) 073901.
- [34] S. D. Bhame and P. A. Joy, *J. Appl. Phys.* 100 (2006) 113911.
- [35] S. D. Bhame and P. A. Joy, *J. Phy. D: Appl. Phy.* 40 (2007) 3263.
- [36] S. H. Song, C. C. H. Lo, S. J. Lee, S. T. Aldini, J. E. Snyder and D. C. Jiles, *J. Appl. Phys.* 101 (2007) 09C517.
- [37] S. J. Lee, C. C. H. Lo, P. N. Matlage, S. H. Song, Y. Melikhov, J. E. Snyder and D. C. Jiles, *J. Appl. Phys.* 102 (2007) 073910.
- [38] G. S. N. Rao, O. F. Caltun, K. H. Rao, B. Parvatheeswara Rao, H. L. Wamocha and H. H. Hamdeh, *Hyperfine Interact.* 184 (2008) 179.
- [39] O. F. Caltun, I. Dumitru, M. Feder, N. Lupu and H. Chiriac, *J. Magn. Magn. Mater.* 320 (2008) e869.
- [40] I. C. Nlebedim, Y. Melikhov, J. E. Snyder, N. Ranvah, A. J. Moses and D. C. Jiles, *J. Appl. Phys.* 109 (2011) 07A908.
- [41] N. Somaiah, T. V. Jayaraman, P. A. Joy and D. Das, *J. Magn. Magn. Mater.* 324 (2012) 2286.
- [42] C. Heck, *Magnetic Materials and their Applications* (Butterworth & Co. Pub. Ltd., London, 1974).
- [43] Z. Zi, Y. Sun, X. Zhu, Z. Yang, J. Dai and W. Song, *J. Magn. Magn. Mater.* 321 (2009) 1251.
- [44] Y. Qu, H. Yang, N. Yang, Y. Fan, H. Zhu and G. Zou, *Mater. Lett.* 60 (2006) 3548.

- [45] R. Sato Turtelli, G. V. Duong, W. Nunes, R. Grossinger and M. Knobel, *J. Magn. Magn. Mater.* 320 (2008) e339.
- [46] J. G. Lee, H. M. Lee, C. S. Kim and Y. J. Oh, *J. Magn. Magn. Mater.* 177 (1998) 900.
- [47] C. Cannas, A. Musinu, D. Peddis and G. Piccaluga, *Chem. Mater.* 18 (2006) 3835.
- [48] K. J. Davies, S. Wells, R. V. Upadhyay, S. W. Charles, K. O'Grady, M. El Hilo, T. Meaz and S. Morup, *J. Magn. Magn. Mater.* 149 (1995) 14.
- [49] L. Zhao, H. Zhang, Y. Xing, S. Song, S. Yu, W. Shi, X. Guo, J. Yang, Y. Lei and F. Cao, *J. Solid State Chem.* 181 (2008) 245.
- [50] C. H. Yan, Z. G. Xu, F. X. Cheng, Z. M. Wang, L. D. Sun, C. S. Liao and J. T. Jia, *Solid State Commun.* 111 (1999) 287.
- [51] N. Kikukawa, M. Takemori, Y. Nagano, M. Sugasawa and S. Kobayashi, *J. Magn. Magn. Mater.* 284 (2004) 206.
- [52] V. Pillai and D. O. Shah, *J. Magn. Magn. Mater.* 163 (1996) 243.
- [53] Y. Ahn, E. J. Choi, S. Kim and H. N. Ok, *Mater. Lett.* 50 (2001) 47.
- [54] L. A. Chick, L. R. Pederson, G. D. Maupin, J. L. Bates, L. E. Thomas and G. J. Exarhos, *Mater. Lett.* 10 (1990) 6.
- [55] JCPDS - *International Centre for Diffraction Data (ICDD)*, PDF Number 22-1086 (Powder Diffraction File-4<sup>+</sup> 2009).
- [56] C. Liu, A. J. Rondinone and Z. J. Zhang, *Pure Appl. Chem.* 72 (2000) 37.
- [57] J. P. Chen, C. M. Sorensen, K. J. Klabunde, G. C. Hadjipanayis, E. Devlin and A. Kostikas, *Phy. Rev. B* 54 (1996) 9288.
- [58] S. Verma and P. A. Joy, *J. Appl. Phys.* 98 (2005) 124312.

- 
- [59] A. S. Albuquerque, J. D. Ardisson, W. A. A. Macedo and M. C. M. Alves, *J. Appl. Phys.* 87 (2000) 4352.
- [60] C. Caizer, *Mater. Sci. Eng. B* 100 (2003) 63.
- [61] S. Deka and P. A. Joy, *Mater. Chem. Phys.* 100 (2006) 98.
- [62] C. H. Chia, S. Zakaria, M. Yusoff, S. C. Goh, C. Y. Haw, S. Ahmadi, N. M. Huang and H. N. Lim, *Ceram. Int.* 36 (2010) 605.
- [63] O. F. Caltun, G. S. N. Rao, K. H. Rao, B. P. Rao, I. Dumitru, C.-O. Kim and C. Kim, *J. Magn. Magn. Mater.* 316 (2007) e618.
- [64] P. A. Joy and S. K. Date, *J. Magn. Magn. Mater.* 222 (2000) 33.
- [65] V. Sreeja, S. Vijayanand, S. Deka and P. A. Joy, *Hyperfine Int.* 183 (2008) 99.
- [66] S. Verma and P. A. Joy, *Mater. Res. Bull.* 43 (2008) 3447.

# Chapter 4

## Effect of Sintering Conditions on the Magnetostriction of Cobalt Ferrite

### 4.1 Introduction

Magnetic materials with high permeability and low magnetic loss are used for many practical applications [1, 2]. In many of the applications, permeability is an important factor which mainly depends on the microstructure, density, porosity, grain size, etc, of the sintered products [2-4]. Therefore, sintering is the most crucial step in the processing of ceramic magnetic materials aimed at various applications. During sintering, the porosity decreases and a suitable microstructure of the material is developed, which is the deciding factor for its final performance. Sintering studies on different ferrites and the corresponding changes in the performance parameters are well documented in the literature [1-7]. It is known that the usual single stage sintering process of raising the temperature of a material, kept in a furnace, to a suitable temperature at a specific heating rate, hold the temperature for a specific period and cool the furnace back to room temperature at a particular rate, is always accompanied by rapid grain growth [8]. Chen and Wang have developed a new method called dual sintering or two-stage sintering for the effective sintering of  $Y_2O_3$  [9]. By the dual sintering method, the grain boundary diffusion is maintained but grain boundary migration could be arrested. Therefore, using

the dual sintering technique, the grain growth at final stage sintering is suppressed to get ceramics with smaller sized grains. This method of sintering has been found to be effective in enhancing the performance parameters of various ceramic materials such as ZnO, Ni-Cu-Zn ferrite, BaTiO<sub>3</sub>, etc [10-12].

Cobalt ferrite is an ideal material for future magnetostrictive applications because of its low cost, easy processability, etc. The main disadvantage of cobalt ferrite is that it is not much useful for high frequency applications because of its low permeability. Therefore, there are not much studies reported on the effect of sintering on the properties and especially on the magnetostriction of cobalt ferrite. Chen *et al* have studied the magnetostriction of sintered metal bonded cobalt ferrite composite which was proposed to be useful for magnetomechanical sensor applications [13]. It was observed that these composites show high magnetostrictive strain of 230 ppm at low applied magnetic fields. Nlebedim *et al* have studied the effect of heat treatment and vacuum sintering on the magnetic and magnetostrictive properties of cobalt ferrite [14]. The studies showed that degradation of magnetostriction and strain derivative is due to the cation redistribution. Bhame and Joy have studied the effect of processing conditions and sintering temperature on the magnetostrictive properties of cobalt ferrite synthesized by the ceramic method [15]. It was found that the magnetostriction of sintered cobalt ferrite mainly depends on the microstructure of the sintered product.

It is widely known that sintered products derived from nanocrystalline powders exhibit improved magnetic permeability compared to the bulk counterparts [16, 17]. The advantage of the nanocrystalline powders is that they are more sinterable due to the fine particle nature as well as the high surface area [18-21]. Since very high magnetostriction coefficient is obtained for sintered cobalt ferrite derived from nanocrystalline powders of very small particle sizes synthesized by the autocombustion method using the corresponding metal nitrates and glycine as the fuel (Chapter 3), we have studied the effect of sintering conditions on the magnetostriction characteristics of the compacts made from small particles.

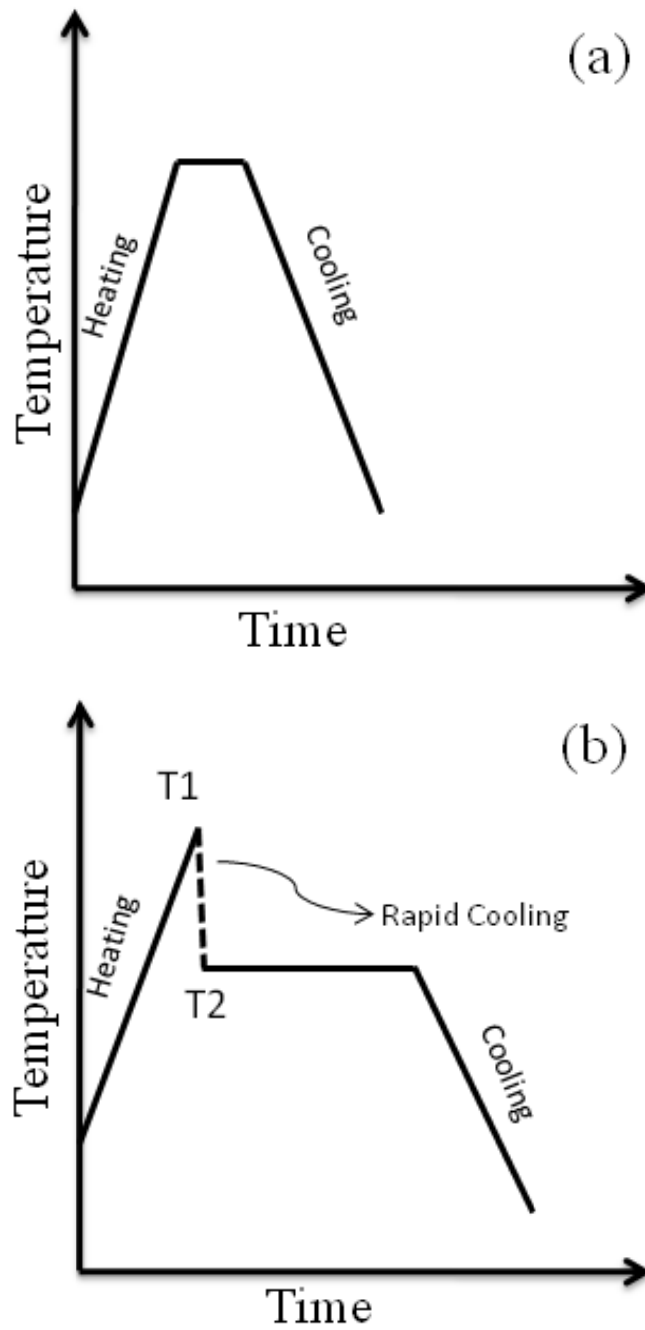


Figure 4.1: Schematic representations of the sintering schedules of (a) single-stage sintering and (b) two-stage sintering or dual sintering.

This chapter describes the effect of single and two-stage sintering on the microstructure and magnetostriction of sintered cobalt ferrite derived from nanocrystalline materials. The powder sample G2 with a particle size of 4 nm (Chapter 3, Table 3.3) which showed highest magnetostriction as well as high strain derivative after sintering at 1450 °C is used for the sintering studies. The schematics of the single and two-stage sintering processes are shown in Figure 4.1. In single stage sintering, the pressed compact is heated from room temperature to high temperature ( $T_1$ ) and held at this temperature for a short time and then cooled back slowly (Figure 4.1a). This sintering process is known to be always accompanied by rapid grain growth. In the case of dual sintering, the sample is heated to a high temperature ( $T_1$ ) and rapidly cooled down to a lower temperature ( $T_2$ ), held at this temperature ( $T_2$ ) for a long time, and finally cooled to room temperature slowly (Figure 4.1b). According to Chen and Wang [9], the success of the two-stage sintering strongly depends on the selection of high temperature ( $T_1$ ), second low temperature ( $T_2$ ), holding time as well as the heating and cooling rates. By the dual sintering method, the grain boundary diffusion is maintained but grain boundary migration could be arrested. Therefore, by the process of dual sintering, the grain growth at the final stage sintering can be suppressed to get ceramics with smaller sized grains. Objective of the present study is to investigate and compare the influence of these two sintering processes on the densification, microstructure, and magnetostriction of sintered cobalt ferrite derived from nanocrystalline materials.

## 4.2 The Sintering Process

In the single stage sintering process, the samples were heated from room temperature to high temperature and held at this temperature for a short time and then cooled back to room temperature slowly, as shown in Figure 4.1a. In this work, samples were sintered at 1500, 1450, 1400, 1300 and 1200 °C with a heating rate of 5 °C/min, cooling rate of 20 °C/min and holding time of 10 minutes, to determine the first heating temperature ( $T_1$ ). From magnetostriction studies on the different sintered samples it was found that sample sintered at 1450 °C show the highest maximum value of magnetostriction. Therefore, in

the case of dual sintering, samples were initially heated to 1450 °C ( $T_1$ ) and rapidly cooled down to a lower temperature ( $T_2$ ), held at this temperature ( $T_2$ ) for a long time, and finally cooled to room temperature slowly, as shown in Figure 4.1b. Samples were initially heated to 1450 °C with a heating rate of 5 °C/min and rapidly cooled to a lower temperature ( $T_2$ ) fixed at 1300 °C and vary the holding time from 10 min to 60 h to determine the holding time. Next, keeping the higher temperature ( $T_1$ ) constant, with a heating rate 5 °C/min, and holding time fixed, the lower temperature was varied as 1100, 1200, 1300 and 1400 °C with a cooling rate 30 °C/min to determine the best lower temperature ( $T_2$ ). Finally, holding time was fixed; the higher ( $T_1$ ) and lower temperatures ( $T_2$ ) were varied.

## 4.3 Studies on Sintered Samples

### 4.3.1 Microstructure and Density

The changes in the microstructural features of the single-stage sintered samples with increase in the sintering temperature from 1200 °C to 1500 °C are shown in Figure 4.2. The grain size is increased drastically with increase in the sintering temperature. The sample sintered at a lower temperature of 1200 °C shows very small and non-uniform grain size whereas high sintering temperature of 1500 °C gives rise to larger sized pores in the grains. The larger sized pores are due to the release of oxygen from the spinel lattice as reported for other ferrites sintered at higher temperatures [22]. Similarly, density is also increased with increase in the sintering temperature, as shown in Figure 4.3. The sample sintered at 1200 °C shows the lowest density of 63% whereas sample sintered at 1500 °C shows highest density of 83 % compared to the theoretical density of cobalt ferrite (5.275 g/cm<sup>3</sup>).

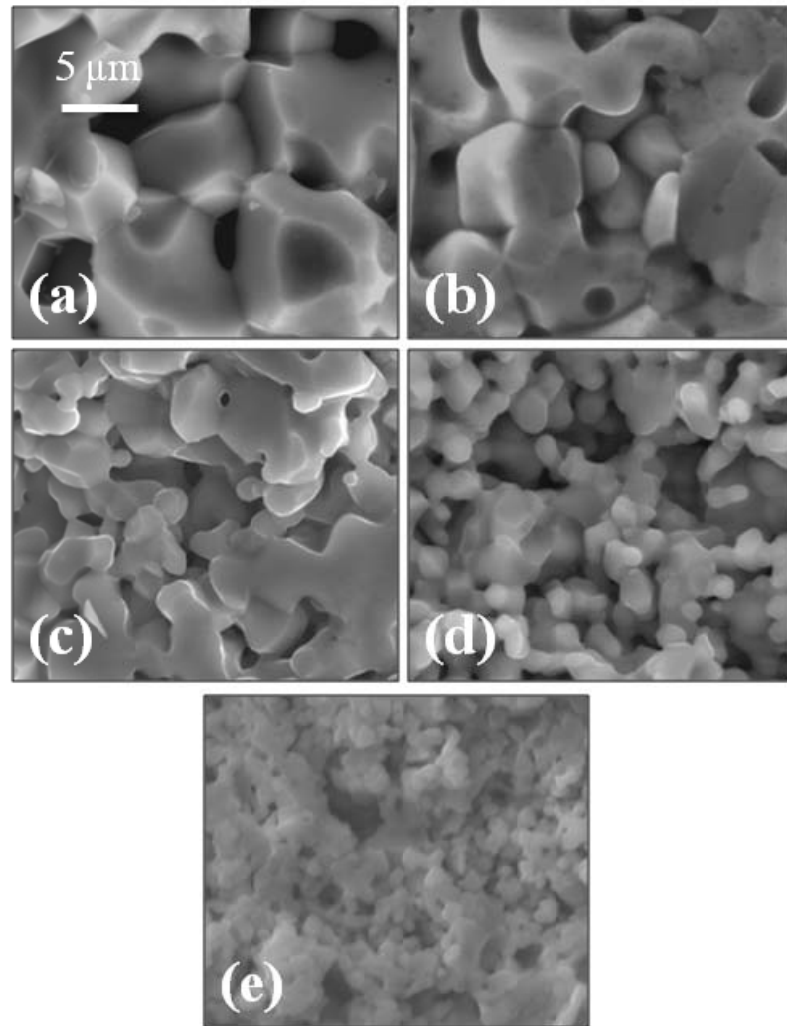


Figure 4.2: SEM images of the single stage sintered samples, sintered at (a) 1500 °C, (b) 1450 °C, (c) 1400 °C, (d) 1300 °C, and (e) 1200 °C.

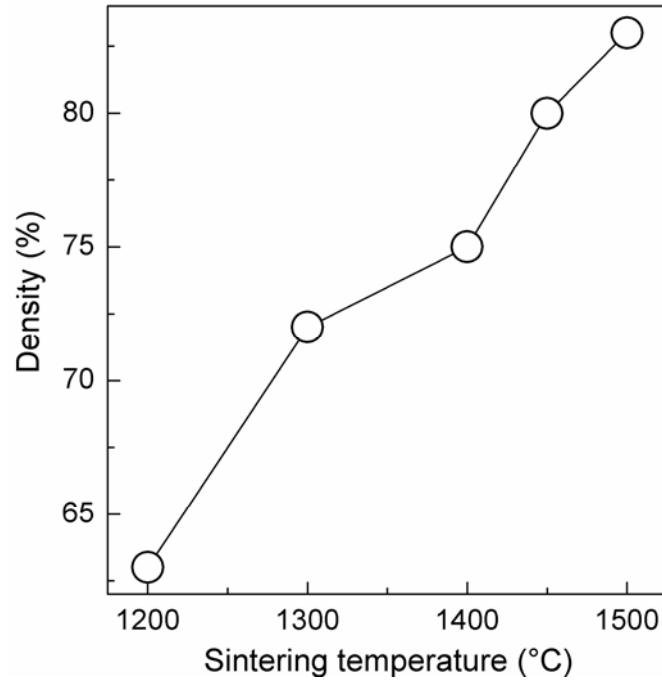


Figure 4.3: Variation of density as a function of sintering temperature for single stage sintered samples.

The SEM images of the two-stage sintered samples, where  $T_1 = 1450\text{ }^\circ\text{C}$  and  $T_2 = 1300\text{ }^\circ\text{C}$ , with different holding times from 10 min to 60 hrs are shown in Figure 4.4. It can be seen that, there are large changes in the microstructure with increasing the holding time. The grain size is increased with increasing the holding time. There is a corresponding increase in the density of the sintered samples, when the holding time is increased. The density is found to be very low (79%) for a holding time of 10 minutes. However, the density increases almost linearly when the holding time is varied from 5 to 60 hours. The density varies from 82% to 90% with increasing holding time above 5 h, as shown in Figure 4.5. Figure 4.4 shows that the sintering temperature combination of the higher temperature at  $1450\text{ }^\circ\text{C}$  ( $T_1$ ) and the lower temperature at  $1300\text{ }^\circ\text{C}$  ( $T_2$ ) and holding time of 20 h give most clear microstructure with grain size of  $10\text{ }\mu\text{m}$  with minimum amount of pores compared to the other sintered samples.

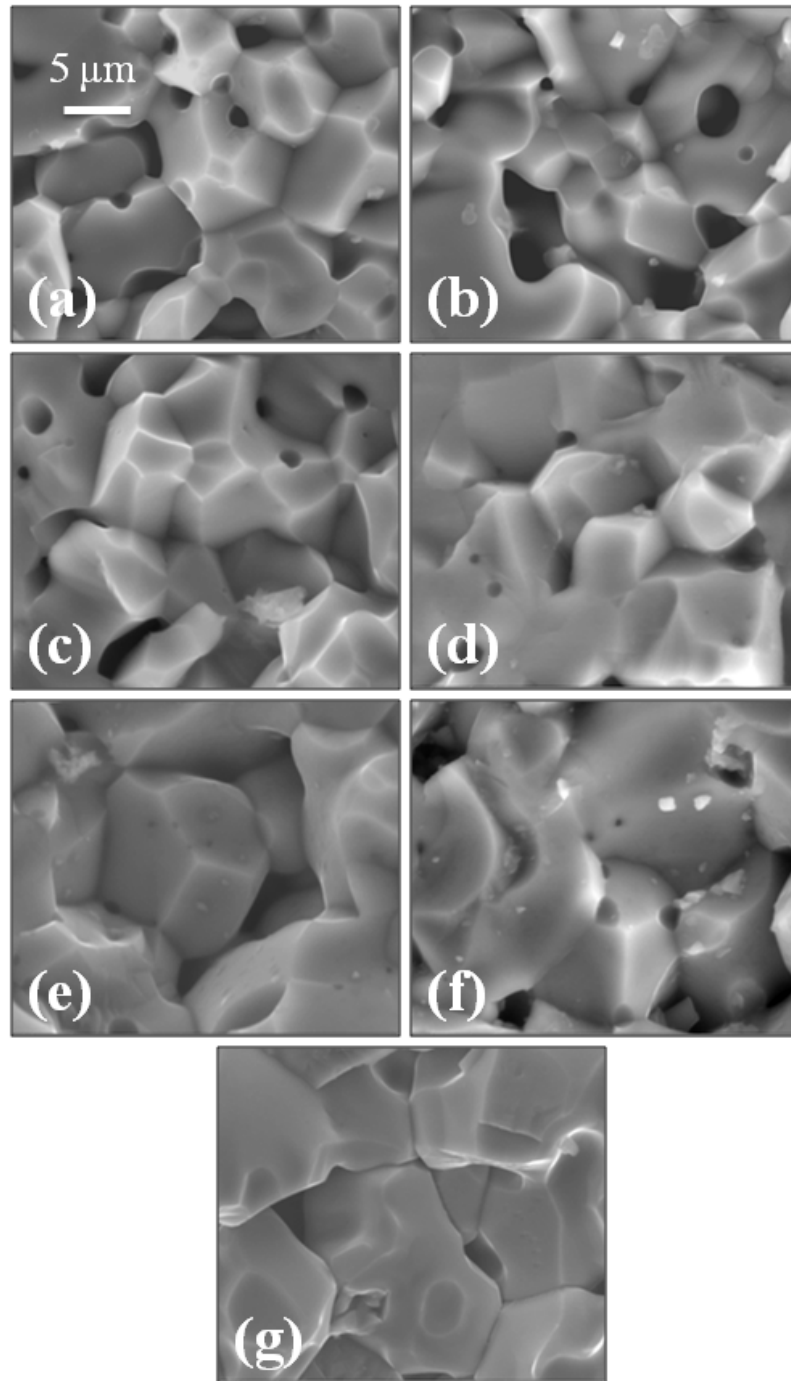


Figure 4.4: SEM images of two-stage sintered samples ( $T_1 = 1450\text{ }^\circ\text{C}$  and  $T_2 = 1300\text{ }^\circ\text{C}$ ) with different holding time at the lower temperature; (a) 10 min, (b) 1 h, (c) 5 h, (d) 10 h, (e) 20 h, (f) 40 h, and (g) 60 h.

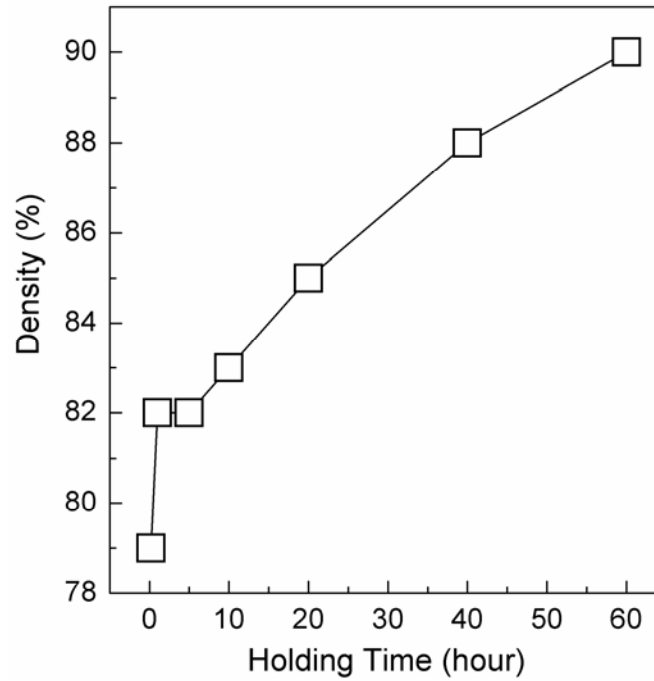


Figure 4.5: Variation of density as a function of holding time for  $T_1 = 1450\text{ }^\circ\text{C}$  and  $T_2 = 1300\text{ }^\circ\text{C}$ .

The microstructures of the two-stage sintered samples with fixed higher temperature as  $1450\text{ }^\circ\text{C}$ , holding time as 20 hrs and different lower temperatures ( $T_2$ ) are shown in Figure 4.6. The grain size increases with increasing the lower temperature. It is found that the best microstructure without many intra-grain pores is obtained for the sample sintered at  $1450\text{ }^\circ\text{C}$  ( $T_1$ )/ $1300\text{ }^\circ\text{C}$  ( $T_2$ ). The density, as indicated in the right hand side of the individual micrographs, increases with increase in the second sintering temperature ( $T_2$ ).

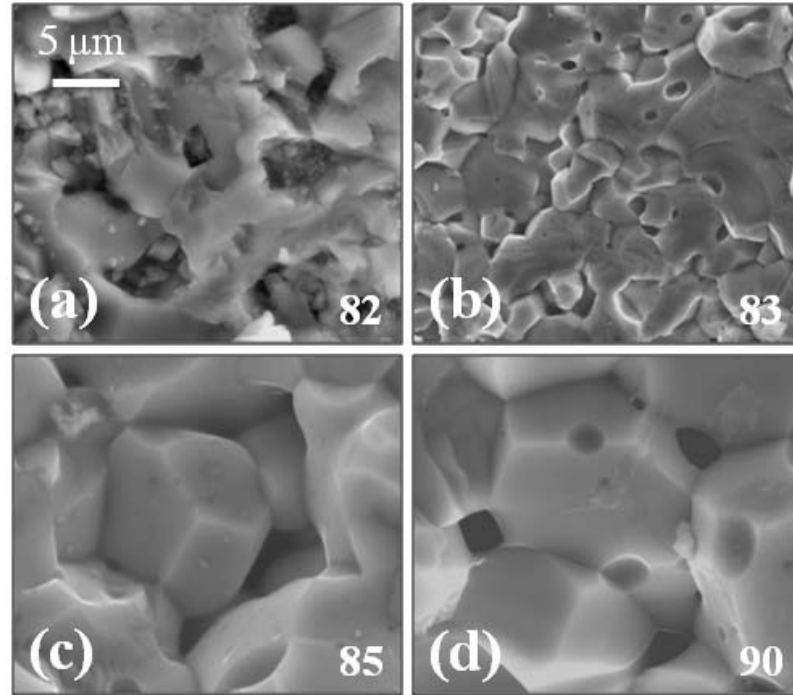


Figure 4.6: SEM images of the two-stage sintered samples with  $T_1 = 1450$  °C and different lower temperatures,  $T_2$  as (a) 1100 °C, (b) 1200 °C, (c) 1300 °C, (d) 1400 °C. The numbers on the right hand side corner indicate the density of the corresponding samples.

The SEM images of the two-stage sintered samples with different high temperatures ( $T_1$ ) and lower temperatures ( $T_2$ ) with the fixed holding time as 20 h are compared in Figure 4.7. The higher sintering temperature of 1450 °C ( $T_1$ ) and lower sintering temperature of 1300 °C ( $T_2$ ) with the holding time 20 h is ideal to get the best microstructure compared to other sintered samples.

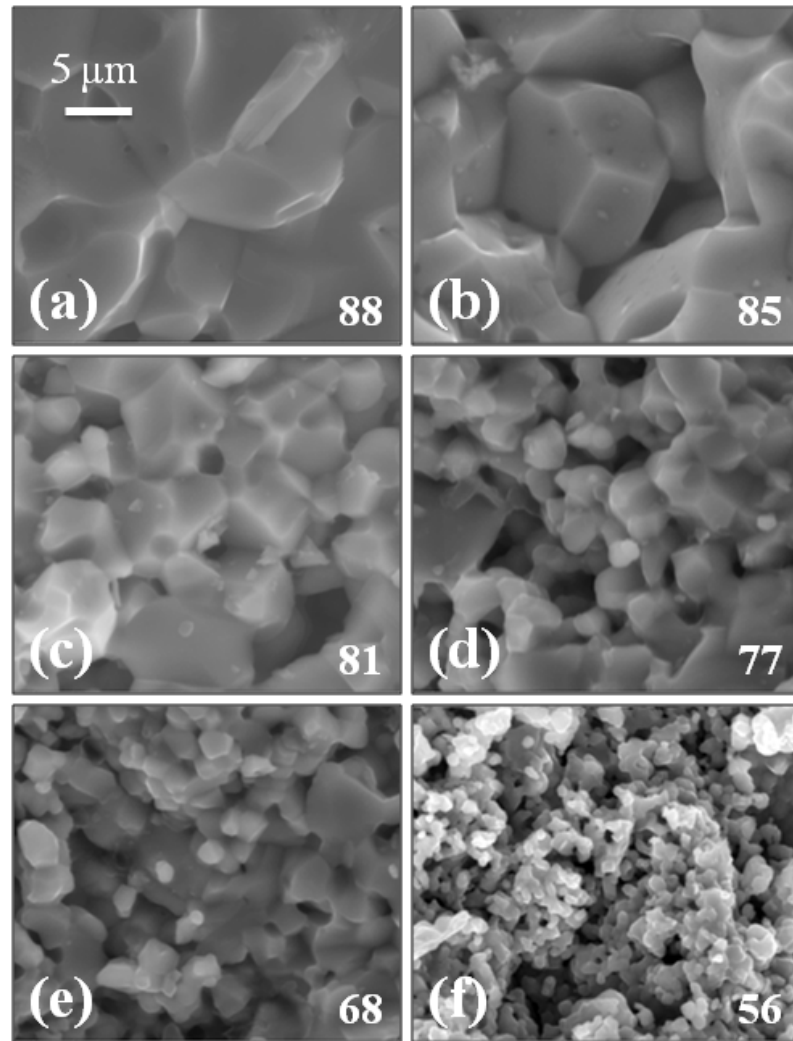


Figure 4.7: SEM images of the two-stage sintered samples with fixed holding time at different  $T_1$  and  $T_2$  as (a) 1500/1300 °C, (b) 1450/1300 °C, (c) 1350/1200 °C, (d) 1300/1150 °C, (e) 1250/1100 °C and (f) 1100/1000 °C. The numbers on the right hand side corner in the individual micrographs indicate the density of the corresponding samples.

## 4.3.2 Magnetic Properties

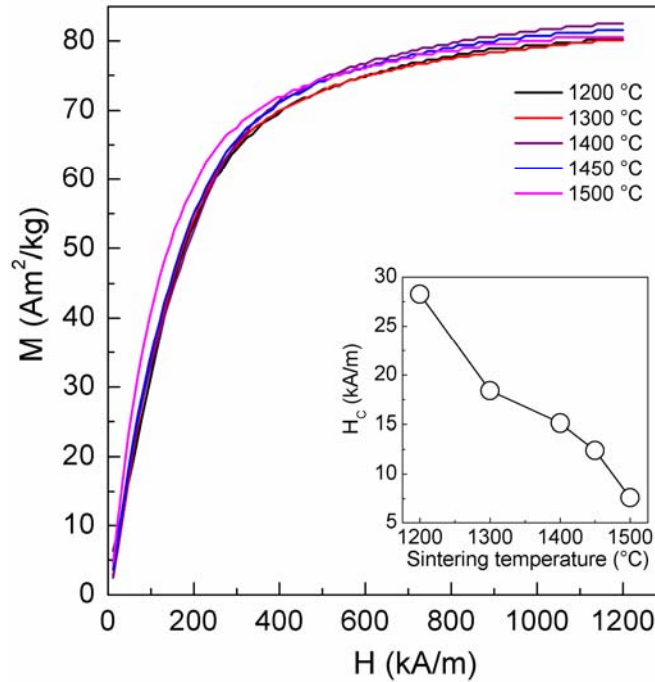


Figure 4.8: Comparison of the room temperature initial magnetization curves of single stage sintered samples. Inset: Variation of coercivity as a function of sintering temperature.

Figure 4.8 shows the room temperature magnetization measurements of the single stage sintered samples. The saturation magnetization values of all the sintered samples are almost comparable with the literature reported value of  $80 \text{ Am}^2/\text{kg}$  for cobalt ferrite [23]. The minor variations are due to the sample shape and orientation (measurements were made on broken pieces of the sintered pellets with irregular shape). On the other hand, the coercivity, as shown in the inset of Figure 4.8 decreases steadily with increase in the sintering temperature. This is due to the increase in the grain size as evidenced from SEM micrographs shown in Figure 4. 2. Above the critical size at which coercivity is maximum when coercivity is plotted as a function of particle size, coercivity decreases with increasing particle size due to the increased number of domains [24].

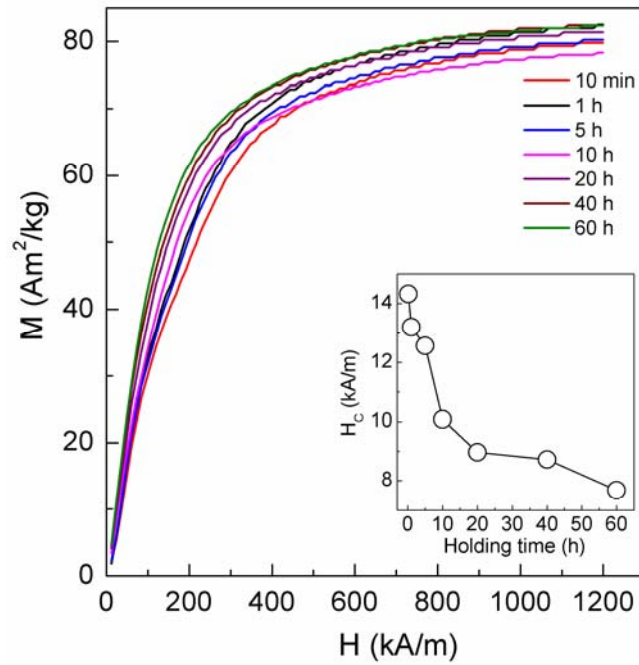


Figure 4.9: Initial magnetization curves of two-stage sintered samples ( $T_1 = 1450^\circ\text{C}$ ,  $T_2 = 1300^\circ\text{C}$ ) for different holding times. Inset: coercivity as a function of holding time.

Figure 4.9 shows the room temperature initial magnetization curves of the two-stage sintered samples at  $T_1 = 1450^\circ\text{C}$  and  $T_2 = 1300^\circ\text{C}$  at different holding times. Inset in Figure 4.9 shows the coercivity as a function of holding time. The coercivity decreases drastically up to a holding time of 10 hrs and further slow decrease is observed as the holding time is increased. These changes are well correlated with the changes in the grain size with holding time, as shown in Figure 4.4. Figure 4.10 shows the room temperature initial magnetization curves of the two-stage sintered samples with different lower temperatures ( $T_2$ ) and fixed high temperature as well as for those samples sintered with different high ( $T_1$ ) and lower temperatures ( $T_2$ ) for a holding time of 20 h. In all cases, coercivity decreases with increasing lower ( $T_2$ ) temperature in the first case and the same trend is observed for samples sintered at different high ( $T_1$ ) and lower temperatures ( $T_2$ ). In all cases, the changes in the coercivity are well correlated with the microstructures. Saturation magnetizations of all the two-stage sintered samples are close to  $80 \text{ Am}^2/\text{kg}$ .

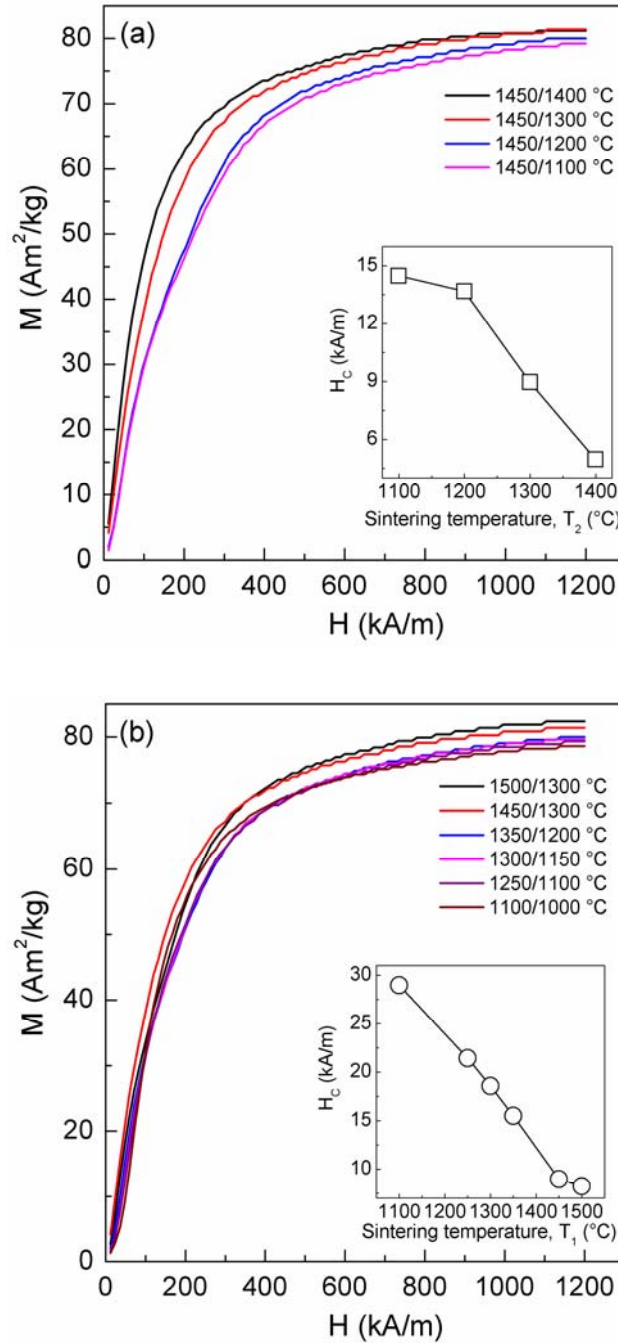


Figure 4.10: Room temperature initial magnetization curves of two-stage sintered samples, (a) for  $T_1 = 1450^\circ\text{C}$  and at different  $T_2$ . Inset: variation of coercivity as a function of  $T_2$ ; (b) both  $T_1$  and  $T_2$  varied as indicated, inset: variation of coercivity as a function of  $T_1$ .

### 4.3.3 Magnetostriction Studies

Magnetostriction curves of the single stage sintered samples are compared in Figure 4.11. A maximum magnetic field of 800 kA/m was applied in the parallel and perpendicular directions. Maximum value of magnetostrictive strain of 315 ppm is obtained in the parallel direction for the sample sintered at 1450 °C whereas lowest value of 201 ppm is obtained for the sample sintered at 1200 °C. Magnetostriction value increases with increasing sintering temperature from 1200 °C to 1450 °C and is then decreased for the sample sintered at 1500 °C. For all samples, the magnetostriction value is negative along the parallel direction. On the other hand, samples sintered at higher temperatures ( $\geq 1300$  °C) show negative magnetostriction along the perpendicular direction (shown in Figure 4.11). The maximum value of magnetostriction as a function of sintering temperature and the corresponding strain derivative curves are shown in Figure 4.12. From Figure 4.12, it can be seen that the sample sintered at 1450 °C shows the maximum value of magnetostriction and largest strain derivative of  $1.97 \times 10^{-9} \text{ A}^{-1}\text{m}$  whereas higher magnetostriction is obtained at lower fields for samples sintered at lower temperatures. From these studies, it is concluded that magnetostriction strongly depends on the sintering temperature, which influences the microstructure.

The parallel and perpendicular magnetostriction curves of the two-stage sintered samples with  $T_1 = 1450$  °C and  $T_2 = 1300$  °C with different holding time are compared in Figure 4.13. Figure 4.14 shows the variation of maximum value of magnetostriction and strain derivative of the two-stage sintered samples as a function of holding time. Magnetostriction value initially increases with increasing holding time up to 20 h then decreases. Both the magnetostriction as well as the strain derivative shows the same trend as a function of the holding time. Maximum value of magnetostriction of 331 ppm is obtained for the sample sintered for 20 h and higher strain derivative is obtained for this sample.

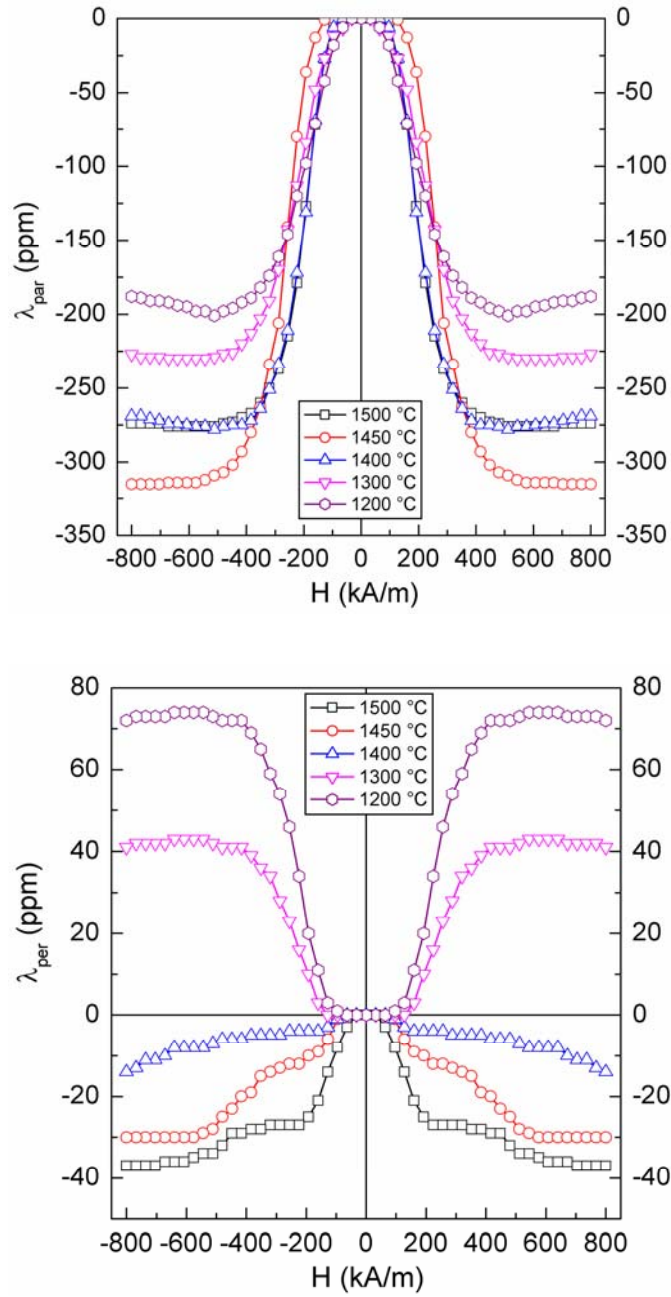


Figure 4.11: Magnetostriction curves measured along the parallel ( $\lambda_{\text{par}}$ ) and perpendicular ( $\lambda_{\text{per}}$ ) directions to the applied magnetic field for the samples sintered (single stage) at different temperatures.

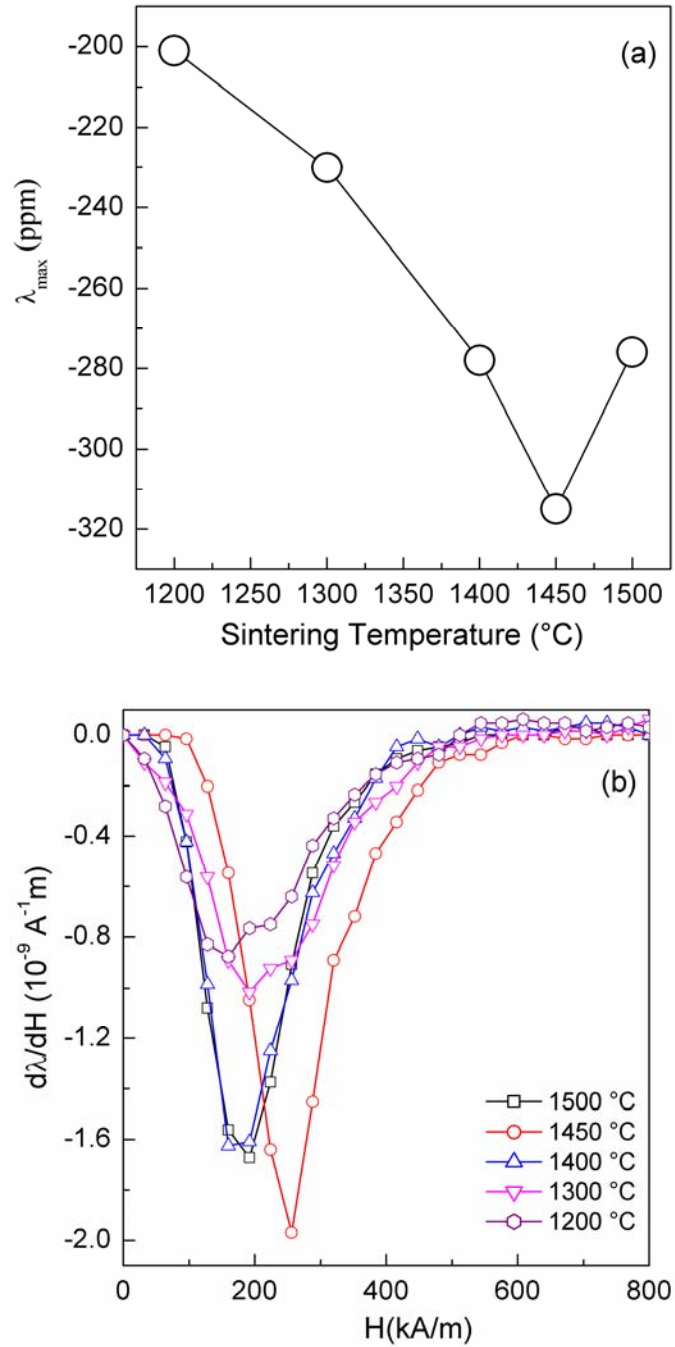


Figure 4.12: (a) Variation of the maximum value of magnetostriction as a function of sintering temperature and (b) strain derivative of samples sintered at different temperatures as a function of magnetic field, measured along the parallel direction.

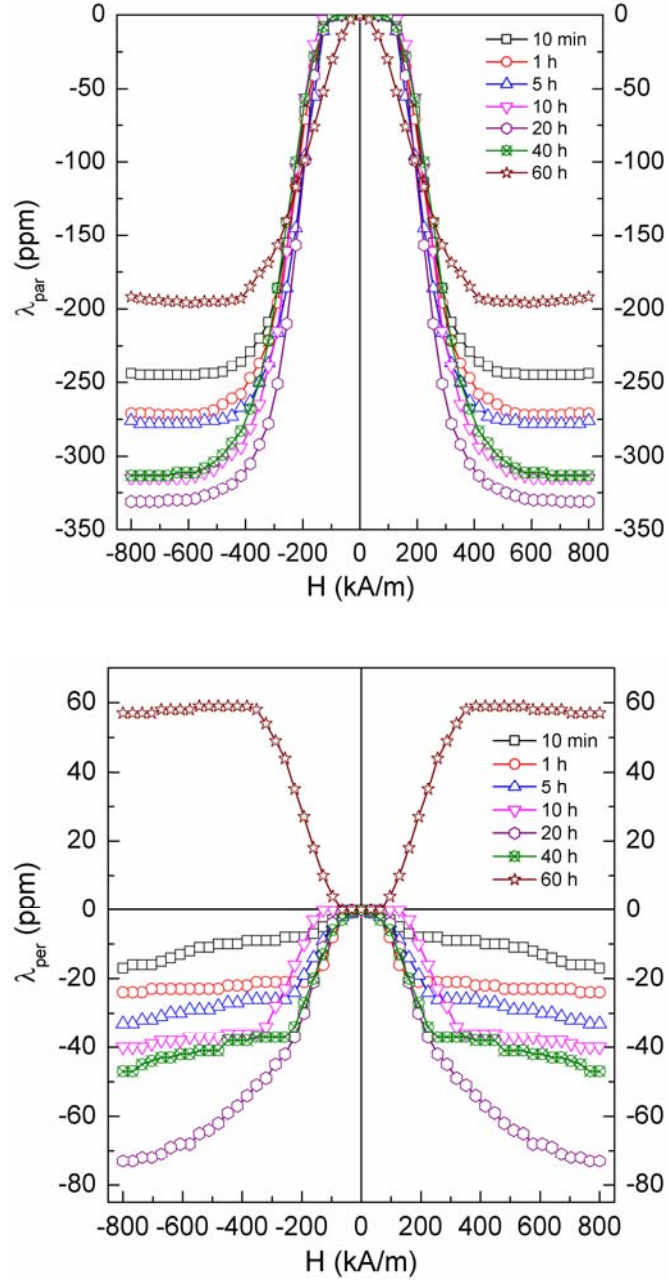


Figure 4.13: Magnetostriction curves measured along the parallel ( $\lambda_{\text{par}}$ ) and perpendicular ( $\lambda_{\text{per}}$ ) directions to the applied magnetic field for the two-stage sintered samples ( $T_1 = 1450$  °C,  $T_2 = 1300$  °C) with different holding time, as indicated.

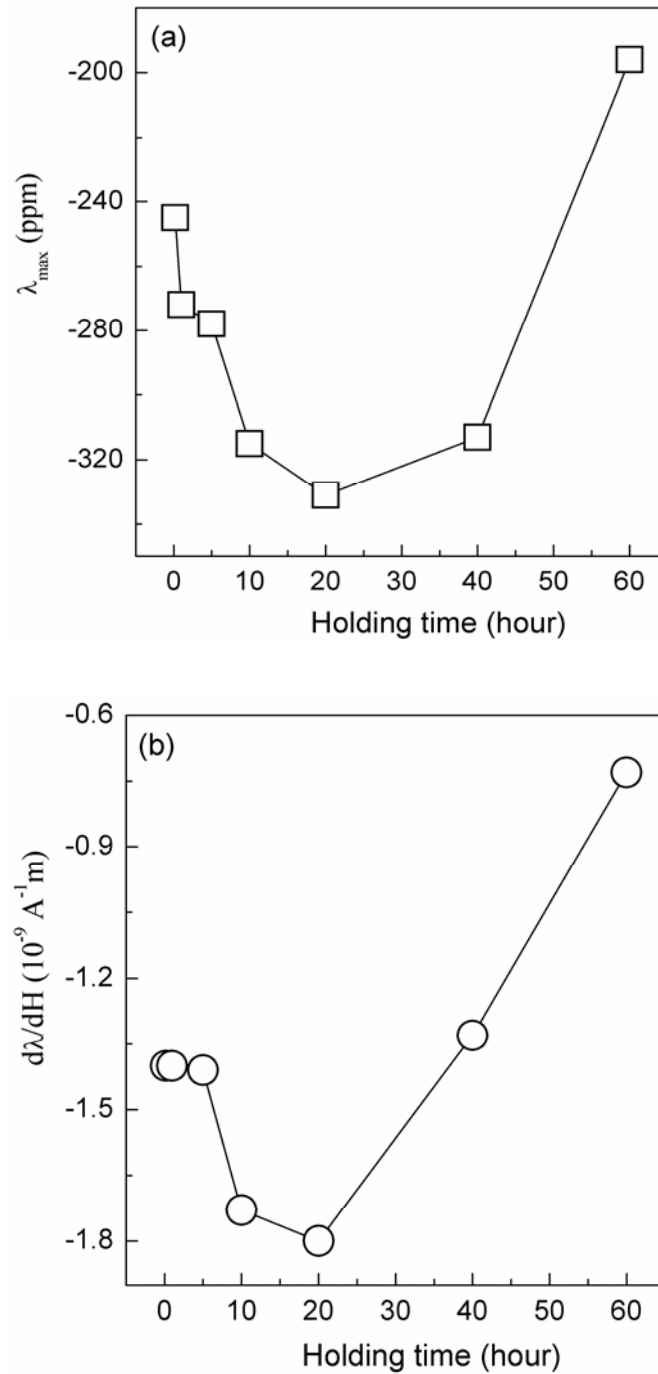


Figure 4.14: Variation of the (a) maximum value of magnetostriction and (b) strain derivative along the parallel direction as a function of holding time for the two-stage sintered samples for  $T_1 = 1450 \text{ }^\circ\text{C}$  and  $T_2 = 1300 \text{ }^\circ\text{C}$ .

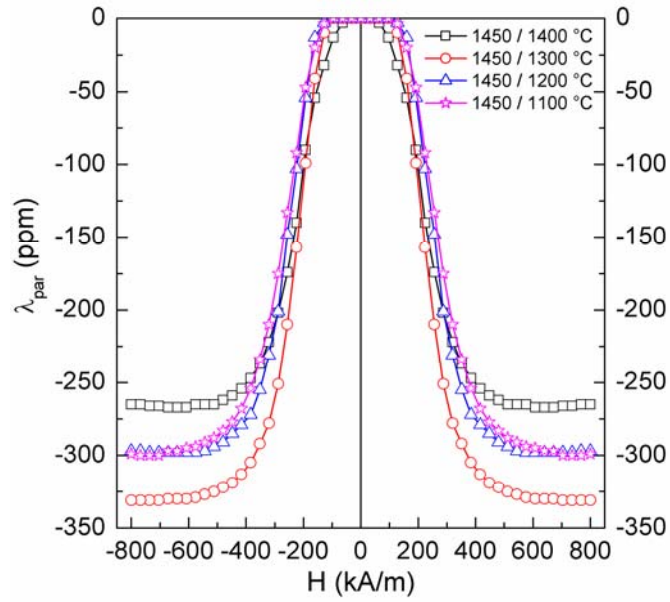


Figure 4.15: Magnetostriction curves measured in the parallel direction for the two-stage sintered samples for  $T_1 = 1450$  °C and for different  $T_2$ , as indicated.

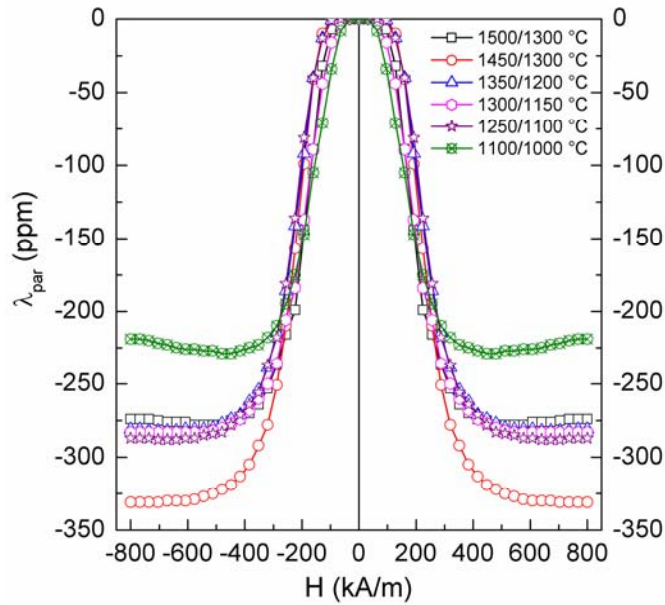


Figure 4.16: Magnetostriction curves measured in the parallel direction to the applied magnetic field for the two-stage sintered samples for different values of  $T_1$  and  $T_2$ , as indicated.

Figure 4.15 shows the magnetostriction curves measured in the parallel direction for the two-stage sintered samples with  $T_1 = 1450\text{ }^\circ\text{C}$  and different lower temperature ( $T_2$ ), sintered for 20 h. Similarly, Figure 4.16 shows the magnetostriction curves measured in the parallel direction for the two-stage sintered samples with different high temperatures ( $T_1$ ) and lower temperatures ( $T_2$ ), sintered for 20 h. Comparison of the magnetostriction characteristics of all the two-stage sintered samples, sintered under different combinations of higher sintering temperature,  $T_1$ , lower sintering temperature,  $T_2$ , and different holding times show that maximum value of magnetostriction of 331 ppm is obtained for the sample sintered at  $T_1 = 1450\text{ }^\circ\text{C}$  and  $T_2 = 1300\text{ }^\circ\text{C}$  for a holding time of 20 h.

#### 4.3.4 Magnetic Field Annealing Studies

In the previous chapter (section 3.5), it was found that magnetic field annealing is effective in raising the magnetostriction as well as strain derivative, due to the induced uniaxial anisotropy. The sample sintered at  $1450\text{ }^\circ\text{C}$  (SG2) showed enhanced magnetostriction as well as strain derivative compared to the values for the same sample before annealing. In the present studies on the samples sintered under different conditions, magnetic annealing has been carried out on two samples, one is on the single stage sintered sample at a lower temperature ( $1200\text{ }^\circ\text{C}$ ) and the second one is on two-stage sintered sample ( $T_1 = 1450\text{ }^\circ\text{C}$  and  $T_2 = 1300\text{ }^\circ\text{C}$  for a holding time of 20 h) showing the highest magnetostriction among all the two-stage sintered samples. Magnetic field annealing of the sintered pellets was carried out at  $300\text{ }^\circ\text{C}$  in a magnetic field of  $400\text{ kA/m}$  for 30 min. The annealing field was applied perpendicular to the cylindrical axis of the sintered pellet which is perpendicular to the measurement direction as well as the direction of the measuring field in the case of  $\lambda_{\text{par}}$ .

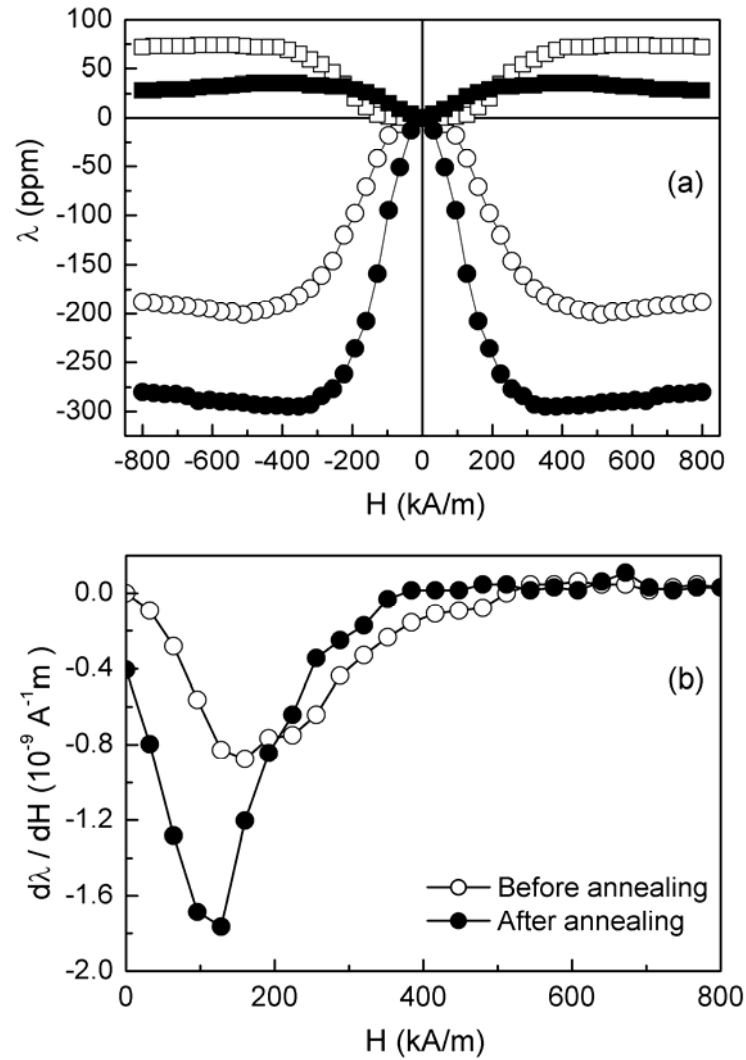


Figure 4.17: (a) Magnetostriction of single stage sintered sample (at 1200 °C) as a function of magnetic field, along the parallel (circles) and perpendicular (squares) directions. (b) Field derivative of magnetostriction along the parallel direction. The open and closed symbols represent before and after magnetic field annealing, respectively.

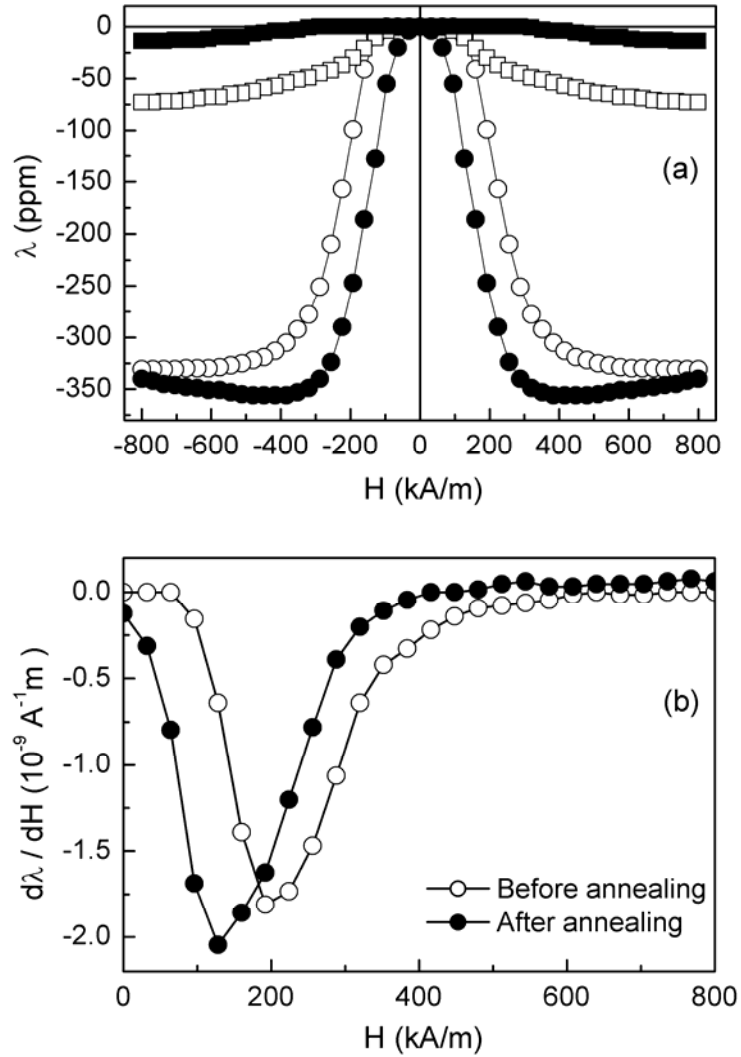


Figure 4.18: (a) Magnetostriction of two-stage sintered sample as a function of magnetic field, along the parallel (circles) and perpendicular (squares) directions. (b) Field derivative of magnetostriction along the parallel direction. The open and closed symbols represent before and after magnetic field annealing, respectively.

Figure 4.17 shows that the magnetostriction and strain derivative of the single stage sintered (at 1200 °C) sample measured as a function of magnetic field, parallel and perpendicular to the applied magnetic field direction before and after annealing in a field of 400 kA/m. It is found that the effect of magnetic field annealing is similar to that found in the case of SG2 (section 3.5) where improved magnetostriction and strain derivative are obtained after magnetic field annealing. Maximum value of magnetostriction for the single stage sintered sample (sintered at 1200 °C) is obtained as 201 ppm with a low strain derivative of  $0.88 \times 10^{-9} \text{ A}^{-1}\text{m}$  before annealing. However, after annealing the sample in a magnetic field, the maximum value of magnetostriction is increased to 295 ppm. Similarly, the strain derivative is doubled from  $0.88 \times 10^{-9} \text{ A}^{-1}\text{m}$  to  $1.77 \times 10^{-9} \text{ A}^{-1}\text{m}$ , after magnetic annealing.

Figure 4.18 shows the magnetostriction curves and the strain derivative for the two-stage sintered sample, before and after magnetic field annealing. In the case of the two-stage (1450/1300 °C for 20 h) sintered sample, the maximum value of magnetostriction is increased from 331 ppm to 356 ppm and the strain derivative is increased from  $1.8 \times 10^{-9} \text{ A}^{-1}\text{m}$  to  $2.05 \times 10^{-9} \text{ A}^{-1}\text{m}$  after magnetic annealing, with considerable increase in the value of magnetostriction at low magnetic fields. In chapter 3, it was found that the same sample sintered at 1450 °C for 10 minutes (single stage sintering) showed a maximum value of magnetostriction of 315 ppm before magnetic field annealing and the value increased to 345 ppm after annealing (Table 3.9). Comparable values are obtained (331 ppm before and 356 ppm after field annealing) when the same powder sample is processed under two-stage sintering at  $T_1 = 1450 \text{ °C}$  and  $T_2 = 1300 \text{ °C}$  when sintered for 20 h. The strain derivatives are also comparable for the single-stage and two-stage sintered samples. Thus, from the present study it is concluded that there is not much advantages on the two-stage sintering process over single stage sintering for getting higher magnetostriction and strain derivative for sintered cobalt ferrite.

## 4.4 Conclusions

Magnetostriction studies on sintered polycrystalline cobalt ferrite derived from nanocrystalline powders obtained by autocombustion method are made after sintering the material under different conditions to evaluate the effect of sintering and the related microstructure on the magnetostriction characteristics. Both single-stage as well as double-stage sintering studies have been performed. It is found that highest magnetostriction is obtained after sintering at 1450 °C under single-stage sintering conditions and the changes in the value of magnetostriction are somewhat correlated with the microstructure. In the two-stage sintering process, grain size remains constant while density continuously increases, unlike in normal sintering in which final stage densification is always accompanied by rapid grain growth. Out of all the experiments, maximum value of magnetostriction of 331 ppm and strain derivative of  $1.8 \times 10^{-9} \text{ A}^{-1} \text{ m}$  are achieved for the sample sintered at 1450 °C ( $T_1$ ) and then at 1300 °C ( $T_2$ ). It is observed that under suitable two-stage sintering conditions, high values of magnetostriction and strain derivative can be achieved. This is because the grain size and densification of the samples are better than those obtained from single-stage sintering. Magnetic field annealing has been shown to be very effective in enhancing the magnetostriction and strain derivative of single and two-stage sintered cobalt ferrite samples. Especially the sample sintered at a low temperature of 1200 °C shows huge increment of magnetostriction as well as strain derivative compared to the two-stage sintered samples after magnetic annealing. The values obtained are much larger than that reported for sintered polycrystalline cobalt ferrite derived from bulk powders, so far reported in the literature. Therefore, it is concluded that higher magnetostriction can be achieved after sintering at relatively low temperatures and with magnetic field annealing for sintered cobalt ferrite derived from nanocrystalline powders synthesized by the autocombustion method.

## References

- [1] C. Heck, *Magnetic Materials and their Applications* (Butterworth & Co. Pub. Ltd., London, 1974).
- [2] A. Goldman, *Modern Ferrite Technology* (Van Nostrand Reinhold, New York, 1990).
- [3] A. Verma and D. C. Dube, *J. Am. Ceram. Soc.* 88 (2005) 519.
- [4] J. Hu, M. Yan and W. Luo, *Physica B* 368 (2005) 251.
- [5] I. P. Kilbride and R. Freer, *IEEE Trans. Magn.* 36 (2000) 375.
- [6] N. Rezlescu, L. Sachelarie, E. Rezlescu, C. L. Sava and P. D. Popa, *Ceram. Int.* 29 (2003) 107.
- [7] D. N. Bhosale, S. R. Sawant, S. A. Gangal, R. R. Mahajan and P. P. Bakare, *Mater. Sci. Eng. B* 65 (1999) 79.
- [8] A. Barba, C. Clausell, C. Feliu and M. Monzo, *J. Am. Ceram. Soc.* 87 (2004) 571.
- [9] I. W. Chen and X. H. Wang, *Nature* 404 (2000) 168.
- [10] M. Mazaheri, A. M. Zahedi and S. K. Sadrnezhaad, *J. Am. Ceram. Soc.* 91 (2008) 56.
- [11] X. H. Wang, X. Y. Deng, H. L. Bai, H. Zhou, W. G. Qu, L. T. Li and I. W. Chen, *J. Am. Ceram. Soc.* 89 (2006) 438.
- [12] C.-S. Hsi, Y.-C. Chen, H. Jantunen, M.-J. Wu and T.-C. Lin, *J. Eur. Ceram. Soc.* 28 (2008) 2581.
- [13] Y. Chen, J. E. Snyder, C. R. Schwichtenberg, K. W. Dennis, R. W. McCallum and D. C. Jiles, *IEEE Trans. Magn.* 35 (1999) 3652.
- [14] I. C. Nlebedim, N. Ranvah, P. I. Williams, Y. Melikhov, F. Anayi, J. E. Snyder, A. J. Moses and D. C. Jiles, *J. Magn. Magn. Mater.* 321 (2009) 2528.

- 
- [15] S. D. Bhame and P. A. Joy, *J. Am. Ceram. Soc.* 91 (2008) 1976.
- [16] T. Nakamura, *J. Magn. Magn. Mater.* 168 (1997) 285.
- [17] S. Deka and P. A. Joy, *J. Am. Ceram. Soc.* 90 (2007) 1494.
- [18] A. Costa, E. Tortella, M. R. Morelli and R. Kiminami, *J. Magn. Magn. Mater.* 256 (2003) 174.
- [19] S. Komarneni, E. Fregeau, E. Breval and R. Roy, *J. Am. Ceram. Soc.* 71 (1988) C26.
- [20] W. C. Hsu, S. C. Chen, P. C. Kuo, C. T. Lie and W. S. Tsai, *Mater. Sci. Eng. B* 111 (2004) 142.
- [21] S. H. Hong, J. H. Park, Y. H. Choa and J. Kim, *J. Magn. Magn. Mater.* 290 (2005) 1559.
- [22] M. Rozman and M. Drofenik, *J. Am. Ceram. Soc.* 81 (1998) 1757.
- [23] A. E. Berkowitz and W. J. Schuele, *J. Appl. Phys.* 30 (1959) S134.
- [24] Y. Qu, H. Yang, N. Yang, Y. Fan, H. Zhu and G. Zou, *Mater. Lett.* 60 (2006) 3548.

# Chapter 5

## Magnetostriction Studies on Self-Composites of Sintered Cobalt Ferrite

### 5.1 Introduction

From the studies on the magnetostriction of sintered cobalt ferrite derived from nanocrystalline powders of different sizes in the range 3 to 80 nm, as discussed in Chapter 3, it was found that compacts sintered from smaller particles gave higher values for maximum magnetostriction. It was also observed that the sintered material derived from the powder sample G8 with a particle size of 40 nm gave higher magnetostriction at low magnetic fields compared to the compacts derived from the powder samples G1 and G2 derived from smallest particle sizes even though the latter showed higher maximum value of magnetostriction at high magnetic fields. Similarly, the compact made from bulk powders of particle size  $> 1\mu\text{m}$  gave higher density with lower porosity when sintered under identical conditions. Hence, we have tried a novel concept of mixing the powders of different particle sizes and made sintered self-composites with an intention to obtain higher magnetostriction at lower magnetic fields with improved sintered density.

In this chapter, we show that much higher values of the magnetostriction coefficient can be obtained for sintered polycrystalline cobalt ferrite by making self-composites obtained by sintering a physical mixture of cobalt ferrite powders with different initial particle sizes. Powders of G1 (3 nm), G2 (4 nm) and G8 (40 nm) samples

obtained by the autocombustion method and G0 ( $>1\mu\text{m}$ ) sample synthesized by the ceramic method are used for making the self-composites.

## **5.2 Preparation of Self-Composites**

The cobalt ferrite self-composites were prepared by thoroughly mixing the powders of cobalt ferrite having different particle sizes. Details of preparation of the powder samples having different particle sizes are discussed in Chapter 3 (section 3.2 and Table 3.1). Starting powders of G1 (3 nm), G2 (4 nm), G8 (40 nm) and G0 ( $> 1\mu\text{m}$ ) were used for making the sintered self-composites. Two different types of composites are prepared; one involving two components and the other with three components, using the above mentioned starting powders. Compacts were made by mixing different powders taking appropriate weight percentages as mentioned in the individual sections in this chapter. Details of compaction and sintering are discussed in Chapter 2 (section 2.3 and 2.4).

## **5.3 Magnetostriction Studies on Self-Composites**

### **5.3.1 Two-Component Systems**

Self-composites involving the starting powders of G1 which showed larger magnetostriction at high magnetic fields after sintering (sample SG1, Figure 3.13) and G8 showing larger magnetostriction at lower magnetic fields after sintering (sample SG8, Figure 3.13) were initially tried for different weight ratios of the powders, as shown in Table 5.1. All the mixed powder samples were compacted under identical conditions as discussed in Chapter 2 (section 2.3). For comparison, all samples are sintered at  $1450\text{ }^{\circ}\text{C}$  for 10 minutes, as it was found that samples sintered at this temperature showed higher magnetostriction after single-stage sintering (Chapter 4, section 4.3.3). Since the magnetostriction measured parallel to the applied magnetic field is important, only these values are shown for comparison.

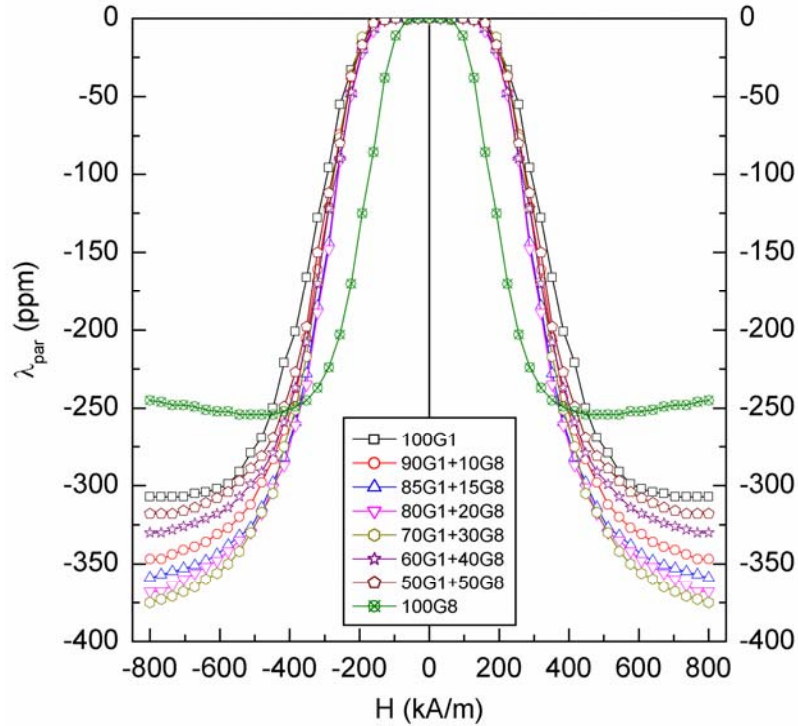


Figure 5.1: Magnetostriction curves measured in the parallel direction for two-component self-composites derived from powders of G1 and G8. The numbers indicate weight percentages of the individual powders.

The magnetostriction curves of the sintered self-composites for different ratios of the powders of G1 and G8 are shown in Figure 5.1. An important observation is that, for the sintered individual components G1 and G8, magnetostriction is saturated at higher magnetic fields, whereas the magnetostriction continuously increases even at higher magnetic fields for all composites. For all the self-composites, the maximum value of magnetostriction is found to be larger than that of the individual components at high fields. Maximum value of magnetostriction initially increases with increasing amount of G8 (particle size 40 nm), reaches a maximum value and then decreases (Table 5.1). The highest maximum value of magnetostriction is obtained for the ratio of 70% G1 and 30% G8 by weight and then decreases. The highest value of maximum magnetostriction is obtained as 375 ppm for this sample with almost comparable value for the 80:20

composite. Moreover, the highest value of the strain derivative of  $1.55 \times 10^{-9} \text{ A}^{-1}\text{m}$  is obtained for the 80:20 composite. However, there is no improvement in the value of magnetostriction at low magnetic fields, even for larger amounts of G8 used, compared to the value for the individual component G8.

Table 5.1: Weight percentages of the powders G1 and G8 used for making the self-composites and the magnetostriction parameters.

<b>Weight % of G1</b>	<b>Weight % of G8</b>	<b>Sintered density (%)</b>	<b><math>\lambda_{\text{max}}</math> (parallel) (ppm)</b>	<b><math>d\lambda/dH</math> (<math>10^{-9} \text{ A}^{-1}\text{m}</math>)</b>
100	0	80	-307	-1.14
90	10	81	-347	-1.34
85	15	82	-360	-1.50
80	20	82	-368	-1.55
70	30	82	-375	-1.48
60	40	82	-330	-1.34
50	50	83	-318	-1.35
0	100	84	-254	-1.35

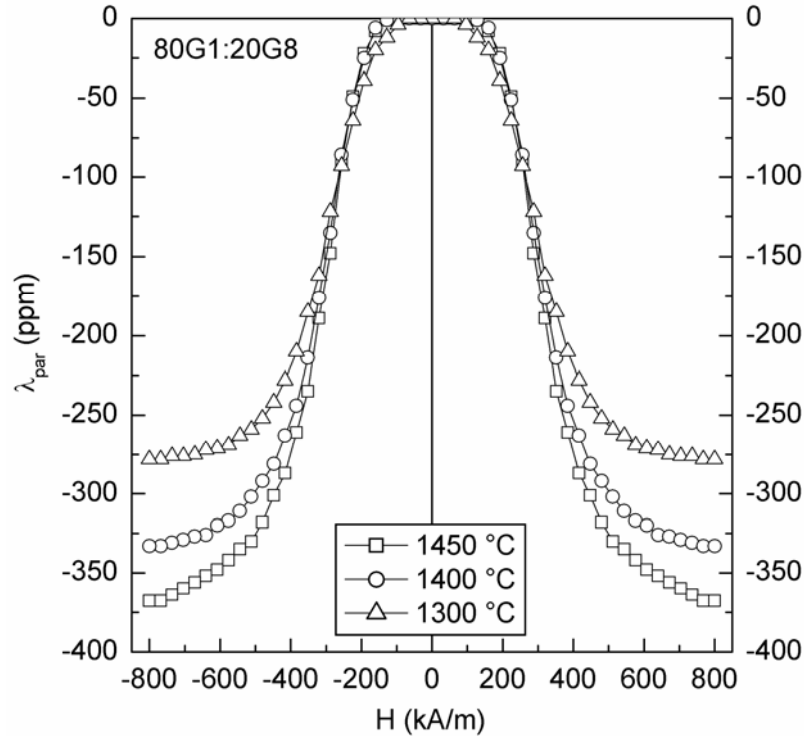


Figure 5.2: Magnetostriction curves measured in the parallel direction for self-composite of G1 and G8 (80:20) sintered at different temperatures.

The effect of sintering temperature on the magnetostriction characteristics is measured for the 80:20 self-composite which showed higher strain derivative when compared to the 70:30 self-composite but with comparable maximum value of magnetostriction. The samples were sintered at three different temperatures for 10 minutes each. The results are shown in Table 5.2 and Figure 5.2. It is found that the composite sintered at 1450 °C shows the highest maximum value of magnetostriction and the value decreases with decreasing sintering temperature. The magnetostriction curves show that the value of magnetostriction below a field of 300 kA/m is not affected by the sintering temperature.

Table 5.2: Effect of sintering temperature on the magnetostriction characteristics of the self-composite with 80% G1 and 20% G8.

Weight % of G1	Weight % of G8	Sintered density (%)	Sintering temperature (°C)	$\lambda_{\max}$ (parallel) (ppm)	$d\lambda/dH$ ( $10^{-9} \text{ A}^{-1}\text{m}$ )
80	20	82	1450	-368	-1.55
80	20	80	1400	-333	-1.40
80	20	69	1300	-278	-1.07

Table 5.3: Characteristics of the self-composites with 80% G1 and 20% of different powder samples, sintered at 1450 °C.

Weight % of G1	Weight % of G2	Weight % of G8	Weight % of G0	Sintered density (%)	$\lambda_{\max}$ (parallel) (ppm)	$d\lambda/dH$ ( $10^{-9} \text{ A}^{-1}\text{m}$ )
100				80	-307	-1.14
	100			80	-315	-1.97
		100		80	-254	-1.35
			100	89	-151	-0.56
80	20	-	-	81	-344	-1.39
80	-	20	-	82	-368	-1.55
80	-	-	20	81	-350	-1.46

The magnetostriction characteristics of the self-composites made from 80% of G1 (3 nm) with 20% of powder samples of different particle sizes; G2 (4 nm), G8 (40 nm) and G0 (>1  $\mu\text{m}$ ) and sintered at 1450 °C for 10 minutes are compared in Table 5.3 and Figure 5.3. For all the self-composites, the maximum value of magnetostriction is larger than the values obtained for the individual components sintered under identical conditions. Even though sintered G0 showed higher density compared to G1, there is not much improvement in the density when 20% G0 is mixed with 80% G1.

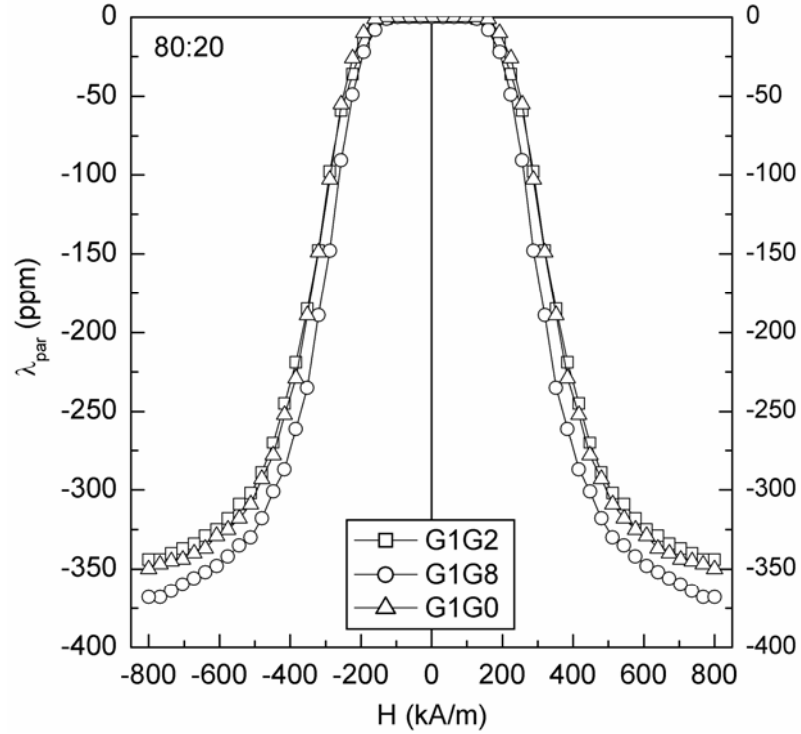


Figure 5.3: Magnetostriction curves measured in the parallel direction for self-composites derived from 80% of G1 and 20% of different starting powders of G2, G8 and G0.

Table 5.4: Characteristics of the sintered self-composite with 80% G2 and 20% G8 as well as G0.

Weight % of G2	Weight % of G8	Weight % of G0	Sintered density (%)	Sintering temperature (°C)	$\lambda_{\max}$ (parallel) (ppm)	$d\lambda/dH$ ( $10^{-9} \text{ A}^{-1}\text{m}$ )
80	20	-	83	1450	-314	-1.41
80	20	-	78	1400	-310	-1.46
80	20	-	68	1300	-278	-1.38
80	-	20	83	1450	-317	-1.49
80	-	20	80	1400	-333	-1.50
80	-	20	67	1300	-280	-1.18

From a comparison of the results on the different combinations of the sintered two-component self-composite samples (G1/G2, G1/G8, G1/G0), it is found that higher magnetostriction and strain derivative are obtained for composites using 80% of G1 and 20% G8. It was also found that the value of magnetostriction strongly depends on the sintering temperature. Better density and higher magnetostriction are obtained after sintering at 1450 °C.

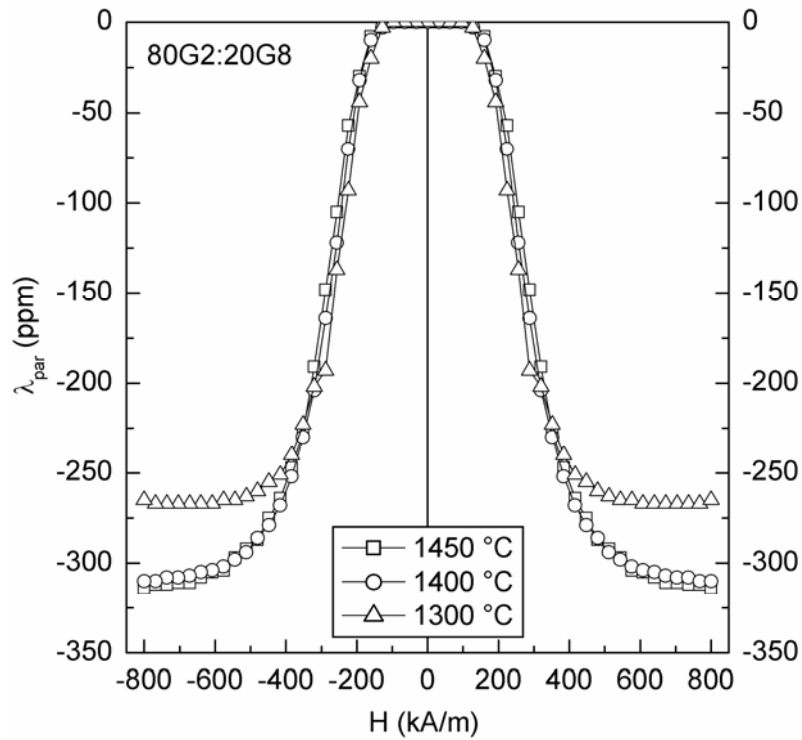


Figure 5.4: Magnetostriction curves measured in the parallel direction for the self-composites of G2 and G8 (80:20) sintered at different temperatures.

Having found that a self-composite made of powders of 80% G1 (particles of size 3 nm) and 20% of G0 (particles of size > 1  $\mu\text{m}$ ) or 20% of G8 (particles of size 40 nm) gave higher magnetostriction and strain derivative, similar studies are made on self-composites made of 80% of G2 (particles of size 4 nm). Initially, the effect of sintering

temperature is studied on the composition containing 80% by weight of G2 and 20% of G8 as well as G0. All the samples are sintered at the respective temperatures for 10 minutes. The results are shown in Table 5.4, Figure 5.4 and Figure 5.5. It is observed that highest maximum value of magnetostriction is obtained for the self-composite made of G2 and G0 sintered at 1400 °C.

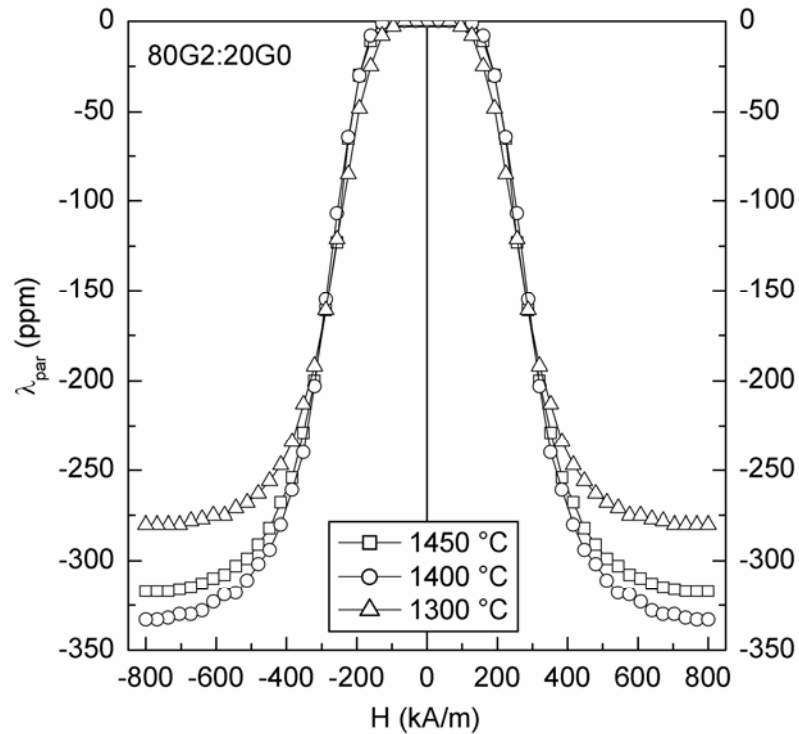


Figure 5.5: Magnetostriction curves measured in the parallel direction for the self-composites of G2 and G0 (80:20) sintered at different temperatures.

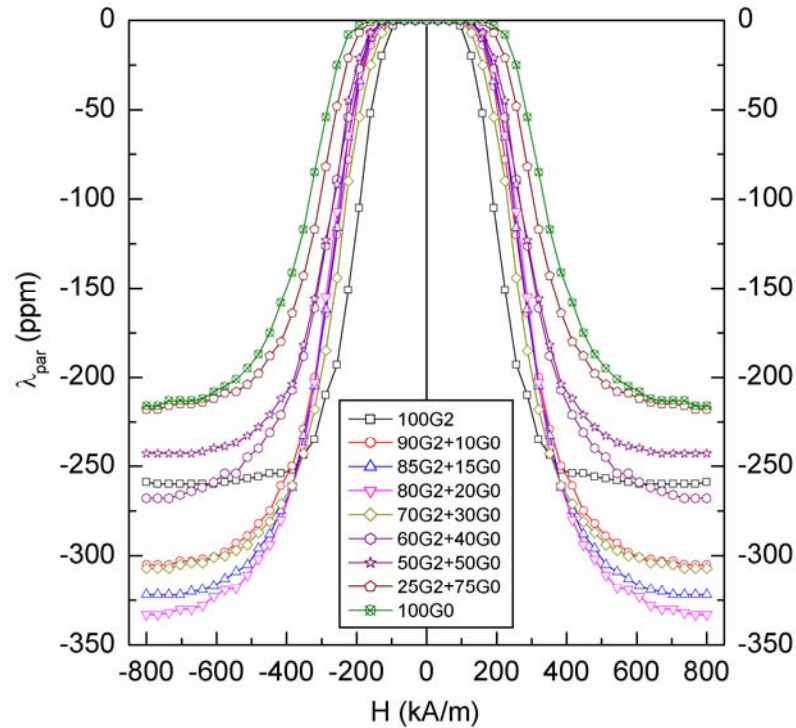


Figure 5.6: Magnetostriction curves measured in the parallel direction for the self-composites derived from powders G2 and G0 for varying compositions and sintered at 1400 °C. The numbers indicate weight percentages of the individual powders.

Since the self-composite of G2 and G0 sintered at 1400 °C showed the highest maximum value of magnetostriction at high magnetic fields, magnetostriction measurements are made on the sintered self-composites of G2 and G0 for different weight ratios. The results are shown in Table 5.5 and Figure 5.6. As observed in the case of the self-composites of G1 and G8 (Table 5.1), the maximum value of magnetostriction initially increases with increasing the contribution of G0 and then decreases after reaching a maximum value of -333 ppm for the 80:20 composite. Highest maximum value of magnetostriction of the 80:20 self-composite is much larger than that obtained for G2 alone with comparable strain derivative of  $\sim 1.5 \times 10^{-9} \text{ A}^{-1}\text{m}$ .

Table 5.5: Characteristics of the self-composites with varying ratios of G2 and G0, sintered at 1400 °C for 10 minutes.

Weight % of G2	Weight % of G0	Sintered density (%)	$\lambda_{\max}$ (parallel) (ppm)	$d\lambda/dH$ ( $10^{-9} \text{ A}^{-1}\text{m}$ )
100	0	75	-260	-1.54
90	10	81	-305	-1.34
85	15	81	-322	-1.51
80	20	80	-333	-1.50
75	25	81	-307	-1.49
60	40	79	-268	-1.13
50	50	80	-243	-1.22
25	75	79	-218	-1.08
0	100	84	-216	-0.98

### 5.3.2 Three-Component Systems

It is found that the two-component self-composites made from starting powders of different sizes, with larger amount of the powder sample with smaller particle size, exhibit different magnetostriction characteristics. Also, using powders of 80% of G1 (3 nm) with 20% G8 (40 nm) as well as G0 ( $> 1 \mu\text{m}$ ) gave higher maximum values of magnetostriction compared to 80% of G2 used instead of G1. Hence, studies are made on three-component self-composites also with powders of G1, G8 and G0 as components. The magnetostriction characteristics of different combinations of the three component self-composites are compared in Table 5.6. Figure 5.7 shows the magnetostriction curves of different combination of three-component self-composites recorded up to a maximum magnetic field strength of 800 kA/m, in the parallel direction ( $\lambda_{\text{par}}$ ) with respect to the direction of applied magnetic field. The self-composite made from the three starting powders of different particle sizes (3 nm, 40 nm and  $> 1 \mu\text{m}$ ) in the ratio of 80:10:10 by

weight shows a very high maximum value of magnetostriction of  $\sim 400$  ppm as well as high strain derivative of  $1.84 \times 10^{-9} \text{ A}^{-1}\text{m}$ .

The individual component powders G1 (3 nm), G2 (40 nm), and G0 ( $>1 \mu\text{m}$ ) with different particle sizes in the increasing order after sintering gave maximum values of magnetostriction as 307, 254, and 151 ppm (sintered samples SG1, SG2, and SG0, respectively, as discussed in Chapter 3), respectively, as shown in Table 5.6, where the value of maximum magnetostriction decreases with increasing particle size of the starting powders. On the other hand, the two-component systems gave a maximum magnetostriction around 350–370 ppm when G1 with the smallest particle size of 3 nm is made in to a composite with larger particles (Table 5.3) and this value is enhanced to  $\sim 400$  ppm for the sintered material derived from the three-component mixture (Table 5.6).

Table 5.6: Magnetostrictive properties of the three-component self-composites.

Sample Code	Ratio (wt %)			$\lambda_{\text{par}}$ (ppm)	$d\lambda/dH$ ( $10^{-9}\text{A}^{-1}\text{m}$ )
	G1	G2	G0		
SG1	100			-307	-1.14
SG2		100		-315	-1.97
SG3			100	-151	-0.56
TC1	80	10	10	-396	-1.84
TC2	70	10	20	-394	-1.58
TC3	60	10	30	-378	-1.53
TC4	60	20	20	-375	-1.59
TC5	70	20	10	-372	-1.56
TC6	80	5	15	-350	-1.45
TC7	80	15	5	-340	-1.45

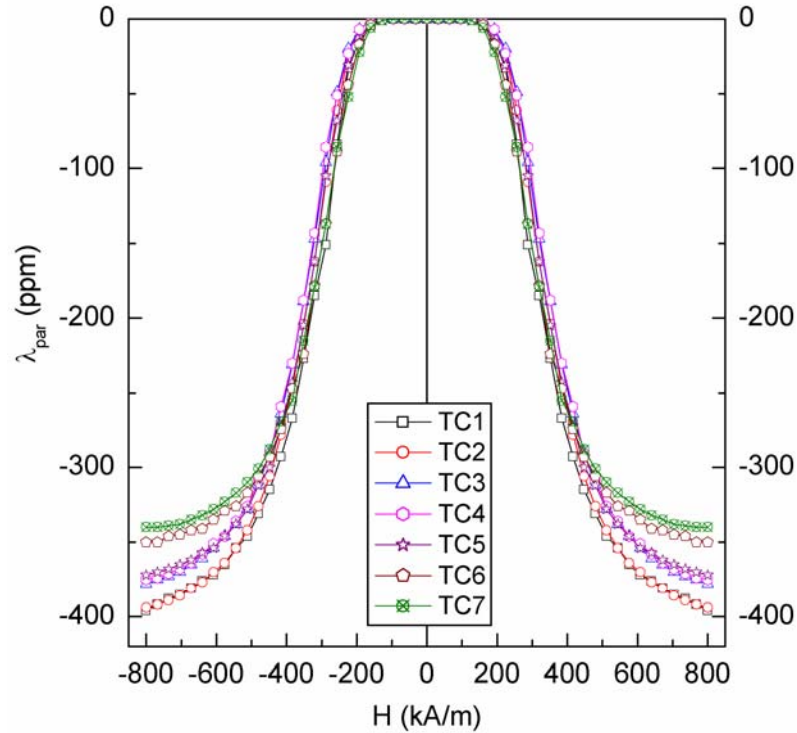


Figure 5.7: Magnetostriction curves measured in the parallel direction for the three-component self-composite samples. The sample codes are defined in Table 5.6.

### 5.3.3 Effect of Magnetic Field Annealing

Magnetic field annealing was found to be very effective in enhancing the magnetostriction coefficient and strain derivative of sintered cobalt ferrite derived from the powder samples G1, G2, G8 and G0 (sintered samples SG1, SG2, SG8 and SG0, respectively, as discussed in Chapter 3, section 3.4.6) due to the induced easy axis direction parallel to the annealing field, which affects magnetization processes and domain configuration. Higher magnetostriction coefficient perpendicular to the direction of the annealing field is achieved by magnetic field annealing because of the reorientation of the domains along the measurement direction, as reported in the literature [1, 2].

## Two-component Systems

Magnetostriction of the two-component self-composites are studied after magnetic field annealing to enhance the magnetostriction coefficient and strain derivative as observed in the case of the individual components. Composites derived from G1, G8 and G0 only are studied which showed higher magnetostriction coefficient compared to the composites derived from G2. As shown in Figure 5.8 and Table 5.7, among the different combination of two-component self-composite samples (G1/G8, G1/G0 and G8/G0), the G1/G8 and G1/G0 self-composites showed higher maximum magnetostriction values of 368 ppm and 350 ppm, respectively, without magnetic field annealing. On the other hand, the highest value of magnetostriction obtained for the individual components is 307 ppm for sample G1 (Table 5.7). For the self-composite G8/G0, the magnetostriction obtained is comparable to that for the sample G8 alone. Even though the sample G8/G0 shows relatively lower maximum magnetostriction (245 ppm), higher magnetostriction value of 364 ppm is obtained after magnetic field annealing, comparable to the values obtained for the other two composites (346 and 371 ppm, respectively, for G1/G8 and G1/G0). Also, unlike in the case of the individual components G8 and G0, there is not much improvement in the magnetostriction of G1/G8 and G1/G0 samples after magnetic field annealing, apart from the increase in the strain derivative. An important observation is that, wherever very small particles are used for the composites, higher magnetostriction is obtained without magnetic field annealing. This shows that making the self-composites using smaller and larger particles of the same material is advantageous over magnetic field annealing.

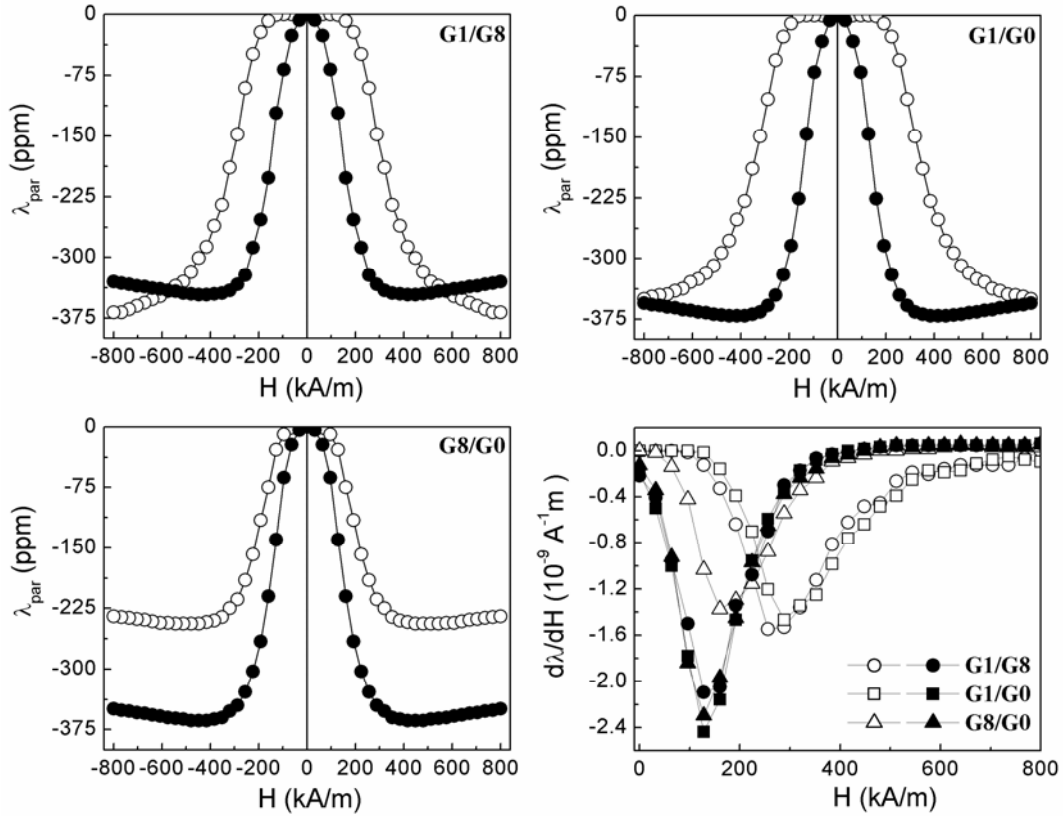


Figure 5.8: Magnetostriction curves of the two-component self-composites G1/G8, G1/G0 and G8/G0, as a function of magnetic field, measured parallel to the applied magnetic field before and after annealing in a field of 400 kA/m and field derivative of magnetostriction along the parallel direction for the different composites. The open and closed symbols represent before and after magnetic field annealing, respectively.

Table 5.7: Magnetostriction characteristics before and after magnetic annealing for the two component self-composites, compared with the individual components.

Sample Code	Ratio (wt %)			Before magnetic annealing		After magnetic annealing	
				$\lambda_{\text{par}}$ (ppm)	$d\lambda/dH$ ( $10^{-9} \text{A}^{-1}\text{m}$ )	$\lambda_{\text{par}}$ (ppm)	$d\lambda/dH$ ( $10^{-9} \text{A}^{-1}\text{m}$ )
	G1	G8	G0				
G1				-307	-1.14	-304	-1.70
G8				-254	-1.35	-353	-2.03
G0				-151	-0.56	-276	-1.38
G1/G8	80	20	-	-368	-1.55	-346	-2.08
G1/G0	80	-	20	-350	-1.50	-371	-2.43
G8/G0	-	80	20	-245	-1.32	-364	-2.29

### Three-component systems

Figure 5.9 shows the magnetostriction and strain derivative of the three-component system TC1 (80%G1, 10%G8 and 10%G0), which showed the highest maximum value of magnetostriction and strain derivative before and after magnetic field annealing. In fact, the maximum value of magnetostriction is reduced considerably (9%) for this composite after field annealing whereas the low-field magnetostriction is considerably increased without any major changes in the strain derivative. Magnetostriction is saturated above a field of 400 kA/m after annealing in the magnetic field whereas the magnetostriction increases continuously up to the maximum field of measurement before annealing.

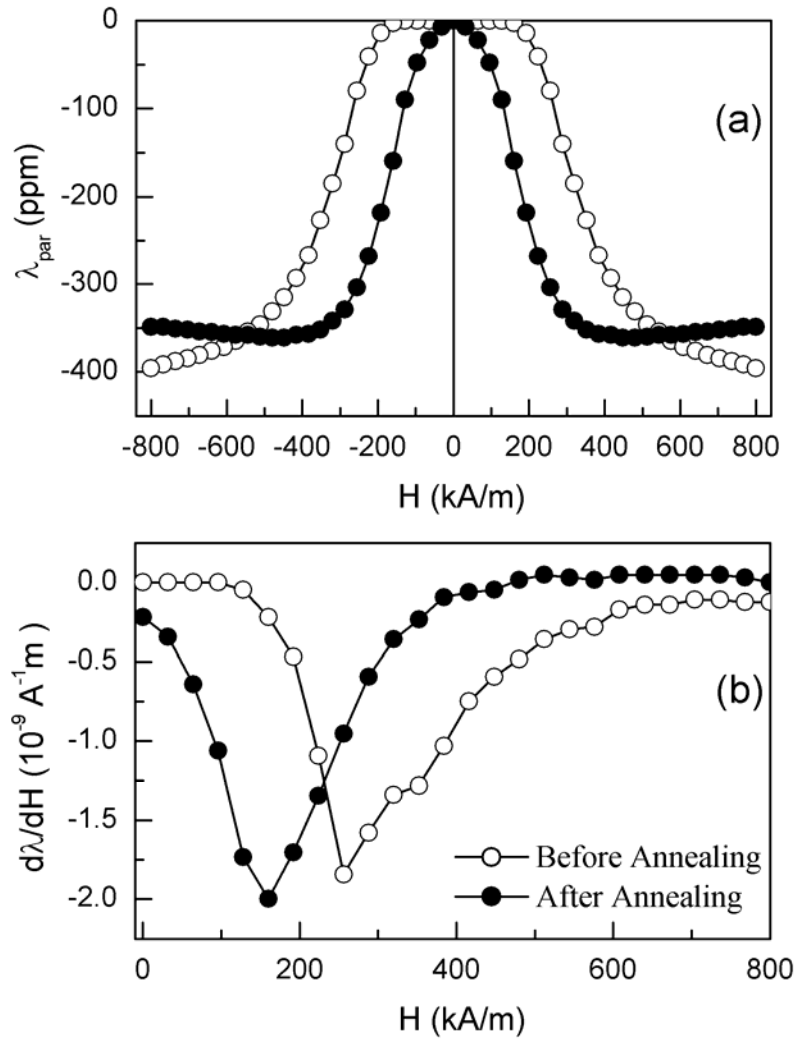


Figure 5.9: (a) Magnetostriction curves of the three-component self-composite G1/G8/G0 as a function of magnetic field, measured parallel to the applied magnetic field before and after annealing in a field of 400 kA/m and (b) field derivative of magnetostriction along the parallel direction. The open and closed symbols represent before and after magnetic field annealing, respectively.

## 5.4 Microstructure

The SEM images of the different two-component composites derived from G1 and G8 as well as G2 and G0 are shown in Figure 5.10 and Figure 5.11, respectively. Similarly, Figure 5.12 shows the SEM images of the different three-component composites. The SEM images of the single components G1, G8 and G0 are compared with the two-component and three-component self-composites showing maximum value of magnetostriction in Figure 5.13. It is found that there is no correlation between the density of the sintered self-composites and the maximum value of magnetostriction. Similarly, the observed microstructures also are not correlated much with the maximum value of magnetostriction.

## 5.5 Discussion

The effect of magnetic field annealing is to increase the magnetostriction at low fields for all samples. As mentioned in Chapter 1, apart from the magnitude of magnetostriction, the slope of the magnetostriction ( $d\lambda/dH$ ) or strain derivative or the magnetomechanical coupling factor is also an important factor for stress sensing applications. Comparison of the strain derivative ( $d\lambda/dH$ ) for different samples before magnetic field annealing shows that the highest value of strain derivative of  $1.97 \times 10^{-9} \text{ A}^{-1}\text{m}$  is obtained for G2 sintered at  $1450 \text{ }^\circ\text{C}$  with a maximum value of magnetostriction of 315 ppm. However, highest value of maximum magnetostriction of 396 ppm is obtained for the three component composite of G1, G8 and G0 (80:10:10). This is much larger than the previously reported values for sintered cobalt ferrite [3, 4]. However, the strain derivative for this composite is obtained as  $1.84 \times 10^{-9} \text{ A}^{-1}\text{m}$ . After magnetic field annealing, highest value of strain derivative of  $2.43 \times 10^{-9} \text{ A}^{-1}\text{m}$  is obtained for the two-component system G1/G0 (80:20) with maximum value of magnetostriction of 371 ppm.

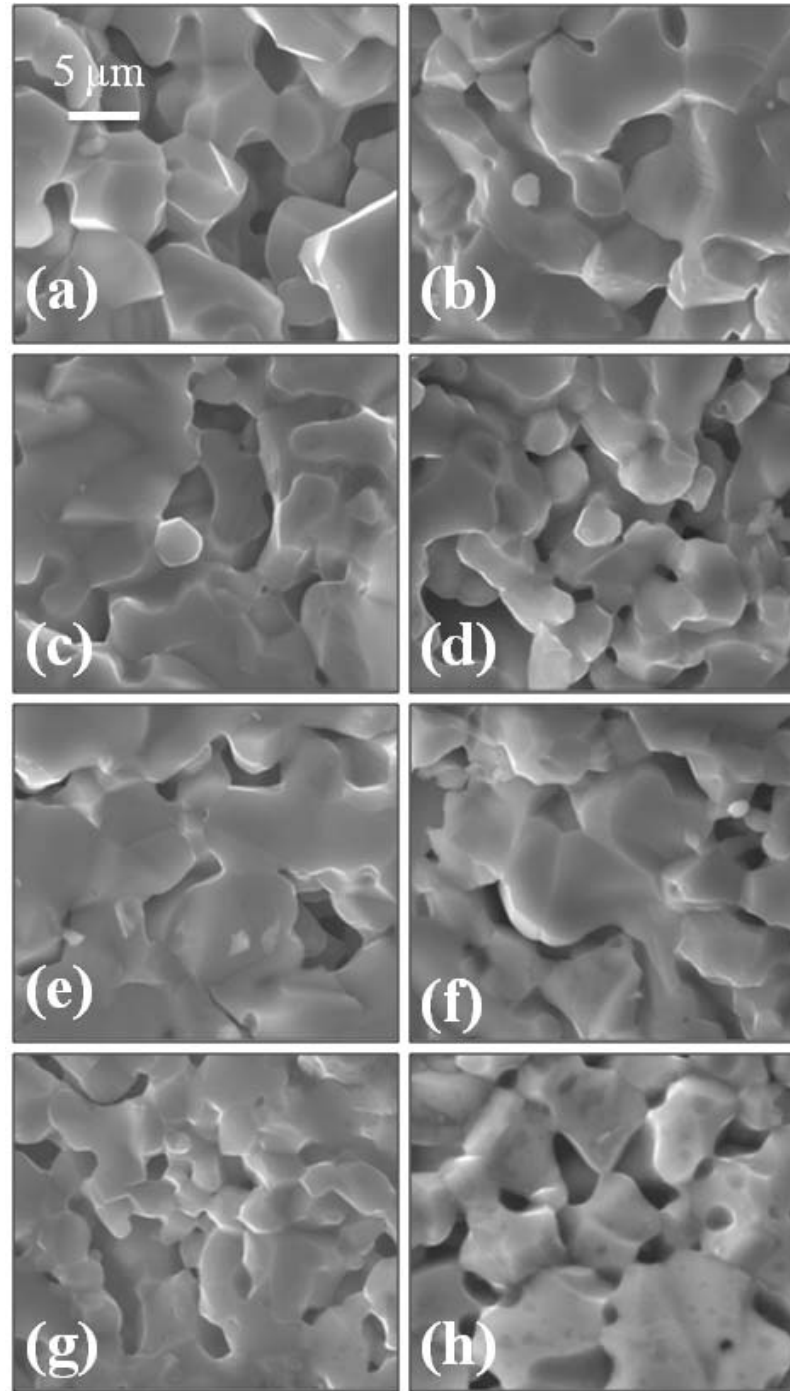


Figure 5.10: SEM images of two-component self-composites of G1 and G8 sintered at 1450 °C. (a) G1, (b) 90G1:10G8, (c) 85G1:15G8, (d) 80G1:20G8, (e) 70G1:30G8, (f) 60G1:40G8, (g) 50G1:50G8, (h) G8.

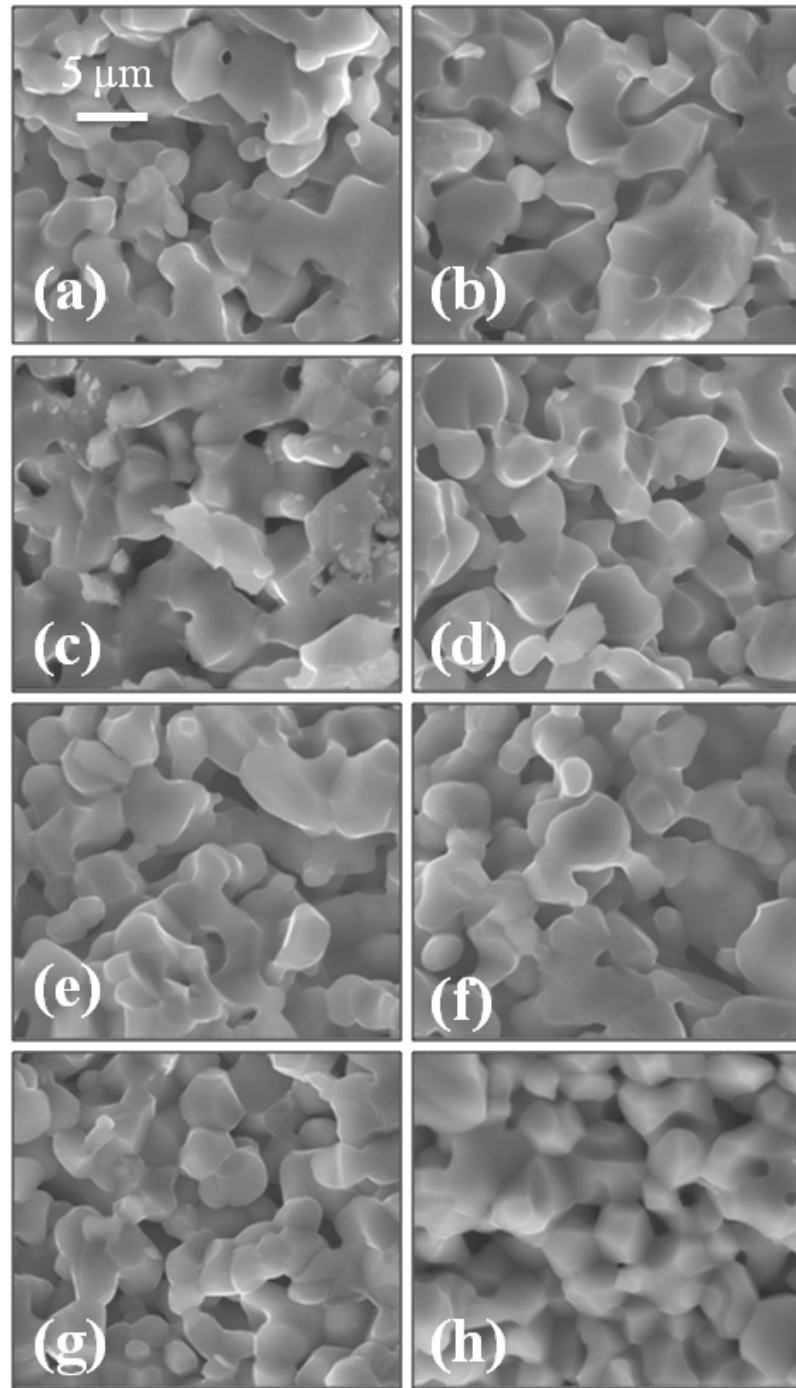


Figure 5.11: SEM images of two-component self-composites of G2 and G0 sintered at 1400 °C. (a) G2, (b) 90G2:10G0, (c) 85G2:15G0, (d) 80G2:20G0, (e) 70G2:30G0, (f) 60G2:40G0, (g) 50G2:50G0, (h) G0.

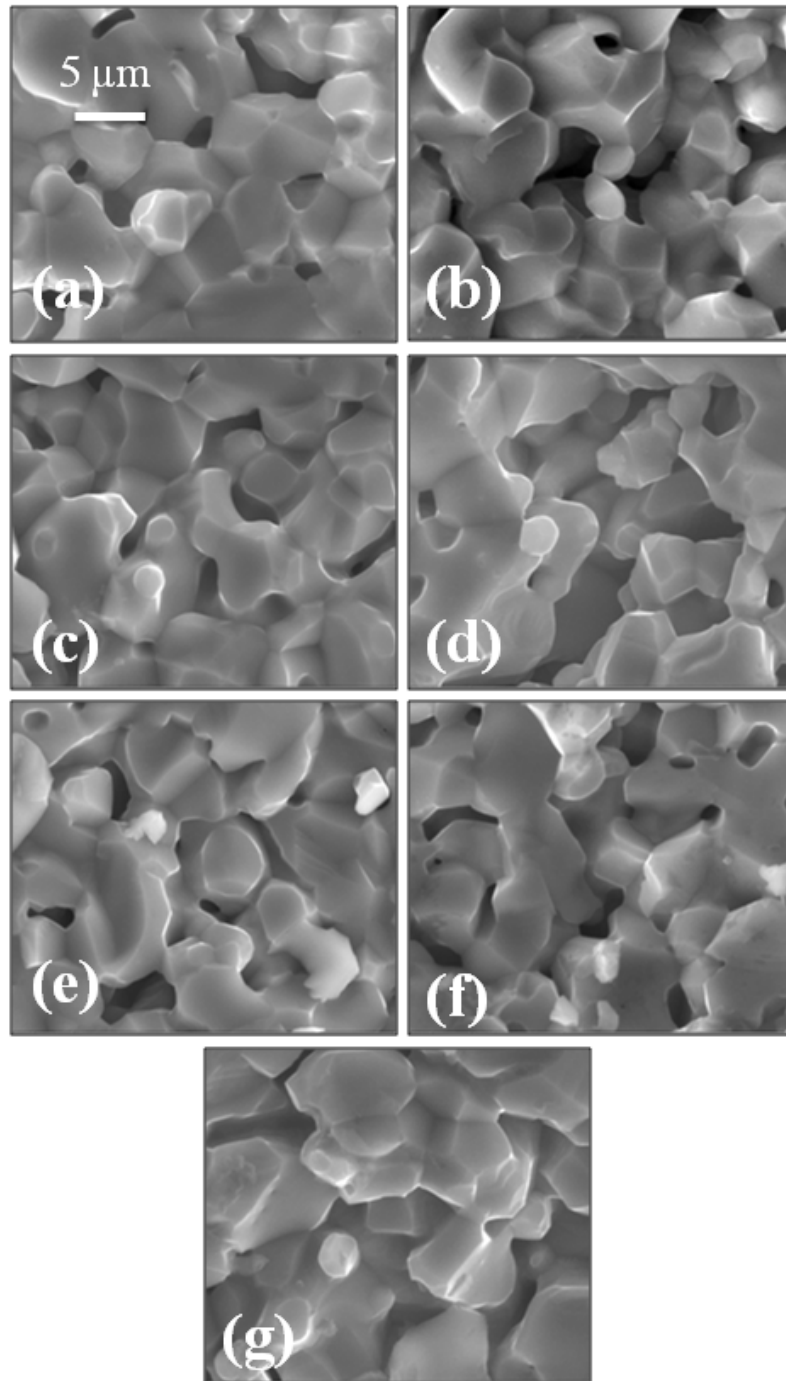


Figure 5.12: Comparison of the SEM images of the three-component self-composites, with different weight percentages of G1/G8/G0. (a) 80/10/10, (b) 70/10/20, (c) 60/10/30, (d) 60/20/20, (e) 70/20/10, (f) 80/5/15, (g) 80/15/5.

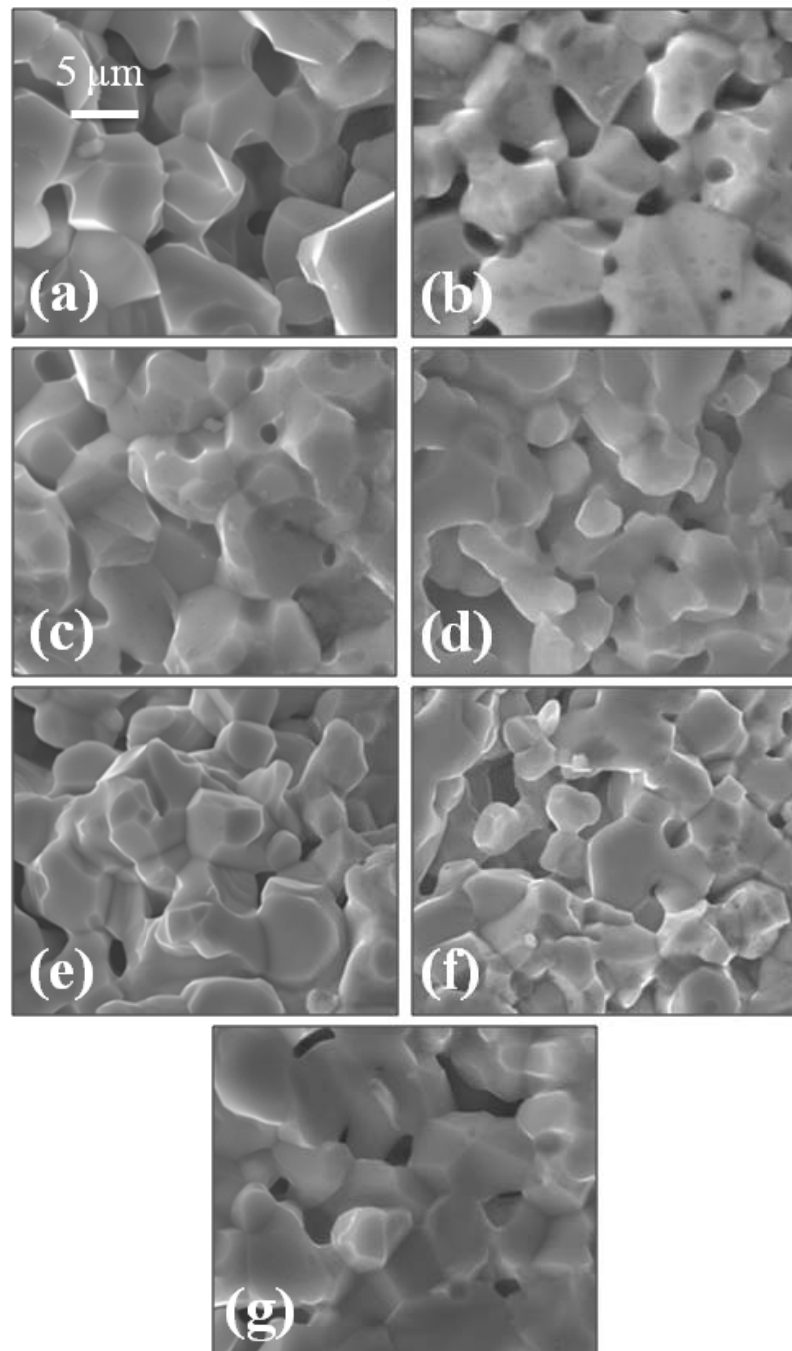


Figure 5.13: Comparison of the SEM images of the sintered samples (a) G1, (b) G8, (c) G0, (d) G1/G8, (e) G1/G0, (f) G8/G0, (g) G1/G8/G0.

For the three component system, the maximum value of magnetostriction is reduced from 396 ppm to 361 ppm after field annealing. After magnetic field annealing, all the self-composites show higher strain derivatives in the range  $2.0\text{--}2.4 \times 10^{-9} \text{ A}^{-1}\text{m}$ . The obtained highest value of magnetostrictive strain of  $\sim 400$  ppm is almost closer to the value reported for single crystals of cobalt ferrite [5, 6] and almost double the value reported for sintered polycrystalline cobalt ferrite samples produced from larger particles. The highest value so far reported for sintered cobalt ferrite derived from bulk powders is 225 ppm, for compacts made under normal conditions and without any magnetic field annealing [7]. Also, the magnitude of magnetostriction close to 400 ppm along the parallel direction is so far reported for samples compacted under very high pressures, sintered for a longer duration and only after magnetic field annealing at very high magnetic fields for a longer duration [8].

From a comparison of the magnitude of maximum magnetostriction and strain derivative of the individual components and self-composites, it is found that when the 3 nm particles (G1) are used for compaction, the magnetostriction is not changed much whereas large changes are observed when larger particles are used (separately or in composites), after magnetic field annealing. Also, there is not much correlation between the changes in the magnitude of maximum magnetostriction and the strain derivative, except that magnetostriction at low fields is enhanced after magnetic field annealing and maximum strain derivative is obtained at lower magnetic fields. This shows that the induced uniaxial anisotropy and the associated changes in the magnetization processes and domain configuration, as reported previously, alone are not sufficient to explain the changes in the value of magnetostriction and strain derivative. A major observation is that the change in the magnetostriction is very small after magnetic field annealing when the smallest particles (3 nm) are used while making the compacts. In fact, a decrease in the magnetostriction is observed for the three sintered samples derived from G1 (−1%), G1/G8 nm (−6%), and G1/G8/G0 (−9%). On the other hand, some increase in the strain derivative is observed for the first two samples. This unusual changes on magnetic annealing is likely to be coupled with the induced anisotropy as well as the

microstructure, because the induced anisotropy can also be affected by the size, shape and orientation of the grains in the sintered samples.

Even though there is not much difference in the microstructures of the different samples (see Figure 5.13), there are some smaller grains present in the images of the composites prepared using the 3 nm particles, which could be the deciding factor for the changes in the magnetostriction and strain derivative of the composites. It is possible that most of the domains in the smaller grains are aligned away from the direction of the measuring field so that there is not much effect of reorienting the domains after field annealing. Another possibility is that, if the direction of magnetization is already aligned in random directions in the smaller grains and is not influenced by magnetic field annealing, contribution from these smaller grains toward magnetostriction will not be influenced on field annealing. Similar effects may be the reasons for the unusual changes in the strain derivative also. However, these observations need to be verified by further detailed studies.

## **5.6 Conclusions**

In conclusion, it has been shown that very high magnetostriction at room temperature can be achieved for polycrystalline sintered cobalt ferrite if compacts are made in to the form of a self-composite where the components in the composites are nano and micrometer sized powders of the same material. Larger maximum value of magnetostriction of ~400 ppm and maximum value of strain derivative of  $2.0 \times 10^{-9} \text{ A}^{-1} \text{ m}$  could be achieved for a self-composite made from powder particles of three different sizes in the nano and micrometer levels, whereas the individual components gave values less than 310 ppm. Unlike for the individual components, the magnetostriction is not saturated at the highest measuring field of 800 kA/m for the three-component composite, indicating that it is further possible to improve the magnetostriction of sintered cobalt ferrite at higher fields. Also, in the case of the self-composites, higher magnetostriction can be achieved without any magnetic field annealing, thereby reducing the processing cost for various applications.

## References

- [1] C. C. H. Lo, A. P. Ring, J. E. Snyder and D. C. Jiles, *IEEE Trans. Magn.* 41 (2005) 3676.
- [2] Y. X. Zheng, Q. Q. Cao, C. L. Zhang, H. C. Xuan, L. Y. Wang, D. H. Wang and Y. W. Du, *J. Appl. Phys.* 110 (2011) 043908.
- [3] Y. Chen, J. E. Snyder, C. R. Schwichtenberg, K. W. Dennis, R. W. McCallum and D. C. Jiles, *IEEE Trans. Magn.* 35 (1999) 3652.
- [4] Y. Chen, J. E. Snyder, K. W. Dennis, R. W. McCallum and D. C. Jiles, *J. Appl. Phys.* 87 (2000) 5798.
- [5] R. M. Bozorth and J. G. Walker, *Phy. Rev.* 88 (1952) 1209.
- [6] R. M. Bozorth, E. F. Tilden and A. J. Williams, *Phy. Rev.* 99 (1955) 1788.
- [7] R. W. McCallum, K. W. Dennis, D. C. Jiles, J. E. Snyder and Y. H. Chen, *Low Temp. Phys.* 27 (2001) 266.
- [8] A. Muhammad, R. Sato-Turtelli, M. Kriegisch, R. Groessinger, F. Kubel and T. Konegger, *J. Appl. Phys.* 111 (2012) 013918.

# Chapter 6

## Magnetostriction Studies on Mn Substituted Cobalt Ferrite Derived from Nanocrystalline Powders

### 6.1 Introduction

Cobalt ferrite is a suitable alternative magnetostrictive material for various applications over the currently used Terfenol based alloys [1]. The major problem for using sintered cobalt ferrite for magnetostrictive applications is the low magnetomechanical coupling factor or the strain derivative, along with the relatively low magnetostriction coefficient [2, 3]. It has been proposed that the strain derivative can be enhanced by suitable substitution by Mn ions [4]. Greenough and Lee have studied the magnetostriction constants of single crystals of cobalt-manganese ferrites  $\text{Co}_x\text{Mn}_{1-x}\text{Fe}_2\text{O}_4$  series as a function of temperature [5]. The authors found that magnetostrictive properties of Mn substituted cobalt ferrite depend on the occupation of cobalt ions at the B sites of the spinel lattice, which can be altered by heating the materials at different temperatures. The observed temperature dependence of magnetostriction was found to be in good agreement with the theoretical predictions. Pointon and Akers have studied the theoretical aspects of substituting Mn for Co and Fe, on the magnetostriction constants of cobalt ferrite [6]. Using *ab initio* calculations, the authors have studied the effect of Mn ions in cobalt ferrite on the magnetostriction coefficients  $\lambda_{100}$  and  $\lambda_{111}$ . These calculations were based on theoretical predictions of the single-ion model. The results showed that  $\text{Mn}^{3+}$  ions

substituted on the octahedral sites have negligible contribution whereas  $\text{Mn}^{3+}$  ions substituted in the tetrahedral sites have a significant contribution on magnetostriction. The calculations also predicted that,  $\text{Mn}^{4+}$  ions, if present in the tetrahedral sites, could be an additional source of magnetostriction whereas  $\text{Mn}^{4+}$  ions in the octahedral sites do not contribute to magnetostriction. Thus, the reported studies revealed the importance of Mn substitution in determining the magnetostrictive properties of cobalt ferrite.

Recent studies have shown that magnetostrictive properties of sintered polycrystalline cobalt ferrite can be controlled and tailored to practical applications through the appropriate choice of substitution of different divalent and trivalent cations. The substitution of different metal ions ( $\text{Mn}^{3+}$ ,  $\text{Cr}^{3+}$ ,  $\text{Zn}^{2+}$ ,  $\text{Si}^{4+}$  and  $\text{Ga}^{3+}$ ) for Fe in cobalt ferrite has been found to increase the strain derivative even though the magnetostriction value is considerably decreased for the material synthesized through the conventional ceramic route [4,7-17]. Paulson *et al* studied the substitution of Mn for Fe in cobalt ferrite,  $\text{CoFe}_{2-x}\text{Mn}_x\text{O}_4$ , to investigate the effects of composition on the magnetostriction coefficient [4]. It was found that magnetization, magnetostriction and Curie temperature were decreased with increasing Mn content. A drastic reduction in the magnetostriction was observed between  $0.2 < x < 0.4$ , with enhanced strain derivative. Caltun *et al* have investigated the effect of Mn substitution for Fe in the series  $\text{CoFe}_{2-x}\text{Mn}_x\text{O}_4$  ( $x$  varies from 0 to 0.6) and found that by adjusting the Mn content and sintering process parameters, the properties of the materials could be optimized for use in magnetomechanical stress sensors, even though the magnetostriction coefficient decreased drastically upon substitution [13, 14]. Bhome and Joy have compared the effect of replacing both Co and Fe by Mn in cobalt ferrite on the magnetostriction coefficient [15-17]. However, a decrease in the magnetostriction coefficient and saturation magnetization, with increasing concentration of the Mn at both Fe and Co sites, was observed, despite the fact that there is an improvement in the strain derivative. Mössbauer spectroscopy studies of  $\text{CoFe}_{2-x}\text{Mn}_x\text{O}_4$  showed that  $\text{Mn}^{3+}$  ions occupy the octahedral (B) sites and displace  $\text{Co}^{2+}$  ions to the tetrahedral (A) sites in the spinel lattice [18]. Similarly, Melikhov *et al* studied the magnetic anisotropy of  $\text{CoFe}_{2-x}\text{Mn}_x\text{O}_4$  and

found that the anisotropy decreases with increasing Mn content [19]. This proved that the change in anisotropy is due to the displacement of Co from the octahedral sites by Mn.

Several reports are available in the literature on the magnetic and magnetostrictive properties of substituted cobalt ferrite. These studies are focused on samples prepared by the ceramic method, where the control over the grain size and their distribution are very hard to be achieved. It is desirable to get higher magnetostriction coefficient along with large strain derivative for Mn substituted cobalt ferrite for practical applications. However, so far there are no reports on the magnetostriction studies of Mn substituted cobalt ferrite derived from nanocrystalline materials. Since cobalt ferrite synthesized by the autocombustion method and sintered under optimized conditions showed very large magnetostriction and strain derivative, as discussed in the previous chapters, we have investigated the influence of the initial particle size of the starting powders of  $\text{CoFe}_{2-x}\text{Mn}_x\text{O}_4$  and  $\text{Co}_x\text{Mn}_{1-x}\text{Fe}_2\text{O}_4$  with  $x$  varying from 0 to 0.3 on the magnetostriction coefficient and strain derivative of the sintered ferrite samples.

## 6.2 Synthesis

Nanocrystalline powders of  $\text{CoFe}_{2-x}\text{Mn}_x\text{O}_4$  (CFM) and  $\text{Co}_x\text{Mn}_{1-x}\text{Fe}_2\text{O}_4$  (CMF) with  $x$  varying from 0 to 0.3 with steps of 0.05 were synthesized by the autocombustion method, using glycine as a fuel, as described in Section 3.2. The G/N ratio of 0.09 used for the synthesis of sample G2, which showed highest maximum value of magnetostriction and strain derivative after sintering (Table 3.3) was used for the synthesis of the Mn substituted compositions. Stoichiometric amounts of cobalt, iron and manganese nitrates were dissolved in distilled water. Glycine, corresponding to the G/N ratio of 0.09 was also dissolved separately in minimum amount of distilled water. All the solutions were mixed together and the mixed solution was evaporated on a hot plate. After the evaporation of water, the resulting thick mass burned spontaneously to give the cobalt ferrite powder.

Magnetic and magnetostriction characteristics of substituted cobalt ferrite are shown to exhibit strong dependence on the sintering temperature and substitution levels [20]. Most of the studies on the magnetostriction of Mn substituted cobalt ferrite have been made on the samples sintered at 1300 °C. Caltun *et al* have studied the effect of chemical composition and sintering conditions on the microstructure, magnetic and magnetostrictive properties of Mn substituted sintered polycrystalline cobalt ferrite [21]. The authors found that the manganese substituted cobalt ferrite sintered at 1300 °C shows maximum value of magnetostriction as well as high strain derivative. Therefore, in the present study, initially the as-synthesized  $\text{CoFe}_{2-x}\text{Mn}_x\text{O}_4$  and  $\text{Co}_{1-x}\text{Mn}_x\text{Fe}_2\text{O}_4$  powders were compacted and sintered at 1300 °C for 10 minutes.

## 6.3 Results and Discussion

### 6.3.1 Powder XRD Analysis

Powder XRD measurements were used to confirm the formation and phase purity of all the samples and some of the patterns are shown in Figure 6.1. Only the most intense reflection of the cubic spinel ferrite is observed in all the XRD patterns. This reflection in the XRD patterns of both  $\text{CoFe}_{2-x}\text{Mn}_x\text{O}_4$  and  $\text{Co}_{1-x}\text{Mn}_x\text{Fe}_2\text{O}_4$  series are very broad, indicating the nanocrystalline nature of the samples prepared with the present approach. The average crystallite size was calculated using the Scherrer formula, estimated from the FWHM intensity for the (311) reflection. The calculated average crystallite size was ~4 nm for all compositions for both series.

XRD patterns of some of the sintered samples in both the  $\text{CoFe}_{2-x}\text{Mn}_x\text{O}_4$  and  $\text{Co}_{1-x}\text{Mn}_x\text{Fe}_2\text{O}_4$  series are shown in Figure 6.2. All the XRD patterns show formation of single phase spinel ferrite. Further confirmation for substitution of Mn in the cobalt ferrite lattice for Co as well as Fe is obtained from Curie temperature measurements as discussed in the next section.

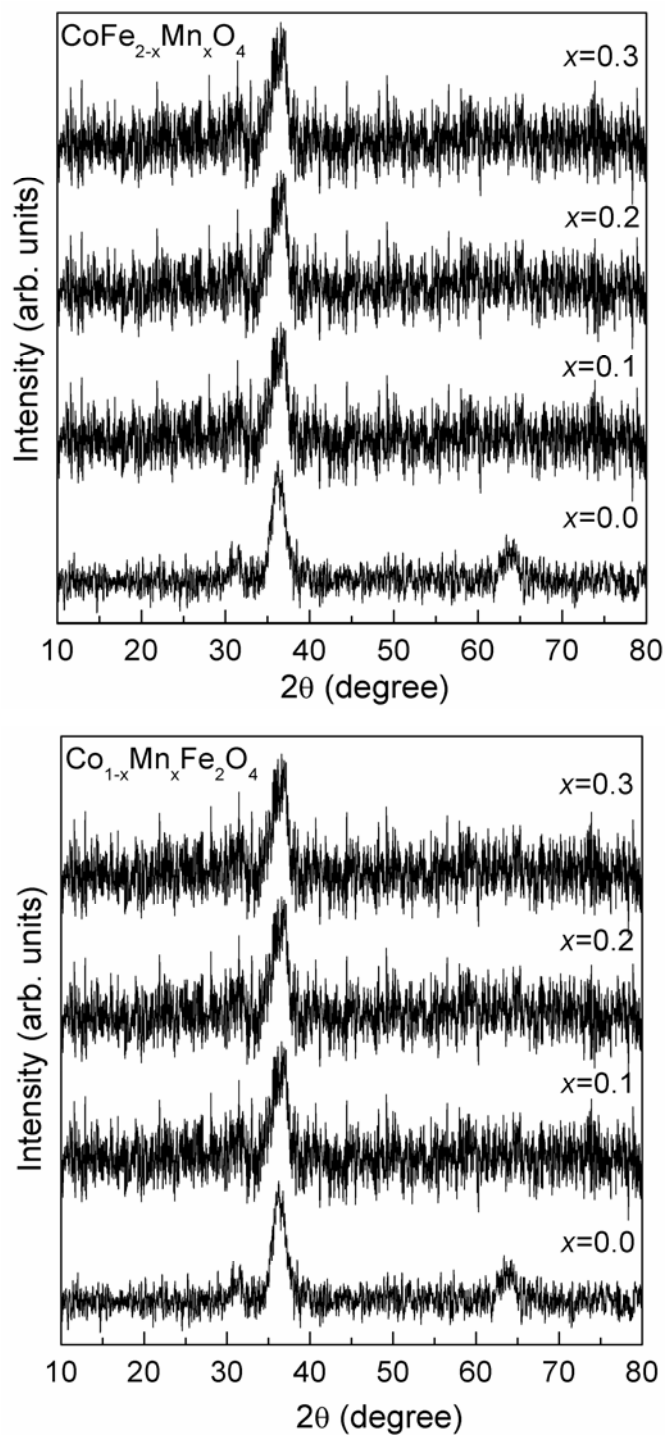


Figure 6.1: Powder XRD patterns of the as-synthesized samples of  $\text{CoFe}_{2-x}\text{Mn}_x\text{O}_4$  and  $\text{Co}_{1-x}\text{Mn}_x\text{Fe}_2\text{O}_4$  for different  $x$  values, as indicated.

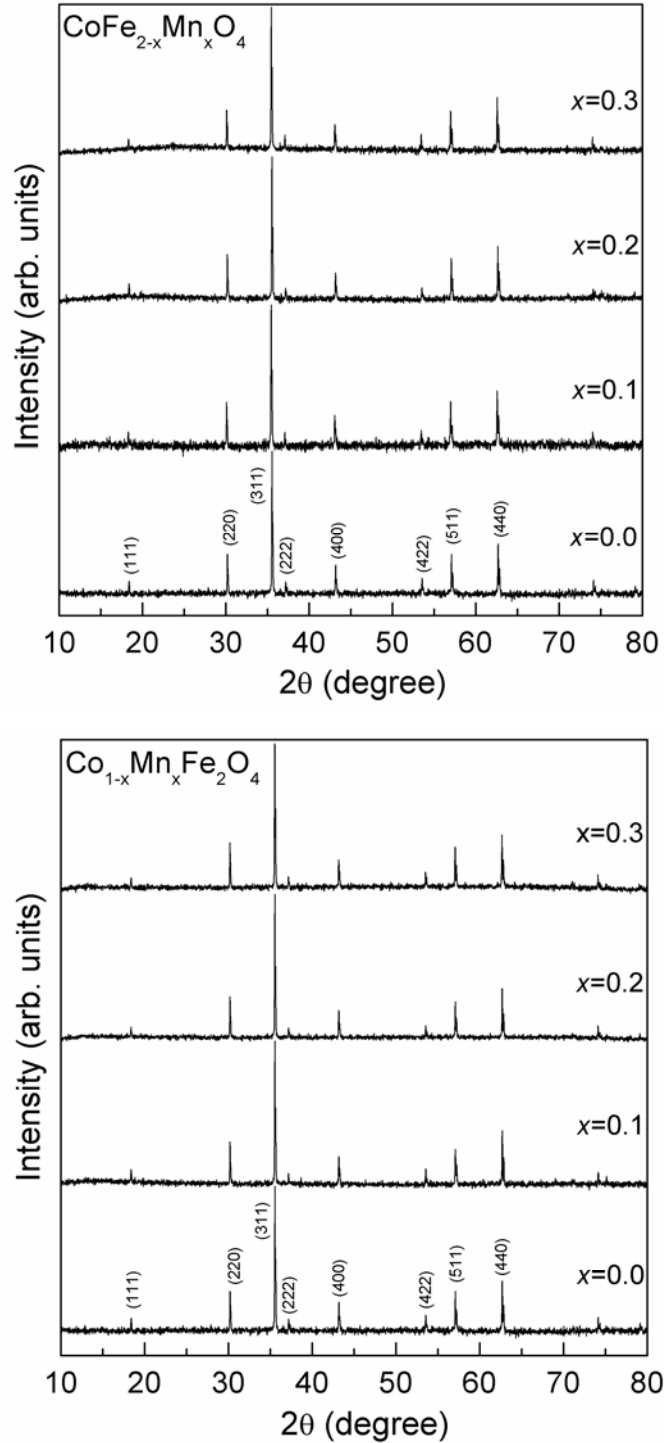


Figure 6.2: Powder XRD patterns of the sintered samples of  $\text{CoFe}_{2-x}\text{Mn}_x\text{O}_4$  as well as  $\text{Co}_{1-x}\text{Mn}_x\text{Fe}_2\text{O}_4$  for different  $x$  values, as indicated.

### 6.3.2 Magnetic Measurements

Magnetic measurements were made on the sintered samples to confirm the formation of the Mn-substituted compositions. The temperature dependence of the magnetization, measured in a magnetic field of 8 kA/m, is shown in Figure 6.3 and the variation of the Curie temperature as a function of Mn concentration for both series is shown in Figure 6.4. It can be seen that Curie temperature ( $T_c$ ) for both series continuously decreases with increasing Mn content. In the  $\text{CoFe}_{2-x}\text{Mn}_x\text{O}_4$  series, the Curie temperature is decreased from 795 K to 712 K for the variation of  $x$  from 0 to 0.3. On the other hand, the variation is from 795 K to 766 K in the case of  $\text{Co}_{1-x}\text{Mn}_x\text{Fe}_2\text{O}_4$  series. For both the series, a linear decrease in the Curie temperature is observed. The trend in the decrease in the Curie temperature is comparable to that reported for bulk  $\text{CoFe}_{2-x}\text{Mn}_x\text{O}_4$  as reported by Paulson *et al* [4] as well as by Bham and Joy [17]. These results confirm the formation of the corresponding Mn substituted compositions.

The difference in the variation of the Curie temperatures of the  $\text{CoFe}_{2-x}\text{Mn}_x\text{O}_4$  and  $\text{Co}_{1-x}\text{Mn}_x\text{Fe}_2\text{O}_4$  series is due to the difference in the cation distributions in the octahedral and tetrahedral sites of the spinel ferrite lattice. When  $\text{Mn}^{2+}$  is substituted for  $\text{Co}^{2+}$ ,  $\text{Mn}^{2+}$  ions preferentially occupy the tetrahedral sites as in the case of  $\text{MnFe}_2\text{O}_4$ . Whereas  $\text{Mn}^{3+}$  ions substituted for  $\text{Fe}^{3+}$  will lead to octahedral site occupancy of the  $\text{Mn}^{3+}$  ions, as in the case of  $\text{CoMn}_2\text{O}_4$ . The reducing amount of strong Fe-O-Fe exchange interactions when Mn is substituted for Fe can affect the Curie temperature drastically. The Curie temperature for  $\text{CoMn}_2\text{O}_4$  is 90 K [22] whereas for  $\text{MnFe}_2\text{O}_4$  it is 573 K [23]. When Mn is substituted for Co, the Curie temperature is expected to decrease but not as rapidly as when compared to Mn is substituted for Fe. In present case, the observed changes in the Curie temperature are in accordance with these conclusions. The magnetic properties of the sintered samples are summarized in Table 6.1.

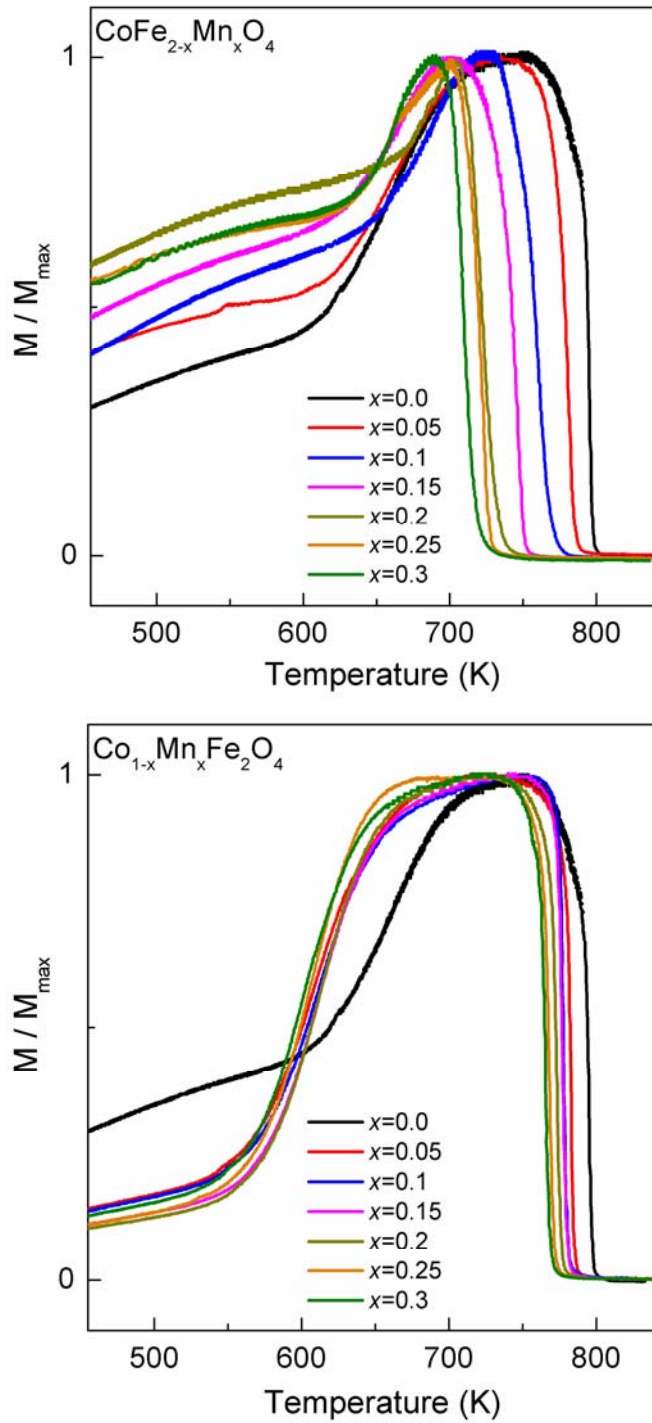


Figure 6.3: Temperature dependence of the magnetization for different compositions of sintered  $\text{CoFe}_{2-x}\text{Mn}_x\text{O}_4$  and  $\text{Co}_{1-x}\text{Mn}_x\text{Fe}_2\text{O}_4$  samples.

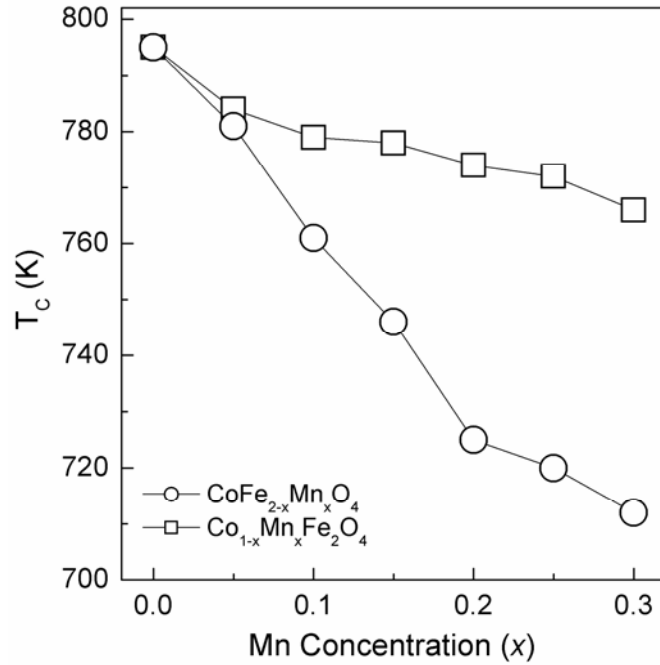


Figure 6.4: Variation of the Curie temperature ( $T_c$ ), as a function of Mn concentration for the  $\text{CoFe}_{2-x}\text{Mn}_x\text{O}_4$  and  $\text{Co}_{1-x}\text{Mn}_x\text{Fe}_2\text{O}_4$  samples.

The room temperature saturation magnetization and coercivity of the sintered  $\text{CoFe}_{2-x}\text{Mn}_x\text{O}_4$  and  $\text{Co}_{1-x}\text{Mn}_x\text{Fe}_2\text{O}_4$  samples are given in Table 6.1. For  $\text{CoFe}_{2-x}\text{Mn}_x\text{O}_4$ , saturation magnetization slightly decreases with substituting the manganese concentration. Similar decrease of the magnetization is already reported when Mn is substituted for Fe in  $\text{CoFe}_2\text{O}_4$  [21]. The decrease in the magnetization is due to the decrease in the magnetic moment from  $5 \mu_B$  for  $\text{Fe}^{3+}$  to  $4 \mu_B$  for  $\text{Mn}^{3+}$ . On the other hand, substitution of  $\text{Mn}^{2+}$  for  $\text{Co}^{2+}$  is expected to enhance the magnetization because of an increase of the total magnetic moments when  $\text{Co}^{2+}$  ( $3 \mu_B$ ) is replaced by  $\text{Mn}^{2+}$  ( $5 \mu_B$ ). The experimental magnetic moments of  $\text{CoFe}_2\text{O}_4$  and  $\text{MnFe}_2\text{O}_4$  are  $3.7 \mu_B$  and  $4.6 \mu_B$ , respectively [24]. However, the expected trend is not observed for  $\text{Co}_{1-x}\text{Mn}_x\text{Fe}_2\text{O}_4$  samples. This may be due to the difference in the processing conditions. Another possibility is that the substituted Mn occupies as  $\text{Mn}^{3+}$  in the octahedral sites and displaces  $\text{Fe}^{3+}$  to the tetrahedral sites so that the effective magnetic moment is decreased.

In the  $\text{CoFe}_{2-x}\text{Mn}_x\text{O}_4$  series, the coercivity continuously decreases with increasing manganese concentration. However, in the case of  $\text{Co}_{1-x}\text{Mn}_x\text{Fe}_2\text{O}_4$  series, coercivity initially increased with manganese concentration of  $x = 0.05$  and then decreases with increasing manganese concentration.

Table 6.1: Magnetic properties of the sintered samples of Mn substituted cobalt ferrite.

Concentration (x)	Density (%)	$M_s$ ( $\text{Am}^2/\text{kg}$ )	$H_c$ ( $\text{kA/m}$ )	$T_c$ (K)
$\text{Co}_{1-x}\text{Mn}_x\text{Fe}_2\text{O}_4$				
0	71	80.8	18.5	795
0.05	70	74.6	30.1	784
0.1	69	75.6	28.9	779
0.15	66	75.8	27.9	778
0.2	67	76.6	26.2	774
0.25	63	75.4	24.1	772
0.3	60	74.6	23.9	766
$\text{CoFe}_{2-x}\text{Mn}_x\text{O}_4$				
0	71	80.8	18.5	795
0.05	71	79.6	16.3	781
0.1	71	78.8	12.0	761
0.15	72	79.4	11.9	746
0.2	72	78.5	10.7	725
0.25	65	78.2	10.3	720
0.3	65	77.4	7.6	712

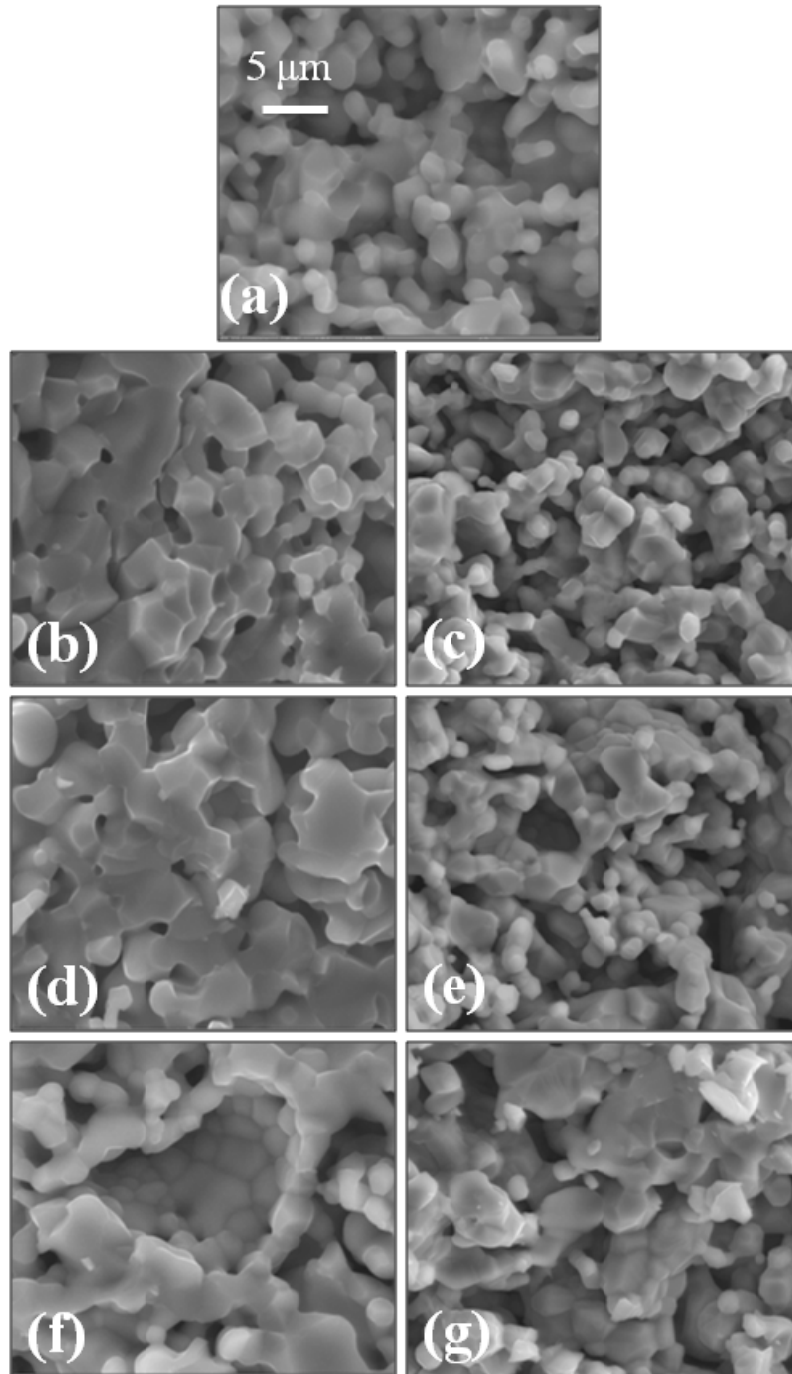


Figure 6.5: SEM images of sintered  $\text{CoFe}_2\text{O}_4$  (a), and for  $x = 0.1, 0.2$  and  $0.3$  in  $\text{CoFe}_{2-x}\text{Mn}_x\text{O}_4$  (b,d,f), and  $\text{Co}_{1-x}\text{Mn}_x\text{Fe}_2\text{O}_4$  (c,e,g).

### 6.3.3 Microstructure

SEM micrographs of the fractured surfaces of the sintered samples of  $\text{CoFe}_{2-x}\text{Mn}_x\text{O}_4$  and  $\text{Co}_{1-x}\text{Mn}_x\text{Fe}_2\text{O}_4$  are shown in Figure 6.5. It can be seen that there is a difference in the microstructure for both the series, compared to the parent sample. The micrograph of the parent sample shows almost uniformly sized grains. However, in the case of the Mn substituted compositions, the porosity and grain size increase with increasing Mn content. This is reflected in the values of the density of the sintered samples also (shown in Table 6.1). The density is decreased in both cases with increasing Mn content. Similar results are reported in the literature for the sintered samples derived from powders synthesized by the ceramic method [15]. In the case of the present samples, grain size is smaller than that reported in the literature for the bulk counterparts [21].

### 6.3.4 Magnetostriction Studies

Figure 6.6 and 6.7, respectively, show the magnetostriction curves of  $\text{CoFe}_{2-x}\text{Mn}_x\text{O}_4$  (CFM) and  $\text{Co}_{1-x}\text{Mn}_x\text{Fe}_2\text{O}_4$  (CMF) series of compositions as a function of magnetic field, measured at room temperature, along the parallel and perpendicular directions to the applied magnetic field. For the CFM series, the maximum value of magnetostriction along the parallel direction ( $\lambda_{\text{par}}$ ) is obtained as 230 ppm for  $x = 0$  above a field of 540 kA/m. Maximum value of  $\lambda_{\text{par}}$  is initially decreased to 203 ppm for  $x = 0.05$  and further increases up to 234 ppm for  $x = 0.2$ . For Mn substituted cobalt ferrite in the series  $\text{CoFe}_{2-x}\text{Mn}_x\text{O}_4$ , so far the highest value reported in the literature is 198 ppm [7]. Also, the maximum value of magnetostriction for  $x = 0.2$  is comparable to that obtained for the unsubstituted cobalt ferrite. Moreover, the field at which the highest value of magnetostriction is obtained is reduced to 360 kA/m for all the CFM series of compositions. The magnetostriction value for CFM for  $x = 0.2$  is larger at low field strengths when compared to that of the unsubstituted cobalt ferrite. For the CMF series, magnetostriction is decreased continuously with increasing manganese concentration ( $x$ ). Magnetostrictive properties of CFM and CMF series of compositions are compared in

Table 6.2. It can be seen that the highest strain derivative of  $1.65 \times 10^{-9} \text{ A}^{-1}\text{m}$  is obtained for  $x = 0.2$  in  $\text{CoFe}_{2-x}\text{Mn}_x\text{O}_4$ , along with the highest magnetostriction. The changes in the maximum value of magnetostriction ( $\lambda_{\text{max}}$ ) along the parallel direction and the corresponding strain derivative ( $d\lambda/dH$ ) of CFM and CMF series as a function of manganese concentration are shown in Figure 6.8. In the case of the CMF series, magnetostriction and strain derivative decreases with increasing manganese concentration ( $x$ ).

Table 6.2: Magnetostrictive properties of  $\text{CoFe}_{2-x}\text{Mn}_x\text{O}_4$  and  $\text{Co}_{1-x}\text{Mn}_x\text{Fe}_2\text{O}_4$  series of compositions.

Concentration ( $x$ )	$\text{CoFe}_{2-x}\text{Mn}_x\text{O}_4$			$\text{Co}_{1-x}\text{Mn}_x\text{Fe}_2\text{O}_4$		
	$\lambda_{\text{par}}$ (ppm)	$\lambda_{\text{per}}$ (ppm)	$d\lambda/dH$ ( $10^{-9}\text{A}^{-1}\text{m}$ )	$\lambda_{\text{par}}$ (ppm)	$\lambda_{\text{per}}$ (ppm)	$d\lambda/dH$ ( $10^{-9}\text{A}^{-1}\text{m}$ )
0	-230	+43	-1.01	-230	+43	-1.01
0.05	-203	+55	-1.08	-212	+93	-1.01
0.1	-209	+49	-1.33	-202	+92	-0.98
0.15	-212	+42	-1.62	-190	+89	-0.87
0.2	-234	+16	-1.65	-171	+90	-0.83
0.25	-194	+35	-1.59	-158	+74	-0.70
0.3	-185	+25	-1.43	-155	+77	-0.70

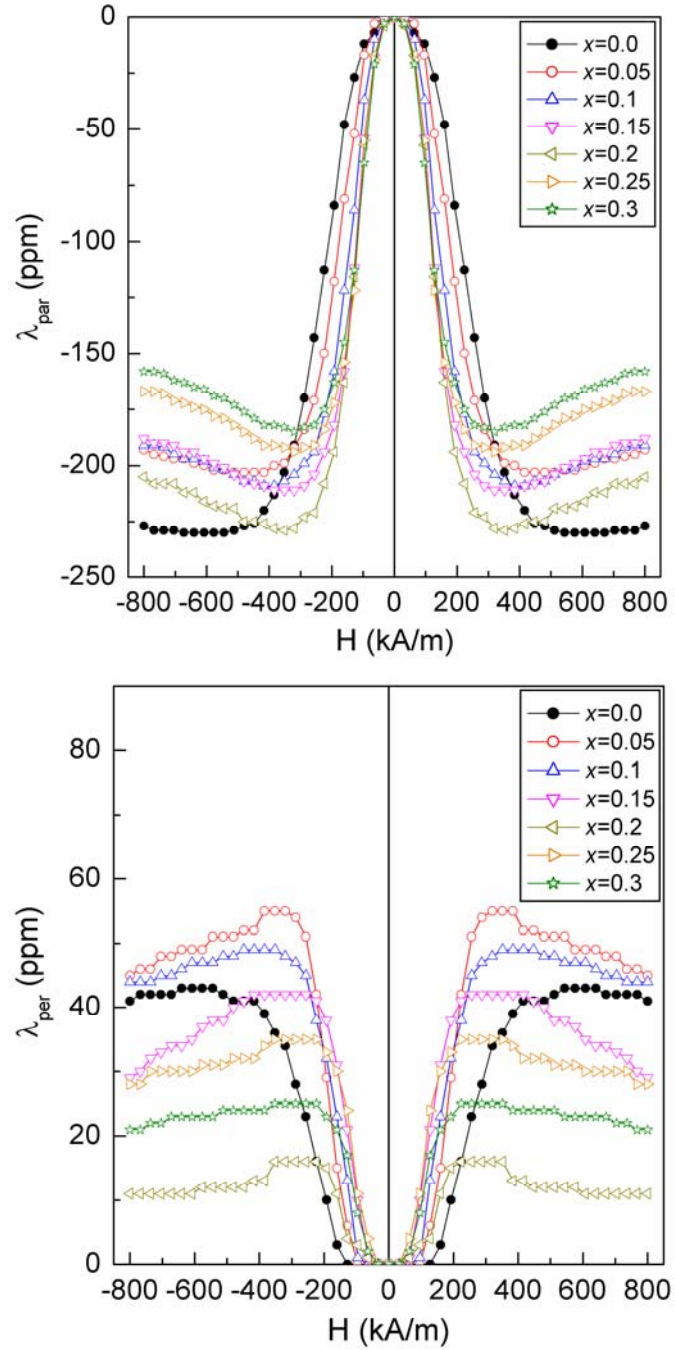


Figure 6.6: Magnetostriction curves of different compositions of  $\text{CoFe}_{2-x}\text{Mn}_x\text{O}_4$  sintered samples as a function of applied magnetic field measured along the parallel ( $\lambda_{\text{par}}$ ) and perpendicular ( $\lambda_{\text{per}}$ ) directions.

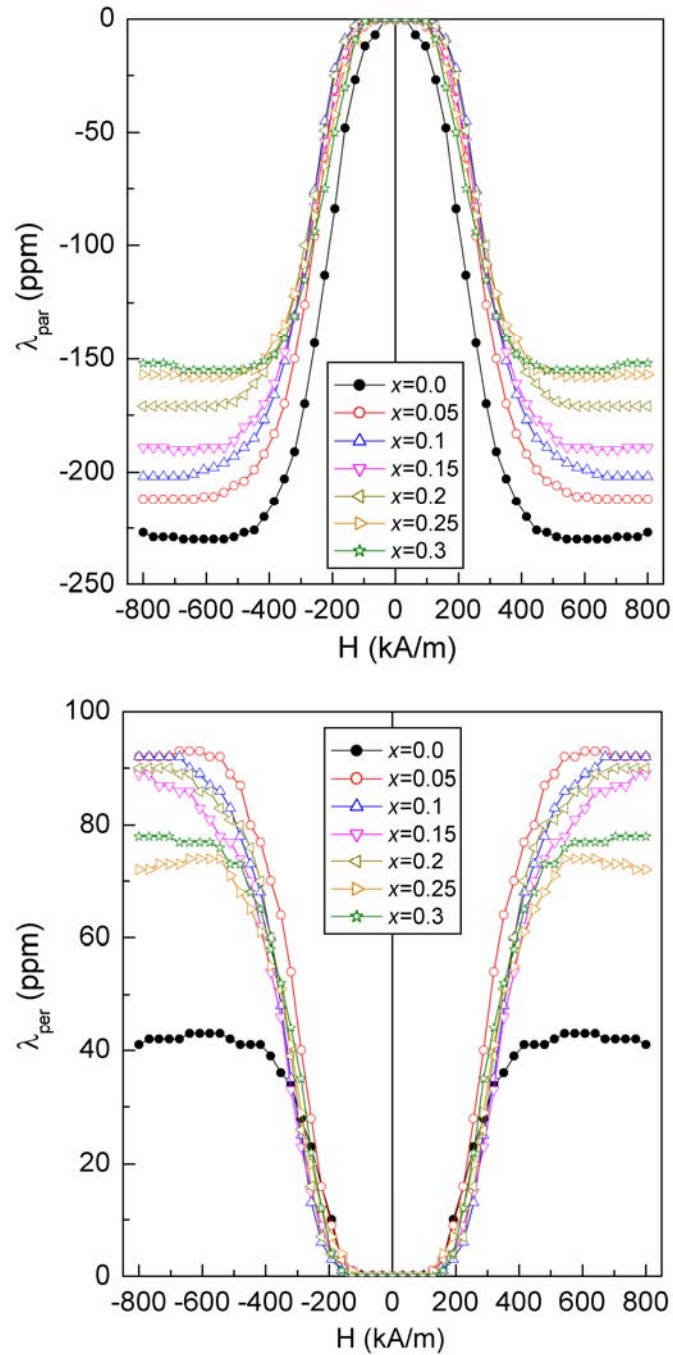


Figure 6.7: Magnetostriction curves of different compositions of  $\text{Co}_{1-x}\text{Mn}_x\text{Fe}_2\text{O}_4$  sintered samples as a function of applied magnetic field measured along the parallel ( $\lambda_{\text{par}}$ ) and perpendicular ( $\lambda_{\text{per}}$ ) directions.

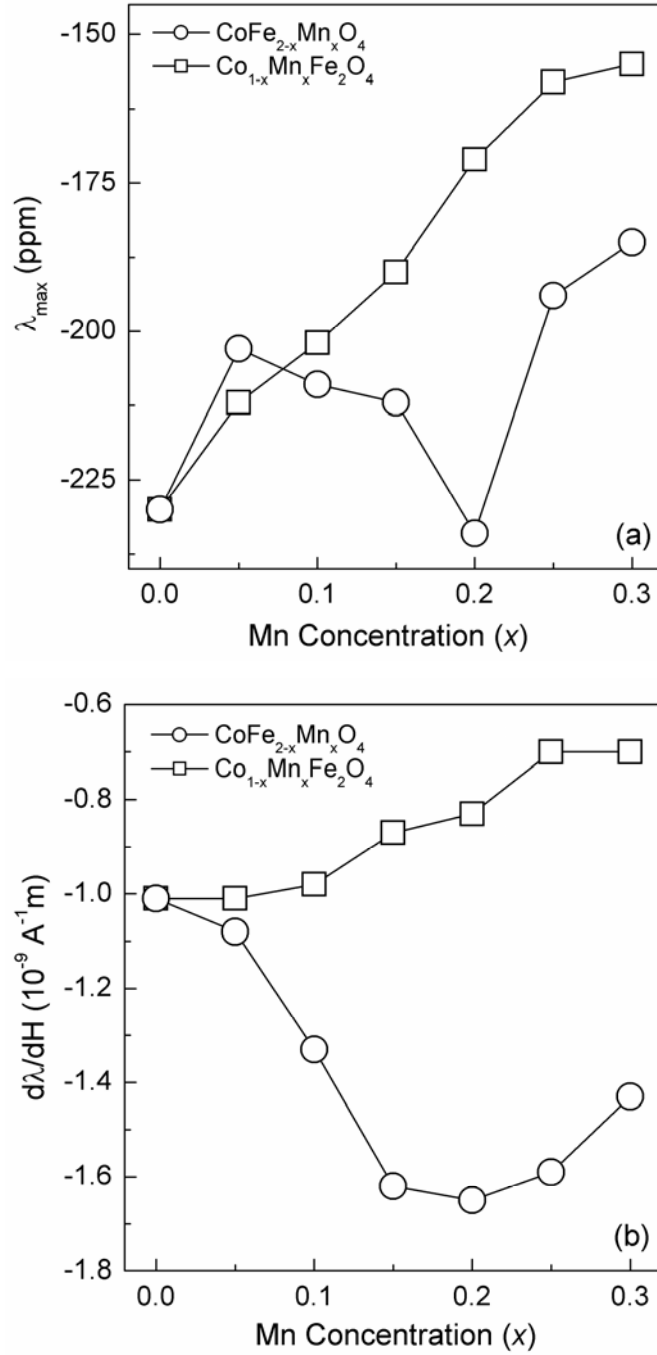


Figure 6.8: Variation of the (a) maximum value of magnetostriction and (b) strain derivative of sintered  $\text{CoFe}_{2-x}\text{Mn}_x\text{O}_4$  (circle) and  $\text{Co}_{1-x}\text{Mn}_x\text{Fe}_2\text{O}_4$  (square) as a function of Mn concentration.

### 6.3.5 Effect of Sintering Temperature on $\text{CoFe}_{1.8}\text{Mn}_{0.2}\text{O}_4$

In Chapter 4, it has been shown that the magnetostriction characteristics strongly depend on the sintering temperature for the unsubstituted cobalt ferrite. Hence, the effect of sintering temperature for the composition  $x = 0.2$  in  $\text{CoFe}_{2-x}\text{Mn}_x\text{O}_4$ , i.e.,  $\text{CoFe}_{1.8}\text{Mn}_{0.2}\text{O}_4$  which showed the highest maximum value of magnetostriction as well as high strain derivative has been studied. SEM micrographs of  $\text{CoFe}_{1.8}\text{Mn}_{0.2}\text{O}_4$  sintered at different temperatures are shown in Figure 6.9. As seen in the figure, there is a change in microstructure with increasing sintering temperature. Samples sintered at a lower temperature of 1200 °C showed smaller grains. Grain size increased drastically with increase in the sintering temperature. Density is also found to be increased with increase in the sintering temperature (shown in Table 6.3).

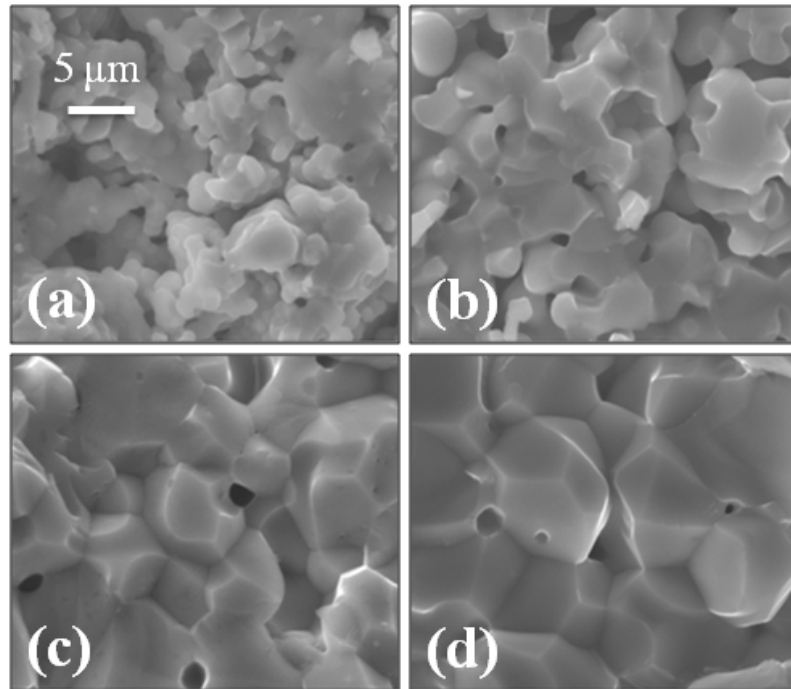


Figure 6.9: SEM images of  $\text{CoFe}_{1.8}\text{Mn}_{0.2}\text{O}_4$  samples sintered at (a) 1200 °C (b) 1300 °C (c) 1400 °C and (d) 1450 °C.

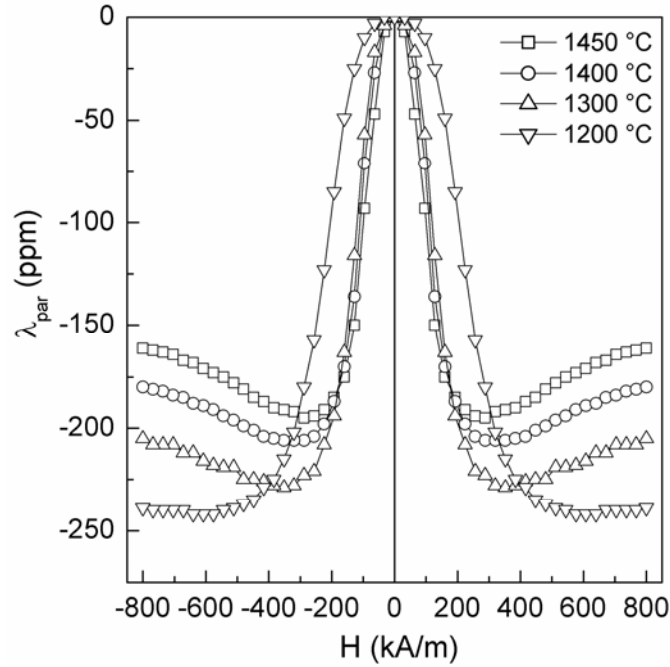


Figure 6.10: Magnetostriction curves measured in the parallel direction to the applied magnetic field for the  $\text{CoFe}_{1.8}\text{Mn}_{0.2}\text{O}_4$  sample sintered at different temperatures.

Table 6.3: Properties of  $\text{CoFe}_{1.8}\text{Mn}_{0.2}\text{O}_4$  sample sintered at different temperatures.

Sintering temperature (°C)	D (%)	$\lambda_{\text{par}}$ (ppm)	$d\lambda/dH$ ( $10^{-9}\text{A}^{-1}\text{m}$ )
1450	81	-197	-1.60
1400	81	-208	-1.60
1300	72	-234	-1.65
1200	63	-242	-1.15

Magnetostriction curves of  $\text{CoFe}_{1.8}\text{Mn}_{0.2}\text{O}_4$  sintered at different temperatures and measured at room temperature in the parallel direction with respect to the applied magnetic field, up to a maximum magnetic field strength of 800 kA/m are shown in Figure 6.10. It can be seen that the value of magnetostriction depends on the sintering temperature. The sample sintered at 1200 °C shows highest maximum value of magnetostriction. However, higher value of magnetostriction is obtained for this sample above a field of 400 kA/m. On the other hand, for all other samples, higher value of magnetostriction is obtained at smaller magnetic fields. For the samples sintered at and above 1300 °C, maximum value of magnetostriction is obtained at a field of 300 kA/m, with a larger strain derivative of  $1.65 \times 10^{-9} \text{ A}^{-1}\text{m}$  for the sample sintered at 1300 °C and the magnetostriction value decreases with increasing sintering temperature. Thus, the results show that sintering the Mn substituted compositions at 1300 °C is ideal for obtaining higher magnetostriction at low fields with larger strain derivative.

### 6.3.6 Effect of Magnetic Annealing on $\text{CoFe}_{1.8}\text{Mn}_{0.2}\text{O}_4$

Figure 6.11 shows the magnetostriction curve and strain derivative of  $\text{CoFe}_{1.8}\text{Mn}_{0.2}\text{O}_4$  before and after annealing in a magnetic field. A maximum magnetostriction value of 234 ppm achieved at 320 kA/m before magnetic field annealing. However, after magnetic field annealing in a magnetic field of 400 kA/m at 300 °C, the maximum value of magnetostriction is further increased up to 262 ppm and the maximum value is obtained at a field as low as 160 kA/m. The strain derivative is also increased to  $2.56 \times 10^{-9} \text{ A}^{-1}\text{m}$ , after field annealing which is much larger than that reported in the literature. Hence the sintered Mn substituted cobalt ferrites derived from nanocrystalline materials are expected to be highly suitable for various applications because of the high magnetostriction and higher strain derivative, especially for the composition  $x = 0.2$  in  $\text{CoFe}_{2-x}\text{Mn}_x\text{O}_4$ , i.e.,  $\text{CoFe}_{1.8}\text{Mn}_{0.2}\text{O}_4$ . In the present work, a high maximum value of magnetostriction of 262 ppm is obtained against 198 ppm [7] which is the largest value so far reported in the literature for Mn substituted sintered cobalt ferrite for the same composition.

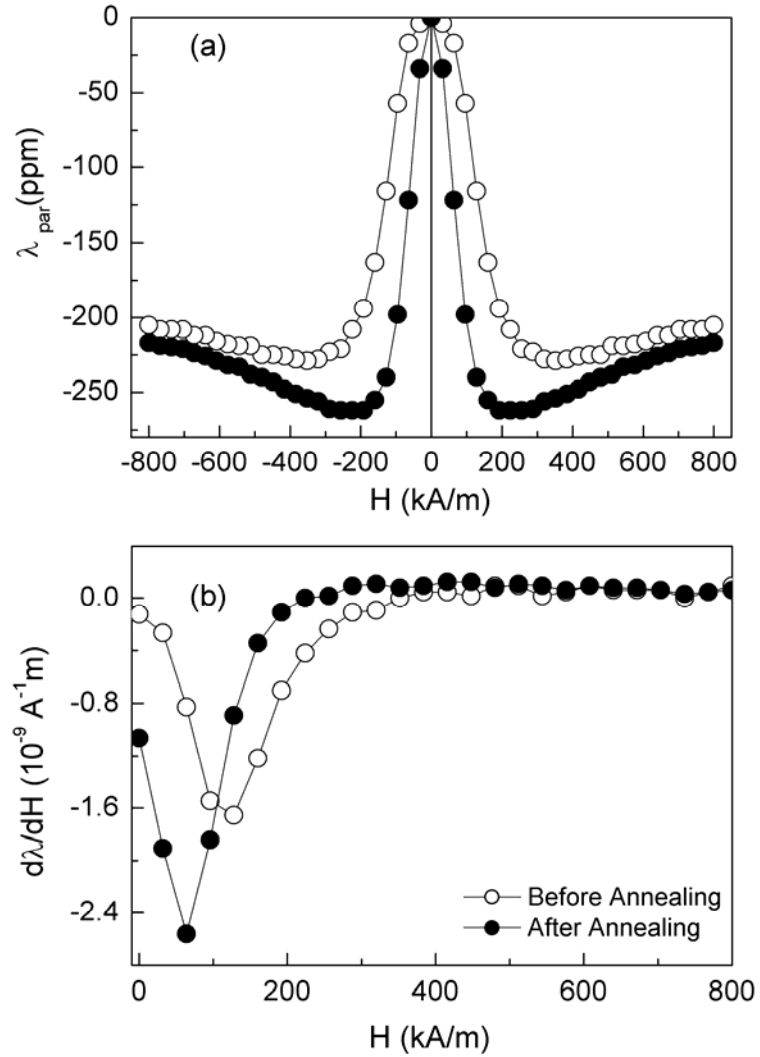


Figure 6.11: (a) Magnetostriction curve of  $\text{CoFe}_{1.8}\text{Mn}_{0.2}\text{O}_4$  as a function of magnetic field measured in the direction parallel to the applied magnetic field before and after annealing, (b) Strain derivative of  $\text{CoFe}_{1.8}\text{Mn}_{0.2}\text{O}_4$ . The open and closed symbols represent measurements before and after magnetic field annealing, respectively.

Table 6.4: Magnetostrictive properties of  $\text{CoFe}_{1.8}\text{Mn}_{0.2}\text{O}_4$  sample before and after magnetic field annealing.

Sample	Before magnetic annealing		After magnetic annealing	
	$\lambda_{\text{par}}$ (ppm)	$d\lambda/dH$ ( $10^{-9}\text{A}^{-1}\text{m}$ )	$\lambda_{\text{par}}$ (ppm)	$d\lambda/dH$ ( $10^{-9}\text{A}^{-1}\text{m}$ )
$\text{CoFe}_{1.8}\text{Mn}_{0.2}\text{O}_4$	-234	-1.65	-262	-2.56

## 6.4 Conclusions

The magnetic and magnetostrictive properties of Mn substituted cobalt ferrite,  $\text{CoFe}_{2-x}\text{Mn}_x\text{O}_4$  and  $\text{Co}_x\text{Mn}_{1-x}\text{Fe}_2\text{O}_4$ , for  $x$  varying from 0 to 0.3 in steps of 0.05, derived from nanocrystalline powders, have been investigated. The magnetostriction coefficient as well as strain derivative are largely affected on substitution of Mn for Co. However, magnetostriction and strain derivative is not much affected when Fe is partially replaced by Mn. The field at which highest magnetostriction value is obtained is shifted to lower values for Mn substituted compositions. For  $\text{CoFe}_{1.8}\text{Mn}_{0.2}\text{O}_4$ , magnetostriction in the parallel direction is comparable to that of unsubstituted cobalt ferrite with enhanced strain derivative when sintered at 1300 °C. Maximum value of magnetostriction and strain derivative are further increased after magnetic field annealing for  $\text{CoFe}_{1.8}\text{Mn}_{0.2}\text{O}_4$ . The present value of 262 ppm is the highest value of magnetostriction coefficient reported till date for Mn substituted cobalt ferrite, suitable for various applications.

## References

- [1] G. Engdahl, *Handbook of Giant Magnetostrictive Materials* (Academic press, San Diego, 2000).
- [2] Y. Chen, J. E. Snyder, K. W. Dennis, R. W. McCallum and D. C. Jiles, *J. Appl. Phys.* 87 (2000) 5798.
- [3] R. W. McCallum, K. W. Dennis, D. C. Jiles, J. E. Snyder and Y. H. Chen, *Low Temp. Phys.* 27 (2001) 266.
- [4] J. A. Paulsen, A. P. Ring, C. C. H. Lo, J. E. Snyder and D. C. Jiles, *J. Appl. Phys.* 97 (2005) 044502.
- [5] R. D. Greenough and E. W. Lee, *J. Phys. D: Appl. Phys.* 3 (1970) 1595.
- [6] A. J. Pointon and N. P. Akers, *J. Magn. Magn. Mater.* 30 (1982) 50.
- [7] O. F. Caltun, I. Dumitru, M. Feder, N. Lupu and H. Chiriac, *J. Magn. Magn. Mater.* 320 (2008) e869.
- [8] S. J. Lee, C. C. H. Lo, P. N. Matlage, S. H. Song, Y. Melikhov, J. E. Snyder and D. C. Jiles, *J. Appl. Phys.* 102 (2007) 073910.
- [9] N. Somaiah, T. V. Jayaraman, P. A. Joy and D. Das, *J. Magn. Magn. Mater.* 324 (2012) 2286.
- [10] G. S. N. Rao, O. F. Caltun, K. H. Rao, B. Parvatheeswara Rao, H. L. Wamocha and H. H. Hamdeh, *Hyperfine Interact.* 184 (2008) 179.
- [11] I. C. Nlebedim, Y. Melikhov, J. E. Snyder, N. Ranvah, A. J. Moses and D. C. Jiles, *J. Appl. Phys.* 109 (2011) 07A908.
- [12] S. H. Song, C. C. H. Lo, S. J. Lee, S. T. Aldini, J. E. Snyder and D. C. Jiles, *J. Appl. Phys.* 101 (2007) 09C517.

- [13] O. F. Caltun, H. Chiriac, N. Lupu, I. Dumitru and B. P. Rao, *J. Optoelectron. Adv. Mater.* 9 (2007) 1158.
- [14] O. F. Caltun, G. S. N. Rao, K. H. Rao, B. P. Rao, C. Kim, C.-O. Kim, I. Dumitru, N. Lupu and H. Chiriac, *Sens. Lett.* 5 (2007) 45.
- [15] S. D. Bhame and P. A. Joy, *J. Appl. Phys.* 99 (2006) 073901.
- [16] S. D. Bhame and P. A. Joy, *J. Appl. Phys.* 100 (2006) 113911.
- [17] S. D. Bhame and P. A. Joy, *J. Phy. D: Appl. Phy.* 40 (2007) 3263.
- [18] K. Kriebel, T. Schaeffer, J. A. Paulsen, A. P. Ring, C. C. H. Lo and J. E. Snyder, *J. Appl. Phys.* 97 (2005) 10F101.
- [19] Y. Melikhov, J. E. Snyder, D. C. Jiles, A. P. Ring, J. A. Paulsen, C. C. H. Lo and K. W. Dennis, *J. Appl. Phys.* 99 (2006) 08R102.
- [20] J. A. Paulsen, C. C. H. Lo, J. E. Snyder, A. P. Ring, L. L. Jones and D. C. Jiles, *IEEE Trans. Magn.* 39 (2003) 3316.
- [21] O. F. Caltun, G. S. N. Rao, K. H. Rao, B. P. Rao, I. Dumitru, C.-O. Kim and C. Kim, *J. Magn. Magn. Mater.* 316 (2007) e618.
- [22] D. G. Wickham and W. J. Croft, *J. Phys. Chem. Solids* 7 (1958) 351.
- [23] G. U. Kulkarni, K. R. Kannan, T. Arunarkavalli and C. N. R. Rao, *Phys. Rev. B* 49 (1994) 724.
- [24] A. Goldman, *Modern Ferrite Technology* (Van Nostrand Reinhold, New York, 1990).

# Chapter 7

## Conclusions and Future Perspectives

Magnetostrictive materials for sensors and actuators have been of great interest because of their variety of applications in the automobile, aerospace, domestic and medical industries such as position sensing, vibration control, stress sensing, magnetostrictive filters etc. Terfenol-D, which is an alloy containing the rare earth elements terbium and dysprosium along with iron, is the currently available magnetostrictive material showing high magnetostrictive strain around 1500 ppm at a relatively low magnetic fields. However, this magnetostrictive material has several limitations and disadvantages including the high cost of the rare earth elements, high brittleness, requirement of single crystals for applications and therefore, the high production cost, etc. Furthermore, the material generates much greater response only when it is subjected to compressive loads, and the power requirement for this class of actuators is greater than those for piezoelectric materials. Therefore, the material is currently used only for strategic applications.

Ceramic oxide based magnetic materials are suitable cheaper alternatives over the currently used alloy-based materials for various applications. Among the different ceramic magnetic oxides, cobalt ferrite,  $\text{CoFe}_2\text{O}_4$ , is known for its high magnetostriction of 600 ppm for single crystals. In addition, this material is very cheap, has good mechanical hardness, chemical stability and can be processed into various shapes and sizes. There have been many attempts to make sintered polycrystalline cobalt ferrite with high magnetostriction at very low magnetic fields. So far only a magnetostriction value of 230 ppm and strain derivative of  $1.3 \times 10^{-9} \text{ A}^{-1}\text{m}$  is attained for sintered cobalt ferrite,

derived by simple processing conditions. It is necessary to achieve relatively large magnetostrictive strain as well as high strain derivative at room temperature for polycrystalline cobalt ferrite for use in various applications which can replace the costly Terfenol-D. The magnetostriction coefficient ( $\lambda$ ) and strain derivative ( $d\lambda/dH$ ) of sintered cobalt ferrite is known to depend on the processing parameters such as the method of synthesis, pressure applied while making the compacts for sintering, sintering atmosphere, temperature, and duration of sintering as well as on the microstructure. So far, there have been no attempts to study the effect of nanocrystalline cobalt ferrite powders as starting materials and the initial particle size on the magnetostriction coefficient. Similarly, there are no studies so far reported on the effect of method of synthesis and sintering conditions on the compacts derived from nanocrystalline materials. In the present work, we have studied the magnetostriction characterization of this material by changing the synthesis and processing conditions.

Nanocrystalline cobalt ferrite of varying particle size is synthesized by autocombustion method, using glycine as a fuel, to study the effect of initial particle size of the powders on the ultimate value of magnetostriction after sintering. The results showed that high values of the magnetostriction coefficient of 315 ppm and strain derivative of  $1.97 \times 10^{-9} \text{ A}^{-1}\text{m}$  are obtained for sintered compacts derived from particles of 4 nm obtained from the autocombustion method and sintered at 1450 °C for 10 minutes. The initial particle size is found to be one of the deciding factor the magnetostrictive behavior of cobalt ferrite. Nanocrystalline cobalt ferrite powders were also synthesized by co-precipitation and citrate methods in order to confirm the correlation between initial particle size and magnetostriction of sintered cobalt ferrite. However, comparison of the effect of the initial particle size derived from the three different methods of synthesis indicated that particle size alone is not the deciding factor for the high values of magnetostriction. Some correlation is observed when the microstructures and densities of the different samples are compared with the values of magnetostriction for the powders derived from the autocombustion method. The observed high magnetostriction value of 315 ppm is further improved to 345 ppm by using

magnetic field annealing at room temperature. Higher magnetostriction is achieved at lower magnetic field after field annealing. These are the highest values reported so far for sintered polycrystalline cobalt ferrite obtained under simple processing conditions.

To study the effect of sintering temperature on magnetostriction, single-stage as well as double-stage sintering studies have been performed. It was found that highest magnetostriction value of 315 ppm is obtained after sintering at 1450 °C under single-stage sintering conditions and the changes in the value of magnetostriction are somewhat correlated with the microstructure. In the case of double-stage sintering, grain size remains constant while density continuously increases, unlike in normal sintering in which final stage densification is always accompanied by rapid grain growth. Out of all the experiments, magnitude of magnetostriction value of 331 ppm is achieved for the sample sintered by the double-stage sintering method at 1450 °C ( $T_1$ ) as the higher temperature and then at 1300 °C ( $T_2$ ) as the lower temperature. It has been found that under suitable two stage sintering conditions, high value of magnetostriction of 331 ppm and strain derivative of  $1.8 \times 10^{-9} \text{ A}^{-1}\text{m}$  can be achieved. Magnetic field annealing has been shown to be very effective in enhancing the magnetostriction and strain derivative of single and two-stage sintered cobalt ferrite samples. Especially, the sample sintered at a low temperature of 1200 °C showed huge increment of magnetostriction as well as strain derivative compared to the two-stage sintered samples after magnetic field annealing. Thus, from the present study it is concluded that there is not much advantages on the two-stage sintering process over single stage sintering for getting higher magnetostriction and strain derivative for sintered cobalt ferrite.

For the first time, we have shown that much higher values of the magnetostriction coefficient can be obtained for sintered polycrystalline cobalt ferrite by making self-composites obtained by sintering a physical mixture of cobalt ferrite powders with different initial particle sizes. Larger maximum value of magnetostriction of  $\sim 400$  ppm and maximum value of strain derivative of  $2.0 \times 10^{-9} \text{ A}^{-1} \text{ m}$  could be achieved for a self-composite made from powders of three different particle sizes in the nano and micrometer levels, whereas the individual components gave values less than 310 ppm.

Unlike for the individual components, the magnetostriction is not saturated at the highest measuring field of 800 kA/m for the three-component composite, indicating that it is further possible to improve the magnetostriction of sintered cobalt ferrite at higher fields. Also, it was found that annealing in a magnetic field reduces the magnetostriction coefficient. Thus, in the case of the self-composites, higher magnetostriction can be achieved without any magnetic field annealing, thereby reducing the processing cost for various applications.

Mn substitution is reported to be very effective in enhancing the strain derivative at the cost of the magnetostriction coefficient. Since higher magnetostriction coefficient and strain derivative could be attained for the sintered unsubstituted material derived from nanocrystalline powders, studies were made on Mn substituted cobalt ferrite powders of particle size 4 nm. The magnetic and magnetostrictive properties of Mn substituted cobalt ferrite,  $\text{CoFe}_{2-x}\text{Mn}_x\text{O}_4$  and  $\text{Co}_x\text{Mn}_{1-x}\text{Fe}_2\text{O}_4$ , for  $x$  varying from 0 to 0.3 in steps of 0.05, derived from nanocrystalline powders of size 4 nm, have been investigated. The magnetostriction coefficient as well as the strain derivative is found to be largely affected on substitution of Mn for Co. However, magnetostriction and strain derivative is not much affected when Fe is partially replaced by Mn. The field at which highest magnetostriction value is obtained is shifted to lower values for Mn substituted compositions. For  $\text{CoFe}_{1.8}\text{Mn}_{0.2}\text{O}_4$ , magnetostriction in the parallel direction is found to be comparable to that of unsubstituted cobalt ferrite with enhanced strain derivative when sintered at 1300 °C. This is the first such report of comparable magnetostriction values for unsubstituted and Mn substituted cobalt ferrite. Maximum value of magnetostriction and strain derivative is further increased after magnetic field annealing of  $\text{CoFe}_{1.8}\text{Mn}_{0.2}\text{O}_4$ . The present value of 262 ppm is the highest value of magnetostriction coefficient reported till date for Mn substituted cobalt ferrite, suitable for various applications.

## Scope for future research

Based on the findings from the present studies on nanocrystalline powders, there is scope for further studies to improve the magnetostriction coefficient and strain derivative of sintered cobalt ferrite. Sintered samples derived from the autocombustion method using glycine as the fuel is found to give very high magnetostriction coefficient and strain derivative compared to literature reports. Studies can be performed using other fuels which may control the surface characteristics of the nanoparticles because of the varying combustion characteristics of different fuels, and this may affect the properties of the sintered products. Similarly, a systematic study of the magnetostriction of sintered products derived from nanocrystalline powders of varying sizes synthesized by different wet chemical methods are required to optimize the best method of synthesis to attain the highest magnetostriction coefficient as well as strain derivative. Since the studies showed that the magnetostrictive properties are correlated with the microstructure of the sintered materials, a systematic study is required on low-temperature sintering and to achieve a suitable microstructure and for understanding the effect of grain size and morphology on magnetostrictive properties. Sintering at low temperatures is possible if the material is synthesized in nanocrystalline form and this can be effective for reducing the processing cost. The sintered materials are found to contain large number of intra-grain pores. These intra-grain and inter-grain pores might be detrimental to the desired properties, which needs to be investigated thoroughly. Similarly, it might be possible to achieve much higher magnetostrictive strains for the sintered products by controlling the grain size by optimizing the processing conditions such as sintering time and addition of sintering aids. Self-composites prepared by mixing nanocrystalline powders of different sizes obtained from different methods of synthesis may be efficient in improving the magnetostriction parameters. Finally, other important factors that need to be considered are the similar studies on substituted cobalt ferrite by replacing Fe by other elements. Enhancing the magnetostriction coefficient of sintered cobalt ferrite up to 500 ppm with high strain derivative may be an achievable target.

## **List of Publications**

1. **K. Khaja Mohaideen** and P.A. Joy, "Enhancement in the magnetostriction of sintered cobalt ferrite by making self-composites from nanocrystalline and bulk powders," *ACS Applied Materials and Interfaces* **4**, 6421-6425 (2012).
2. **K. Khaja Mohaideen** and P.A. Joy, "High magnetostriction and coupling coefficient for sintered cobalt ferrite derived from superparamagnetic nanoparticles," *Applied Physics Letters* **101**, 072405-072408 (2012).
3. **K. Khaja Mohaideen** and P.A. Joy, "Influence of initial particle size on the magnetostriction of sintered cobalt ferrite derived from nanocrystalline powders," *Journal of Magnetism and Magnetic Materials* (2012) (Communicated).
4. **K. Khaja Mohaideen** and P.A. Joy, "Effect of sintering on the magnetostriction of sintered cobalt ferrite derived from nanocrystalline materials," (Manuscript under preparation).
5. **K. Khaja Mohaideen** and P.A. Joy, "Magnetostrictive properties of Mn substituted sintered cobalt ferrite derived from nanocrystalline materials," (Manuscript under preparation).

## **Patent**

1. Composite material with high magnetostriction based on sintered cobalt ferrites, **K. Khaja Mohaideen** and P.A. Joy, (0137-DEL-2012), 17/01/2012.

## **Conference Presentation**

1. **K. Khaja Mohaideen** and P.A. Joy, "Magnetostrictive properties of Mn substituted sintered cobalt ferrite derived from nanocrystalline materials," 19<sup>th</sup> International Conference on Magnetism (ICM-2012), Bexco, Busan, South Korea, 8-13 July 2012.